

The University of Maine

DigitalCommons@UMaine

Electronic Theses and Dissertations

Fogler Library

Winter 12-30-2019

Modeling, Simulation, and Validation of Process-Structure-Property Relationships in Fused Filament Fabrication

Aaron Grant

University of Maine, aaron.grant@maine.edu

Follow this and additional works at: <https://digitalcommons.library.umaine.edu/etd>



Part of the [Mechanical Engineering Commons](#)

Recommended Citation

Grant, Aaron, "Modeling, Simulation, and Validation of Process-Structure-Property Relationships in Fused Filament Fabrication" (2019). *Electronic Theses and Dissertations*. 3149.

<https://digitalcommons.library.umaine.edu/etd/3149>

This Open-Access Thesis is brought to you for free and open access by DigitalCommons@UMaine. It has been accepted for inclusion in Electronic Theses and Dissertations by an authorized administrator of DigitalCommons@UMaine. For more information, please contact um.library.technical.services@maine.edu.

**MODELING, SIMULATION, AND VALIDATION OF PROCESS-STRUCTURE-PROPERTY RELATIONSHIPS IN
FUSED FILAMENT FABRICATION**

By

Aaron Grant, P.E.

B.S. University of Maine, 2013

A THESIS

Submitted in Partial Fulfillment of the

Requirements for the Degree of

Master of Science

(in Mechanical Engineering)

The Graduate School

The University of Maine

December 2019

Advisory Committee:

Dr. Masoud Rais-Rohani, Richard C. Hill Professor and Chair, Mechanical Engineering

Dr. Brett Ellis, Associate Professor, Mechanical Engineering Technology

Dr. Keith Berube, Assistant Professor, Mechanical Engineering Technology

Copyright 2019 Aaron Grant

All Rights Reserved

MODELING, SIMULATION, AND VALIDATION OF PROCESS-STRUCTURE-PROPERTY RELATIONSHIPS IN FUSED FILAMENT FABRICATION

By Aaron Grant

Thesis Advisors: Dr. Masoud Rais-Rohani & Dr. Brett Ellis

An Abstract of the Thesis Presented
in Partial Fulfillment of the Requirements for the
Degree of Master of Science
(in Mechanical Engineering)
December 2019

As additive manufacturing (AM) grows in popularity, the need for better simulation tools to predict the process-structure-property relationships of AM parts becomes ever more necessary to employ the technology in design of functional parts with varying degrees of complexity and performance requirements. Many simulation tools and techniques have been developed that aim to achieve this goal, and the main purpose of this research is to explore how well different simulation tools and modeling approaches can capture various AM-specific features such as inter-raster and end-of raster voids, and residual stresses induced by dissimilar rates of thermal expansion. Process simulation of fused filament fabrication (FFF) through FEA-based code (ABAQUS) and affiliated programs combined with performance simulation through a nonlinear user-material model (GENOA) to predict the tensile and bending properties of Polylactic Acid (PLA) samples. Following the examination of different process parameters such as rate of extrusion per distance travel, fan speed, and nozzle temperature through a multi-factor design of experiments, an optimal setting was identified and used to explore the effect of raster architecture on tensile response of dog-bone specimens based on ASTM D638 standard, and bending response of rectangular beam specimens based on ASTM D790 standard.

Comparison of the experimental data from nearly 300 tests with the simulation-based results indicate that the Young's modulus, ultimate tensile strength, and bending strength predictions are very sensitive to how FFF-induced voids and temperature effects are modeled, and that it is possible to achieve reasonably good agreements (<5% difference in ultimate strength, <8% difference in strain to failure). The results also support future efforts in developing process-informed design optimization tools tied to additive manufacturing.

DEDICATION

This thesis is dedicated to my advisors Dr. Masoud-Rais-Rohani, and Dr. Brett Ellis, without which this work would not have been possible.

ACKNOWLEDGEMENTS

The author would like to extend thanks to Dr. Keith Berube for many aspects of aid in performing experimental evaluation of tensile specimen, shear specimen, and in aiding with overall equipment knowledge. The author would also like to thank Dr. Masoud Rais-Rohani for funding and support throughout this project, and Dr. Brett Ellis for expecting the highest standard of robust logic to source from this work.

TABLE OF CONTENTS

DEDICATION	iii
ACKNOWLEDGEMENTS	iv
TABLE OF CONTENTS.....	v
LIST OF TABLES.....	vii
LIST OF FIGURES.....	viii
LIST OF EQUATIONS	xvi
LIST OF ABBREVIATIONS	xvii
Chapter 1: INTRODUCTION	1
1.1: COMMONLY RECOGNIZED METAL AM AND POLYMER AM METHODS.....	2
1.2: THE RELEVANT POINTS OF RELATED LITERATURE REVIEW	7
1.3: SIMULATION OF AN AM PROCESS	13
Chapter 2: THE GEOMETRY, THE SLICER SETTINGS, AND THE G-CODE	17
2.1: SPECIFICATION OF PREFERRED SETTINGS:.....	19
2.2: JUSTIFICATION OF PREFERRED SETTINGS AND PROGRESSION OF MATERIAL PROPERTIES:.....	21
2.3: MEANS OF EDITING G-CODE:.....	39
2.3.1: THE STRUCTURE OF THE EXCEL-BASED POST-PROCESSOR:.....	40
2.3.2: MATLAB POST-PROCESSOR:.....	42
2.3.3: G-CODE SYNTAX AND SLICER SETTINGS WHICH OFFERED BENEFICIAL FREEDOMS:.....	43
Chapter 3: PRINTING AND TESTING ASTM D638 HALF-AND FULL-SCALE PLA SPECIMENS	44
Chapter 4: EXPERIMENTAL DETERMINATION OF PROCESS SETTINGS FOR AM OF PLA	51
Chapter 5: UNDERSTANDING DEFECT MODELING	60
5.1: ACCOUNTING FOR HOMOGENIZED VOID EFFECTS.....	64
5.2: THE DEFAULT APPROACH	72
5.3: THE SHORTFALLS OF THE DEFAULT APPROACH	73
5.4: USER INFORMED CALIBRATION APPROACH	77
Chapter 6: ACCOUNTING FOR TEMPERATURE EFFECTS	86
Chapter 7: PROCESS-INFORMED MATERIAL MODELING	93
7.1: DISCUSSION OF THE REQUISITE INPUTS TO THE MESH/MODEL GENERATOR.....	96
7.1.1: THE DESCRIPTION AND SPECIFICATION OF FILE-BASED INPUTS	97
7.1.2: DESCRIPTION AND SPECIFICATION OF THE TEXT-FIELD BASED INPUTS	101

7.2: PROCESS OF GENERATING ALL SIMULATION FILES	103
7.3 MODIFICATION OF INPUT FILES	107
7.3.1: MODIFICATION OF THE THERMAL SIMULATION	107
7.3.2: THE MODIFICATION OF THE RESIDUAL STRESS SIMULATION	111
7.3.3: THE GENERATION OF THE SERVICE LOADING SIMULATION	112
7.4: RUNNING THE FILES AND PROCESSING THE OUTPUTS	117
Chapter 8: RESULTS AND DISCUSSION FOR VALIDATION OF THE DEFAULT APPROACH	120
8.1: DISCUSSION OF SIMULATION RESULTS FOR THE DEFAULT APPROACH	133
Chapter 9: THE USER-INFORMED CALIBRATION APPROACH	135
9.1: THE PRESENTATION OF THE USER-INFORMED CALIBRATION APPROACH	135
9.1.1: THE FIRST PHASE OF THE USER-INFORMED CALIBRATION APPROACH	138
9.1.2: THE SECOND PHASE OF THE USER-INFORMED CALIBRATION APPROACH	144
9.2: RESULTS AND DISCUSSION OF THE USER-INFORMED CALIBRATION APPROACH	150
9.2.1: DISCUSSION REGARDING PATHCOVERAGE	154
9.2.2: DISCUSSION REGARDING THE USER-INFORMED CALIBRATION APPROACH	158
Chapter 10: CONCLUSION	160
REFERENCES	163
APPENDIX A: A TUTORIAL TRACING THE GENERATION OF A SIMULATED TENSILE RESPONSE	167
APPENDIX B: PRESENTATION OF SHEAR DATA FROM DIC TESTING	225
BIOGRAPHY OF THE AUTHOR	234

LIST OF TABLES

Table 2.1	Modified Cura v3.6.0 [1] slicing parameters.....	19
Table 4.1	Inputs and outputs for the DOE to optimize 22 tensile strength.....	52
Table A.1	Case specific Cura v3.6.0 [1] slicing parameters for D638HS simulation.....	172

LIST OF FIGURES

Figure 1: Schematic of a PBF process [7]	3
Figure 2: A schematic of a DED process [9]	4
Figure 3: Schematic of an EBAM process [12]	5
Figure 4: A schematic of a BJP process [12]	6
Figure 5: A schematic of an FDM process	7
Figure 6: A map depicting relations between process, structure, properties, and performance	10
Figure 7: SEM images of an FFF mesostructure, a.) printed at 190 °C, b.) at 210 °C [28]	11
Figure 8: The schematic of the path leading to test data (A) or simulated response (B)	14
Figure 9: The geometry of an ASTM D638, type 1, dog bone specimen	18
Figure 10: Depiction of raster orientations for 11, 22, and 33 tensile specimen	19
Figure 11: A chart showing the batches and the settings used	22
Figure 12: Elliptical raster cross-sections for various printing strategies	24
Figure 13: The similar triangles which exist between connected centers of two nested ellipses	25
Figure 14: Percent theoretical density versus Z-compress	27
Figure 15: Raster strategy depictions for various specimen orientations	29
Figure 16: Fractured tensile specimens produced with a 11-direction raster strategy	31
Figure 17: Three batch "S" specimens which exhibiting fracture patterns in the gauge length	32
Figure 18: A visualization of the scan strategy of a longitudinal (11) specimen in Cura	33
Figure 19: The longitudinal (11) specimen generated from the scan strategy shown in Figure 18	34
Figure 20: A nozzle drag on a transverse (22) tensile specimen	37
Figure 21: Removal of a clear PLA ½-scale D638 tensile dog bone specimen with putty knife	44
Figure 22: The folding-and-peeling process, removing brim rasters from a tensile specimen	46
Figure 23: Drawing of custom centering jig utilized specimen positioning in MTS grips	47

Figure 24: The fitment of a tensile specimen to the centering jig	47
Figure 25: MTS Advantage wedge-action grips	48
Figure 26: The 25-mm extensometer used for testing	49
Figure 27: cross-sections of tensile specimens.....	50
Figure 28: The operations to complete a multiquadric radial basis training and prediction	55
Figure 29: Surface plots depicting the two optimal combinations of process settings.....	57
Figure 30: A Stress-Strain graph for the validation of the DOE surrogate model results.....	58
Figure 31: The deformation pattern of a traditionally modeled tensile response	60
Figure 32: A simulated tensile response showing localization in one region.....	61
Figure 33: Outline of the procedure for qualifying 3D-printed material in MCQ-Chopped	64
Figure 34: The initially specified matrix and particle properties	66
Figure 35: A schematic of the derivation of the inclusion settings for a transverse tensile sample	67
Figure 36: A logic map of the iterative process to calibrate simulated strength prediction	68
Figure 37: Orientation settings defining the user-defined coordinate system in Figure 33 (Step H).....	69
Figure 38: The failure criteria settings employed in the process given by Figure 33	70
Figure 39: The settings used for the simulated tensile test in the process given by Figure 33.....	71
Figure 40: The transverse (22) stress-strain data used to calibrate the simulated tensile test	71
Figure 41: The user material constants generated by MCQ-Chopped	72
Figure 42: Material properties through detriment introduction, given the Default Approach	75
Figure 43: Material properties through detriment introduction, given 1 st recommendation.....	78
Figure 44: Material properties through detriment introduction, given 2 nd recommendation.....	80
Figure 45: Material properties through detriment introduction, given 3 rd recommendation	81
Figure 46: A depictions of key differences between a tensile test and a bending test.....	82
Figure 47: Simulated tensile response throughout various stages of simulated loading.....	83

Figure 48: The regions shown to be localizing and recovering in a tensile specimen	84
Figure 49: The global effect of residual stress, presenting in a layer-by-layer fashion	87
Figure 50: Parts of the modeling framework associated with qualification of temperature effects	88
Figure 51: Matrix definitions for each orientation used to execute cure kinetics predictions	89
Figure 52: Description of the mechanical properties generated by MCQ-Composites.....	91
Figure 53: The matrix definitions for multifactor coefficients to generate properties in Figure 52	92
Figure 54: The parts of the modeling framework associated with the process modeling	94
Figure 55: The default settings for the mesh/model generator	96
Figure 56: Varying 33 specimen thickness from a.) to b.) to appropriately generate infill rasters	98
Figure 57: Graphical depictions shown when loading the PathCoverage module	99
Figure 58: A visualization of the external mesh for A.) 11 & 22 specimen, and B.) 33 specimen	100
Figure 59: Visualization of the scan strategy for layer 1 of 22 specimen in PathCoverage	104
Figure 60: Display of key bindings in PathCoverage	105
Figure 61: A depiction of the calculated void ratio map in PathCoverage	106
Figure 62: A depiction of the empirically evaluated temperature gradient during 3D-printing	109
Figure 63: The post-calibration temperature gradient for a 3D-printed tensile specimen.....	110
Figure 64: The cooldown step and the plate removal step for the residual stress simulation	112
Figure 65: The temperature-independent material definition provided to service loading	113
Figure 66: The truncation point in the thermal simulation copy.....	115
Figure 67: Selection of the set "Fixed_node" in ABAQUS CAE	116
Figure 68: The omitted part instance references in the copied node set definitions	116
Figure 69: Specifications of at the end of a service loading input file	117
Figure 70: Command window syntax for the submission of simulations	118
Figure 71: Graphical depictions shown when loading the PathCoverage module	120

Figure 72: Depiction of raster orientations for 11, 22, and 33 tensile specimen	121
Figure 73: Baseline 11-tensile response compared to an experimental 11- tensile response.....	122
Figure 74: Simulated vs Baseline tensile response, strategy of Figure 71A.....	123
Figure 75: The worsening non-convergent condition provided by a sharp-cornered mesh	124
Figure 76: Running PathCoverage on a domain generated by the internal mesh feature	125
Figure 77: Simulated vs Baseline tensile response, strategy of Figure 71b.....	126
Figure 78: The void patterns generated by PathCoverage given differing mesh boundaries	127
Figure 79: The void patterns generated by PathCoverage given consistent 3D data.....	127
Figure 80: The approach angle comparison for 11 specimens (a) versus 22 & 33 specimens (b).....	128
Figure 81: The flow of 3D data from the CAD model to PathCoverage.....	129
Figure 82: Void pattern generated by passing the same 3D data to Cura and ABAQUS.....	130
Figure 83: Void pattern generated by passing the same 3D data to Slic3R and ABAQUS.....	131
Figure 84: Simulated vs Baseline tensile response, strategy of Figure 71c	132
Figure 85: Reformed definition at the initiation of the User-Informed Calibration approach.....	135
Figure 86: The verification tensile test for the 11-direction, given a new filament reel	136
Figure 87: The verification tensile test for the 22-direction, given a new filament reel	136
Figure 88: The verification tensile test for the 33-direction, given a new filament reel	137
Figure 89: The geometry of the 3D-printed bending specimen	138
Figure 90: A depiction of the mesh for the 11-bending and 22-bending specimens	139
Figure 91: A dual definition, separating the compressive definition from the tensile definition	140
Figure 92: Iterative trials given by adjusting the stress-strain response of the bending simulation.....	141
Figure 93: Depiction of raster strategies for 11, 22, and 33 bending specimens	142
Figure 94: A depiction of the mesh for the 33-bending specimen	143
Figure 95: The Load vs Deflection response given by calibration to 11, 22, and 33 bending data	144

Figure 96: The geometry used to match the 11, 22, and 33 tensile response	145
Figure 97: A depiction of the mesh strategy for 11 and 22 tensile specimen	146
Figure 98: The material definition used for the first trial of matching a 11-tension.....	147
Figure 99: the defective region assumed to exist given the details of the scan strategy.....	148
Figure 100: The simulated 11-tensile response given the User-Informed Calibration Approach	149
Figure 101: The simulated 22-tensile response given the User-Informed Calibration Approach	149
Figure 102: The simulated 33-tensile response given the User-Informed Calibration Approach	150
Figure 103: The Load vs Deflection response for both simulated and empirical bending specimens	151
Figure 104: The Stress vs Strain response for both simulated and empirical tensile specimens	152
Figure 105: The final material definition configured for prediction of a bending response	153
Figure 106: The final material definition configured for prediction of a tensile response.....	154
Figure 107: Screenshot of PathCoverage interface, isolating results of 5 elements	155
Figure 108: Structure of the PathCoverage readout	155
Figure 109: Raster orientations for uniaxial service loading trials.....	156
Figure 110: A schematic of the uniaxial service loading simulation to test void result.....	157
Figure 111: The result of varying void on normalized strength across a rectangular section.....	157
Figure 112: Tensile defect magnitude over tensile baseline magnitude for various orientations	158
Figure 113: The 1:2 scale working dimensions	167
Figure 114: The cut rounding the 1:2 scale working dimensions	168
Figure 115: The orientation and locale of 3D-printing coordinate system convention	169
Figure 116: Magnitudes from the "measure "tool" and application of the "Move Face" command.....	170
Figure 117: The application of a rotational "Move Face" to align coordinate system convention	171
Figure 118: Using "Move Face" to apply the g-code offsets from the first travel command.....	174
Figure 119: Adding the baseplate geometry in Solidworks	175

Figure 120: Quartering the tensile specimen and baseplate.....	176
Figure 121: D638HS.IGES import in ABAQUS, highlighting the 1 st and 3 rd gauge length contours.....	177
Figure 122: Display of ABAQUS mirror and cut operations	178
Figure 123: Various partitioning sketch steps to isolate the outer raster boundary	179
Figure 124: A depiction of the tensile specimen before and after completion of partitioning.....	180
Figure 125: A depiction of three points used to create a datum plane.....	181
Figure 126: A depiction of the spacing of datum planes	182
Figure 127: An exploded view of the seven closed contours defined by face partitions	183
Figure 128: Using Ctrl and Alt click and drag to reposition the graphics in ABAQUS CAE	185
Figure 129: The four sets of points used to create 3-point planes for baseplate partitioning.....	186
Figure 130: The four baseplate cell partitions made using “Partition Cell: Use Datum Plane”	187
Figure 131: The geometry after all quarter-model partitioning is complete	187
Figure 132: The model after both “Create Mirror” commands have been executed	188
Figure 133: Four box selections to isolate vertical edges in the baseplate while in “Left View”	189
Figure 134: The deactivation of instance keywords in part and assembly files	190
Figure 135: The five steps involved in job creation and writing a mesh input file	191
Figure 136: The 5-step process to restoring previous settings from a blank GENOA project	193
Figure 137: The required text-field-based and file-based settings to generate input files	194
Figure 138: The color-coded chronology shown by PathCoverage	199
Figure 139: A depiction of the missing mesh overlay on layer 13 in PathCoverage.....	199
Figure 140: The PathCoverage void computation mode window	201
Figure 141: The ABAQUS working directory at various stages throughout the procedure.....	203
Figure 142: A depiction of the section assignments made in the thermal simulation input file.....	205
Figure 143: the specification of initial conditions for the printed material.....	205

Figure 144: A depiction of the syntax for executing the thermal simulation	206
Figure 145: The viewing of a status file in Notepad++.....	206
Figure 146: Two instances of adding the “-VOID” suffix to the material name.....	207
Figure 147: A depiction of the section assignments made in the residual stress input file	207
Figure 148: The syntax for two added steps at the end of the residual stress input file	208
Figure 149: The material definition for the loading simulation, “D638HS11_load”	210
Figure 150: The process of removing the base plate element definitions	211
Figure 151: The solid section assignment in the loading simulation	212
Figure 152: The loading simulation following the removal of all residual stress step definitions	212
Figure 153: The truncation of the copy of the thermal simulation in Notepad++	213
Figure 154: The orphan mesh from the imported copy of the thermal simulation	214
Figure 155: A front view of the orphan mesh of the tensile specimen and baseplate.....	214
Figure 156: Navigating to a set definition to reform either the name or node assignments.....	215
Figure 157: A depiction of the selection of “Fixed_node” and “Load_node”	216
Figure 158: Instance keyword removal for discarded input files to extract node set definitions.....	217
Figure 159: The lines to change the material definition to an implicit simulation.....	219
Figure 160: The lines to change the loading step to an implicit simulation	219
Figure 161: Post-process steps for thermal, residual stress, and service loading simulations	220
Figure 162: The 7-step process to query reaction forces	221
Figure 163: The 6-step process to sum reaction forces.....	221
Figure 164: The 6-step process to measure the cross-sectional area	222
Figure 165: The 5-step process of calculating engineering stress	222
Figure 166: The 9-step process of querying nodal displacement.....	223
Figure 167: The 9-step process of determining strain.....	223

Figure 168: The process of determining engineering stress vs engineering strain	224
Figure 169: Simulated tensile response compared to Baseline definition tensile response.....	224
Figure 170: The orientations investigated for shear testing per ASTM 5379.....	225
Figure 171: The dimensions of the printed shear specimen (millimeters).....	226
Figure 172: Depiction of the scan strategy for vertical specimens.....	226
Figure 173: A depiction of the geometry of the vertical shear specimens.....	227
Figure 174: The shear specimens tested, after undergoing testing	228
Figure 175: Shear Stress vs Shear Strain, Specimen “R01”	228
Figure 176: Shear Stress vs Shear Strain, Specimen “R02”	229
Figure 177: Shear Stress vs Shear Strain, Specimen “R03”	229
Figure 178: Shear Stress vs Shear Strain, Specimen “R04”	230
Figure 179: Shear Stress vs Shear Strain, Specimen “R05”	230
Figure 180: Shear Stress vs Shear Strain, Specimen “R06”	231
Figure 181: Shear Stress vs Shear Strain, Specimen “R08”	231
Figure 182: Shear Stress vs Shear Strain, Specimen “R09”	232
Figure 183: Shear Stress vs Shear Strain, Specimen “R10”	232

LIST OF EQUATIONS

Equation 1	Cartesian ellipse equation relation	25
Equation 2	The decline in layer height	25
Equation 3	Z-compress calculation.....	25
Equation 4	The Z-compress relation, stated in terms of layer height specifications.....	25
Equation 5	The Z-compress relation, stated independent of layer height.....	26
Equation 6	Relative density, Rho.....	26
Equation 7	A full-quadratic multivariate polynomial fitting relation	53
Equation 8	The definition of radial distance per the Euclidian norm	54
Equation 9	The definition of phi, per the radial basis formulation	54
Equation 10	Solving for lambda given the radial basis formulation	54
Equation 11	The steepest descent relation.....	56
Equation 12	The Multifactor relationship	90
Equation 13	The heating ratio calculation	197

LIST OF ABBREVIATIONS

DOE: Design of Experiments, a procedure in which the responses of a system are cast as a function of any number of parameter inputs, in the aim to model the system in terms of input parameters and output responses. By optimizing the system model, optimal input parameters may be determined.

RBF: Radial Basis Function: A function that predicts an arbitrary point in the domain on the basis of the radial distance between the arbitrary point and the training points used to train the function, rather than using Cartesian, polar, or spherical coordinates.

GUI: Graphical user interface: A software interface that provides the end user a graphical means of exploiting software functions, a possible example being ABAQUS CAE.

UTS: Ultimate strength in tensile loading, this refers to the breaking strength in the case of brittle failure from empirically recognized tensile data, and the maximum loading prior to any “load-dropping” effects in the case of ductile failure.

ST: Neat strength in tensile loading, this is a numerically-defined ideal state of a material’s ultimate strength in tension. This idealized measure of strength is absent all effects of manufacturing, including but not limited to: porosity, voids, residual stresses, end-of-raster voids. This material state is also free from all effects of testing, including stress concentrations, compressive stresses introduced by the jaws of the load frame gripping the grip-region of a tensile sample. This definition is strictly applicable to the realm of numerical simulation.

MB1: Mouse-button 1, (Left-click).

MB2: Mouse-button 2, (Right-click).

MB3: Mouse-button 3, (Scroll-wheel click).

Chapter 1: INTRODUCTION

Traditional materials processing techniques are responsible for a vast majority of the parts we see in everyday life, but they are often limited by the technique. Casting is generally a good way of producing high-volume parts, but the process requires the raw material be molten, so the process does not lend itself easily to producing fine-featured internal cavities. There are also casting limitations for external features, on the basis of a parts ability to free from a mold. Machining may be more given to creating fine-featured details, but the process requires any cut geometry to have sufficient fixturing as to prevent deformation, and the ability to clear a machining tool in order to make the cut.

Additive manufacturing (AM), or 3D printing (3DP), is a process that encompasses several methods of layerwise fabrication of a 3D part. With AM, each deposited layer has a finite thickness, and a process of creating sequential layers atop one another leads to the creation of a 3D geometry. Commonly, stereolithography is credited for being the first form of AM to have been patented back in 1986, a process which solidifies a selectively deposited polymer via exposure to UV light [2]. As AM parts are built with a layerwise approach, AM offers the potential to achieve design geometries earlier prohibited by limitations of manufacturing technique. However, AM faces many technique-based challenges which must be addressed prior to industry adoption. Though small complex parts often present feasible opportunities to employ AM, the ability to economically produce large part volumes has always existed as a struggle. Additionally, many AM parts are given to suffering from poor quality consistency. Many machines also only offer the ability to print one part at a time, so scalability is a natural concern [3].

1.1: COMMONLY RECOGNIZED METAL AM AND POLYMER AM METHODS

ASTM 52900 recognizes several types of AM processes, including powder bed fusion (PBF), directed energy deposition (DED), material extrusion, otherwise known as fused filament fabrication (FFF) or fused deposition modeling (FDM), material jetting, binder jetting, sheet lamination, and vat photopolymerization (stereolithography or SLA) [4]. Of these types, machines which use PBF and DED processes constitute a majority of the metal based AM industry, and machines which use FDM and SLA processes constitute a majority of the polymer-based AM industry [5].

PBF is a process in which a thin bed of build powder is rolled over a build volume with each sequential layer, followed by a laser which traces the scan path of the current layer. The region immediately surrounding the path of the laser, or the melt pool, is liquefied by the laser, followed by cooling into a solid state. Following each layer, the build plate then lowers, and the process repeats, leading to the creation of a 3D part [6]. Several studies have been conducted on the basis of varying process parameters in a PBF process, such as laser intensity, layer height, and particle size distribution of the raw material [7]. A schematic of a PBF process is shown in Figure 1:

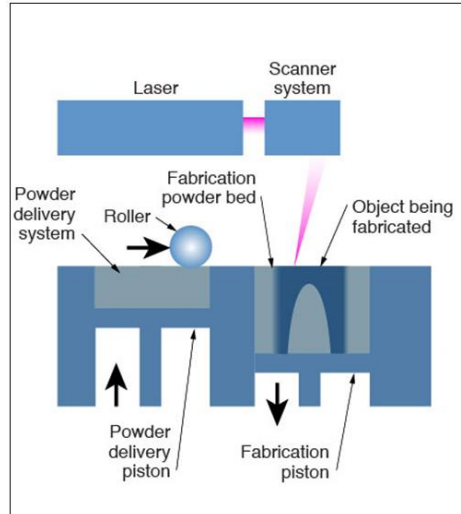


Figure 1: Schematic of a PBF process [7]

DED is a process much like PBF, but the build powder in a DED process is selectively deposited into the melt pool, rather than being raked over each layer. This allows the DED process to be practically purposed towards repairs in a way that a PBF process cannot. DED processes are also capable of swapping material systems on the fly, lending the process to being able to functionally grade materials from one material system to the next [8]. A schematic for a DED processes is shown below, in Figure 2.

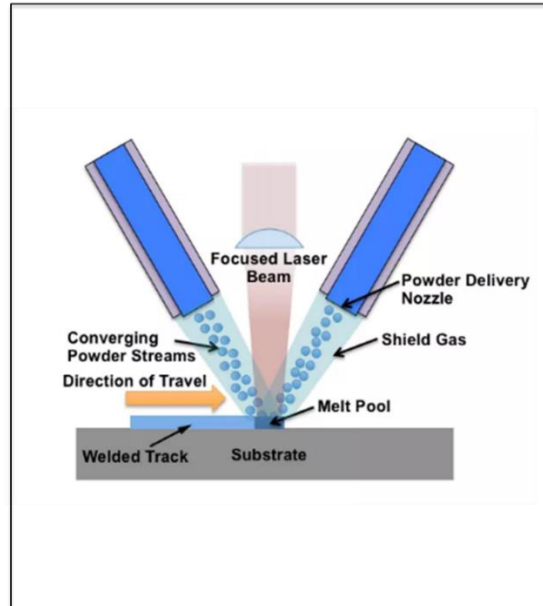


Figure 2: A schematic of a DED process [9]

Electron beam additive manufacturing (EBAM) is a variant of a DED process which employs an electron beam rather than a laser to solidify the deposition of metal. The most popular form of feedstock in an EBAM process is commonly utilized welding wire, allowing most EBAM processes to build off a well-developed raw material infrastructure, rather than depending on the availability and technology of lesser-available powdered metals[10]. Sciaky, the primary OEM of EBAM machines, specializes in the production of large-scale metal AM parts, able to build rectangular build volume parts of up to 19'x4'x4' [11]. Employing welding wire also affords Sciaky the ability to offer a wide range of material selections, offering the ability to print Titanium, 4043 Aluminum, 4340 Steel, Niobium, Inconel 625, Inconel 718,

and Tungsten [11]. A schematic of an EBAM process is shown in Figure 3:

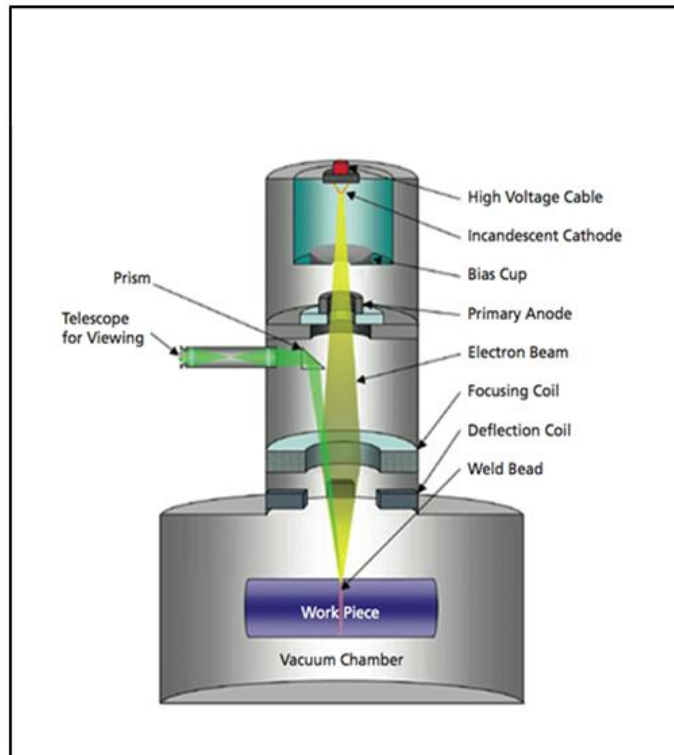


Figure 3: Schematic of an EBAM process [12]

Binder jet processes are most similar to PBF processes, except they aim to adhere a rolled bed of build powder by jetting a binder over each layer's footprint using an inkjet print head. Following the printing process, the part is heated in an oven, burning out the binder, and sintering the part[12]. A schematic of a BJP process is shown in Figure 4.

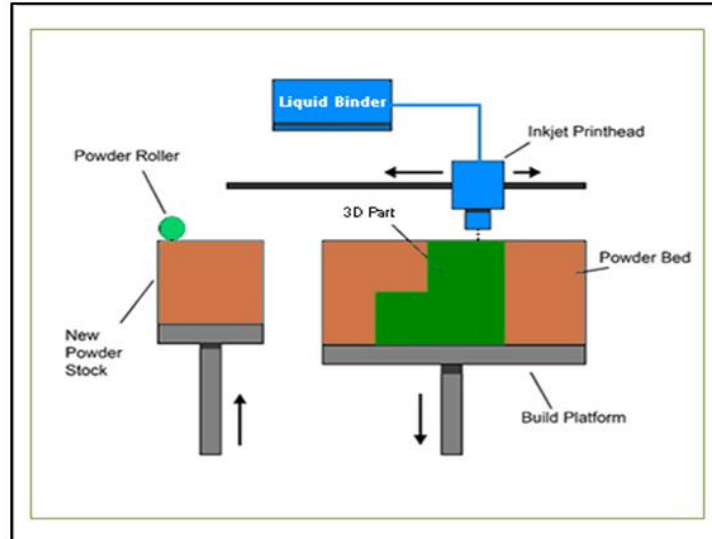


Figure 4: A schematic of a BJP process [12]

Polymer-based AM processes include vat photopolymerization, selective laser sintering, and fused deposition modeling (FDM), also known as Fused Filament Fabrication. The most common process, FDM, utilizes a filament-type feedstock fed into an extruder head mounted on a gantry system, heating the filament to a near-liquid state and selectively depositing material which defines the footprint of each layer [13]. The material undergoes a phase change from semi-liquid to solid upon cooling, allowing successive layers to be built atop of the previous layer. A schematic of an FDM process is shown in Figure 5.

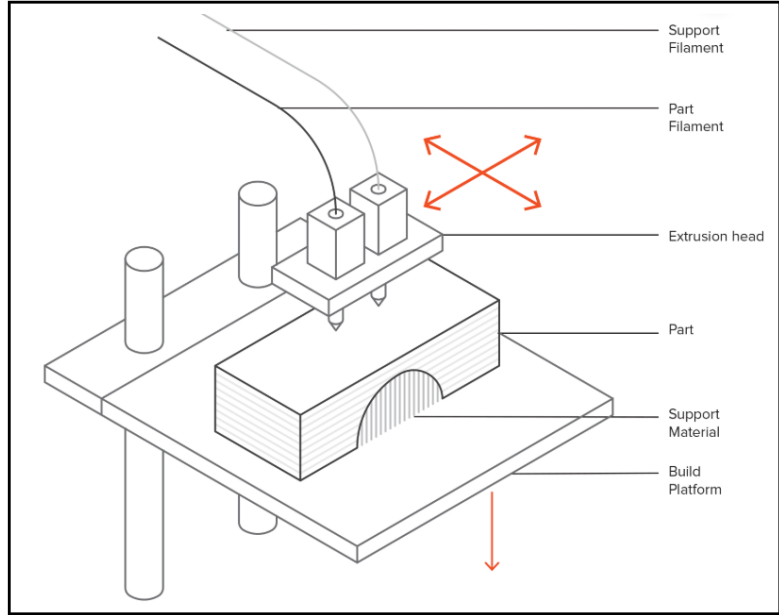


Figure 5: A schematic of an FDM process

An FDM approach offers a solution for polymer manufacturing that does not lend itself easily to metal-based AM, as the necessary processing temperatures and pressures of most molten metal filaments would be too demanding on the design of the material for the extruder nozzle.

1.2: THE RELEVANT POINTS OF RELATED LITERATURE REVIEW

There are many parallels between the finer points of metal-based AM and polymer-based AM, with one of the most prevalent interests being the minimization of voids toward the effect of maximizing mechanical properties. Several metal-based AM methods report being able to achieve between 96% and 99% of theoretical density [14],[15],[16], with the key aim being to generally approach the theoretical density of the homogenous material. Such is the aim with polymers, with reports of the same metric falling within the same range [17],[18]. Reports of achievable percentage density in polymers tend to be less often reported, which is most likely due to the relative ease of adding

reinforcement to a polymer matrix when in pursuit of the overall goal of improving strength (as compared to the difficulty of introduction of fibers in a metallic process).

Another aspect for metallic and polymer AM which has been commonly explored is the exploration of differing process parameters toward differing goals. Most reports of parameter exploration in metal-based AM vary fewer parameters over a narrower range than the ranges reported for polymers, most likely due to the elevated cost and difficulty of exploring the full space of metallic AM process parameter variation. Keist and Palmer studied the effect of build geometry in printed Ti-6Al-4V on achievable tensile strength, concluding a slight improvement in strength with an increasing wall thickness. Wang et al. [20] studied the effect of varying heating input in a DED process, concluding that a lower power input improves the tensile strength of printed 304L steel. Wolff et al. explored a similar variation of heating input for printed Ti-6Al-4V, excising tensile samples from three cubes manufactured with differing heating inputs[21]. This study concluded that samples excised from the core of each cube and aligned with the scan direction proved strongest, with the cube manufactured with the highest heating input proving most favorable. Letcher and Waytashek [22] studied three scan orientations in 3D-printed PLA (0, 45, and 90), and observed the response in tensile, flexure, and fatigue testing, concluding that the 45-degree scan orientation produced the most favorable response in tension and in fatigue. Lanzotti et al. [23] studied the effect of varying infill orientation, layer thickness, and number of perimeter rasters on the elastic modulus and tensile strength of printed PLA, concluding that optimal ultimate strength is achieved by using a layer thickness of 0.2mm, a 0-degree infill orientation, and 3 perimeter rasters. Torres et al. [24] used a fractional factorial DOE study to assess the importance of nozzle temperature, build speed, infill direction, infill density, and layer thickness, reporting optimal process settings for general use, tensile-specific, and fracture-specific design. Chacon et al. [25] investigated the effect of build orientation, feed rate, and layer thickness on a tensile response, concluding respective sets of

process parameter selections for each build orientation. Results from the study performed by Chacon [25] achieved significantly higher ultimate tensile strength (UTS) values than were found elsewhere, presenting at nearly 140% of the ultimate strength achieved in the present study for longitudinal samples (termed “flat” in Chacon et al. [25]).

Regardless of material choice or printer type, to print a part, the 3D geometry given by the CAD model must first be converted into a series of finite-thickness layers by a program commonly referred to as a slicer. This interface introduces control mechanisms for a multitude of process parameters which may be specified by the user, offering the freedom to adjust (among other settings) layer thickness, print speed, raster orientation, or extruder rate. The material microstructures and properties resulting from choice of process parameters is a research topic which has been investigated by others [23]–[30], generally building toward the understanding of the relationship that exists between process parameters and part performance. A conceptual set of relationships are shown in a PSPP framework in Figure 6 (adapted from the framework set forth by Olson, 1997)

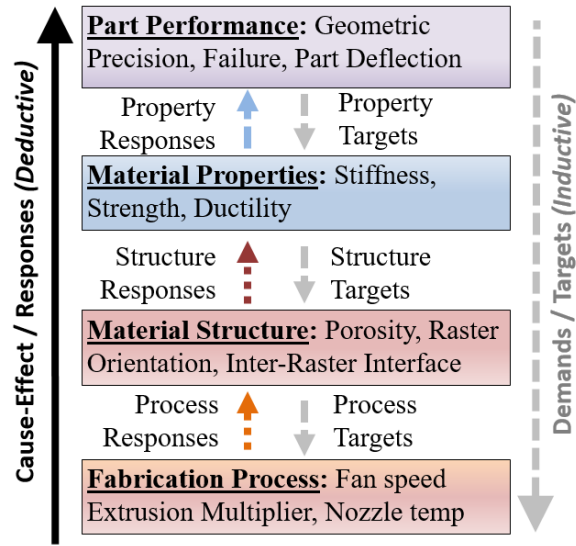


Figure 6: A map depicting relations between process, structure, properties, and performance

In Figure 6, the relationships between a fabrication process and the resultant part performance are most fundamentally defined by relating the fabrication process to the material structure, the material structure to the material properties, and the material properties to part performance. When assessing these relations from a cause-and-effect standpoint, the responses feed upward, such as a higher temperature extrusion process reducing porosity, or a reduction in porosity of a mesostructure producing a higher tensile strength. When assessing these relations for goals or targets, demands feed downward, such as an excessive part deflection driving the need to pursue stiffer material properties, or the need for stronger material driving the pursuit of a reduction in porosity. The improvement of FFF mesostructure with increasing nozzle temperature may be seen in SEM images offered by literature, an example of such an improvement is shown below, as Figure 7 [28].

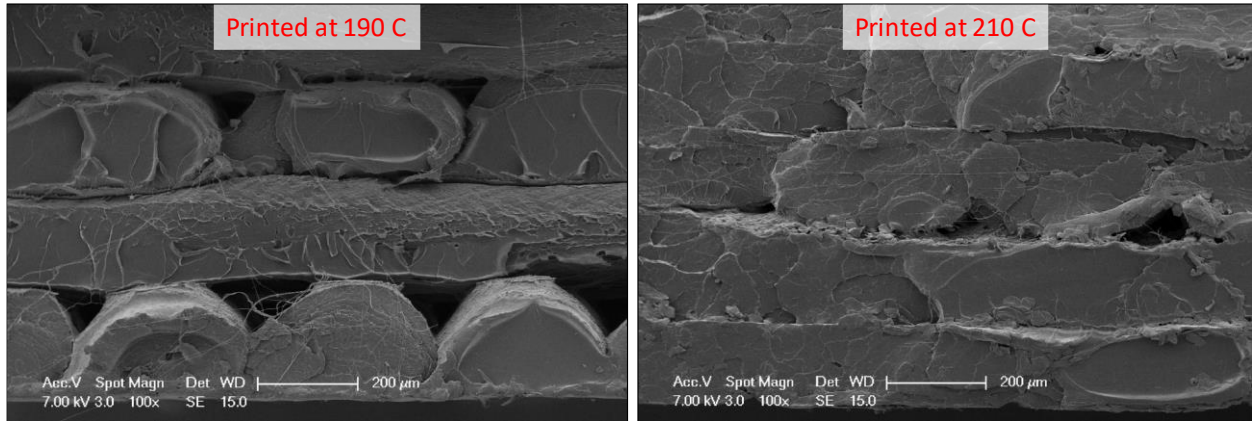


Figure 7: SEM images of an FFF mesostructure, a.) printed at 190 °C, b.) at 210 °C [28]

Quantifying PSCP relations and the uncertainty of PSCP relations is key to being able to exploit AM to its full potential. Thus, a fundamental research question is to determine the most efficient means of exploring and quantifying these relations. The answer to this question largely depends upon the scope of the intended application. If the scope is to print single geometrically-fixed part, the scope collapses to finding a successful set of print settings for a single part via one of three empirical approaches. The first empirical approach, repetitive iterations of trial-and-error, augment successive results with intuitive logic to inform the next iteration. This approach can often be inefficient, particularly when desired process settings are contrary to the intuition of the researcher or when interactions between process settings are significant. Convergence upon accepted parameters is also a shortcoming of the trial-and-error approach since convergence is based upon intuitive judgement and satisficing responses are not guaranteed. A second empirical approach, one factor at a time, involves collecting empirical results on the basis of several variations of the same parameter. This approach eliminates a degree of intuition from this approach, providing a generally marked improvement in efficiency. However, as only one setting is varied per trial, effects due to interaction between process settings are seldom captured. A third approach, design of experiments (DOE), is one of the most efficient empirical approaches. Within DOEs, process settings are varied within sensible ranges to populate the design space with test data

from systematic permutations of all the varied settings. A surrogate model is fit to the design space, which is then optimized to obtain the optimal print settings.

Although a DOE provides an efficient empirical approach, highly nonlinear responses may be given from geometric changes in assuming the optimal solution to the surrogate model applies to an arbitrary geometry, so if one expects to determine print settings for an arbitrary geometry, this poses a different problem altogether. One must investigate how the manufacturing technique affects part performance in an arbitrary sense, predicting part performance by quantifying the effect of strategy-dependent flaws introduced in the manufacturing process. In theory, an approach consisting of strictly computational and analytical methods may be possible to address such a situation, but such an approach would generally fail to capture the often pronounced degree of mechanical property dependency on the basis of several factors: (1) the machine used, (2) the differences in a material from one supplier to another, and (3) differences from the use of differing slicer software or differing slicer settings [23]–[30]. It is believed that due mainly to these factors that an approach consisting of a combination of computational, analytical, and empirical techniques is best suited to capturing the relationship between processing parameters and part performance, relying mainly upon empirical data to inform a predominantly computational and analytical approach on the specifics of the above-cited factors. Furthering the pursuit of computational approaches is a key aim of the Materials Genome Initiative (MGI) [31], a formal recognition of the needed national pursuit of computational tools for material design.

Once a framework has been established and validated to quantify the relations between processing parameters and part performance, to what degree may these tools be trusted, and what types of behavior may they be used to predict? Though the answer to this question will naturally continue to

evolve with the evolution of the software and methods applied to capture the relations, an expected baseline starting point is the prediction of empirical test data, aiming to qualify the level of discrepancy introduced by the technique.

1.3: SIMULATION OF AN AM PROCESS

As AM gains in popularity, the need for a strategy for predictive mechanical simulation stands as one of the largest hurdles to be overcome prior to industry-wide acceptance of the technology. In recent years, software packages have been developed towards realizing this goal, such as Simcenter 3D (by Siemens) or GENOA (by AlphaSTAR). The software GENOA aims to predict the mechanical response of AM parts through a multi-stage process. This process begins with characterizing neat material properties, which are then degraded to account for process-induced voids in the geometry. Several temperature-dependent properties are then used to predict residual stresses given by the thermal history of the process, allowing the loading simulation to account for both geometrically-induced and thermally-induced process degrade.

The scope of this work aims to trace the procedure of characterizing a mainstream AM material, Polylactic acid (PLA), with the overall goal being to compare between an experimentally-derived mechanical response and a computationally simulated mechanical response. As the computationally simulated response in this case consists partially by empirical test data, the first phase of generating the computational model involves the gathering of test data.

The process of either testing or simulating a tensile dog bone geometry both begin with the model geometry (CAD file). The necessary interfaces and file types for each step of either path are shown in Figure 8, and are further detailed below:

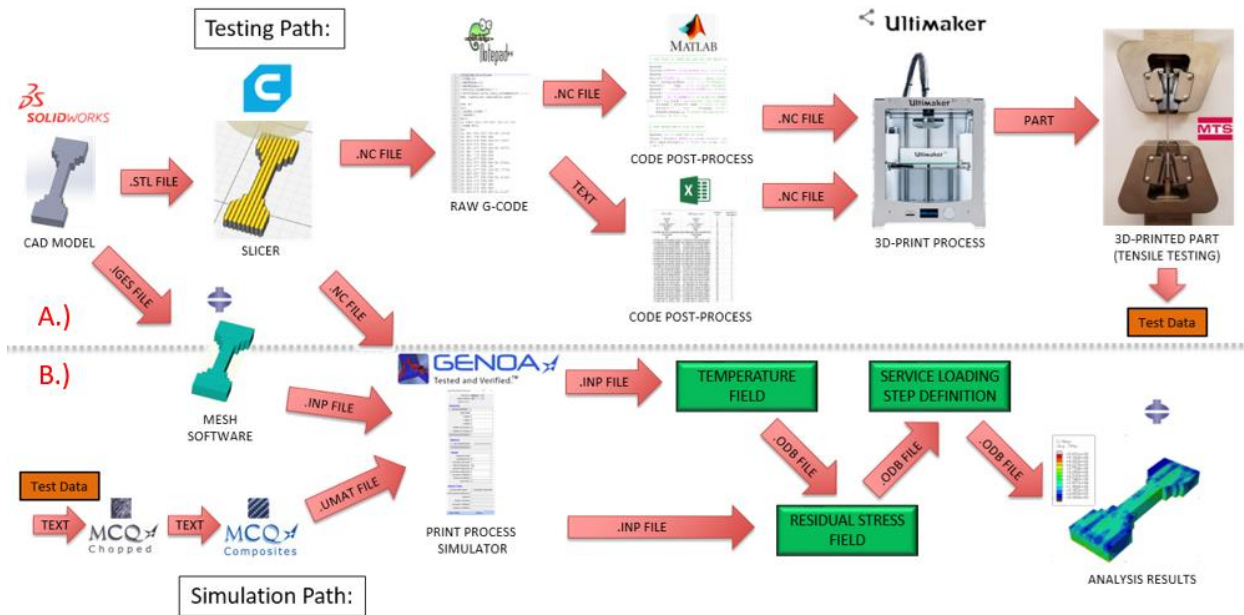


Figure 8: The schematic of the path leading to test data (A) or simulated response (B)

In Figure 8, tracing the testing path, the CAD file is first sent to a slicer (Cura) as an “.STL” file, converting the geometry into a series of tetrahedral elements, and approximating all curved surfaces as a series of linear interpolations. The slicer discretizes the thickness dimension of the volume domain into a series of thin layers which are printed sequentially. Within the slicer, several features of each layer’s build settings, including layer thickness, scan path, infill density, and others may be manipulated per the user’s preference before the file is exported to a g-code format. (.NC or .GCODE). The description, selection and specification of these settings are discussed further in Chapter 2. The g-code that is generated by a slicer is specific to a 3D-printing process, though similar in characteristic to a traditional CNC process. Following the export to g-code, the code may be viewed in a text editor, such as Notepad++. This raw code may be broken down and manipulated further in a post-processing interface, such as Matlab or Excel. Depending upon the level of investment into constructing the post-processor, post-process manipulations may offer the ability to: make edits to scan strategy, modify the process temperature, or simply verify that slicer settings are producing the intended print strategy. Post-

processor description, use, and manipulation is discussed further in Chapter 2. Once the code is finalized, it is saved to an SD card which is physically inserted into the 3D printer. During printing, additional live changes may be made to adjust or modify settings typically specified by the g-code, such as material flow rate, nozzle temperature, or heated bed temperature (to name a few). Following fabrication, samples are strained to fracture in an MTS Criterion tensile load frame. The tensile testing process is further detailed in Chapter 3. Repetitive executions of the above-described “testing path”, coupled with either informal, one-factor-at-a-time process tuning, or formal, design of experiments (DOE) process tuning gave rise to the selection and preference of a set of process-parameters and slicer settings, which are discussed further in Chapter 4.

In Figure 8, tracing the simulation path, the CAD file is again first sent to a slicer, generating the g-code for the printing process. Additionally, the CAD file is sent to a meshing interface, such as ABAQUS, to define a mesh of finite-elements which represent the geometry of the 3D-printed part. Both the g-code and the mesh are fed into an interface in GENOA, which, in conjunction with a material definition, serves to generate two files which, when sequentially executed, simulate the printing process. The results of the sequential execution (the residual stress field in Figure 8) may be fed forward to a service loading simulation which, in many ways, is comparable to a traditional explicit simulation on a traditionally manufactured part.

There are two methods to simulate an AM part presented in this work. A more precise detailing of how they differ is covered throughout Chapter 5, but both methods begin with the execution of the steps presented in 5.1. The first method presented, termed “The Default Approach” stage is further detailed in 5.2. The Default Approach is seen to have several shortfalls. These shortfalls are detailed further in

5.3. The second presented method to simulate an AM part, termed “The User-Informed Calibration approach”, is detailed further in 5.4.

Given the Default Approach, the procedure to generate the files to numerically simulate a 3D printed part is a three-stage process. The first stage aims to capture the effect of inter-raster voids introduced in the printing process. As the inter-raster voids are accounted for by an effective property calculation that smears the effects of inter-raster voids across an effective Baseline definition, the first stage is hereafter referred to as “accounting for homogenized voids”. The first stage is further detailed in 5.1. The second stage aims to define the necessary temperature-based degradation parameters to predict thermally-induced residual stresses introduced by the printing process. The second stage is further detailed in Chapter 6. The third stage aims to capture the effect of end-of-raster voids, and simulate the printing process. The third stage is further detailed in Chapter 7. Results of the Default Approach are presented in Chapter 8.

Given the User-Informed Calibration approach, the procedure first involves the generation of a material definition. The generation of this material definition provides an material definition highly subject to change, but the procedure of generating this initial state is identical to the procedure conducted in 5.1 for the Default Approach. The initial material definition then undergoes a two phase process. In the first phase, the initial state material definition evolved in 5.1 is subject to change on the basis of iterative logic informed by successive simulations of a bending test. The first phase is further detailed in 9.1.1. In the second phase, the material definition resulting from the first phase is used to define a tensile simulation. Additionally, a defective region is assigned by a pattern of elements informed by the user’s intuition of the regions end-of-raster defects are judged likely to occur. Successive simulations of a tensile test are performed, toward the goal of establishing the level of defect seen to be necessary to

arrive at a tensile match. The second phase is further detailed in 9.1.2. The result of the User-Informed Calibration approach is presented and discussed in 9..

Chapter 2: THE GEOMETRY, THE SLICER SETTINGS, AND THE G-CODE

In order to produce a test specimen, several stages of specification are necessary [32]. First, the geometry must be specified in a CAD interface, such as SolidWorks. This CAD file is then exported as a Standard Tessellation Language (STL) file format, which approximates all solid bodies and surfaces with a series of tetrahedral elements. The STL file is then sent to a slicer, such as Cura3.6.0 [1]. A slicer intersects the geometry given by the STL file with a series of cut planes parallel to the build plate, separated by the specified layer thickness, to define finite layer footprints for each layer. By providing further specifications, the details of strategy concerning the printing of each layer are defined. A g-code file is exported from the slicer, which may be edited or sent directly to the printer. Generally, each layer consists of a series of sequentially printed lines called rasters, with each raster representing a simultaneous translational move of the print gantry while extruding material through the print nozzle. For the printing of solid bodies, the exterior perimeter of each layer's footprint is often specified to be one or more continuous raster paths, or "perimeter rasters" or "shells," to improve surface quality. For the printing of bodies with interior cavities, the interior perimeter may also be specified by one or more continuous raster paths. The remaining area in each footprint is specified by a choice of infill strategies, one may choose from a variety of grid-like strategies to fill the remaining area, all of which offer the ability to save print time and extruded material. In the scope of this research, perimeter rasters ranged from zero to two, and the infill strategy used was that of adjacent parallel rasters, separated by the specification of raster width.

A series of ASTM D638 [33], Type 1, dog bone specimens were printed with longitudinal (11), transverse (22) and vertical specimen orientations (33), all while maintaining 90-degree raster orientations per raster orientation convention defined in Cura. Figure 9 shows the specimen geometry; Figure 10 shows a depiction of each raster strategy. It should be noted that, for a majority of the test data generated, a model geometry of $\frac{1}{2}$ scale was used, both for the purpose of reducing material usage and accelerating the process of gathering test data.

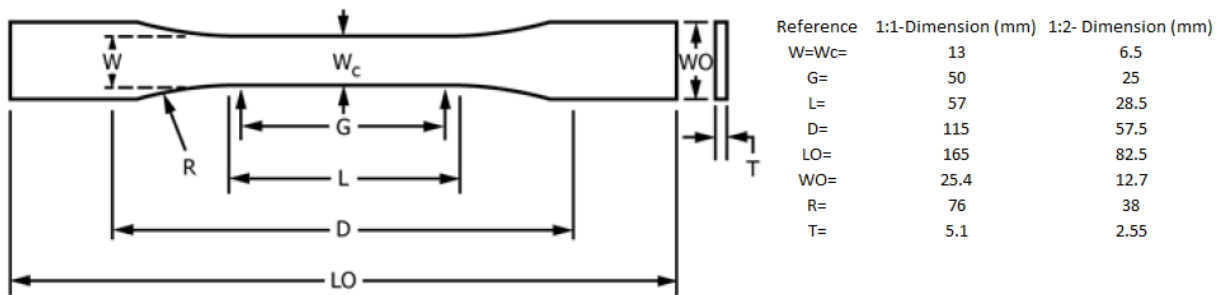


Figure 9: The geometry of an ASTM D638, type 1, dog bone specimen

ASTM D638 permits user-definition of dimensions “WO”, “LO”, and “T” based upon convenience of either manufacturing or testing (adapted from ASTM D638 [ref]).

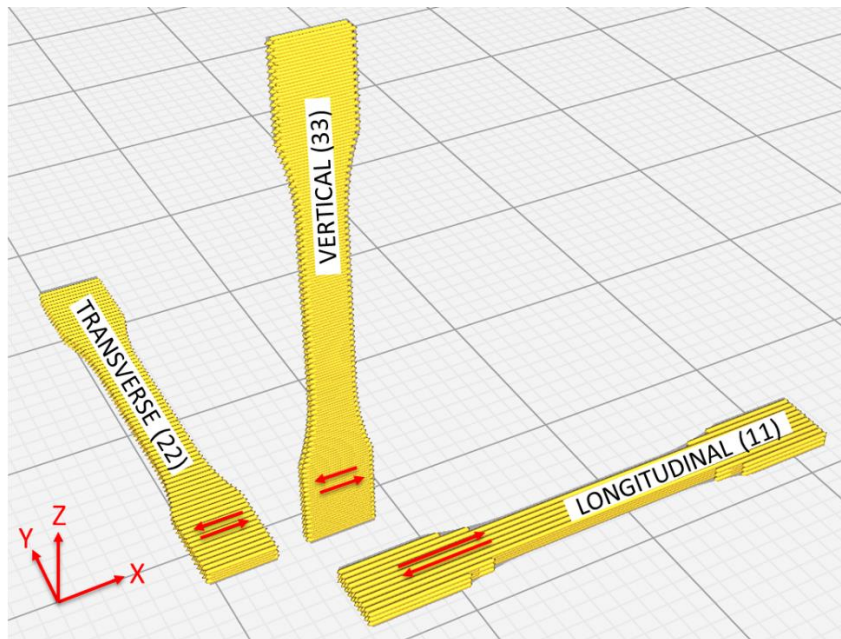


Figure 10: Depiction of raster orientations for 11, 22, and 33 tensile specimen

(Note: 1:8 scale specimens are depicted for the purpose of better rendering of raster strategy)

Following the drawing of a dog bone model, conversion of the solid model geometry into an STL file, and slicing the STL file in Cura, an instance of the part is manufactured on an additive manufacturing machine, in this case an Ultimaker 2+ [34].

Over the course of several batches of test data, a series of preferential slicer settings came to be favored over the default settings. The remainder of this chapter is organized into three subsections. Subsection 2.1 specifies the preferred Cura slicer settings. Subsection 2.2 discusses the justification of the preferred Cura slicer settings, including the progression of material properties throughout the testing process. Subsection 2.3 discusses G-code edits, offering an additional capability to tune the printing process.

2.1: SPECIFICATION OF PREFERRED SETTINGS:

Improved tensile properties of ½-scale ASTM D638 Polylactic Acid (PLA) tensile specimens were achieved by modifying 41 of Cura v3.6.0's 150 default slicing parameter values.

Table 2.1 shows the grouping, slicing parameters, and the modified values for each of the 41 modified slicing parameters; slicing parameters set to default Cura v3.6.0 values were omitted from Table 2.1.

Table 2.1. Modified Cura v3.6.0 [1] slicing parameters.

Quality settings:

Layer Height:	0.15 mm
Initial Layer Height:	0.15 mm

Shell settings:

Wall Line Count:	2 (This setting varied from dataset to dataset)
Outer Wall Wipe Distance :	0 mm
Top/Bottom Thickness:	0 mm
Bottom Layers:	0
Outer Wall Inset:	0
Outer Before Inner Walls	Enabled
Alternate Extra Wall:	Enabled
Compensate Wall Overlaps	Disabled
Print Thin Walls:	Enabled
Z Seam Alignment:	User Defined
Z Seam X, Z Seam Y:	Located by least critical point (typically in grip region)
Seam Corner Preference:	Hide or Expose

Infill Settings:

Infill Density:	100%
Infill Line Directions:	[90] (This setting varied from dataset to dataset)
Infill Overlap:	0.1 mm
Infill Wipe Distance:	0.0875 mm
Infill Before Walls:	Disabled

Material Settings:

Retract at Layer Change:	Enabled
Retraction Minimum Travel:	6.0 mm (This value varied from dataset to dataset)
Minimum Extrusion Distance Window:	0 mm

Speed Settings:

Print Speed:	15 mm/s (This value varied from dataset to dataset)
Wall Speed:	15 mm/s (matched to print speed)
Outer Wall Speed:	15 mm/s (matched to print speed)
Travel Speed:	30 mm/s
Initial Layer Print Speed:	15 mm/s
Initial Layer Travel Speed:	30 mm/s
Skirt/Brim Speed:	15 mm/s

Travel Settings:

Combing Mode:	Off
Layer Start X:	Located by least critical point (typically in grip region)
Layer Start Y:	Located by least critical point (typically in grip region)
Z Hop When Retracted:	Enabled
Z Hop Height:	3 mm

Cooling Settings:

Minimum Layer Time:	0 seconds (This value varied from dataset to dataset)
Lift Head	Enabled

Support Settings: (Activation varied per dataset)

Enable Support Brim:	Enabled
----------------------	---------

Build Plate Adhesion Settings:

Build Plate Adhesion Type:	Brim
Brim Only On Outside:	Disabled

Dual Extrusion Settings: (No modified settings)**Mesh Fixes: (No modified settings)****Special Modes: (No modified settings)****Experimental Settings:**

Infill Travel Optimization	Enabled
Maximum Resolution	0.001 mm
Make Overhang Printable	Enabled

2.2: JUSTIFICATION OF PREFERRED SETTINGS AND PROGRESSION OF MATERIAL PROPERTIES:

A series of 16 test batches of tensile tests were conducted to investigate the effects of slicer settings, specimen sizes, and post-process g-code edits. Test batch sizes ranged from as few as 5 specimens to as many as 88 specimens. Batch “P” was generated as a Latin hypercube design of experiments, toward the goal of optimizing transverse (22) tensile strength (See Chapter 4). The division between each batch was defined on the basis of investigation of a differing technique or setting from the previous batch. Figure 11 shows a chart depicting the batch studied versus the employed slicer parameter settings.

BATCH# DETAILS:	B	C	D	E	F	G	H	J	K	L	M	N	P	Q	R	S
Full Scale Sample	X	X	X	X	X	X	X									
1/2 Scale Sample								X	X	X	X	X	X	X	X	X
60 mm/s speed	X	X														
50 mm/s speed			X	X												
30 mm/s speed					X	X	X	X	X	X	X	X	X			
15 mm/s speed														X	X	
10 mm/s speed																X
Include Z-Hops & Retractions?					X	X	X	X	X	X	X	X	X	X	X	X
Offset Layers?	X	X	X	X	X	X	X	X	X	X						
Z-Compress?						X	X	X	X	X	X					
Extensometer Data?						X	X		X	X	X	X	X	X	X	X
Overextruding?											X	X	X	X	X	X
High Print Temp (240C)													X	X	X	X
Rapidly Cooled Bed?											X	X				
No Cooling Fans?											X	X				
Quality Material, Well-Kept?											X	X	X	X	X	X
Smooth Contour Reduction (Waterjet)?												X				
Analyze Effect of Support?															X	
All Perimeter Rasters			X													
2 Perimeter Rasters																X
Min Strength, 11-direction (MPa)	37	N/A	37	44	46	52	N/A	42	N/A	N/A	59	44	N/A	N/A	N/A	36
Max Strength, 11-direction (MPa)	40	N/A	43	44	47	53	N/A	52	N/A	N/A	29	61	N/A	N/A	N/A	64
Min Strength, 22-direction (MPa)	N/A	4	22	N/A	29	40	N/A	N/A	N/A	N/A	11	0	12	N/A	N/A	N/A
Max Strength, 22-direction (MPa)	N/A	9	30	N/A	35	40	N/A	N/A	N/A	N/A	34	39	59	N/A	N/A	N/A
Min Strength, 33-direction (MPa)	N/A	13	5	N/A	N/A	N/A	31	N/A	N/A							
Max Strength, 33-direction (MPa)	N/A	29	17	N/A	N/A	N/A	52	N/A	N/A							

Figure 11: A chart showing the batches and the settings used

In favoring settings which maximize a printed PLA specimens ultimate tensile strength, Figure 11 shows, across the timeline of batch generation and testing, that the best results for printed PLA are achieved by printing a sample with six best processing practices:

- Print with a relatively slow print head speed (less than or equal to 15mm/s)
- Print with retractions and z-hops activated
- Print with an over-extrusion of material (120%)
- Print with a relatively high nozzle temperature (240 °C)
- Employ a PLA filament free from hygroscopic effects (kept in a dry box) [35]
- Employ a scan strategy with 2 perimeter rasters

Controlling the print head speed, activating retractions and z-hops, and modifying the scan strategy to include two perimeter rasters were all adjustments made by adjusting slicer settings. The modification made to the rate of extrusion per distance travel, and the modification made to the nozzle temperature was made by editing the g-code generated by the slicer. Modifications to individual slicer settings are discussed in the remaining paragraphs in this subsection, organized by the same setting category as presented in Ultimaker Cura: Quality settings, Shell settings, Infill settings, Material Settings, Speed Settings, Travel Settings, Cooling Settings, Support Settings, Build Plate Adhesion Settings, and Experimental Settings.

Quality settings:

Batches B through L explored the effect of offsetting odd-numbered layers. The aim was to nest individual rasters into rasters from the preceding layer more efficiently, thus decreasing voids and increasing stacking efficiency, resulting in an improvement in tensile strength. This aim was temporary,

as the test results from batch K supported the conclusion that offsetting odd-numbered layers was a practice that reduced the ultimate tensile strength in the 33 direction. In attempting to explore this variant of print strategy, an approximate model of raster cross-section was defined in SolidWorks, given by a repeating elliptical raster pattern. Each raster was given by a major axis diameter of 0.35 mm, and a minor axis diameter of 0.15-mm. These cross-section width and height dimensions are consistent with the raster width and layer height specifications in the slicer, respectively. Figure 12 shows elliptical cross sections for: (a) a traditional printing strategy, (b) an offset strategy with no detriment made to the layer height (referred to hereafter as z-compress factor), C.) an offset printing strategy with an optimal z-compress factor, and D.) an offset printing strategy with an excessive z-compress factor.

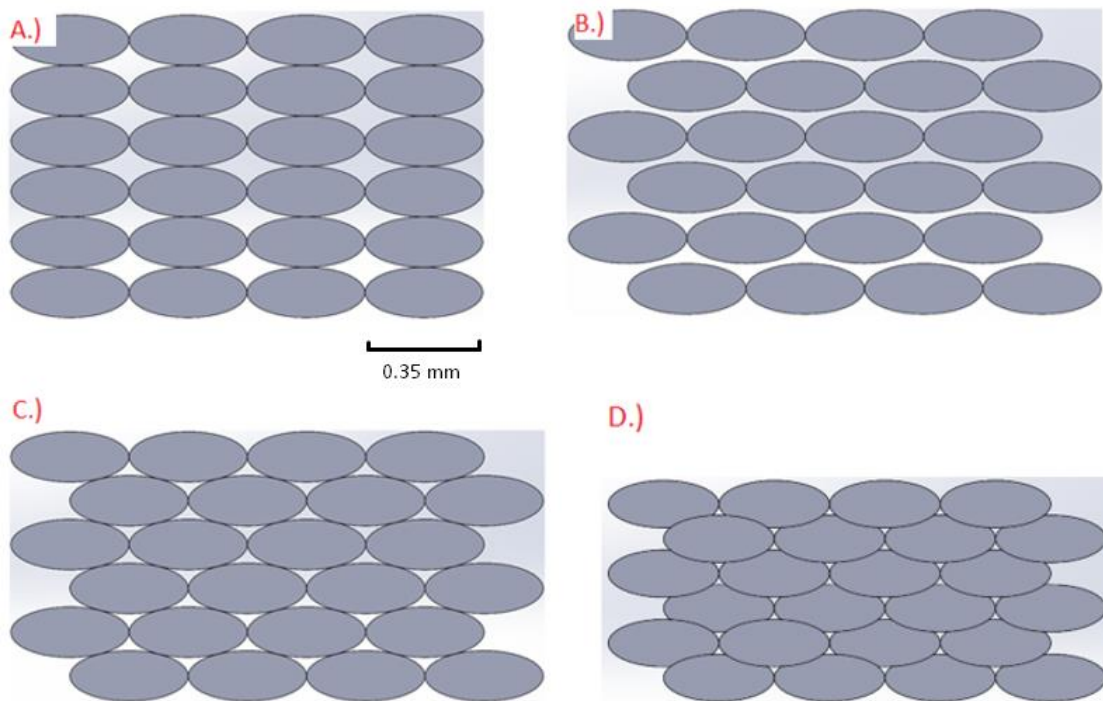


Figure 12: Elliptical raster cross-sections for various printing strategies

(a) a traditional printing strategy, (b) an offset printing strategy with no z-compress, (c) an offset printing strategy with a z-compress factor suited to the assumed elliptical cross-section, and (d) an offset printing strategy with excessive z-compress factor

By assuming an elliptical cross section, the z-compress factor may be calculated analytically by combining a Cartesian ellipse definition with similar triangle relations. Defining an elliptical cross-section of width $2*a$, and height $2*b$, these relations are shown in a graphic in Figure 13, and are analytically defined in Equation 1 through Equation 5.

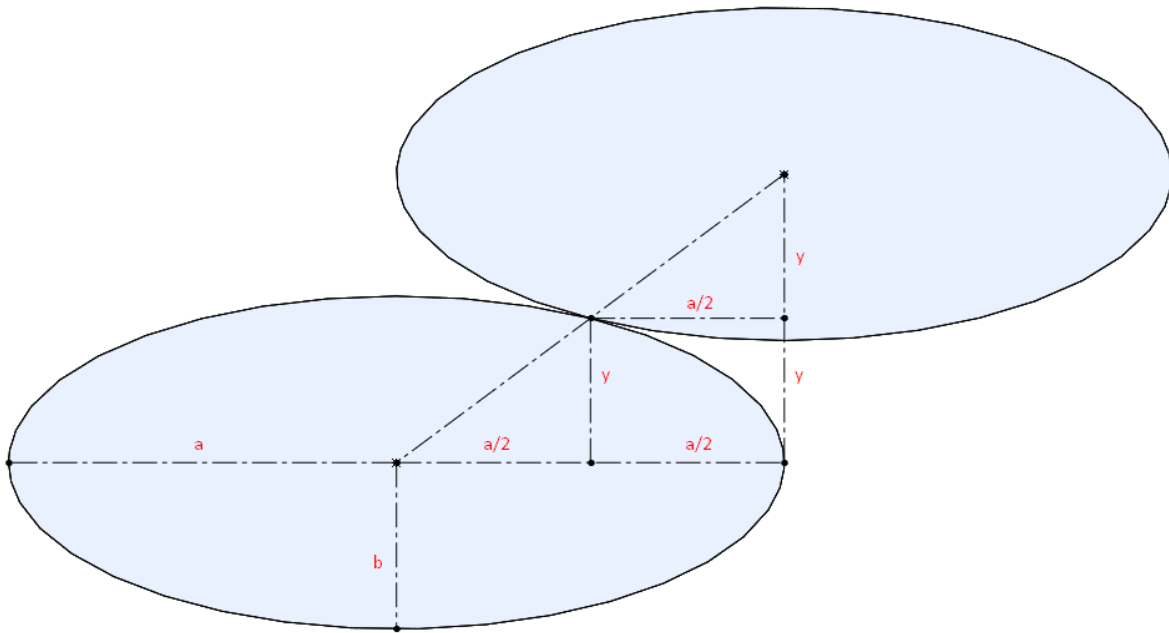


Figure 13: The similar triangles which exist between connected centers of two nested ellipses

$$y = \left(\sqrt{1 - \left(\frac{x}{a}\right)^2} \right) * b \quad \text{Equation 1}$$

$$dec = 2 * b - 2 * y \quad \text{Equation 2}$$

$$zcomp = \frac{dec}{2 * b} \quad \text{Equation 3}$$

$$zcomp = \frac{2 * b - 2 * \left(\sqrt{1 - (1/2)^2} \right) * b}{2 * b} \quad \text{Equation 4}$$

$$z_{comp} = 1 - \left(\sqrt{\frac{3}{4}} \right) \approx 0.134 \quad \text{Equation 5}$$

The relation shown in Equation 5 and depicted in Figure 12 depicts a raster cross-section that exists strictly theoretically. Though Figure 12 depicts the cross-sectional shape as elliptical, the true shape of a raster's cross-section may be asymmetric, non-uniform, locale-dependent, and may vary as a function of time. Though empirical techniques exist which may quantify the actual size and shape of a raster's cross section, imaging the cross-section would provide only a part of the necessary information to determine the optimal value for a single variable. Therefore, the z-compress factor was determined by iteratively printing rectangular block samples with z-compress values between 5% and 20%, in increments of 5%. By weighing the as-printed samples, and measuring the length, width, and depth of the as-printed samples, the relative density of a sample was calculated as shown in Equation 6, where ρ_{rel} is the relative density, m_{exp} is the measured mass, V_{exp} is the measured volume, m_{nom} is the nominal mass, and V_{nom} is the nominal volume. In Equation 6, as increasing values of z-compress were evaluated for a corresponding relative density, the value of m_{nom} remained constant, and the value of V_{nom} changed only in its assumed value in the dimension normal to the print bed.

$$\rho_{rel}(\%) = 100 * \left(\frac{\frac{m_{exp}}{V_{exp}}}{\frac{m_{nom}}{V_{nom}}} \right) \quad \text{Equation 6}$$

As shown in Figure 12, z-compress factors less than 10% resulted in reduced densities, and were assumed to result in cross sections similar to Figure 12B. A potential explanation is that cumulative gaps from each successfully positioned layer increase the distance between the print surface and the nozzle tip until pre-placement raster solidification leads to a flaw formation, introducing air pockets and reduced densities. In contrast, z-compression factors greater than 10% were assumed to result in a cross section similar to Figure 12D, which although resulting in increased density, were seen to present

three possible types of flaws. The first type of flaw presented in the case of a sufficiently rigid print surface as to restrict flow from the nozzle tip for a sufficiently long duration as to slip the extruder drive. The first flaw type restricted feeding of the filament, thus reducing the mass successfully deposited. The second type of flaw presented from a print surface proximate enough to the nozzle to restrict flow, but insufficiently rigid to sustain the restriction. With the second flaw type, earlier rasters are displaced by the placement of later rasters, often bulging the footprint of the printed layer. The third type of flaw presented in the case of a sufficiently rigid print surface as to restrict flow from the nozzle tip, but only for a sufficiently long duration as to delay filament feeding. Given the third flaw type, nozzle pressure accumulated during the placement of each raster, but at the end of each raster, the pressure relieved by oozing filament. As the samples generated with z-compress factors equal or greater than 15% all presented with the third flaw type, all samples were measured, recorded, milled across the raster-ends, measured, and recorded again. The data from the 10 rectangular block trials is shown in Figure 14.

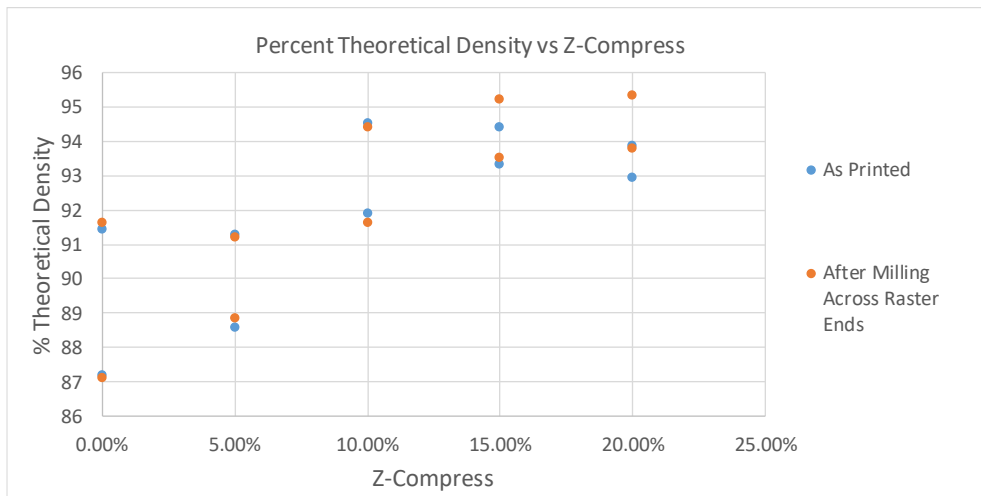


Figure 14: Percent theoretical density versus Z-compress (As-printed, and after milling across raster-ends)

In Figure 14, as samples with z-compress values equal or greater than 15% presented with type 3 flaws, the z-compression factor was judged to be set at 10% of layer height, corresponding to approximately a 93% relative density, both before and after milling.

Rather than the default 0.27 mm, initial layer height was specified to be 0.15 mm to be consistent with subsequent layer heights and to allow 1st- and subsequent-layer z-compress factors to be consistent.

Shell settings:

Shell setting values differed from default setting values based upon intuition and logical judgement.

Modified setting value included Outer Wall Wipe Distance (0 mm), Top/Bottom Thickness (0 mm), Bottom Layers (0), Outer Wall Inset (0 mm), and Compensate Wall Overlaps (Disabled).

As the greater scope and value of this work would likely extend to the printing and testing of other more complex geometries, a decision was made to enable both the setting “Alternate Extra Wall”, and the setting “Print Thin Walls”. The setting “Alternate Extra Wall” defines an additional perimeter raster on even-numbered layers. The setting “Print Thin Walls” allows the slicer to print features thinner than the nozzle size. Additionally, the tooltip describing their function indicated promotion of the engagement between infill and perimeter rasters [1]. Though their activation was judged unlikely to have a significant impact on test data, investigation of the significance of their activation would likely fall within the scope of further investigation.

Values for the remaining shell settings – Outer Before Inner Walls, Z Seam Alignment, and Seam Corner Preference – were changed from their default settings based upon judgement to eliminate or mitigate the effect of surface flaws. Though the occurrence of the flaw could not be avoided, by repositioning a

start/stop location of a perimeter raster to a corner of the specimen rather than on the gauge reduction or on the gauge length, fracture behavior was seen to be unaffected by these flaws.

An example of a quasi-continuous path absent perimeter rasters may be seen in the raster strategy of a transverse (22) tensile sample shown in Figure 15. The raster strategy shown in Figure 15a represents a quasi-continuous path, not a continuous path as extrusion operations terminate at the end of each raster. For the raster strategy for a longitudinal (11) sample absent perimeter rasters shown in Figure 15b however, regardless of starting location or raster progression, only so many rasters may be laid adjacent to one-another before the print head must unavoidably pause extrusion and make a significant travel move in order to continue layer progression. In such a case, the layer is divided into a minimal number of zones which may be printed with a quasi-continuous paths, and the zones are printed sequentially. An example of a discontinuous path is shown in Figure 15b.

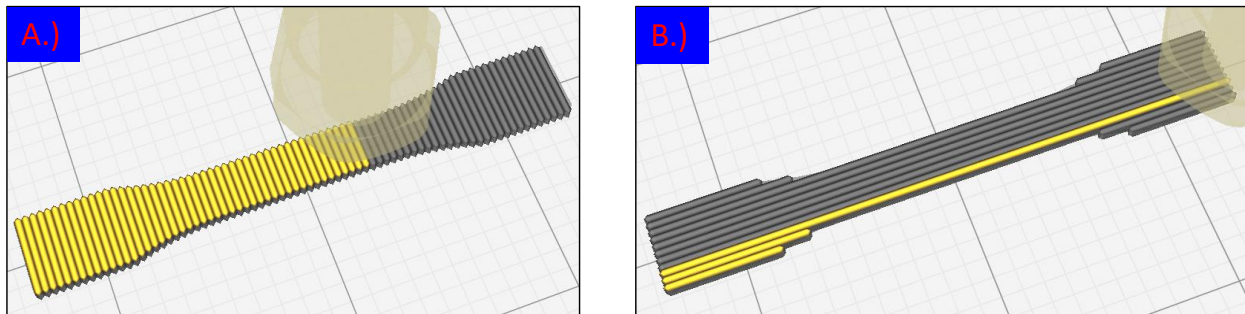


Figure 15: Raster strategy depictions for various specimen orientations

(a) a transverse “22” tensile sample, and (b) a longitudinal “11” tensile sample. The raster strategy in (a) represents a quasi-continuous path, and the raster strategy in (b) has multiple zones and a discontinuity.

In the case of such a situation as is presented in Figure 15b, all specimens failed at the start-stop points defined by path discontinuities. This failure mode was typical of longitudinal samples sans perimeter rasters. In batch “S”, the introduction of two perimeter rasters into the scan strategy was seen to mitigate the tensile response being governed by path discontinuities.

Infill Settings:

The majority of the data collected aimed to isolate the response of pure 100% infill in the three orientations presented in Figure 10, governing the settings “Infill Density” and “Infill Line Directions.” Prior to batch “S,” no perimeter rasters were introduced, as these were seen to perhaps offer the possibility of improvement of ultimate tensile strength, but at the cost of adulterating test data with other factors apart from those which sought investigation.

The omission of perimeter rasters forced the slicer to approximate exterior contour curves, such as the gauge reduction, with a jagged edge, terminating each raster at the best possible point which would mimic the geometry of the contour. This approximation of the gauge reduction contour may be visualized in Figure 15. As the finite modeling of this jagged edge presented a stress singularity which governed the simulated response (particularly in “11” specimen), batch “S” aimed to include perimeter rasters in order to provide an “apples-to-apples” comparison between experimental “11” data and simulated “11” data which would not be skewed by such a fundamental flaw in finite modeling.

Specimen produced with rasters aligned in the 11-direction sans perimeter rasters exhibited a fracture pattern initiating at one of four possible zone start/stop locations. These locations are indicated with a red “X” in Figure 16. Any 11-direction scan strategy which seeks to employ exclusively a repeating series of adjacent linear rasters must either start or stop a raster path at each of the indicated locations in Figure 16.

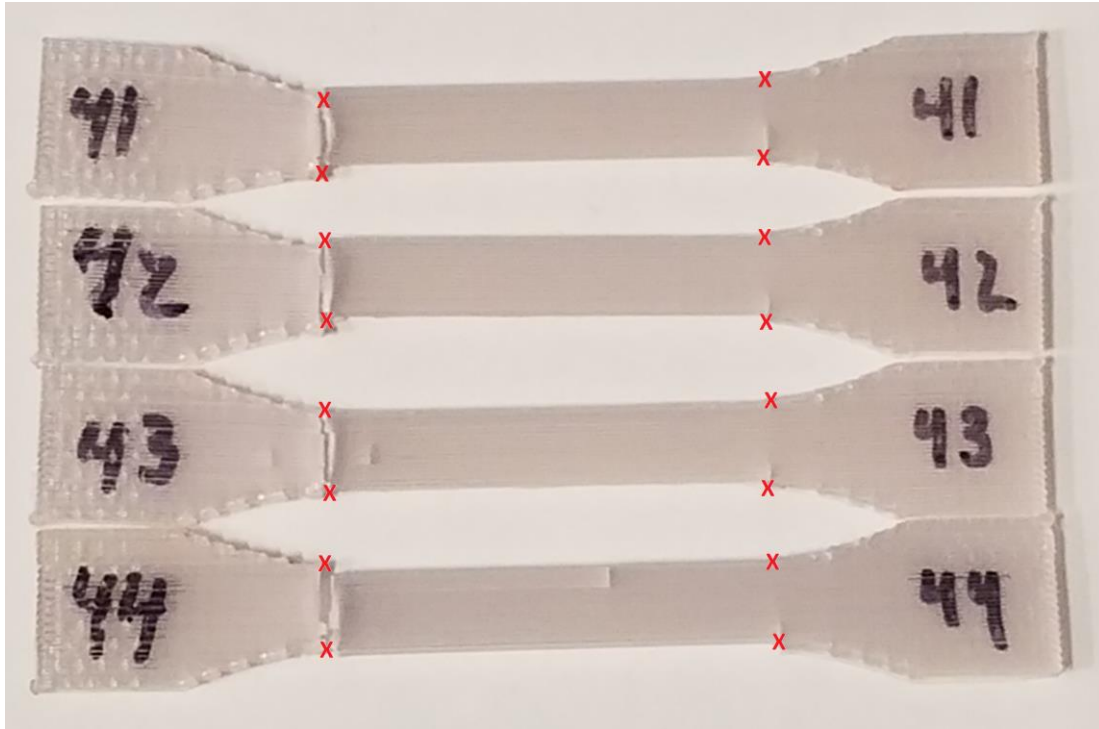


Figure 16: Fractured tensile specimens produced with a 11-direction raster strategy

(All specimens were printed absent perimeter rasters; nozzle start/stop locations depicted with an “X”)
In an attempt to eliminate the influence of the unavoidable defect in these locations, in batch “S”, the scan strategy for 11-direction specimen was modified to include two perimeter rasters. The settings “Infill Overlap”, “Infill Wipe Distance”, and “Infill Before Walls” were modified with the goal of improving the engagement, or strength of the connection, between the infill rasters and perimeter rasters. This “better engagement” was only pursued to the end of observing a fracture significantly enough away from the end of the gauge reduction that one could conclude the gauge reduction was mechanically stronger than the gauge length. Three samples from batch “S” which exhibit fracture patterns away from the end of the gauge reduction are shown in Figure 17.

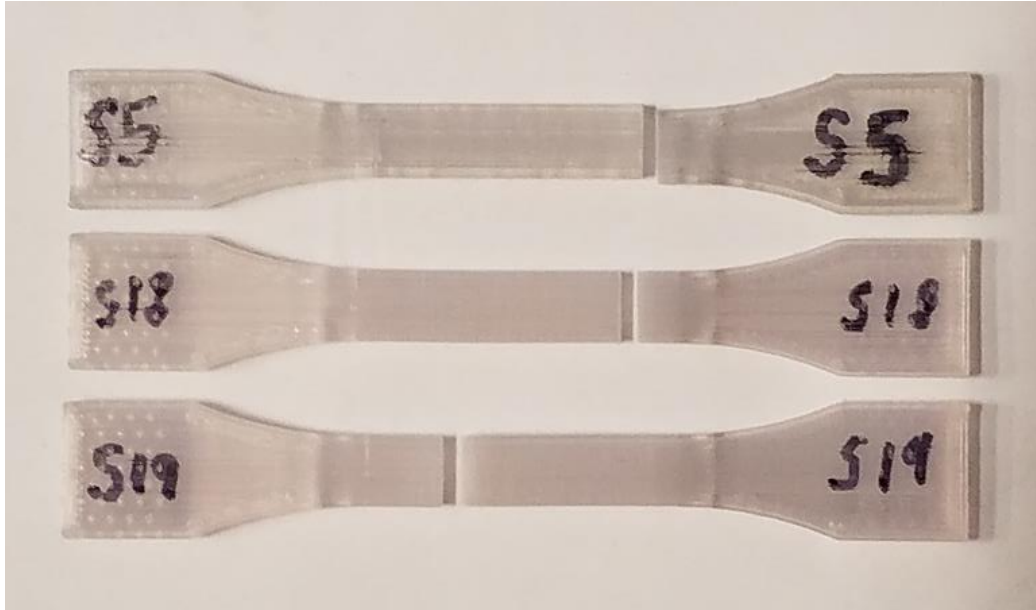


Figure 17: Three batch "S" specimens which exhibiting fracture patterns in the gauge length

Optimization of the modified infill settings “Infill Overlap”, “Infill Wipe Distance”, and “Infill Before Walls” were not conducted, but may be a source of continued work.

Material Settings:

The specifics regarding how a path discontinuity is handled would require further investigation, as well as necessary further refinement of slicer software. There are two main strategies for executing the necessary translation between the end of one continuous print zone and the start of the next, both of which have their shortfalls. The first strategy is to cease extrusion, translate the extrusion gantry and resume normal printing by starting the extruder. The second strategy entitled “retraction and z-hops” ceases extrusion, retracts the filament, lowers the build platform, translates the extrusion gantry, raises the build platform, and unretracts the filament before resuming normal printing. The threshold by which the slicer decides which of these strategies to implement is based on Euclidian travel distance between extrusion stop and start coordinates. When a travel-type move (following an extrusion-type move) has a distance less than the “Retraction Minimum Travel,” Cura employs the first strategy, i.e.,

translate with neither retractions nor z-hops. When that distance exceeds the “Retraction Minimum Travel”, retractions and z-hops are performed. The first strategy may result in excess pressure in the nozzle, causing the thermoplastic build material to ooze out, leaving blobs between the end of the prior zone, and the start of the next. When performing retractions and z-hops, the nozzle tip pauses momentarily at the site of the filament retraction, causing a divot-like flaw which is often observed to be a point of failure initiation. Both these defects may be visualized in both Cura, as well as in the specimen itself, and are shown in

Figure 18, and in Figure 19, respectively.

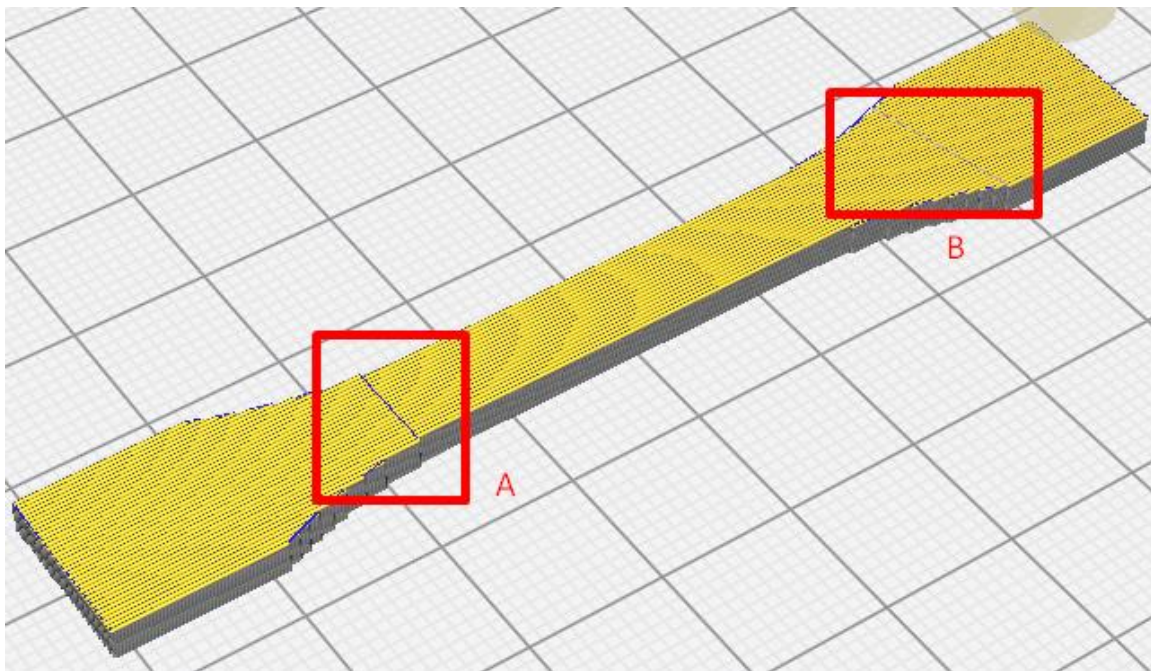


Figure 18: A visualization of the scan strategy of a longitudinal (11) specimen in Cura Showing A.) a travel move less than the Retraction Minimum Travel, prone to an ooze-type defect, and B.) a travel move greater than the Retraction Minimum Travel, prone to a divot-type defect

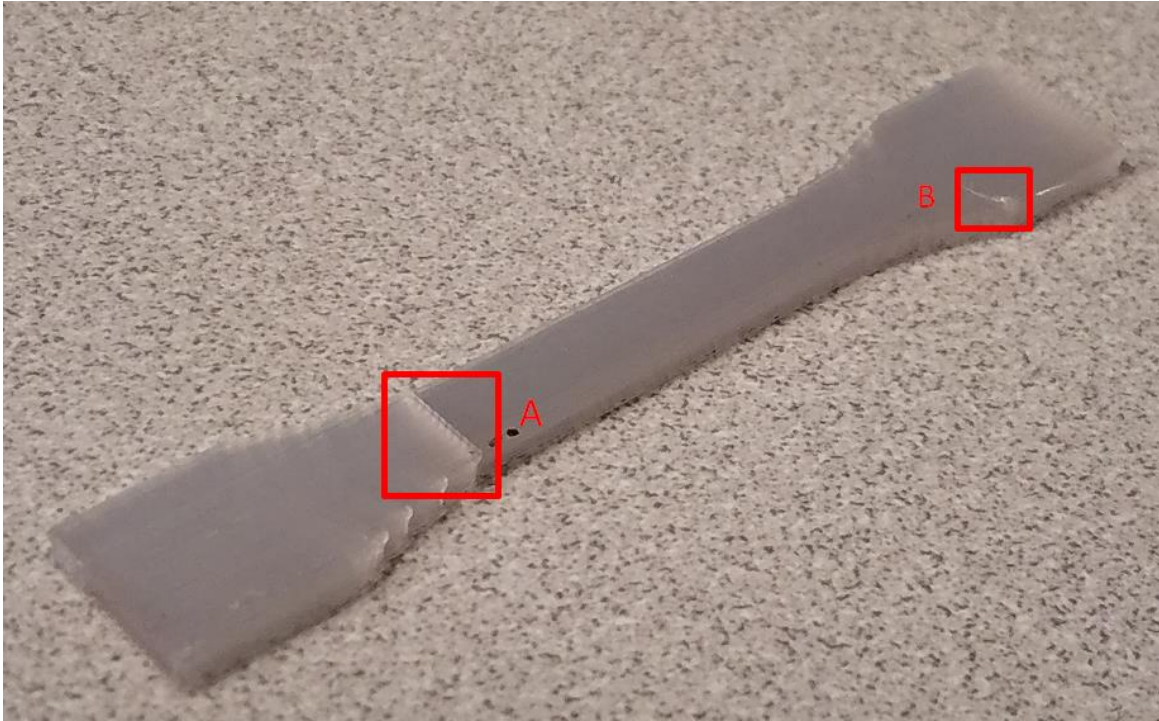


Figure 19: The longitudinal (11) specimen generated from the scan strategy shown in Figure 18

Showing A.) an ooze-type defect caused by a direct translation travel move, and B.) a divot type defect caused by a travel move preceded by a retraction and z-hop

Though the oozing given by the former strategy usually introduced a more detrimental defect, there were times this did not always hold true, such as retractions performed on the perimeter rasters of 33 specimens. Though the activation of the setting “Outer Before Inner Walls” eliminated the need for retractions in such a situation, the value of “Retraction Minimum Travel” was still adjusted on an as-needed basis to minimize the number of retractions while still preventing oozing.

The minimization of filament retractions is generally sought for the purpose of mitigating filament grinding, especially in printers which use Bowden-type extruders, such as the Ultimaker 2+. The knurled teeth which grip the filament will tend to wear the filament rapidly, but are necessary to overcome the internal friction of the Bowden tube and drive the material through the extruder. This rapid wearing is a condition which is worsened by successive translations of the knurled teeth over the same section of

filament. The number of successive translations and the length of filament over which the translations occur are actively constrained by the settings “Retraction Count” and “Minimum Extrusion Distance Window”. In the scope of this work, the setting “Minimum Extrusion Distance Window” is set to zero, nullifying the constraint. A failed print will occur due to filament grinding and lack of filament forwarding before the above-noted settings will limit retractions

Speed Settings:

Above almost any other single setting, reducing the print speed was seen to have the most pronounced effect on increasing print quality and breaking strength. The default speed is set to 60 mm/s, a value which was produced zero usable D638 tensile samples. A 44 MPa breaking strength in a 11-specimen was achieved by reducing the speed to 50 mm/s in batch “D”. A 52 MPa breaking strength in a 11-specimen was achieved at 30 mm/s in batch “G”. Speeds as slow as 15 mm/s were investigated in later batches for 11-specimens, and were seen to produce breaking strengths of 64 MPa, but other process settings were not held constant. A formal study including the independent influence of process speed was not performed. Though process speed is seen to be a heavily influential process setting, it is believed that the degree of influence of this setting is determined by the given printer’s ability to match the rate of extrusion to the rate of head translation. It was assumed that any further gains from successively decreasing the process speed would be outweighed by producing unrealistically high print times. Parts with a build-height-to-minimum-build-width ratio of 10:1 or more, such as Vertical “33” tensile specimens, were the exception to this assumption. Parts which fulfilled this criterion tended to suffer from a large deflection due to loads exerted upon the print surface as the part grew to cantilever further and further from the print bed.

The values of “Wall Speed”, “Outer Wall Speed”, “Initial Layer Print Speed”, and “Skirt/Brim Speed” were all available to be independently adjusted, but the potential effects of these adjustments were not investigated (they were simply matched to the print speed). The values of “Travel Speed” and “Initial Layer Travel Speed” were matched to one-another and a speed of 30 mm/s was selected as travel speeds \leq 30 mm/s produced more pronounced retraction defects.

Travel Settings:

The most significant setting modified in the Travel Settings was the combing mode. Typically set to “All”, this setting keeps the nozzle within the current layer footprint during a travel move. Presumably, the oozing that occurs in the translation between quasi-continuous print paths will generally leave a defect which will be covered up by the fabrication of the following layer. As, aesthetically, setting the combing mode to “All” is thought to eliminate the need for retractions, this combing configuration effectively disables all retraction and z-hop settings. Prior to the discovery of this setting, both manual and automated post-processing of the g-code were performed to add in the necessary z-hops and retractions.

Z-hops were added as a means of preventing the occurrence of nozzle drags. As each raster was laid with an excessively wide and short cross-section, with a temperature at or above the glass transition, this cross-section was inferred to deform over time to a narrower, taller cross-section, becoming prone to scarring from a nozzle translation. Allowing for this inferred behavior required the build platform to be lowered between nozzle translations in order to avoid scarring the tops of the rasters with the nozzle tip. The selection of a Z-hop height of 3 mm was arbitrary. An example of a nozzle drag may be seen in Figure 20.

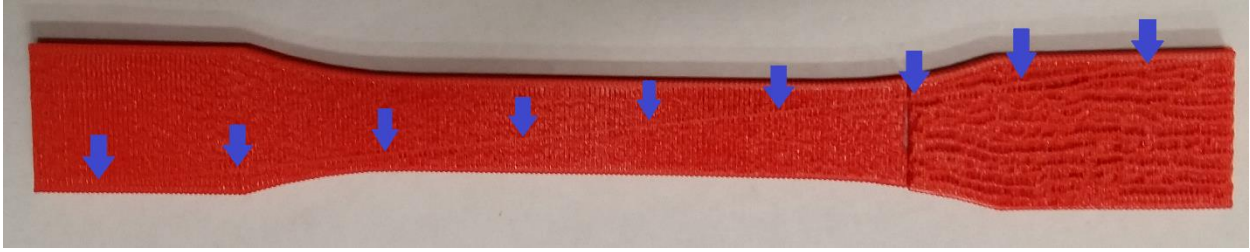


Figure 20: A nozzle drag on a transverse (22) tensile specimen

Often, the points selected by the slicer to begin extruding the perimeter raster were poorly selected, presenting a flaw on the outer contour of either the gauge length or the gauge reduction. As such, the values of “Layer Start X” and “Layer Start Y” were modified to relocate this flaw to the grip section, a less critical portion of the specimen.

Cooling Settings:

In some of the earlier samples in the Q-batch, vertical samples were printed with an elevated nozzle temperature (240°C), an over-extrusion of material (120%), and no cooling (this combination of parameters in transverse samples was formally investigated with a Latin-hypercube design of experiments in the P-batch and was deemed optimal). In vertical samples, these settings were seen to produce a severe distorting effect in which the nozzle, in the process of depositing material, would “pull along” a significant portion of each layer in the direction of travel before allowing it to solidify, introducing the net effect of distorting a rectangular cross-section into a cross-section similar to a parallelogram. (graphic?) Several attempts to correct for this observation were made by skewing the CAD file in a way that mirrored the direction of the observed distortion; these attempts resulted in limited success, but were largely unsuccessful. One successful technique to mitigate this effect was realized, however, in reversing the path of every other layer, eliminating both the need for end-of-layer retractions, as well as the distorting effect. Though eventually successful, the judgement was made to favor the local optimum observed at 100% fan modulation over the local optimum observed at 0% fan

modulation, as the distorting effect would preclude the practicality of more complex parts requiring overhung geometry and support structures. The Latin hypercube DOE is presented in Chapter 5.

The specification of “Minimum Layer Time” to a value of zero seconds effectively disabled any pause of printing operations at the end of any layer. This had a pronounced effect on Q-batch samples printed without cooling, however, apart from small-scale samples printed vertically, this setting constrained a set of criteria which was almost never observed in this work.

Support Settings: (Activation varied from dataset to dataset)

The support settings were investigated in the R-batch, to the end of determining what support settings would need to be modified to make effective use of the optimized print settings determined in the P-batch in order to allow support material to be removed without causing flaws. Also, to determine the magnitude of effect caused by unavoidable surface-quality flaws induced by support removal. Largely, this investigation remains incomplete, as the slicer settings which are currently available offer only statically prescribed values which govern the support for the entire print. What is deemed necessary to truly optimize support settings are settings which vary per the geometry printed, particularly as a function of overhanging mass, and the strength and temperature of the cantilevered print geometry in the localized area surrounding the overhang.

One setting deemed necessary to achieve a successful print was the activation of a brim-type build plate adhesion for the support material. Without the brim-type build plate adhesion, the support material tended to delaminate from the build plate.

Build Plate Adhesion Settings:

Many build plate adhesion techniques are available in Cura, though they were only investigated to the end of successfully halting delamination from the build plate. A “Brim”-type adhesion was seen to successfully accomplish this, sometimes the value of “Brim Width” needed adjustment. For the purposes of more complex prints, the setting “Brim Only On Outside” was disabled, as this was seen to reduce some occurrences of delamination.

Dual Extrusion Settings, Mesh Fixes, Special Modes:

No adjustments were made from the defaults for “Dual Extrusion”, “Mesh Fixes”, or “Special Modes”.

Experimental Settings:

In the experimental settings, “Infill Travel Optimization” was enabled, though it was not entirely clear what would specify the decision process in the selection of travel path absent the activation of this setting. Maximum Resolution was set to 0.001 mm, and “Make Overhang Printable” was enabled.

2.3: MEANS OF EDITING G-CODE:

This work utilized two primary means of editing G-code. The first means was to directly edit of g-code via MS Excel. The second means was a Matlab script that read a source g-code and wrote a modified g-code. **2.3.1** discusses the structure of the Excel-based post-processor; **2.3.2** discusses the structure of the Matlab-based post-processor; and **2.3.3** provides the singular lines of code and slicer settings which offered beneficial freedoms.

2.3.1: THE STRUCTURE OF THE EXCEL-BASED POST-PROCESSOR:

The Excel-based post-processor consisted of cell-based formulas which identified segments of g-code from one line at a time. As the g-code is text-based, manipulations via Excel consisted of five steps: (1) Add a space to the end of each line, (2) Use the spaces at the end of successive code segments to identify where each code segment terminates, (3) Isolate and sort the code segments, organizing a tabular command summary, (4) Modify the command summary as necessary using coded logic to generate a preferred modification to the code, and 5.) Reconstruct the code as originally modified, truncating the space added at the end of each line.

There were several goals which were pursued in the course of using the Excel-based interface, including the shifting of odd-numbered layers, the addition of retractions and z-hops, modifying the nozzle flow to under- or over-extrude, and reversing the path of odd-numbered layers.

Offsetting of odd-numbered layers by half the measure of raster width was investigated in batches “B” through “L”. Observation of fractured samples generated with this technique under low-powered magnification indicated that the execution of the layer shift was successful, but no substantial tensile strength benefits were realized that could not be gained easier via alternate techniques, e.g., over-extrusion. It is worthy of note that simply shifting the odd-numbered layers by half the raster width in-plane was not seen to exploit the full benefit of this modification. The combination of the in-plane odd-numbered layer shifts with an appropriate z-compression value (experimentally found to be 10% of layer height) was found to provide the best results. The derivation of the z-compression value is discussed in Section 2.2, Quality settings. However, in studying the results of batches “K” and “L”, it was seen that offsetting alternate layers provided a detriment in achievable vertical “33” tensile response. This was

mostly attributed to the half-raster-width surface flaw left by each odd-numbered layer shift (Figure?). It is presumed that this effect may be partially or fully mitigated through some means of filling this surface flaw, but the execution of this measure was not investigated. Further batches generated samples with a traditional layer stacking (no odd-numbered layer offsets).

The addition of retractions was, for a brief interval of time, added manually with the Excel-based interface, due to the ignorance of the effect of the combing mode. The strategy was as follows: 1.) use the distance formula to calculate the magnitude of a travel move, 2.) Scan the code for travel moves exceeding a user-defined 6-mm threshold value, 3.) insert the necessary lines of code to retract the filament, lower the build platform, translate the gantry, raise the build platform, and unretract the filament. A Matlab code was developed solely for this function and provided a much more efficient means of making these modifications, though shortly after, the correction of the above-mentioned combing mode setting was found to eliminate the need for this modification altogether.

The modification of nozzle flow was, for a time, executed in the Excel-based interface. The default format of the extruder coordinates as “absolute” coordinates proved a more difficult modification to make, as well as more computationally intensive. The strategy was as follows: 1.) for each extrusion move (G1), calculate distance traveled and the amount of filament forwarded, 2.) calculate the ratio of filament forwarded to the distance traveled and multiply this value by a desired percentage of flow, 3.) multiply by distance traveled and add this value to the running summation of filament forwards, giving the absolute extruder coordinate. This strategy was seen to work, but the cumulative summation of the filament forwards from each extrusion move proved considerably computationally expensive. This same effect may be accomplished by either tuning the print live at the printer following the initiation of the print, or by use of extrude factor override percentage command (further discussed in **2.3.3**). The latter

technique is recommended, as it provides one less thing to remember, and the ability to track the modification.

In later samples of the Q-batch, which largely investigated distortion of printing vertical samples with an elevated nozzle temperature (240°C), an over-extrusion of material (120%), and no cooling, a technique which proved to mitigate the observed distortion very effectively was the reversal of odd-layer scan paths. (Graphic?) The strategy was to offset each odd-numbered layer by the width of the cross-section (across the X-axis direction), and reverse the direction of X-axis movements in each odd-numbered layer. Though the technique was successful, it could only be effectively applied to objects which did not change in width of cross section, due to the method of execution. Additionally, further pursuit of print settings which offered no process cooling were abandoned shortly thereafter in favor of a more geometrically stable print process, though a more generic form of this general approach is thought to possibly offer a better-performing process with respect to the achievable quality of overhung geometry.

2.3.2: MATLAB POST-PROCESSOR:

The Matlab [36] post-processor was constructed originally as a means of automating an otherwise manual process of adding retractions and z-hops, reducing a process of several hours to a matter of a minute or less. Though efficient and robust, the level of expertise in Matlab required to further this post-processor generally prevented it from being advanced. Additionally, the general need for its use was nullified upon the discovery of a slicer setting which allowed retractions and z-hops to be added automatically. It is worthy of note, however, that if further investigation be invested into manipulating or evolving scan path strategy, Matlab would provide a worthy interface to evolve the framework. Given a part of significant complexity, it is not uncommon to see between tens-of-thousands and

millions of lines of code. Once the length of the file grows beyond the tens-of-thousands of lines, an Excel-based post processor starts to become more and more cumbersome, to the extent of becoming largely impractical.

2.3.3: G-CODE SYNTAX AND SLICER SETTINGS WHICH OFFERED BENEFICIAL FREEDOMS:

The Batch-P DOE concluded that several optimal process settings be held for generating a transverse (22) tensile specimen. Once identified, these settings were held constant throughout the remainder of the test batches. Executing these changes was found to be most practically accomplished by adding lines of g-code to the code generated by the slicer [37].

M104 S240: An M104 g-code command sets the nozzle temperature in °C to the value listed after “S” setting. This code changes the nozzle temperature from whatever the default setting for the current material (210 °C for PLA) to 240 °C. This differs from a M109 command, as the M109 command will wait until the requested temperature change is achieved to resume printing move/travel commands.

M221 S120: This code changes the material extrusion per distance traveled to 120% of the rate specified by the g-code. This has the same net effect as increasing the flow rate at the machine after initiating a print.

M106 S255: This turns the fans on at full speed, modulated control may be achieved by adjusting the number following the “S”. Integer values between zero (0%, i.e., off), and 255 (100%) are writable. Although typically automatically added by the slicer, this command may be user modified.

Chapter 3: PRINTING AND TESTING ASTM D638 HALF-AND FULL-SCALE PLA SPECIMENS

After being prepared in Cura and editing as necessary, individual g-code files were uploaded to an SD-card, which was inserted into an Ultimaker 2+ printer. Although a single g-code file may specify printing instructions of multiple specimens within a single print (or “build”), all ½-scale and full-scale ASTM D638 specimens were printed separately requiring between half an hour to a full hour to print and cool. Cooling was afforded for a minimum of 15 minutes before removal from the base plate. If necessary, a thin putty knife was utilized to dislodge the specimen, taking care not to subject the specimen to bending stresses. Removal of a ½-scale D638 tensile dog bone specimen with the putty knife is shown in in Figure 21:



Figure 21: Removal of a clear PLA ½-scale D638 tensile dog bone specimen with putty knife

For specimens allowed to cool more than approximately 3 to 4 hours, the putty knife was unnecessary, as the adhesion between the glass surface and the first layer diminished as the build plate approached room temperature. On several occasions prior to batch “P”, the build plate was observed not to have

cooled long enough to dislodge the part without waiting for further cooling. In some of these instances, the glass build plate was removed with the part attached, and cooled manually, by running water over the back side of the plate, with the rapid cooling allowing the dislodging of the part without mechanical removal. However, in the analysis of batch “M”, this “rapid cooling” technique was found to decrease tensile strength, therefore, the “free convection cooling” method was selected as the preferred method of specimen removal.

One point of specification that should be emphasized is the hydrophilic nature of PLA was mitigated during the printing process by storing the filament in a dry box, but subsequent to the printing process specimens were left exposed to atmospheric effects for the duration of time until batches were tested. At times, this interval was short, and likely contributed an insignificant effect. Other times, it is possible the interval may have allowed the specimen to absorb ambient humidity. It is thought that future work should seek to isolate from these effects by bagging specimens as they finish the printing process.

Prior to testing, the brim rasters, which may be seen under the leading edge of the putty knife in Figure 21, were mostly removed by hand, without the use of any tool, by simply folding-and-peeling each brim raster against the edge of the part. The sharp corners were typically the most effective place to begin the folding-and-peeling process, as is shown in Figure 22. Any brim rasters remnants were removed using an X-ACTO knife, with a sawing motion, exercising extreme caution not to cut into the part, especially on brim rasters which traced the perimeter of the gauge length.

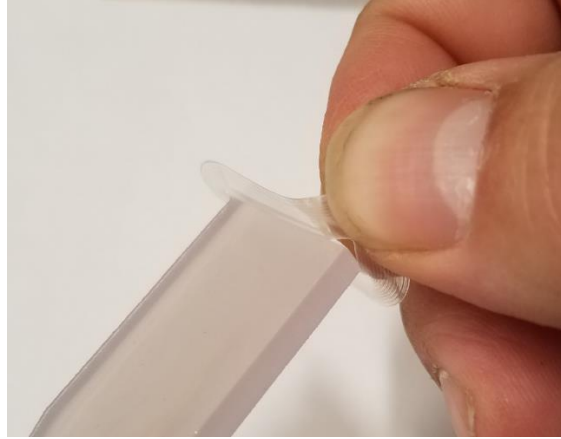


Figure 22: The folding-and-peeling process, removing brim rasters from a tensile specimen

After removal of the brim rasters, each sample was loaded into an MTS Criterion series model 43 load frame [38]. Whereas full-scale specimens were consistently placed in the load frame grips using the grips as a centering jig, ½- scale specimens were consistently placed in the load grips utilizing a custom-manufactured centering jig. Dimensions for this centering jig are shown in Figure 23. The jig was placed upright, on the bottom set of jaws, squaring the outside corner of the grip region of each sample to the inside corner of the positioning jig. This fitment of tensile specimen to positioning jig is shown in Figure 24.

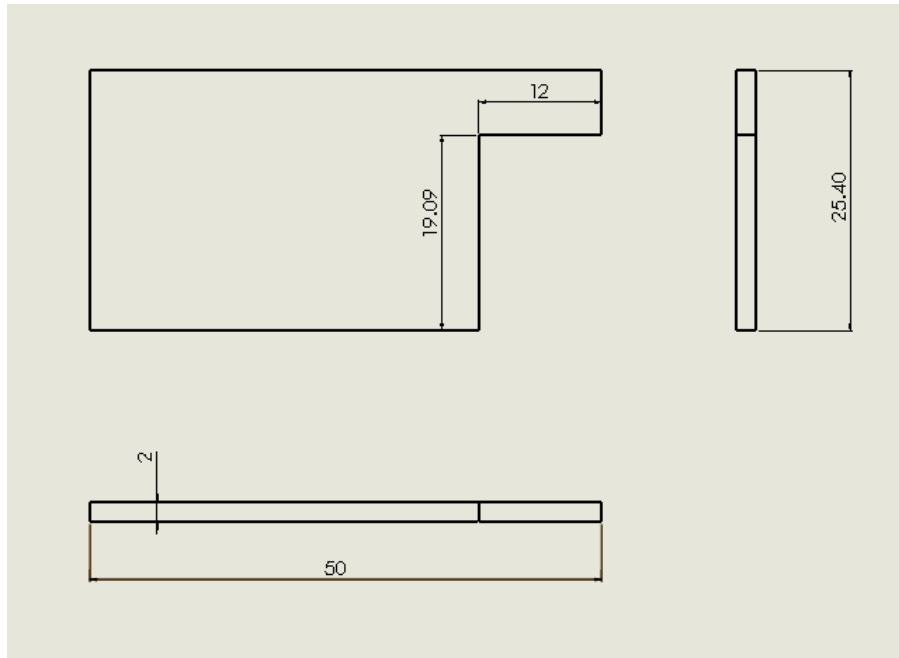


Figure 23: Drawing of custom centering jig utilized specimen positioning in MTS grips



Figure 24: The fitment of a tensile specimen to the centering jig

Once the specimen was positioned, the load frame was powered on, and each sample was tightened into the load frame using wedge-action grips. These grips are shown in Figure 25. The bottom set of grips was tightened first, as a discontinuity of handle travel in the bottom grips was seen to cause a sudden shift in loading during the tightening phase if the top set of grips were already tightened to support said loading. An estimated 4-5 N force at the end of the handle was applied to tighten first the bottom, then the top set. The wedge-action of the grips tightened further during testing, but only as

necessary to support the loading applied. When tightening the top grip set, caution was exercised to apply a minimal torque to minimize tensile preloading due to tightening of the grips.



Figure 25: MTS Advantage wedge-action grips

Once each sample was tightened into the wedge-action grips, manual control of the load frame's crosshead movement was activated at the handset, and the loading on the sample was set to between 4-5 N in tension. In the computer-controlled interface MTS TestSuite, the project was loaded, the 2.5-mm/min crosshead rate for ½-scale specimens (or 5-mm/min crosshead rate for full-scale specimens) was verified (), and the controller was interlocked. The MTS P/N 634.11F-24 extensometer, shown in Figure 26, and its corresponding cable were then connected to the load frame, and both the load cell and the extensometer were verified. The extensometer was then attached to the specimen, the lock pin

was removed, and the reading was set to zero. The strap that attaches the lock pin to the extensometer was held to ensure fracture of the specimen did not allow the sensor to incur damage from a fall, and the test was then initiated.



Figure 26: The 25-mm extensometer used for testing

Each specimen was monotonically loaded in tension at room temperature until fracture, after which the pieces were unloaded from the wedge-action grips, and the interface was reset to readiness for subsequent specimens. Load and extension data were written into .CSV format, and saved to a thumb drive, from which stress and strain were calculated.

When measuring the cross-sectional area of each specimen, per D638, both width and thickness were measured at three locations across the gauge length. The minimal cross-section area from each of the three pairs of combinations of width and thickness were used to determine axial stress. A point that is deemed worthy of note is that, especially under the effects of modifying extruder temperature and flow rate, the cross-section was seen to vary from the nominal measurements which assume a rectangular cross-section. To quantify the specifics of the geometry, no means save for estimation based on visual inspection were available, but a model was constructed in Solidworks to depict a cross-section thought

to be more accurate for each raster orientation. The actual measurements of the gauge width and thickness for tensile specimens in each orientation is given as the “out-to-out”, or maximum dimension across widest and thickest point, respectively. The distorting effect in 11 is thought to be credited to the Poisson’s ratio under the effects of thermal contraction, the distorting effect in 22 is thought to be directly due to thermal contraction effects, and the distortion in 33 is thought to be primarily due to over-extrusion causing a bulging of the footprint of each layer. The approximated “true” geometric boundaries of each orientation of cross-section is shown below, as Figure 27, with raster directions indicated by black lines. Estimating upon the basis of the figure, measurements of a specimen tend to over-estimate the loading area, providing the area of the grey boundary, whereas the actual boundary is shown in red. The estimated ratio of over-estimation is given by the percentage in Figure 27.

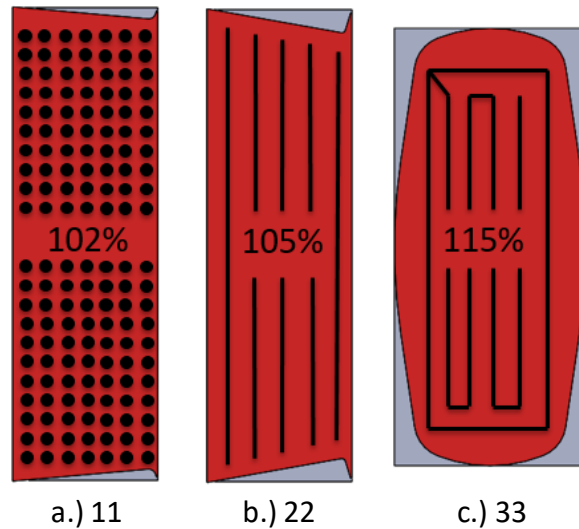


Figure 27: cross-sections of tensile specimens

Showing “as-measured” cross-section (grey) vs the “estimated actual boundaries” of cross-section (red), for 11, 22, and 33 tensile specimens

Chapter 4: EXPERIMENTAL DETERMINATION OF PROCESS SETTINGS FOR AM OF PLA

The primary goal of this chapter is to detail the procedure and results in the conduction of the design of experiments (DOE) which governed the process settings for extrusion multiplier, fan speed, and nozzle temperature. Remaining process settings were chosen based on informal observations and intuitive logic, giving preference to whichever setting values produced the strongest specimen. Further details specifying the scope and logic of informal investigation are found in

2.2.

The conducted DOE was designed to optimize the process settings for the printing of a transverse (22) tensile sample. DOE specimens were labeled as Batch-P, with subsequent batches employing the same set of process settings for nozzle temperature, fan speed, and extruder flow. A similar procedure could be executed toward the goal of optimizing process parameters for longitudinal (11) and vertical (33) samples, which may be seen to offer differing results. Though not performed, DOEs to optimize tensile strengths of longitudinal (11) and vertical (33) specimens would fall under the scope of continued work.

The overall structure of the DOE was as follows: A.) Employ a Latin hypercube sampling for twenty variants of three process parameters, B.) Generate the g-code, print, and tensile test said variants, building a vector of twenty ultimate tensile strength (UTS) values, C.) Use the matrix of parameter variants and the vector of UTS values to build two surrogate models (a second-order full polynomial fit and a multiquadric radial basis fit), and D.) Optimize both surrogate models to obtain process settings which will give the highest UTS.

A three-parameter, twenty-sample Latin hypercube parameter sampling was generated in Matlab. The raw sampling was multiplied by 100, and then rounded to the nearest integer value. These values were taken to represent a percentage of variation for twenty samples, across an exploration range of three process settings: extruder flow (from a default setting of 100% to 120%), fan speed (from 0% to a default setting of 100%), and nozzle temperature (from 100% to 117% of a default 210 °C). The rounded hypercube samples were then mapped to the corresponding normalized exploration ranges, generating twenty variant samples. G-code was then generated for the twenty variants. Then, the variants were printed and tested using the printing and testing strategies outlined in Chapter 3, recording a response vector of twenty ultimate tensile strength (UTS) values. The process parameters for the twenty variants and the twenty corresponding UTS values are shown in Table 4.1.

Table 4.1: Inputs and outputs for the DOE to optimize 22 tensile strength

Input Parameters			Output Response
Percentage of Extruder Setting Range (100%-120%)	Percentage of Fan Setting Range (0%-100%)	Percentage of Nozzle Temperature Range (100%-114%)	Ultimate Tensile Strength, MPa
98	86	35	42.6
21	49	54	22
10	80	59	29.8
16	10	86	46.2
84	19	73	52.2
76	35	99	49.7
68	43	11	33.3
43	0	21	41.9
51	57	2	15.6
72	69	63	42.5
35	75	7	12.3
49	6	91	49.2
90	39	81	50.5
29	52	80	42.7
64	75	26	36.4
86	24	34	45.7
32	95	41	29.6
58	94	16	32.7
5	61	70	32.2
1	26	46	33.5

Two surrogate models – a 2nd order full polynomial and a multiquadric radial basis function – were then formed from the data given in Table 4.1 to capture the relation between the varied process settings and the corresponding UTS values.

In the formulation of the 2nd order full polynomial surrogate, the last column of Table 4.1 was grouped as a 20x1 vector “B”, and the first three columns of Table 4.1 were grouped as a 20x3 matrix “A”. The matrix “A” and the vector “B” were passed to a sub function containing a multivariate polynomial regression fitting algorithm. The multivariate polynomial regression fitting algorithm then generated a 10x1 vector of constants according to the relation shown in Equation 7.

$$P = C_1X^2 + C_2X + C_3Y^2 + C_4Y + C_5Z^2 + C_6Z + C_7XZ + C_8XY + C_9YZ + C_{10} \quad \text{Equation 7}$$

In Equation 7, “P” represents the UTS value from Table 4.1, “X” represents the percentage across the extruder setting range from Table 4.1, “Y” represents the percentage across the fan setting range from Table 4.1, and “Z” represents the percentage across the nozzle temperature setting range from Table 4.1. The constants, C₁ through C₁₀ are calculated by the regression algorithm and are passed back to the main program in order to form a surrogate model to represent the design space.

The formulation of the multiquadric radial basis function surrogate is accomplished in a two stage process, as outlined by Wang [39]. First, the algorithm must be trained to represent the design space by predicting each of the training points. Next, the algorithm is utilized to predict an arbitrary point. To first train the algorithm, the last column of Table 4.1 was grouped as a 20x1 vector “B”, and the first three columns of Table 4.1 were grouped as a 20x3 matrix “A”. The matrix “A” and the vector “B” were passed to a sub-function containing a multiquadric radial basis fitting algorithm. For each row in matrix

“A”, the 1st, 2nd, and 3rd column entries were used to define x, y, and z Cartesian coordinates for training points, respectively. The sub-function first evaluates the Euclidian distance, “r”, given by Equation 8.

$$[r_{Mi}] = \sqrt{(x_M - x_i)^T (x_M - x_i)} \quad \text{Equation 8}$$

In Equation 8, “r” is a symmetric MxN matrix, where N is the number of training points, and M is the number of points to predict. “x_i” is a point defined by Cartesian coordinates given by each row in matrix “A”. When training the algorithm, one must predict all the training points. Therefore, when training the algorithm, “x_M” is also a point defined by Cartesian coordinates given by each row in matrix “A”. When training the algorithm, as each row and column pair corresponding to the same index evaluate the Euclidian distance between one training point and itself, the matrix “r” is symmetric about a diagonal of zeroes. Next, the matrix “r” is passed into a multiquadric radial function, Φ, which is shown in Equation 9.

$$[\Phi(r_{Mi})] = \sqrt{r_{Mi}^2 + c^2} \quad \text{Equation 9}$$

In Equation 9, “Φ” is a symmetric NxN matrix, where N is the number of training points, and “c” is a value of one. When training the algorithm, as the matrix “r” is symmetric about a diagonal of zeroes, the matrix Φ is symmetric about a diagonal of ones. Next, a Nx1 column vector of unknown lambdas are determined by solving the relation shown in Equation 10.

$$[\Phi(r_{Mi})] * \{\lambda\} = \{B\} \quad \text{Equation 10}$$

In Equation 10, the matrix “Φ” represents the matrix as represented in Equation 9, and the vector “B” represents the vector of UTS values as introduced in the description leading to Equation 8. Once the

lambda values were determined, Equation 10 was then utilized to solve for an arbitrary UTS value, given the reformulation of Equation 8 and Equation 9 on the basis of arbitrary selections of the three input parameters in Table 4.1. The vector and matrix dimensions and the procedure reflecting the differences between training the algorithm and making a prediction using the algorithm are shown in Figure 28.

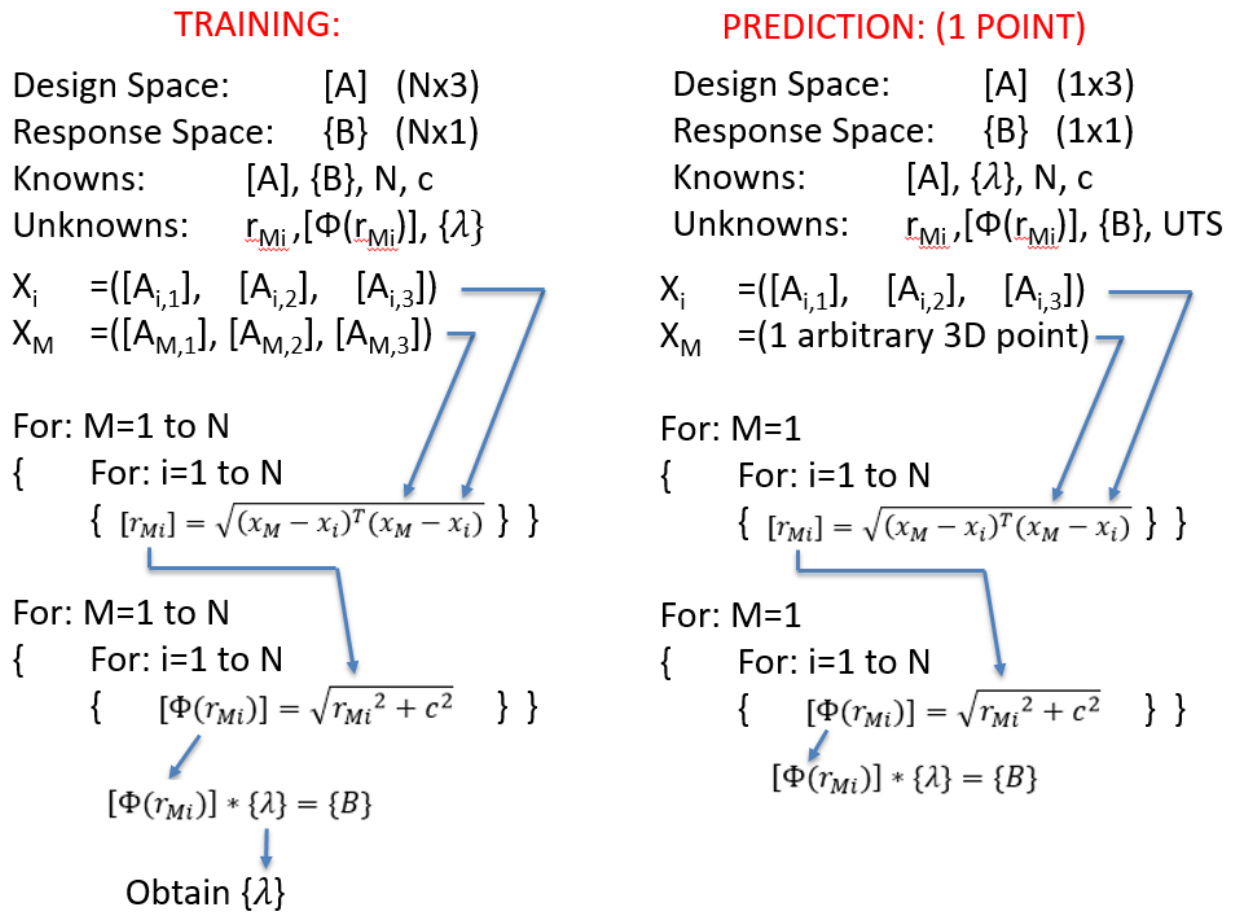


Figure 28: The operations to complete a multiquadric radial basis training and prediction

As their domains spanned four dimensions, both surrogate models were represented graphically as a series of 3D surface plots, with each plot displaying a fixed value of extruder temperature. Both models exhibited highly similar surface contours, and both models predicted both optimal sets of process settings.

The two surrogate models were subjected to a modified version of the steepest descent algorithm in the formal approach to finding the local maxima of both the 2nd-order full polynomial fit and the multiquadric radial basis fit. The steepest descent algorithm is a stepwise minimization algorithm in which successive iterations minimize a function's value by searching along a vector given by the negative of the partial with respect to each dependent variable[40]. The algorithm is shown below, in Equation 11:

For: a function, $f(\mathbf{X})$:

$$\mathbf{X}^{(k+1)} = \mathbf{X}^{(k)} - \alpha_k \nabla f^{(k)} \quad \text{Equation 11}$$

Where:

$$\nabla f(x_1, x_2, x_3) = \begin{cases} \frac{\partial f}{\partial x_1} \\ \frac{\partial f}{\partial x_2} \\ \frac{\partial f}{\partial x_3} \end{cases}$$

$$\mathbf{X}^{(k)} = (x_1, x_2, x_3)^{(k)}$$

In Equation 11, The optimum step size, α_k , is evaluated by selecting the lowest evaluation of function value, $f(\mathbf{X})$, in the direction defined by the vector $-\nabla f^{(k)}$. The coordinate, represented by \mathbf{X} , may be a function of any number of dependent variables. In Equation 11, there are three dependent variables, x_1 , x_2 , and x_3 .

A numeric derivative was calculated with respect to each varied setting, and a gradient was then assembled from these derivatives, establishing a search direction vector. This search direction was then

subject to a bounded step size, alpha. As the observed maxima existed at the boundaries of the design domain, as and where the step size crossed the boundary of a design domain, the component in the search vector corresponding to the crossing of that boundary was then nullified. The location corresponding to that boundary was then assumed maximum, and the search vector was reformed on the basis of the remaining derivatives. This approach identified two local maxima for each surrogate model. The first local maxima (OPT1) occurred at 240°C extruder temperature, 120% extruder multiplier, and 0% fan speed. The second local maxima (OPT2) occurred at 240°C extruder temperature, 120% extruder multiplier, and 100% fan speed. The surface plots depicting the location of both maxima as predicted by the full polynomial fit and by the multiquadric radial basis fit are shown in Figure 29.

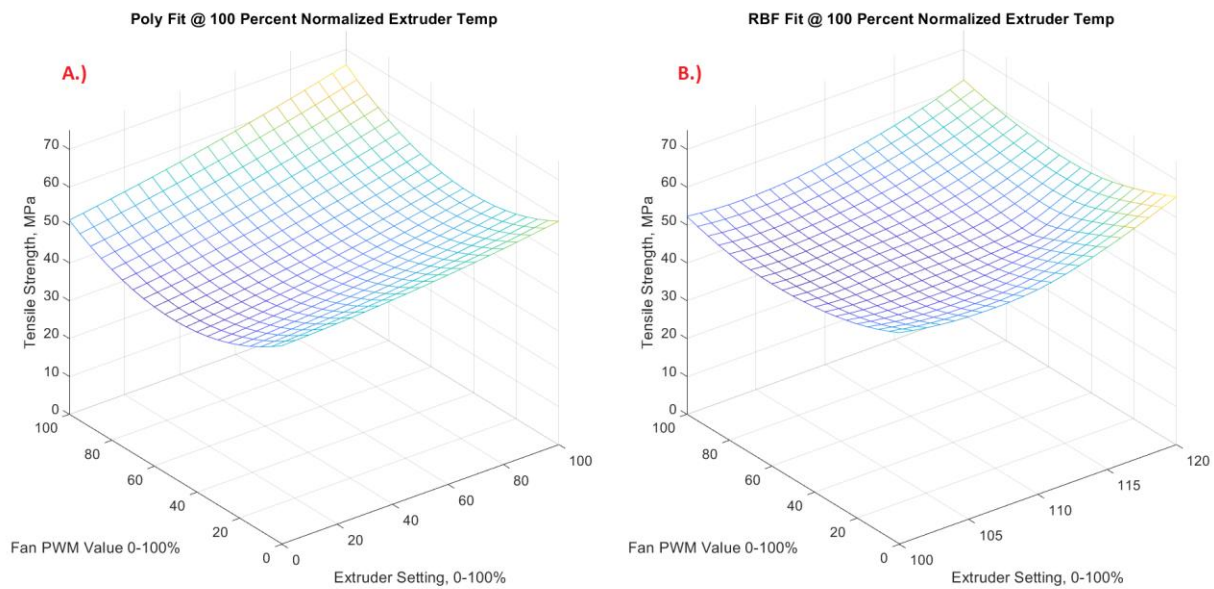


Figure 29: Surface plots depicting the two optimal combinations of process settings
 A.) a full polynomial response surface, and B.) A multiquadric radial basis function

To empirically validate the two optimal combinations of process settings predicted by both models, a tensile test specimen was printed and tested with each of the optimal sets of settings predicted by the surrogate models. The stress-strain response of the two validation specimens are shown in Figure 30.

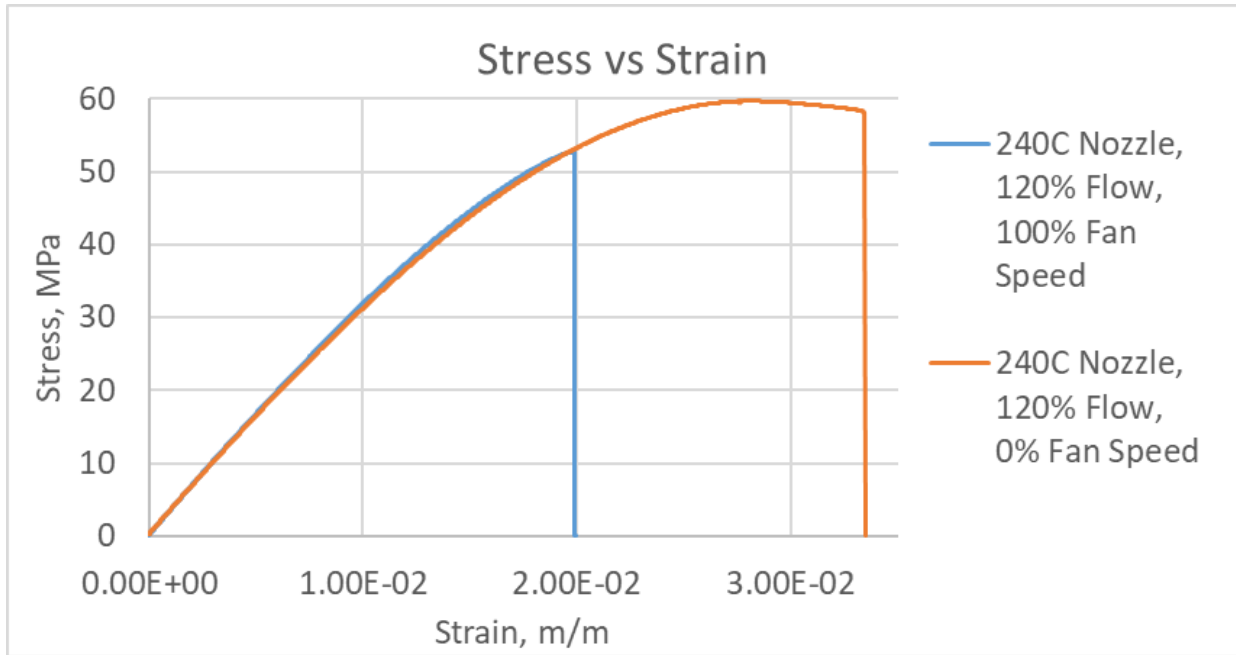


Figure 30: A Stress-Strain graph for the validation of the DOE surrogate model results

The specimen produced by settings corresponding to OPT1 achieved an UTS of 52.7 MPa, and the specimen produced by settings corresponding to OPT2 achieved an UTS of 59.6 MPa. Despite the more favorable strength given by OPT2's settings, subsequent test specimens were generated with OPT1's settings, in favor of maintaining dimensional stability.

Related research involving the practicality and applicability of both styles of surrogate model tends to support an approach utilizing a radial basis surrogate model for most situations[39]. In reference 39, twenty benchmark problems are solved to proof the level of error in a variety of surrogate modeling techniques, with the benchmark problems ranging in design domain characteristics. Some benchmark problem characteristics include differing levels of dimensionality, differing levels of nonlinearity, differing levels of noisiness, and the number of training points. Comparing the variety of surrogate modeling techniques, nearly all characteristics of design domain produced the least error when modeled

using a RBF. There is one recognized advantage of a polynomial response surface technique however, in the inherent intuition of the terms used to model the design domain.

Chapter 5: UNDERSTANDING DEFECT MODELING

One of the many goals of any numerical simulation is to match the nature of reality. However, in this work, the techniques used to approach the numerical modeling of tensile loading through failure are fundamentally different from the techniques typically used to model a numerical response in the elastic region or elastic-plastic region. For example, in ABAQUS CAE, by applying elastic and plastic properties to a tensile specimen geometry, fixing one end, and forcing a displacement upon the opposing end, the characteristic of deformation produced is shown in Figure 31.

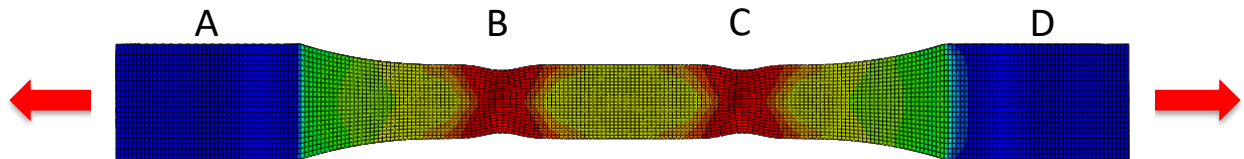


Figure 31: The deformation pattern of a traditionally modeled tensile response

In the simulation giving rise to the result shown in Figure 31, elastic properties were defined by a Young's modulus of 3.27 GPa, and a Poisson's ratio of 0.36. Plastic properties were defined by a single-line definition consisting of a yield stress of 45 MPa, and a plastic strain of zero. The geometry modeled was that of a 1:2-scale D638 Type 1 tensile specimen [33]. The model was meshed with a global mesh size of 0.35 mm, end "A" was prescribed an Encastre boundary condition, and end "D" was prescribed a forced displacement of a 3 mm magnitude. Though detailed, the particulars of the geometry and material definitions in the simulation leading to Figure 31 are of little importance here, the key observation is the deformation pattern, particularly at locations "B" & "C". As may be expected, the prescription of a significant enough forced displacement at end "D" will introduce a localized deformation in the gauge length region. What may likely be unexpected, as it is indeed unrealistic, is

that there be two localized deformation regions, one presenting at “B”, and one at “C”. This occurs because there is an unrealistic level of uniformity to the material definition. In a realistic test specimen, produced by any means of manufacturing, various regions throughout the part will exhibit a range of material properties. In the present work, the variability of material properties is assumed to be due to a presence of defects imposed on a flawless material definition. The magnitude of these defects are location-specific, allowing some regions to be stronger than others. By applying the concept of a variable material definition to the simulation shown in Figure 31, one may assume the material surrounding location “C” is slightly less defective, or given by a yield strength definition of 50 MPa, rather than 45 MPa. This will produce the deformation pattern shown in Figure 32.

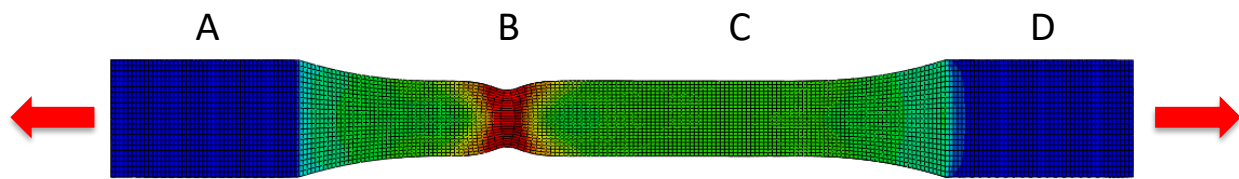


Figure 32: A simulated tensile response showing localization in one region

This deformation pattern may be introduced by reforming the yield strength to 50 MPa in the region surrounding location “C”

Though the characteristic of response shown in Figure 32 may be reasoned to be more realistic than the response shown in Figure 31, it is worth asking the question: The material at location “B” is no more defective than the material immediately to the left or the right of location “B”; Why is this specimen more prone to localization at “B” than any other region along the gauge length? This is because the radius of the gauge reduction introduces a stress concentration. This stress concentration creates a pattern that causes the stress to peak at location “B”, introducing the localization effect at location “B” before any alternate location. Though this result may appear to offer the correct characteristic of response, it is a response that is governed by the role of a purposeful-geometric defect rather than a

method-specific-material defect. Physically, the reason the tensile specimen geometry is purposefully contoured from the wider grip region down to the narrower gauge length is twofold. First, the inevitable compression stresses required to grip the ends of the specimen are given the length of the gauge reduction to allow for the increased stress to dissipate via the Saint-Venant principle. Second, the radius of the gauge reduction is sufficiently sized as to mitigate the effect of the stress concentration, such that the defects present on the gauge length are allowed to be the predominant factor governing the occurrence and locale of the localization effect. In the simulation giving rise to the deformation pattern shown in Figure 32, compressive stresses of the grip section are not modeled, and no material defects are introduced. Thus, it is posed that, although the approach employed in the generation of Figure 32 may offer a comparable characteristic of result, and may also potentially offer a satisfactory match to tensile data, it arrives at such for the wrong reasons.

In order to employ the approach favored in the present work, the properties of two states of a working material must be defined, i.e., the properties in a neat state (assumed), and the properties in a flawless-printed state (calculated) as described below.

Material in a neat state is given mechanical properties which apply to material manufactured with a level of perfection only achievable in the realm of numerical simulation. Neat material is defined to be free from all effects of manufacturing, including voids, residual stresses, and end-of-raster defects.

Though some methods of manufacturing may be reasoned to produce fewer defects than others, there exists no manufacturing method capable of producing a specimen consisting of defect-free neat material, thus by definition, a neat specimen cannot be produced. Additionally, neat material properties are also free from the effects of testing, such as compressive stresses introduced in the grip section, and

stress concentrations from the radius of the gauge reduction, thus by definition, neat material properties cannot be physically tested, even were samples of neat material able to be manufactured.

Material in a flawless printed state excludes the detrimental effects of residual stresses and end-of-raster defects, but accounts for the detrimental effect from air inclusions (voids) between neighboring rasters, giving Baseline Material an orthotropic definition, whereas neat material is isotropic. Baseline Material is assumed to be the most perfect achievable state of material in the physical realm. As Baseline Material exists in the physical realm, this presents the theoretical opportunity to capture these properties experimentally. To do so, one must find a way of manufacturing and testing a test article free from the effects of both residual stresses and end-of-raster defects.

The process of numerically qualifying a material begins with accounting for the role of voids occurring between adjacent rasters (inter-raster voids). MCQ-Chopped, a software produced by AlphaSTAR, LLC for material calibration and qualification [41] accounts for inter-raster voids through a process of feeding estimates of neat material properties through predictive algorithms to evaluate a definition of Baseline Material. This process is described further in section 5.1. Following the initial calibration of the material model in MCQ chopped, there are two possible approaches which may extend to a calibration of the material model. The first approach, termed the “Default Approach”, follows the procedure recommended by the software developers (AlphaSTAR, LLC). The Default Approach aims to evaluate the definition of Baseline Material by tuning the values of neat properties and assumed void volume ratio in MCQ-Chopped. These values are tuned toward the goal of matching a predicted tensile response in MCQ-Chopped with the mechanical response from empirical tensile data. The Default Approach is discussed further in 5.2, giving rise to a process that continues through Chapter 6 and Chapter 7, with results presented in Chapter 8. The second approach, termed the User-Informed Calibration approach,

aims to evaluate the definition of Baseline Material by tuning the definition of Baseline Material itself, toward the goal of matching a simulated bending specimen in ABAQUS to that of empirical bending data. The User-Informed Calibration approach is discussed further in Section 5.3, giving rise to a process that is further detailed in Chapter 9.

5.1: ACCOUNTING FOR HOMOGENIZED VOID EFFECTS

MCQ-Chopped predicts the effect of inclusions on the material properties of otherwise neat material. Generally, an inclusion describes a fiber-like material embedded in a matrix. The effect of introducing inclusions generally enhances matrix properties such as strength and stiffness; however, in the case of unreinforced or unfilled material, air pockets between individual rasters (inter-raster voids) can be treated as inclusions that actually reduce the overall properties of the matrix material. The procedure for developing a material model with inclusions relies on several modules in MCQ-Chopped as outlined in Figure 33.

- A.) Specify Particle () and neat Matrix () properties
- B.) Estimate volume fractions in chopped composite ()
- C.) Run chopped mechanics () to refine volume fraction estimate, matching UTS of test data
- D.) Define orientation of material () to match test data
- E.) Specify failure criteria ()
- F.) Define simulated test ()
- G.) Define stress-strain test data to match ()
- H.) Run Aligned Layer Non-Linearity () to match strain-dependent modulus degrade to test data
- I.) Future predictions may be made with progressive failure analysis ()

Figure 33: Outline of the procedure for qualifying 3D-printed material in MCQ-Chopped

In Figure 33 (step A), both the neat matrix (PLA) material properties, and the particle (Air) material properties are specified as constituents with properties shown in Figure 34. The neat material properties for PLA were obtained from a datasheet[42], and the properties for air were pulled from a tutorial in MCQ-Chopped which aimed to employ a similar approach. It should be noted that the properties of air are not consistent with the zero-value magnitudes that one would typically expect, but are instead prescribed a value 3-4 orders of magnitude lower than the magnitude of the matrix of material they aim to be combined with in the effective property calculation. Though fictitiously defined, the practice of estimating fiber properties to 3-4 orders of magnitude lower than matrix properties is thought to overcome a commonly encountered limitation of solution tolerance in a finite solver. As the solver, (by either iteration, inversion, or factorization) must arrive at a solution for displacements that satisfy $KU=f$, and as the tolerance this solution may achieve is fundamentally governed by the compliance of the most compliant material in the makeup (air). Prescribing realistic values for the more compliant constituent proves problematic when the constituents differ by more than 3-4 orders of magnitude. Thus, in practice, when working with constituents that differ by 5-6 orders of magnitude (as realistic values of air would), this limitation is avoided via estimating the stiffness of the secondary constituent to 3-4 orders of magnitude lower than the primary constituent in the makeup.

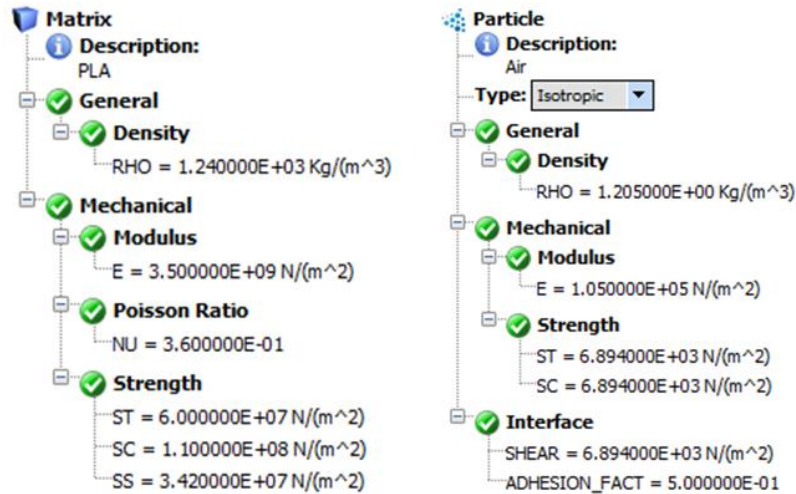


Figure 34: The initially specified matrix and particle properties

RHO= Theoretical density, NU=Poisson's ratio, E=Young's Modulus, ST=Neat strength in tension, SC=Neat strength in compression, SS=Neat shear strength SHEAR=interface shear strength, ADHESION_FACT=adhesion factor

In Figure 33 (step B), these properties are used to make a composite material with an assumed volume fraction of inclusions. The assumed volume fraction of inclusions was estimated following the logic presented in Figure 35.

Figure 35 shows the graphic logic by which the dimensions of the assumed cylindrical voids in the predictive model were established. In Figure 35, a short section of the gauge length in a transverse tensile specimen was first modeled in Solidworks. This section model assumed rasters to have rectangular cross-sections with rounded corners. The assumption from the section model gave rise to the inclusion geometry shown in red, and converting this cross-section to a cylinder of equivalent cross-section gave rise to the geometry shown in blue.

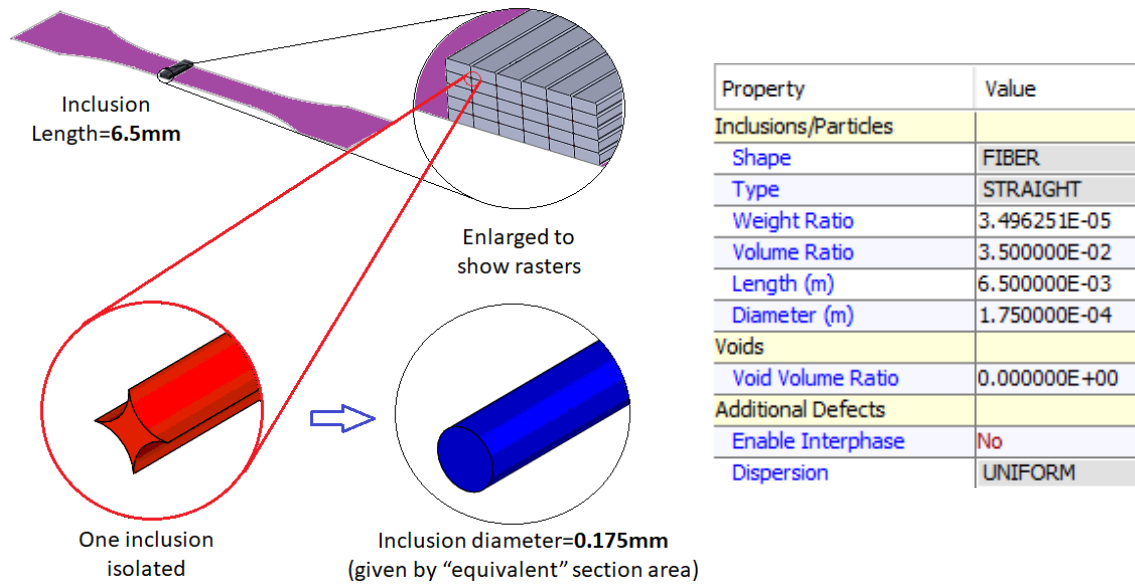


Figure 35: A schematic of the derivation of the inclusion settings for a transverse tensile sample

In Figure 33 (step C), the chopped mechanics module is executed using the settings shown in Figure 34 and Figure 34, to predict the ultimate tensile strength. Through an ensuing iterative process that includes adjusting the assumed volume ratio of inclusions and rerunning the simulated tensile test, the simulated ultimate tensile strength is matched to that of an empirical tensile result. The logic driving the iterative process performed is shown in Figure 36, with the logic loop that governed the specifics of this execution outlined with red arrows.

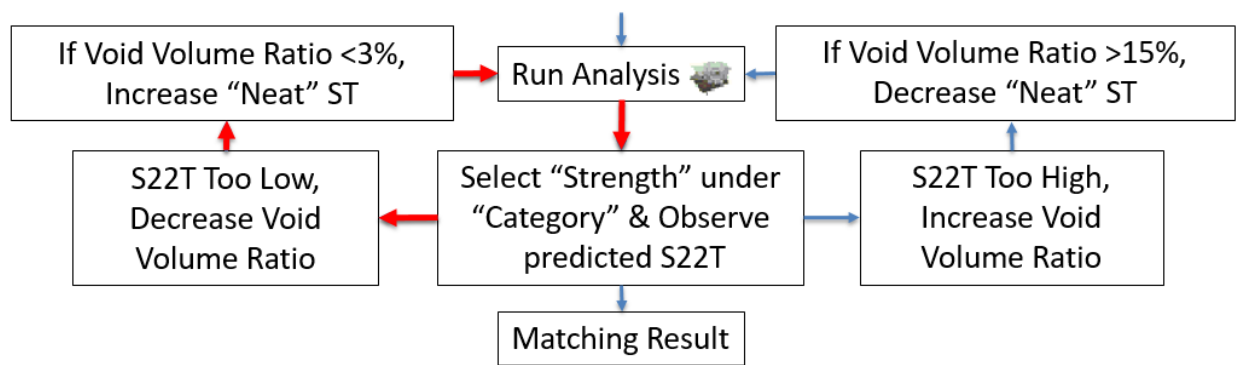


Figure 36: A logic map of the iterative process to calibrate simulated strength prediction

In Figure 36, it is assumed that fused filament fabrication results in a void volume ratio of between 3% and 15% was expected. The initial estimate of neat strength gave rise to unrealistically low void volume ratios, thus the assumed value of “ST” in Figure 34 was adjusted to 62 MPa. Additionally, as the value of “SS” was maintained at a proportional 57% of the value of “ST”, this drove the adjustment of “SS” to 35.4 MPa. Reforming these settings allowed the iterated volume ratio to fall within those limits. This gave rise to the inclusion settings shown in Figure 35. Through several trials of the above process, primarily given the characteristic of uniform dispersion of voids, it was noted that the setting which provided the greatest influence upon simulated ultimate strength of Baseline material was the inclusion volume ratio, rather than the dimensions.

To simulate a tensile test given by Figure 33 (step H), four preparation steps are needed. According to Figure 33 (step D), the material orientation is specified in a manner consistent with the process steps A through C in Figure 33. The corresponding orientation settings are shown in Figure 37. The failure criteria settings per Figure 33 (step E) are shown in Figure 38, (selecting Tsai-Hill failure criteria to capture in-plane failure, and selecting both “S33T” and “Relative Rotation” to capture out-of-plane failure) whereas the simulated tensile test settings per Figure 33 (step F) are shown in Figure 39, and the

experimental stress-strain data per Figure 33 (step G) for the simulated tensile test to match is shown in Figure 40.

Enable Orientation

Total Thickness (m)

Number of Aligned Layers

Orientation Angle Mode ▼

Material Type ▼

Enable Strain Limits

User Defined Orientation Angles		
	Layer Orientation	Thickness (m)
1	90.0	1.0

Angle Offset

Figure 37: Orientation settings defining the user-defined coordinate system in Figure 33 (Step H)

Name	Damage	Failure
Maximum Stress Based Failure Criteria	Yes	Yes
Fiber Failure Criteria		
(S11T) Longitudinal Tensile	No	No
(S11C) Longitudinal Compressive	No	No
(F11C) Fiber Micro-Buckling	No	No
(R11C) Fiber Crush	No	No
(D11C) Delaminations	No	No
Matrix Failure Criteria		
(S22T) Transverse Tensile	No	No
(S22C) Transverse Compressive	No	No
(S33C) Normal Compressive	No	No
(S12S) In-Plane Shear	No	No
Delamination Failure Criteria		
(S33T) Normal Tensile	Yes	Yes
(S23S) Transverse Normal Shear	No	No
(S13S) Longitudinal Normal Shear	No	No
(RROT) Relative Rotation	Yes	Yes
Maximum Strain Based Failure Criteria	No	No
Fiber Failure Criteria		
(EPS11T) Longitudinal Tension Strain	No	No
(EPS11C) Longitudinal Compression Strain	No	No
Matrix Failure Criteria		
(EPS22T) Transverse Tension Strain	No	No
(EPS22C) Transverse Compression Strain	No	No
Delamination Failure Criteria		
(EPS33T) Normal Tension Strain	No	No
(EPS33C) Normal Compression Strain	No	No
(EPS12S) In-plane Shear Strain	No	No
(EPS13S) Long. Out-of-plane Shear Strain	No	No
(EPS23S) Trans. Out-of-plane Shear Strain	No	No
Interactive Failure Criteria		
(MDE) Modified Distortion Energy	No	No
(TSAI) Tsai Wu	No	No
(HILL) Tsai Hill	Yes	Yes
(HOFF) Hoffman	No	No
(HASH) Hashin	No	No
(PUCK) PUCK	No	No
(SIFT) Strain Invariant Failure Theory	No	No
Honeycomb Failure Criteria	No	No
(WRNK) Wrinkling for Honeycomb	No	No
(CRMP) Crimping for Honeycomb	No	No
(DIMP) Dimpling for Honeycomb	No	No
Miscellaneous		
(CFC) Customized Failure Criteria		No
(UDFC) User Defined Failure	No	No
UMAT Damage Index	67109377	67109377

Figure 38: The failure criteria settings employed in the process given by Figure 33

Name	Value
Material	
Type	PLY
Name	Orthotropic
Strain Rate in SS-Curve	0.000000E+00
Loading	XT
Loading Steps	100
Strength	S11T
Strength Upper-Bound Factor	1.100000E+00
Stiffness	E11
Strain (X-AXIS)	
Strain Mode	LAMINATE
Strain Type	EPSXX
Stress (Y-AXIS)	
Stress Mode	LAMINATE
Laminate Stress Type	SIGXX

Figure 39: The settings used for the simulated tensile test in the process given by Figure 33
(The definitions of Stress and Strain categories are used to create a results plot for the simulated test)

	EPSXX (m/m)	SIGXX (N/(m ²))	
1	0.000000E+00	0.000000E+00	} Et= 3.184E+09, (100% of E22 @ 20% S22T) } Et= 3.024E+09, (94.9% of E22 @ 40% S22T) } Et= 2.887E+09, (90.6% of E22 @ 60% S22T) } Et= 2.606E+09, (81.8% of E22 @ 80% S22T) } Et= 1.832E+09, (57.5% of E22 @ 100% S22T) (To generate 11 response, swap E22 & S22T for E11 & S11T, respectively)
2	3.335262E-03	1.061931E+07	
3	6.847113E-03	2.123861E+07	
4	1.052536E-02	3.185792E+07	
5	1.460042E-02	4.247723E+07	
6	2.039690E-02	5.309654E+07	

Figure 40: The transverse (22) stress-strain data used to calibrate the simulated tensile test
(This stress-strain data is used in the process given by Figure 33)

Next, in Figure 33H, following the four preparations given by Figure 33D, E, F, and G, a simulated tensile test was conducted. As the simulated tensile test progressed, a predictive algorithm matched the rate of tangent modulus degrade with increasing strain to that of the same rate given by the empirical test data. The rate of tangent modulus degrade with increasing strength is assumed to hold constant for all

orientations of loading, allowing the generation of a stress-strain curve for each orientation of loading, provided an orientation-specific modulus and ultimate strength.

Next, results were exported to a UMAT, creating an input file containing the user material constants to be used by ABAQUS. The final values for these constants are shown below, in Figure 41.

```
*MATERIAL, NAME = SPLYOrthotropic
*USER MATERIAL,CONSTANTS= 45
**      E11,      E22,      E33,      G12,      G13,      G23,      NU12,      NU13,
3.376820E+09, 3.183950E+09, 3.183950E+09, 1200070000, 1200070000, 1177620000, 3.600140E-01, 3.600140E-01,
**      NU23,      S11T,      S11C,      S22T,      S22C,      S33T,      S33C,      S12S,
3.518570E-01, 59830200, 106150000, 52570900, 93270900, 52570900, 93270900, 29965400, 29965400,
**      S13S,      S23S,      RHO,      DFACTT,      DFACTC,      DFACTS,      FFACT,      DAMAGE,
29965400, 29770500, 1.196650E+03, 1.000000E-02, 2.000000E-01, 1.000000E-01, 1.000000E-02, 67109377,
**      FRACTURE,      EPS11T,      EPS11C,      EPS22T,      EPS22C,      EPS33T,      EPS33C,      EPS12S,
67109377, 1, 1, 1, 1, 1, 1, 1,
**      EPS23S,      EPS13S,      STRAIN_1,      STRESS_1,      STRAIN_2,      STRESS_2,      STRAIN_3,      STRESS_3,
1, 1, 0, 0, 4.591180E-03, 1.561074E+07, 1.160373E-02, 3.761987E+07,
**      STRAIN_4,      STRESS_4,      STRAIN_5,      STRESS_5,      MUP,
1.456068E-02, 4.534584E+07, 1.857702E-02, 5.302805E+07, 0,
```

Figure 41: The user material constants generated by MCQ-Chopped

At this stage, the procedure varies depending upon the approach. Given the Default Approach, the subsequent strategy is outlined in 5.2, expanding to the strategy covered in Chapter 6 and Chapter 7, with results presented in Chapter 8. The Default Approach was seen to have shortfalls, giving rise to the User-Informed Calibration approach. These shortcomings are detailed in 5.3. Given the User-Informed Calibration approach, the subsequent strategy is outlined in 5.4, expanding to a strategy covered in Chapter 9.

5.2: THE DEFAULT APPROACH

The Default approach takes the outputs of MCQ Chopped and applies further temperature-based effects in another software tool, MCQ Composites, to account for the effects of residual stress. These temperature-based effects are discussed in Chapter 6. Following the introduction of these temperature-

based effects, a temperature-dependent material definition is used to generate three sequential simulations; the first predicting a temperature field, the second making use of the temperature field to predict a residual stress field, and the third using the stress field prediction to predict the service loading response. In a parallel path, prior to the execution of the three sequential simulations, both a G-code and a mesh representing the printed part are read into an interface termed “PathCoverage” which aims to qualify the effect of end-of-raster defects, or, as termed by AlphaSTAR, “bald-spots”. The results of qualifying these end-of-raster defects are used to inform the residual stress and service loading simulations. The procedure of qualifying end-of-raster defects is discussed further in Chapter 7.

5.3: THE SHORTFALLS OF THE DEFAULT APPROACH

As detailed in Figure 33, the Baseline approach hinges upon the ability to reasonably estimate the mechanical properties of neat material. Though some means of estimating neat properties may be reasoned to provide better estimates than others, the neat material properties themselves cannot be obtained directly by any experimental technique. This is because all forms of physical test articles contain defects regardless of the means by which the test articles are manufactured. The inevitable presence of these defects governs mechanical behavior, thus defeating any attempt to capture neat properties through experimental means.

Following the prescription of an assumed value for neat material properties, the Default Approach continues to combine the neat material properties with assumed values of void volume ratio, toward the goal of matching tensile test data. There are two main issues with continuing the procedure in this fashion: the first being the inevitably assumed nature of the neat material properties combined with the assumed value of void volume ratio presents a non-unique solution. If one aims to match the value

of ultimate tensile strength, several combinations of assumed values for both neat material properties and void volume ratios may achieve that target, so an inability to specify one presents an inability to determine the other. The second issue is that of the target itself. In this formulation, there exist three effects which are detrimental to an otherwise neat material stress-strain response, the combined effect of introducing these three effects aims to detriment neat properties to properties that are consistent with reality. The first detrimental effect accounts for the detriment from inter-raster voids, the second detrimental effect accounts for thermally-induced residual stress, and the third accounts for the detrimental effect from end-of-raster defects. How can one expect to match flawless printed properties to empirical tensile data, and then continue to formulate and introduce the effects from both residual stresses and end-of-raster defects, and yet also expect to see a match to the response generated in service loading? The latter two of these detrimental effects have yet to be calculated, so it is difficult to qualify the decision to neglect their contribution.

Considering the procedure in Figure 33, the aforementioned issue of the target itself also raises the question: If the procedure outlined in Figure 33 is not performed toward the goal of matching tensile test data, how should one expect to arrive to a match with tensile test data? Figure 42 presents a flow chart illustrating how material properties are thought to be properly degraded with the Default Approach, from their initially highest assumed values, as neat material properties, all the way down to zero, at the point of fracture in the service loading simulation.

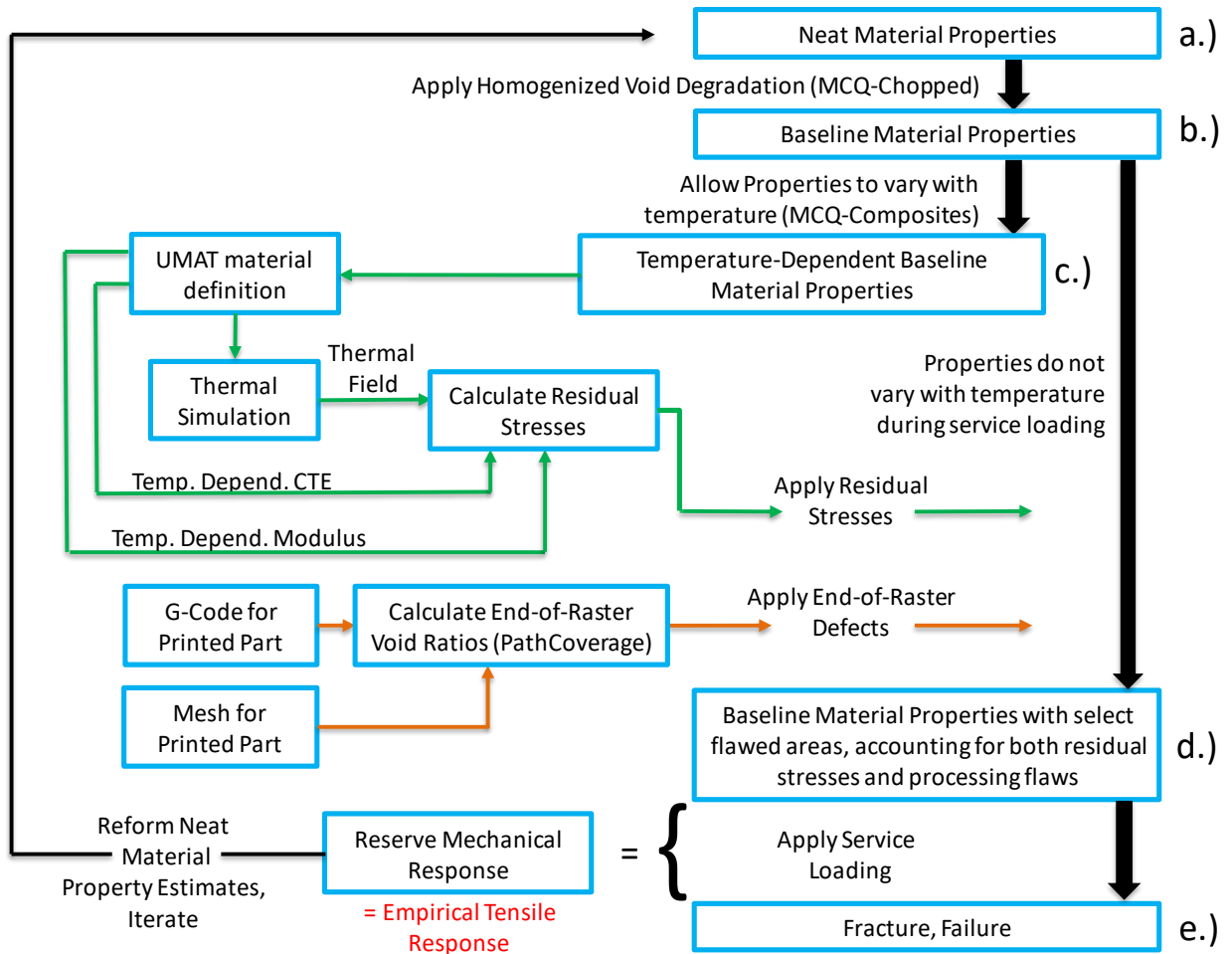


Figure 42: Material properties through detriment introduction, given the Default Approach (Tracing the path of material properties from their initially specified definitions as neat properties, down to zero at the fracture point)

In Figure 42, the Reserve Mechanical Response is the reserve of ability to support mechanical loading between the state of fracture and the state at Figure 42 (box d). At Figure 42 (box d), all three sources of detrimental effects, homogenized voids, residual stresses, and end-of-raster voids, have been introduced. The Reserve Mechanical Response is the most appropriate place to make a match to empirical tensile data. However, how would this realization reform the procedure given by the Baseline approach? One would begin at Figure 42 (box a), by estimating the working material's neat mechanical properties. Properties which, again, exist only in the numerical realm and for which there are no direct

ways of determining. One would then proceed to combine these neat property estimates with another estimate, that of the void volume ratio. This calculated makeup of partially unknown constituents, combined in estimated ratios, is formed toward the goal of defining the state in Figure 42 (box b); a state at which a means of matching to empirically derived data has not yet been offered, necessitating the whole process to be iterative in nature. The state definition in Figure 42 (box b) is then read into MCQ-Composites, where another process follows toward the goal of introducing temperature-dependent properties necessary for the introduction of residual stress, achieving the state in Figure 42 (box c). Once the temperature dependent definition is generated, it is coupled with a mesh, a path defined by a G-code, and several text field-based entries specific to the geometry, toward the goal of generating three sequential simulations (thermal, residual stress, and service loading). The thermal simulation and the residual stress simulation are given the material state in Figure 42 (box c), and the service loading simulation assumes the definition in Figure 42 (box b). PathCoverage then utilizes an estimate of bead width to sweep the path defined by the G-code through the domain defined by the mesh, generating a potential void ratio for each finite element. The thermal simulation is then post-processed and executed, generating a thermal field definition. Next, the residual stress simulation is post-processed and executed, generating residual stress results informed by the results of the generated thermal field. The service loading simulation is then passed the results of the residual stress simulation and the void ratio calculations, producing the material state in Figure 42 (box d). By executing the service loading simulation, i.e., simulating a strain-to-fracture, one may obtain the reserve mechanical response. The reserve mechanical response is viewed in ABAQUS, where, by querying two quantities, the first being the summation of nodal reaction forces, and the second being the relative displacement of two points on opposing ends of the gauge length, a simulated result of engineering stress vs engineering strain is obtained. By comparing the simulated result of engineering stress vs engineering strain against empirical tensile data, one may revise the estimate of neat properties for the next

iteration. However, In the Default Approach, there are three sources of detrimental effects, homogenized voids, residual stress, and end-of-raster voids. By matching a tensile response at the end of this process, one may conclude that the summation of the three detrimental effects is correct, but the approach is largely absent a means of separating the contribution of each of these three sources. Given the case that one successfully matches empirical tensile data to the Reserve Mechanical Response, there is no way of knowing, for example, whether this is due to an over-weighted effect of homogenized voids in conjunction with an under-weighted effect of residual stress. Many other combinations of the effects of homogenized voids, residual stresses, and end of raster voids may be seen to correctly sum to a net detrimental effect that allows a match to tension, but absent a means to separate them, and verify each detrimental effect independently, it is difficult to evaluate the validity of the technique.

5.4: USER INFORMED CALIBRATION APPROACH

The User-Informed Calibration approach aims to differ the strategy presented by the Default Approach on the basis of four recommendations. The first recommendation suggests that the definition of Baseline Material properties may be operated upon directly using a text editor, rather than returning to the MCQ-Chopped GUI to generate a new Baseline Material by reforming the estimates of neat material properties and void volume ratio. Accepting the first recommendation changes the path of Material properties posed by Figure 42 to the framework shown below, as Figure 43.

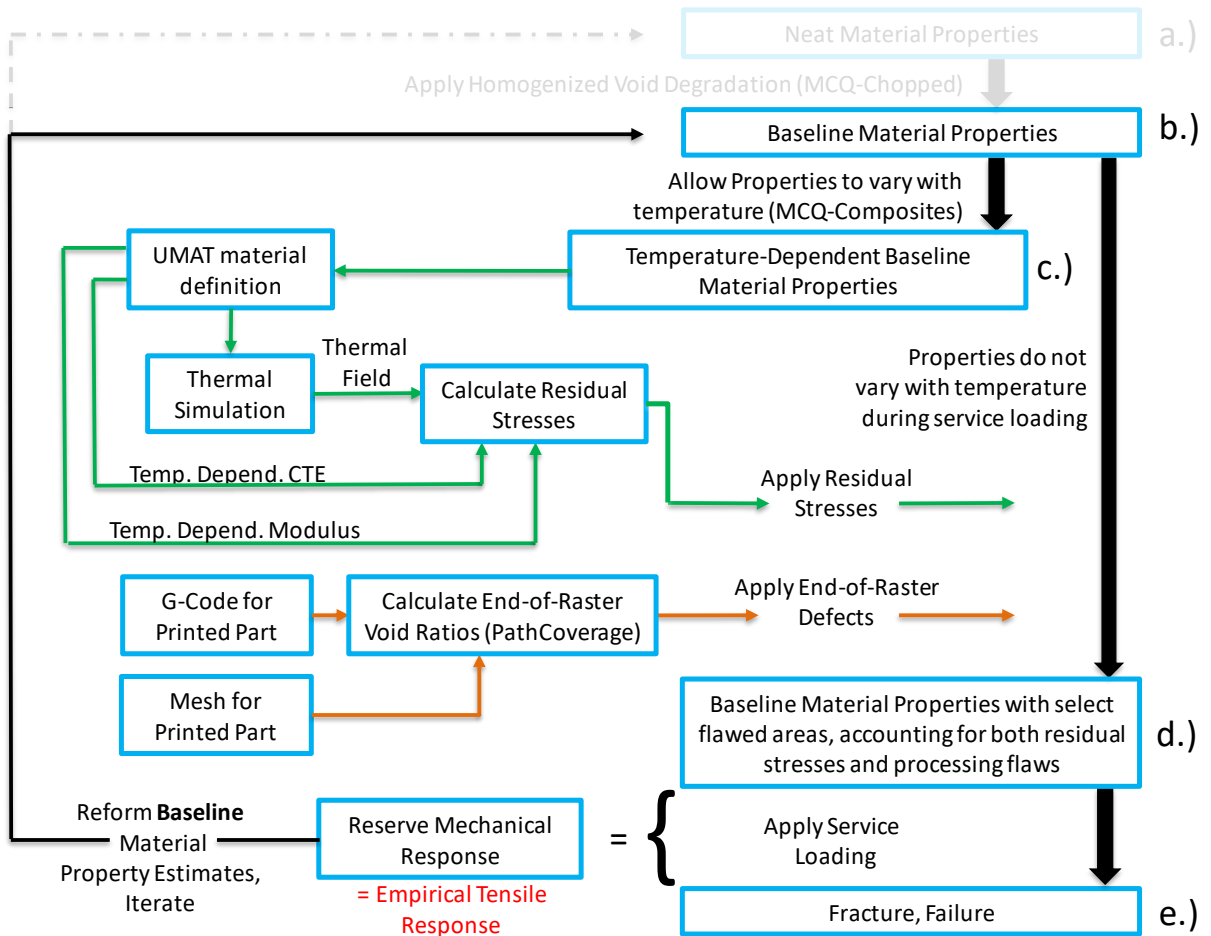


Figure 43: Material properties through detriment introduction, given 1st recommendation
 (Tracing the path of material property definitions, from initially being specified as Baseline properties, down to zero at the fracture point)

The first recommendation cuts the required time commitment to execute iterations in two ways. First, by eliminating neat properties from the path of detriment introduction, and second, in the means by which these iterations are conducted. The first recommendation suggests that Baseline Material properties, a state that independently stands as an unknown state of material, needs not be formulated in terms of further unknowns to be obtained. Baseline Material properties may simply be modified or created directly. Further, the first recommendation suggests the most efficient means to modify a new Baseline Material definition is to modify the input file for the service loading directly in a notepad editor.

The Default Approach, upon determining a new Baseline Material Definition in MCQ-Chopped, would suggest this definition be exported to another text file. The directory the new Baseline Definition file exists in would then need to be located, opened, and combed for the appropriate content to merge into the service loading file. The former strategy suggested by the first recommendation amounts to changing 2-3 characters in the service loading file, whereas the latter strategy suggested by the Default Approach requires more steps, and is more given to the probability of introducing syntax errors.

The second recommendation reasons that the detrimental effect from residual stresses produce a stress result that is near-negligible for this length scale, (between 0.5 and 6 MPa [43]). However, calculating the means to introduce these stresses provides 60-70% of the iterative time investment considering the path of Material Properties posed by Figure 43. The second recommendation poses that the detrimental effect from residual stresses may be temporarily absorbed into the detrimental effect of inter-raster voids, forcing the detrimental effect of residual stress to be accounted for by the detrimental effect of homogenized voids. Accepting the second recommendation changes the path of Material properties posed by Figure 43 to the framework shown below, as Figure 44.

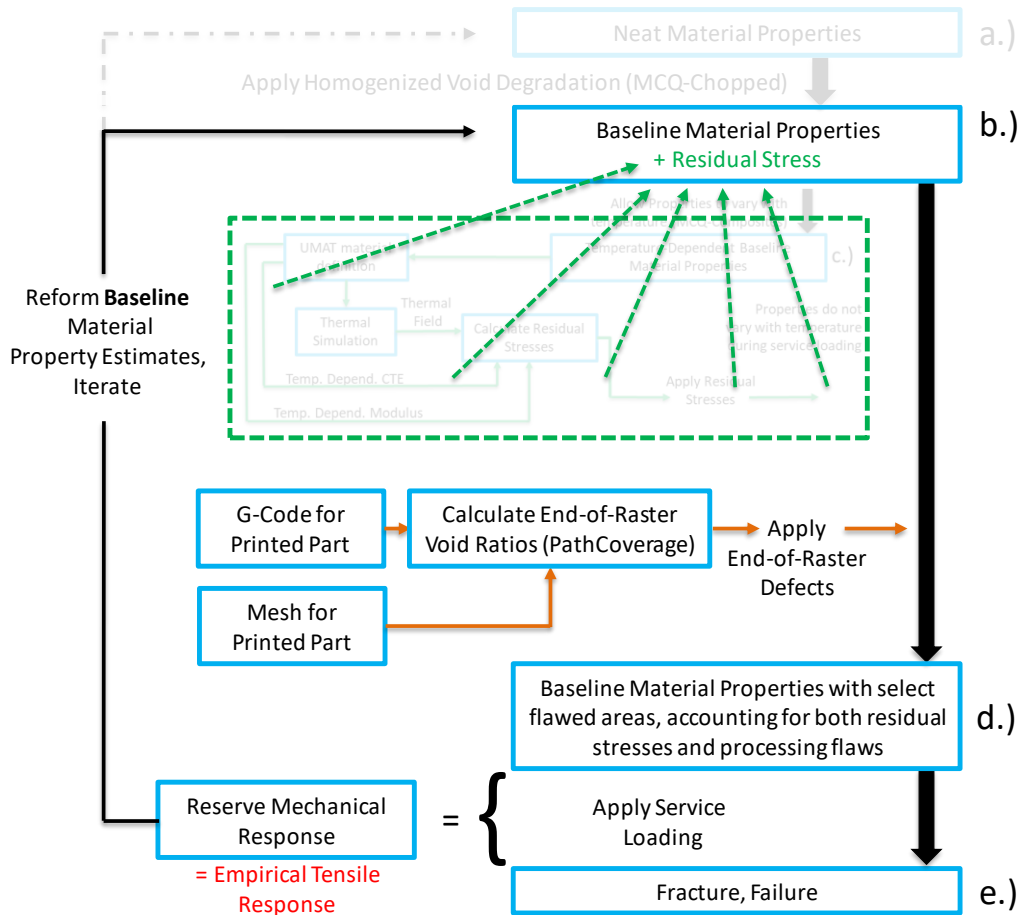


Figure 44: Material properties through detriment introduction, given 2nd recommendation (Tracing the path of material property definitions, from initially being specified as Baseline properties, down to zero at the fracture point)

Considering the path of material properties in Figure 44, accepting the 2nd recommendation provides for significantly shorter iterations. Once iterations are seen to converge upon a Baseline material definition with an absorbed residual stress effect, residual stress may then be introduced by leading this Baseline Material Definition through the process absent the absorption, as detailed by Figure 43. The net goal of the second recommendation aims to conduct significantly shorter iterations (given by Figure 44) while distant from a convergent Baseline Material definition, moving only to the longer iterative path (given by Figure 43) once the shorter iterations exhibit convergent behavior. Though this step is not performed

in this work, the strategy suggested by the 2nd recommendation is thought to promote a more expectantly convergent Baseline Material definition.

The third recommendation suggests that the definition of Baseline Material properties at the state of Figure 44b may be iteratively modified toward the goal of matching a tensile-dominated empirical bending data in a service loading response. This recommendation is effectively equivalent to assuming that end-of-raster voids play no role in a bending test. Accepting the third recommendation changes the path of Material properties posed by Figure 44 to the framework shown below, as Figure 45.

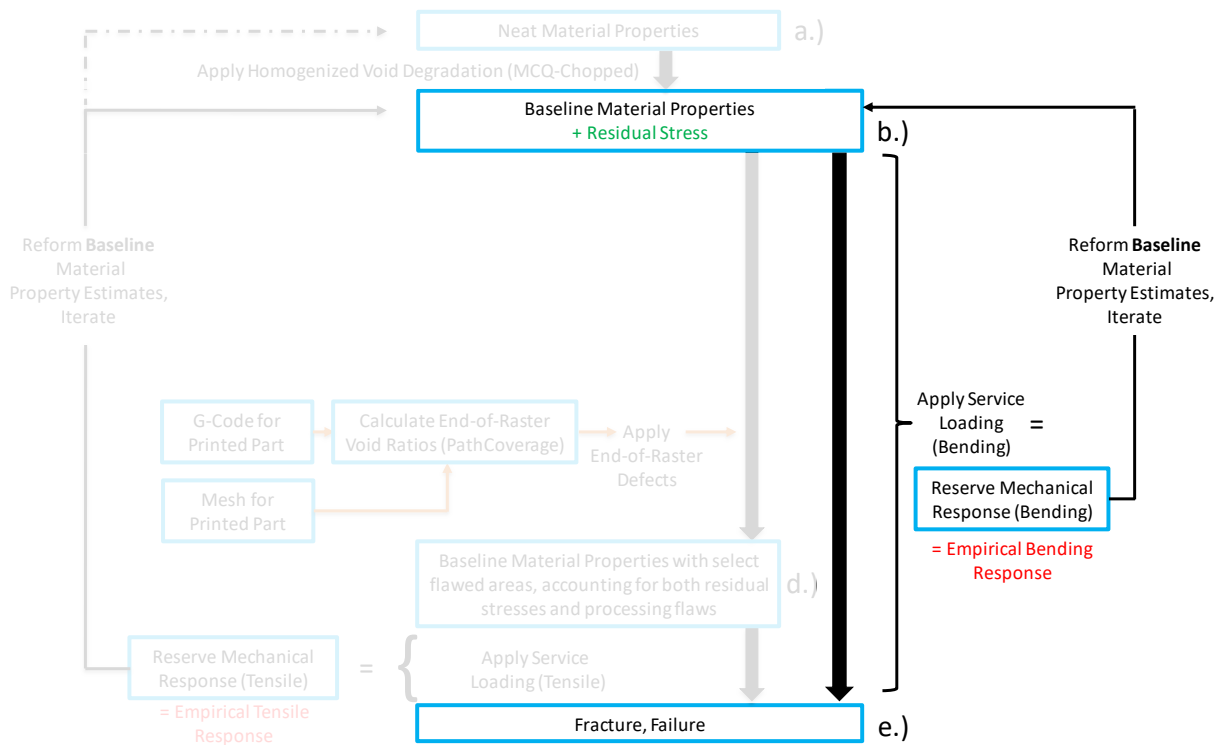


Figure 45: Material properties through detriment introduction, given 3rd recommendation (Tracing the path of material property definitions, from initially being specified as Baseline properties, down to zero at the fracture point)

The third recommendation is effectively equivalent to assuming that end-of-raster voids do not contribute to the response in a bending test. The proximity of the region where end-of-raster voids are introduced is seen to be more distant from the region assumed to govern mechanical response with a bending specimen than the same comparison made for a tensile specimen. Thus, it is conceivable that a consistently introduced defect would likely skew the result of the test shown in Figure 46b before a defect of the same magnitude would skew the result of the test shown in Figure 46a. This conclusion is shown in a graphic in Figure 46.

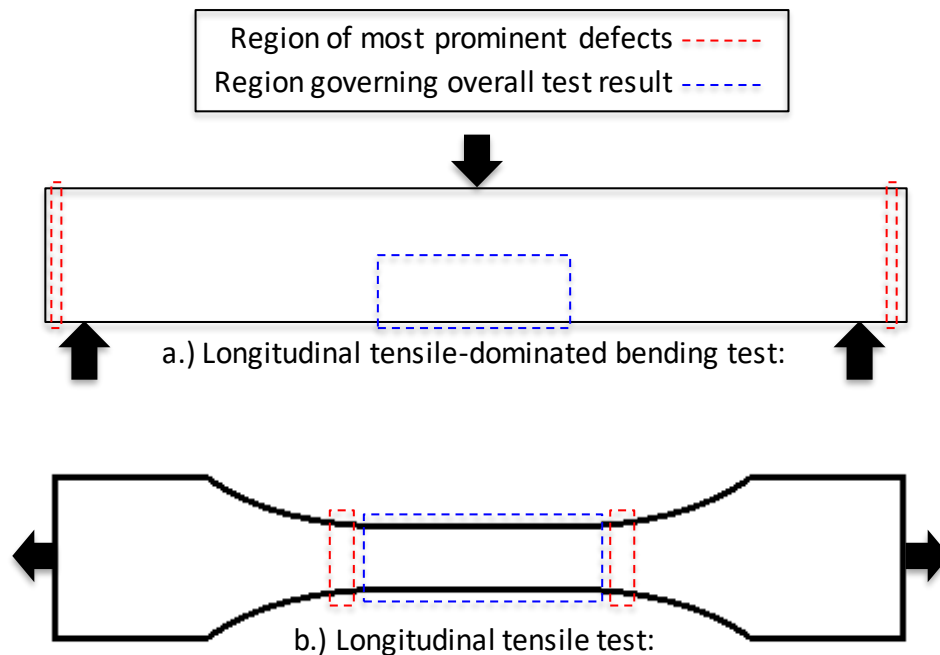


Figure 46: A depictions of key differences between a tensile test and a bending test

Each figure displays the region defect-introduction occurs (red) and the region expected to govern the overall test result (blue), both for a 11-bending specimen (top) and for a 11-tensile specimen (bottom)

To address another reasoning in favor of supporting the third recommendation, it is helpful to return to the simulation of a tensile specimen first introduced in Figure 32 of Chapter 5. A depiction of the stress pattern of this simulation at various stages of progression is shown below, as Figure 47.

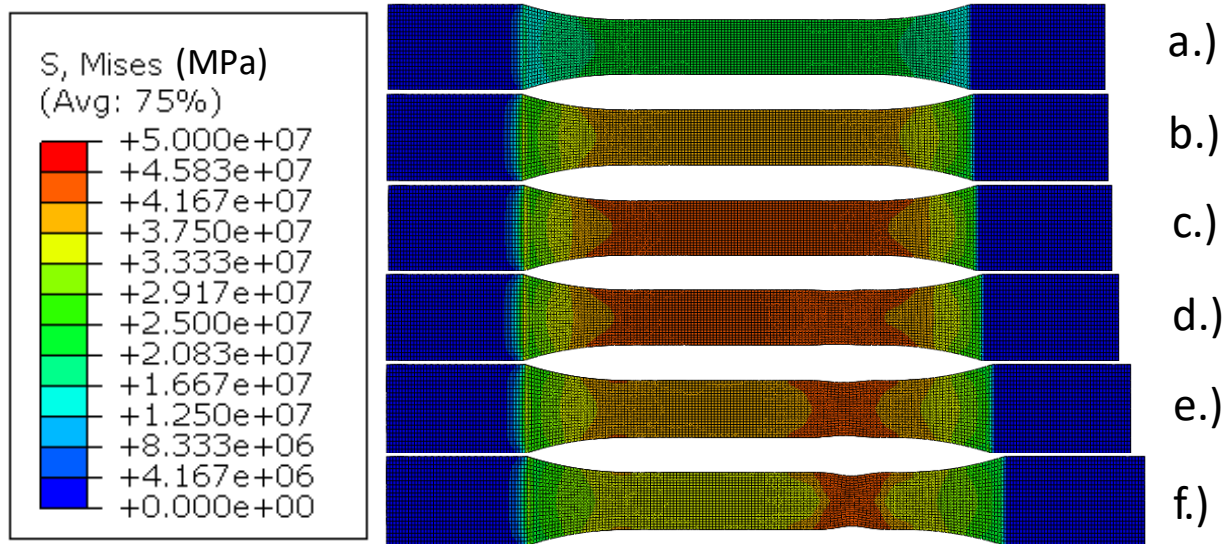


Figure 47: Simulated tensile response throughout various stages of simulated loading

In Figure 47, all of the color-indicated stresses are drawn to the same gradient scale. This scale is shown to the left of Figure 47. As noted in the introduction of this example tensile response, Chapter 5, no defects have been introduced to the material along the gauge length, and compressive behavior of the grip section is not modeled. However, in the realistic design intent of a tensile specimen, the intended mechanism targeted to initiate localization is a defect along the gauge length, rather than the stress concentration concluded to initiate localization in the discussion surrounding Figure 32. Though the simulation shown in Figure 47 is thought not to initiate localization via the intended mechanism true to the nature of reality, the pattern of stress along the gauge length is thought to be realistic. The stress pattern along the gauge length in Figure 47 rises from Figure 47a to Figure 47c. However, upon reaching localization behavior in Figure 47d, the stress pattern in the localized portion of the gauge length continues to rise, while the stress pattern in the gauge length away from the localized portion is seen to fall. The pattern of progression in Figure 47d through Figure 47f is due to the elastic recovery of the portion of the gauge length away from the localized portion. Let the localized region of the gauge length

be termed “localized region” and the portion of the gauge length away from the localized portion be termed “recovering region”, as shown in Figure 48.

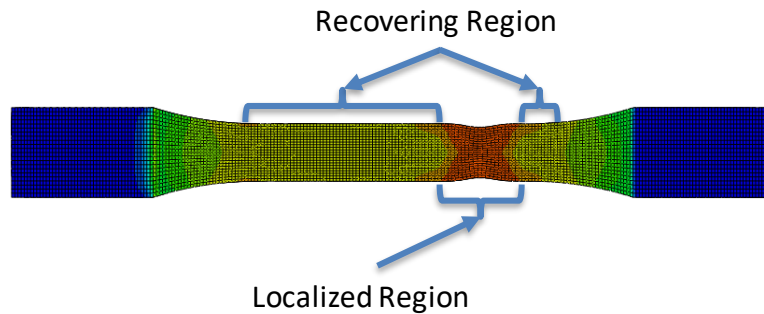


Figure 48: The regions shown to be localizing and recovering in a tensile specimen

From Figure 47d to Figure 47f, as the localized region of the gauge length is coupled to the recovering region, the elastic recovery of the recovering region progresses the failure of the localized region rapidly and in an uncontrolled manner. This presents an issue for calibration of the material model because, in realistic tensile testing, the behavior displayed in Figure 47 is initiated due to the presence of defects on the gauge length. The only mechanism that one has experimentally to capture this behavior is an extensometer. Further, an extensometer will only report useful data to inform a model as long as the window it observes undergoes the same behavior. As soon as defects start to govern the reading one obtains from the extensometer, the reading is no longer useful. Therefore, one must seek to match to a test that does not jump to a governed state upon incurring a failure of a small defective portion of the test specimen.

The fourth recommendation poses that if one calibrates the Baseline Material definition to an empirical bending test as suggested in Figure 45, the discrepancy that then exists in mechanical response between

a simulated tensile response of Baseline Material and empirical tensile data must be due to the detrimental effect of end-of-raster voids. Further, the fourth recommendation reasons that the effect of end-of-raster voids may be introduced by either a generalized detriment-prediction tool such as PathCoverage, or by manually introducing an appropriately-weighted defect at the end of raster-boundaries where failure is seen to occur. Either method of introducing the effect of end-of-raster voids should be seen to arrive at a matching tensile result, however, in exploring the formulation of PathCoverage, it is deemed likely that the current formulation builds a prediction as to the effect of end-of-raster voids, but builds this prediction strictly as a function of the ratio of the void-to-filled volume in each element contained within the finite mesh.

Several topics regarding the User-Informed-Calibration Approach are further detailed in Chapter 9. In section 9.1, the approach itself is presented, and detailed with regard to calibration to a tensile dominated bending test (section 9.1.1), and calibration to a uniaxial tension test (section 9.1.2). In section 9.2, the results of the User-Informed-Calibration Approach are presented and discussed, including a continuance and detailing of the discussion regarding PathCoverage eluded to in the previous paragraph (section 9.2.1), and a discussion of the results of the User-Informed-Calibration Approach 9.2.2.

Chapter 6: ACCOUNTING FOR TEMPERATURE EFFECTS

In FFF, thermoplastic material (e.g., PLA) is heated as it is extruded from the print-head nozzle. Due to the positive coefficient of thermal expansion, PLA shrinks as it cools. If the effect of thermal expansion is unrestrained, the effect of thermal expansion presents as a thermally-induced strain. If the effect of thermal expansion is restrained, the effect of thermal expansion presents as a thermally-induced stress. Above the glass transition temperature (T_g), the material is in a molten state, thermal expansion is unrestrained, and the material cannot support a significant mechanical load. As printed material falls below T_g , thermal expansion begins to transition from being unrestrained to restrained, and the material's ability to support mechanical loading grows as the material solidifies. By the time printed material reaches ambient temperature, thermal expansion is fully restrained, and the printed material's ability to support mechanical loading is at a maximum. Hence, the uneven cooling or temperature variation in the printed part can lead to residual stresses, which can also affect the service loading response of the printed part. The effect of thermally-induced residual stresses presents both locally, in a raster-by-raster fashion, as well as globally, in a layer-by-layer fashion. The global effect of layer-by-layer residual stresses is shown below, as Figure 49.

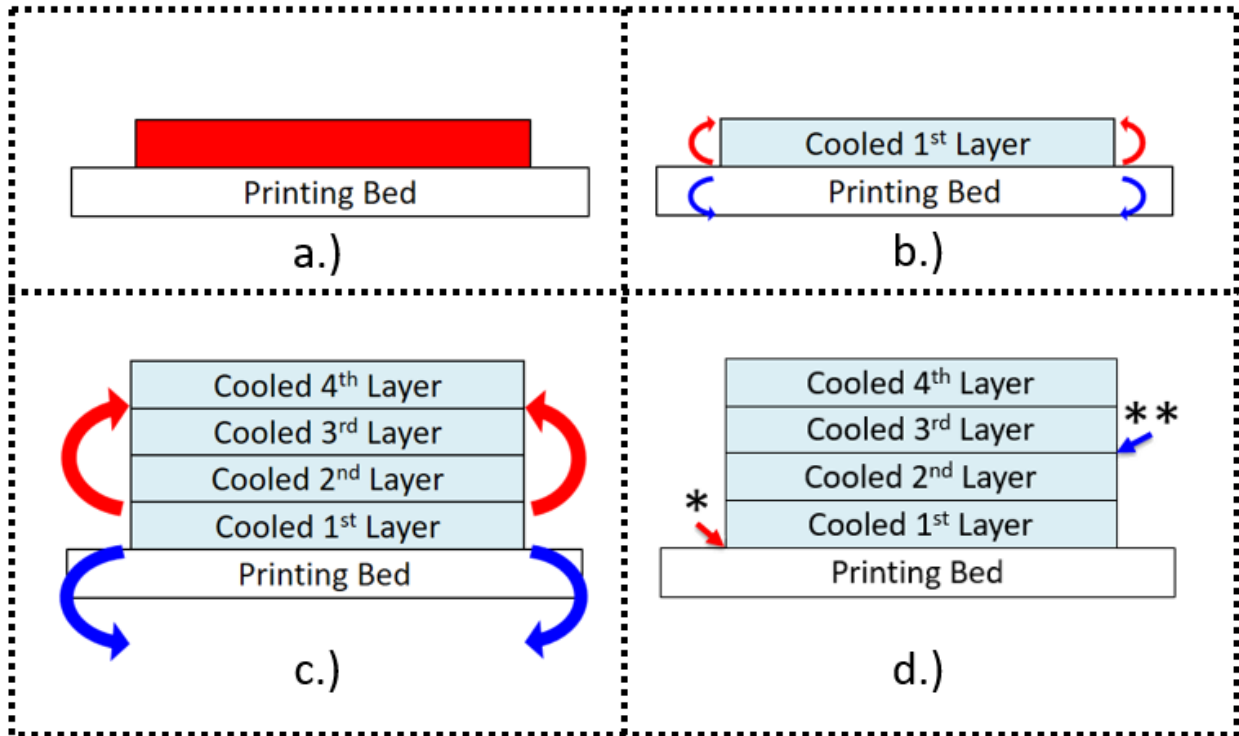


Figure 49: The global effect of residual stress, presenting in a layer-by-layer fashion

Figure 49a shows the molten 1st layer. Figure 49b shows the moment coupling introduced by the cooling of the 1st layer. Figure 49c shows net moment coupling introduced by successively deposited-and-cooled layers, both growing and shifting upward as more layers are printed. Figure 49d shows locations delamination may be seen to result from the effects of thermally-induced residual stresses, both between the 1st layer and the print bed (noted by *), and between printed layers (noted by **).

To predict the residual stresses, the Baseline material property definition must evolve to represent how strength and stiffness vary with temperature, as well as qualifying several other properties that are seen to vary with temperature, such as coefficient of thermal expansion, specific heat, and density. Figure 42, is re-stated below, as Figure 50, focused on the framework associated with temperature effects.

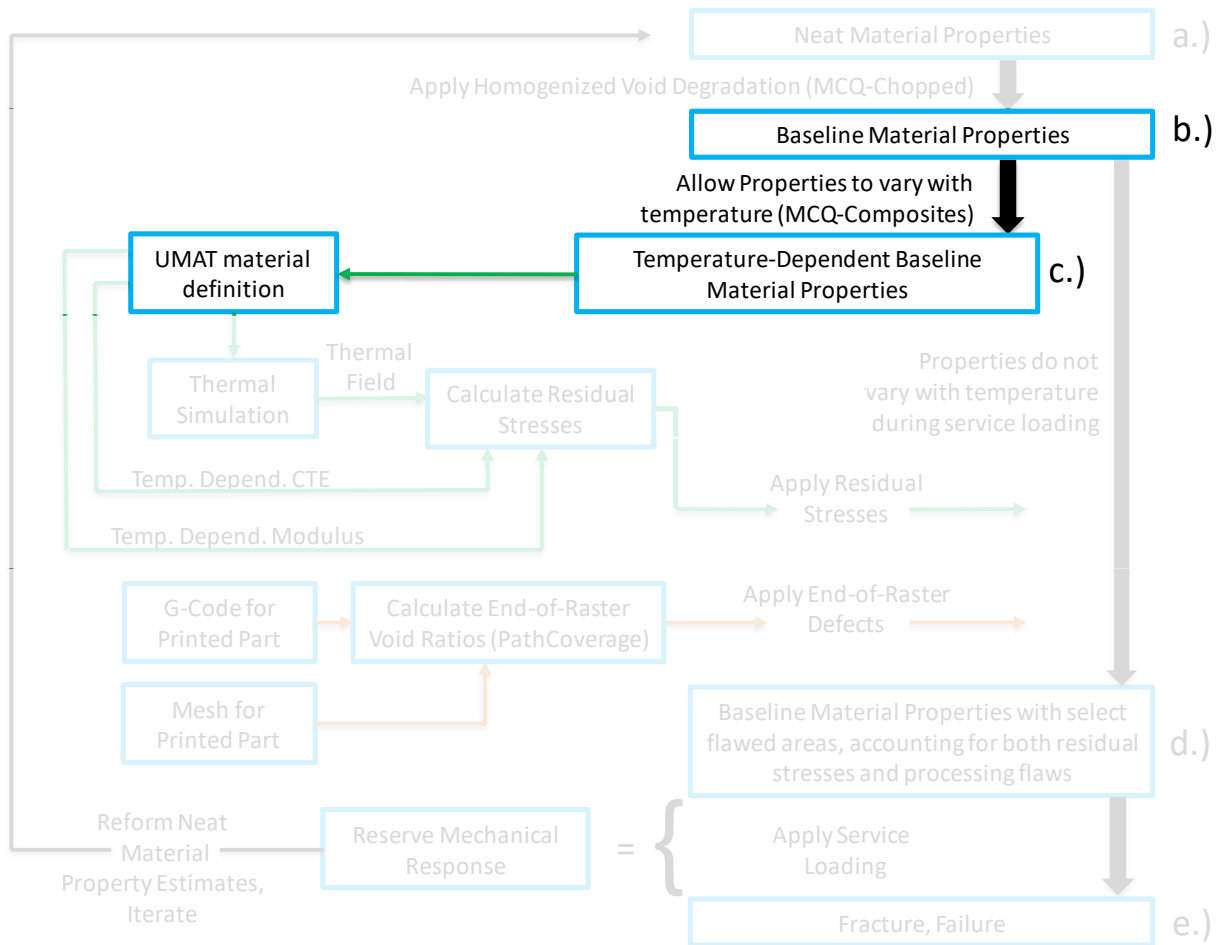


Figure 50: Parts of the modeling framework associated with qualification of temperature effects

MCQ-Composites[41] provides the ability to predict thermally-induced residual stresses. However, with the use of a finite element analysis tool such as ABAQUS, the transient nature of residual stresses may be modeled in a layer-by-layer or even in an element-by-element fashion.

The first step in MCQ Composites is to qualify the rate of modulus decay of neat PLA with increasing temperature. This relationship, extracted from literature, was used to tune an analytically-derived cure kinetics approach. Whereas MCQ-Composites deals strictly with directionally-independent properties, the cure kinetics approach requires separate definitions for material properties in 11, 22, and 33 orientations. Both a matrix, as shown in Figure 51, and single-layer laminate definitions are needed to

make the curing predictions for all orientations. To execute the curing process, the modulus definition is shifted from “E” under the category “Mechanical” to “CURE_EMO” under the category “Curing”.

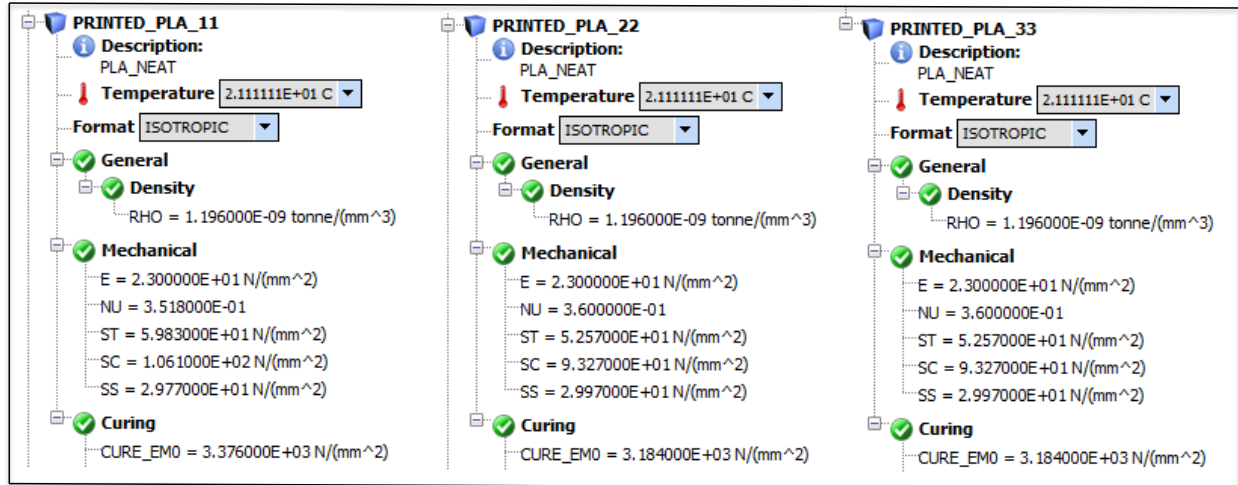


Figure 51: Matrix definitions for each orientation used to execute cure kinetics predictions (Predictions are made of Young’s modulus in 11, 22, and 33 directions)

Published data [44] for tensile testing under a range of temperatures was used to extract a relationship between Young’s modulus and temperature for injection molded tensile specimens. Given material-specific pre-exponential factors and activation energies for Arrhenius rate equations [45], MCQ Composites analytically determines the rate of modulus decay with increasing temperature for an assumed fraction of transformation. By adjusting the fraction of transformation, termed the “degree of cure”, the analytical determination of Young’s modulus vs temperature was calibrated to the empirically extracted result.

Once the calibration of the cure kinetics prediction is complete, the second step is to apply this same curing process to the Baseline material properties derived in MCQ Chopped, under the assumption that geometric effects such as homogenized voids and end-of-raster voids remain independent of thermal

transformation effects. Hence, the same rate of modulus decay calibrated to injection-molded PLA was applied to the Baseline material properties.

The procedure of applying cure kinetics to both neat PLA and the flawless printed material properties only served to predict the Young's modulus in 11, 22, and 33 directions. For simulation purposes, all strength and stiffness properties in tension, compression and shear) as well as the Poisson's ratios were calculated using a multifactor approach, effectively assuming that all mechanical properties degraded with rising temperature at a rate which matched that for the Young's modulus. The multifactor relationship is shown below, in Equation 12: $\sigma_i(T, \alpha_i) = \sigma_0 \left(\frac{T_g - T}{T_g - T_0} \right)^{\alpha_i}$ Equation 12

where σ_i is the mechanical property of interest at a desired temperature (T), σ_0 is the mechanical property of interest at ambient temperature (T_0), α_i is the multifactor coefficient, and T_g is the glass transition temperature. The counter variable, i , dictates that a new multifactor must be calculated at each benchmark where the multifactor prediction of Young's modulus is matched to its predicted value from the cure kinetics. This matching was performed at total of five elevated temperature benchmarks below the glass transition temperature (30.34 °C, 40.65 °C, 50.97 °C, 54.83 °C, and 59.99 °C). These temperature benchmarks corresponded to the temperatures in the five elevated-temperature tensile tests in the empirically extracted result[44].

Use of the multifactor relationship was a two-phase process: (1) Use cure kinetics predictions of Young's modulus for Baseline material at five temperature benchmarks (excluding ambient at 21.11 °C) to solve for five corresponding multifactor coefficients using Equation 12, verifying that a multifactor prediction of directional Young's modulus may be seen to match a cure kinetics prediction of directional Young's modulus. (2) Calculate the values of fifteen further mechanical properties using Equation 12 at each of the five temperature benchmarks based on their corresponding values at ambient temperature and the

derived multifactor coefficients. The three directional modulus predictions, together with the fifteen further mechanical properties predicted by the multifactor approach, represent an orthotropic material. These eighteen properties are described in Figure 52. Each of the properties in Figure 52 must be evaluated at ambient (given directly by MCQ-Chopped) as well as at each of the five elevated temperature benchmarks (given by cure kinetics in conjunction with the multifactor approach). The execution of this process gave rise to a total of 108 mechanical properties.

Name	Symbol
Longitudinal Modulus	E11
Transverse Modulus	E22
Out-Of-Plane Modulus	E33
Shear Modulus	G12
Shear Modulus	G23
Shear Modulus	G13
Poisson's Ratio	NU12
Poisson's Ratio	NU23
Poisson's Ratio	NU13
Tensile Strength	S11T
Compressive Strength	S11C
Tensile Strength	S22T
Compressive Strength	S22C
Tensile Strength	S33T
Compressive Strength in 33 Direction	S33C
Shear Strength in 12 Direction	S12S
Shear Strength in 23 Direction	S23S
Shear Strength in 13 Direction	S13S

Figure 52: Description of the mechanical properties generated by MCQ-Composites

Similar to the procedure described previously in Figure 51, a matrix definition and a single-layer laminate model are used to make the multifactor predictions for all orientations. The matrix definitions defining the laminates are shown in Figure 53.

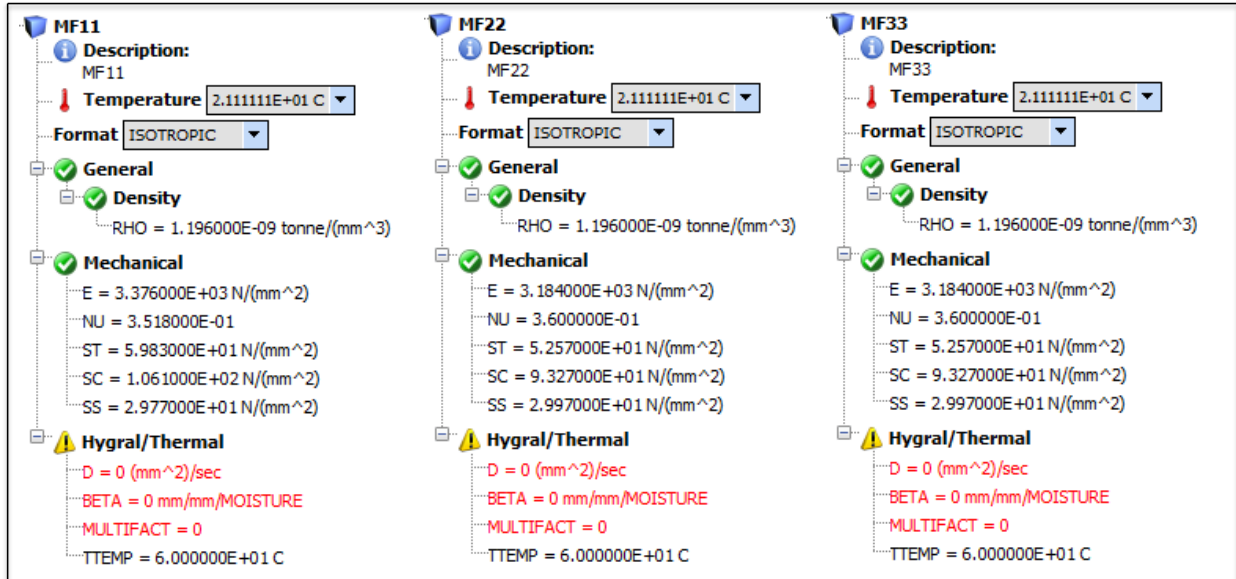


Figure 53: The matrix definitions for multifactor coefficients to generate properties in Figure 52

The laminate definitions used to derive the five multifactor values were then used to predict the stress-strain response in tensile loading at each of the five temperature benchmarks by using the progressive failure analysis feature in MCQ-Composites.

Each of the ninety mechanical property values generated with the multifactor approach were populated into a ply definition, along with the tensile stress-strain responses at each temperature benchmark. The laminate mechanics module in MCQ-Composites was then run, and the ply definition was exported to form a UMAT. Several edits were made to the UMAT file using a text editor, generally appending content to the existing file. A temperature-and-direction-dependent definition of conductivity was generated in MCQ-Chopped, which was then copied manually into the UMAT. Temperature-dependent definitions of density [46], specific heat [46], and coefficient of thermal expansion [47] were also added. By using the UMAT file from one of the tutorials in GENOA [41] as a template (AM3DP-FDM-ABS), the baseplate definition was copied into the UMAT representing PLA, then the baseplate material was

modified from steel to borosilicate glass [48], for consistency with the 3D printer used in this study (Ultimaker 2+).

The use of the multifactor relationship only applied to the prediction of mechanical properties below the glass transition. Above the glass transition temperature of PLA (60 °C), the strength and stiffness properties in Figure 52 were assumed to stay at the same values predicted at the glass transition temperature.

Chapter 7: PROCESS-INFORMED MATERIAL MODELING

In the process-informed simulation of a 3D printing process, realistic material is assumed to be represented by nominally perfect or neat material, degraded by the presence of three types of defects introduced by the process. Figure 42 is re-stated below, as Figure 54.

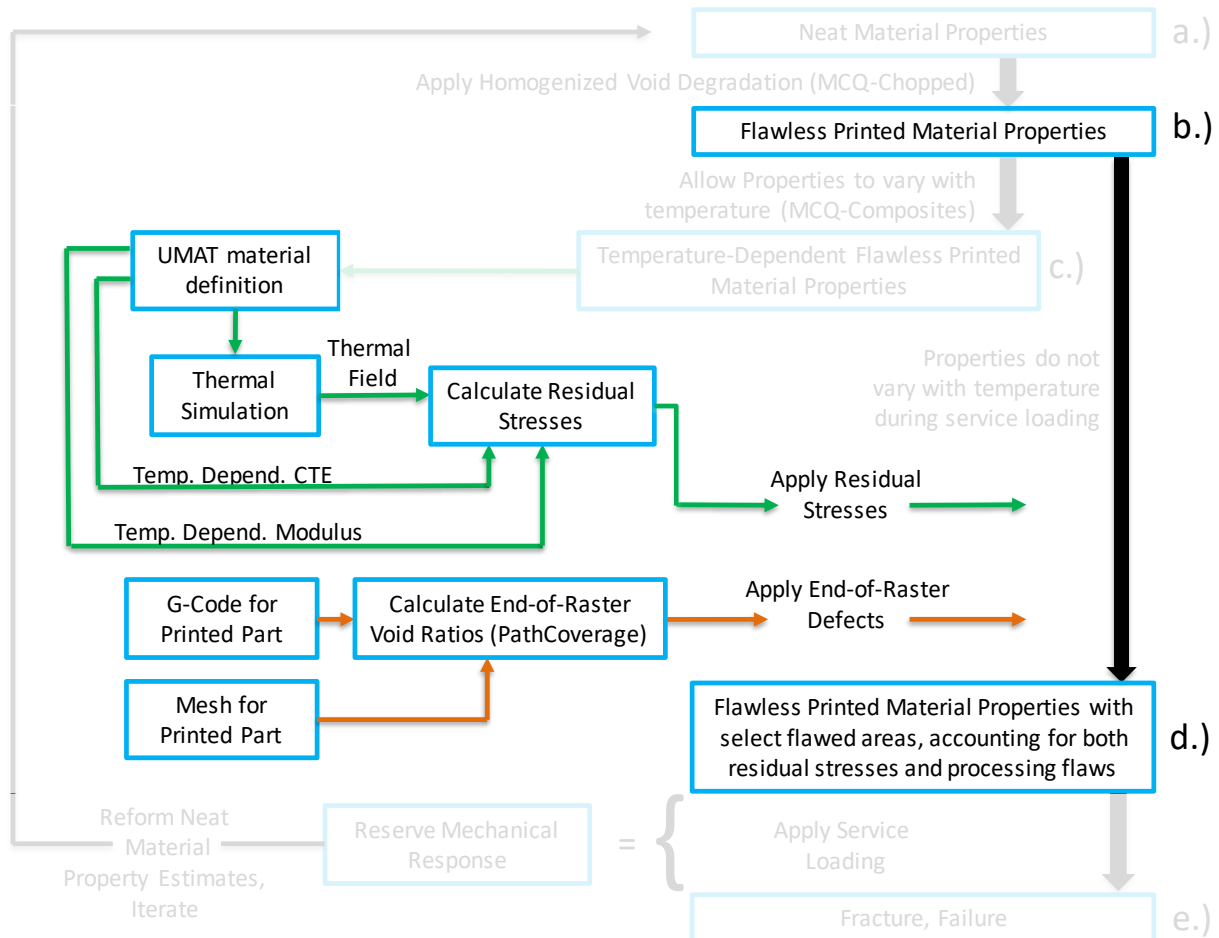


Figure 54: The parts of the modeling framework associated with the process modeling

The first effect is given by the presence of inter-raster voids. These inter-raster voids are imposed upon neat material properties to generate composite effective properties representing Baseline Material, accounting for the first effect. The second effect is given by the presence of residual stresses. These residual stresses are calculated by coupling the results of a thermal simulation with a temperature

dependent definition of both the coefficient of thermal expansion and the modulus. The third effect is given by the presence of end-of-raster voids. The effect of the presence of end-of-raster voids is calculated by sweeping an estimate of bead width along the path defined by the g-code through the domain defined by the mesh, generating a potential void ratio for each finite element in the mesh. Though the first effect has been calculated and accounted for, the second and third effects have not, and are calculated and accounted for in the process model itself.

GENOA is used to generate ABAQUS input files to simulate a 3D printing process. The necessary specifications are made in a module of the software, the Mesh/Model Generator, which is accessed by unfolding the tree toolbar in the GUI. By selecting: Analysis >> 3D Printing >> Mesh/Model Generator. These default settings are shown in Figure 55. To generate input files, the generator requires both file-based and field-based inputs. A process then follows to generate files, and the input files need modification prior to execution. Section 7.1 details the requisite inputs, section 7.2 discusses the generation process, section 7.3 discusses the modifications to the generated files, and 7.4 discusses the specifics of executing the input files. It should be noted that a more comprehensive overview of the strategy and steps of the complete execution of the process modeling of a tensile specimen is provided in APPENDIX A.

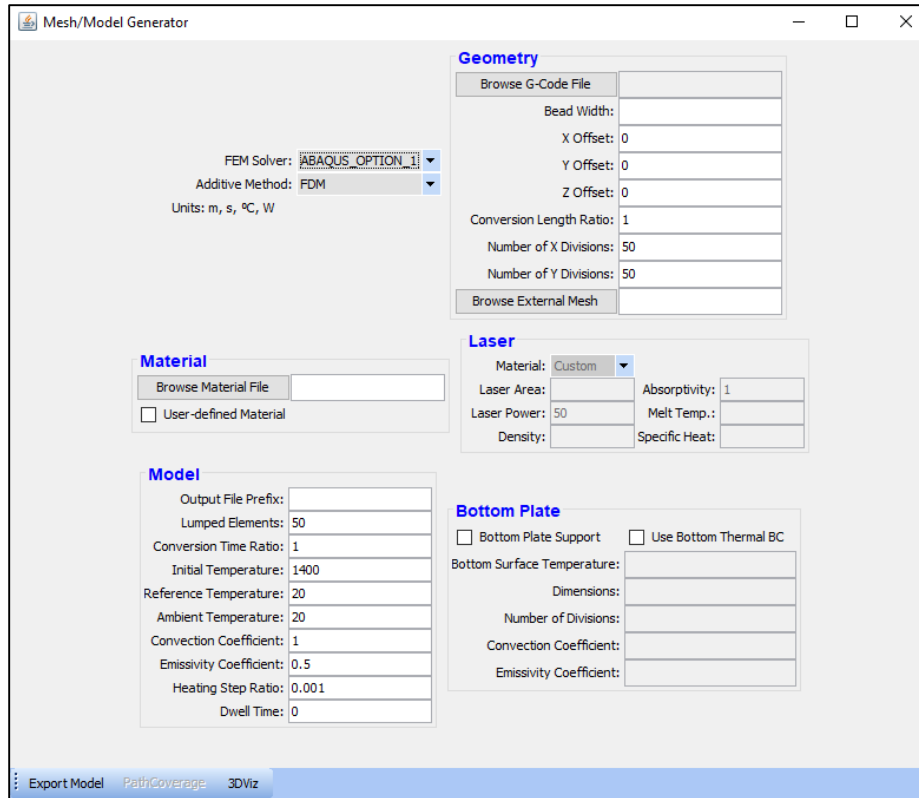


Figure 55: The default settings for the mesh/model generator

7.1: DISCUSSION OF THE REQUISITE INPUTS TO THE MESH/MODEL GENERATOR

Depending upon overall analysis technique, there are either two or three file-based inputs necessary to generate input files, as well as numerous field-based inputs. It is a worthy detail to note that all file-based inputs must reside in the same file path. Section 7.1.1 describes the file-based inputs, and section 7.1.2 describes and specifies the field-based inputs.

7.1.1: THE DESCRIPTION AND SPECIFICATION OF FILE-BASED INPUTS

There are a total of three file-based inputs that must be specified to the mesh-model generator in order to create ABAQUS input files: The G-code, the material file, and the mesh. The details of each of the file-based inputs to the mesh/model generator are discussed in the following paragraphs.

The first file-based input is the G-code as generated by the slicer. Given the desire to maintain consistent element dimensions, (X-&Y-dimensions equal to raster width and Z-dimension equal to layer height) the computational cost of simulating even a 1/2-scale ASTM D638 Type 1 specimen was very taxing. Therefore, a 1/8-scale specimen was analyzed as it required fewer elements to capture the domain of the part. One geometry was analyzed for both the 11-direction and 22-direction tensile specimens, and geometry analyzed for 33-direction specimen varied only in specimen thickness. The reasoning for the dissimilarity in the 33 specimen was due to the desire to simulate a specimen in 33 which had, at minimum, 3 raster widths across the thickness, affording the ability to generate a scan strategy with both an infill pattern and a perimeter rasters. Given a geometry thinner than a minimum of three raster widths across the thickness in 33 specimens, infill rasters were seen not to generate; this is shown in Figure 56a. The preferred case of 3 raster widths across the thickness is shown in Figure 56b. It is noted that the dimension given by 7 layers of raster thickness in 11 and 22-specimen (7×0.15 mm), and 3 elements of raster width in the 33-specimen (3×0.35 mm) would have provided for the same thickness of analyzed sample, regardless of orientation.

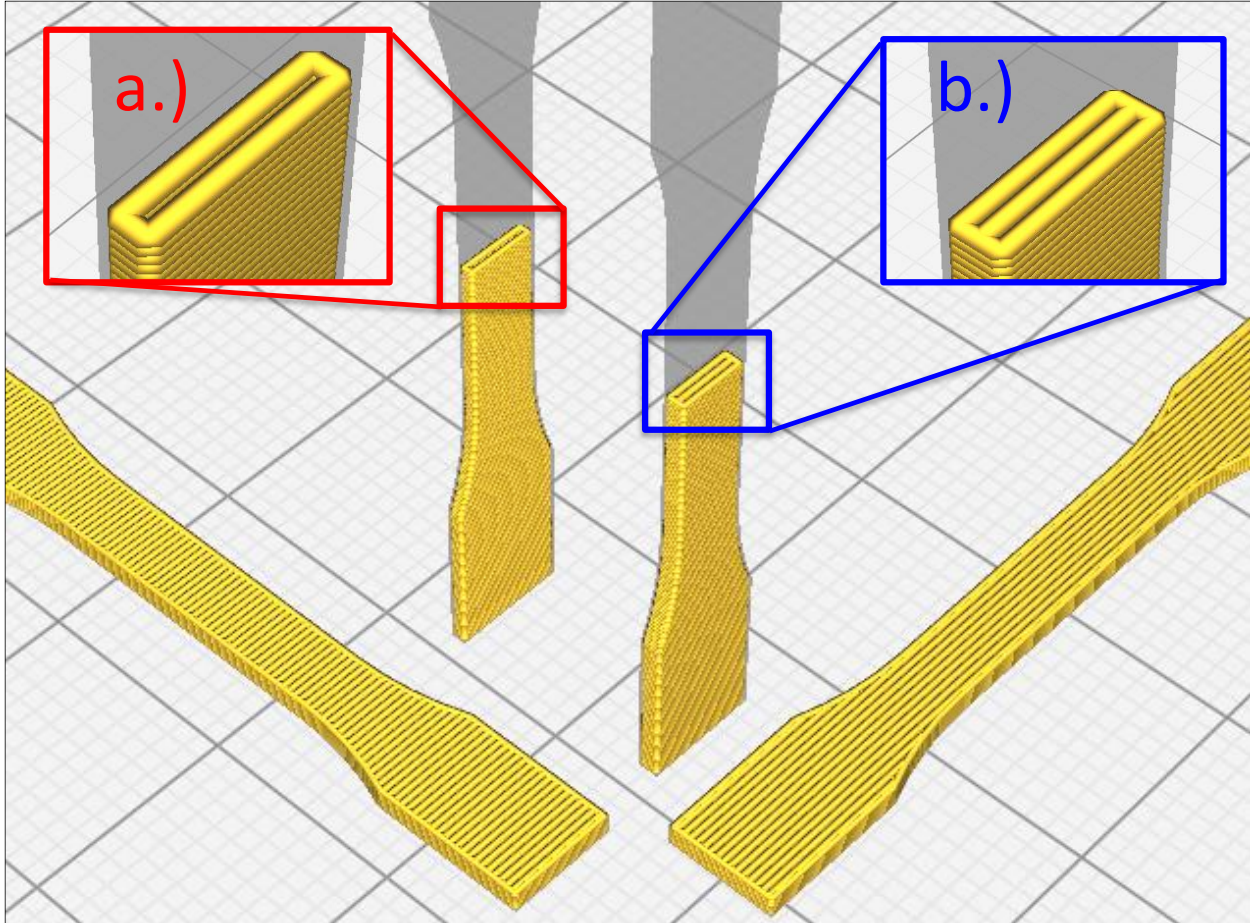


Figure 56: Varying specimen thickness from a.) to b.) to appropriately generate infill rasters

In addition to analyzing three orientations of a very similar geometry, three simulation strategies were investigated. The first simulation technique aimed to explore the three investigated orientations using the internally-generated mesh feature in the mesh/model generator to predict a scan strategy given by pure infill (absent any perimeter rasters). The second simulation strategy aimed to explore the same three investigated orientations by employing an externally generated mesh in conjunction with the PathCoverage module in GENOA to predict a scan strategy given by pure infill (absent any perimeter rasters). The third simulation strategy aimed to explore the same three investigated orientations by employing an external mesh in conjunction with the PathCoverage module to predict a scan strategy with two perimeter rasters in each layer. It should be noted that due to specimen size limitations, when

using the third simulation strategy, the 33 specimen needed to have only one perimeter raster. Whether the external mesh is used or omitted, the PathCoverage module may be loaded to visualize how well the rastering strategy present in the G-code aligns with the mesh (given either an internally generated or an externally generated mesh). An example of the PathCoverage module being loaded for various meshing strategies is shown in Figure 57.

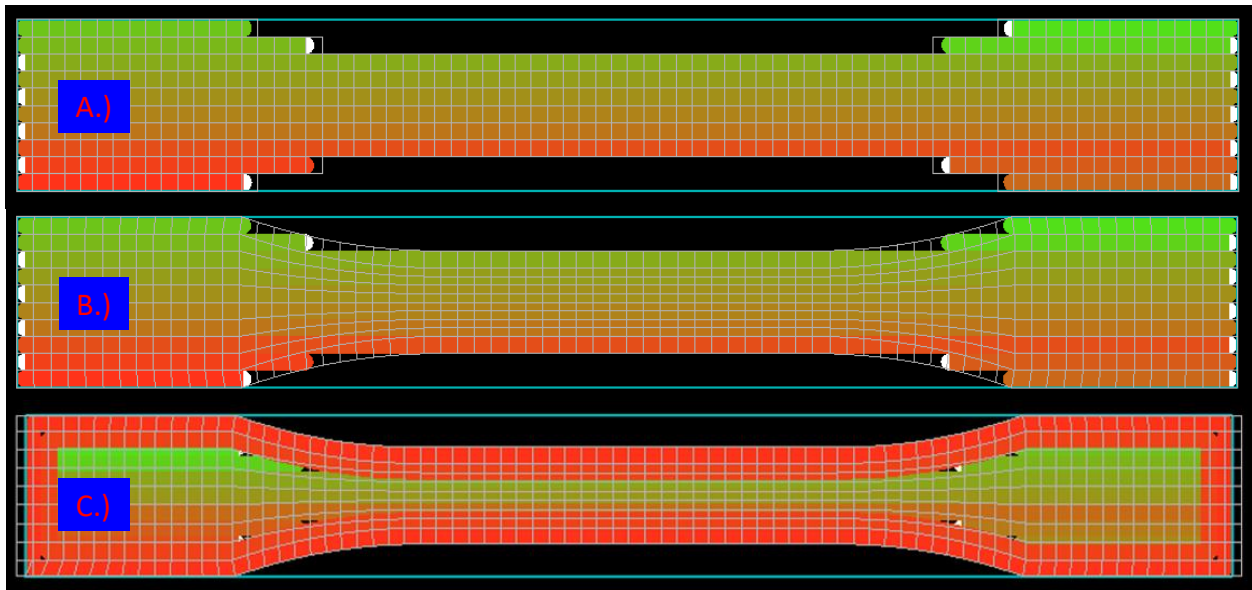


Figure 57: Graphical depictions shown when loading the PathCoverage module

The PathCoverage module is loaded for A.) No perimeter rasters and an internal mesh, B.) No perimeter rasters and an external mesh, and C.) 2 perimeter rasters and an external mesh

The second file-based input is the material file, which is the UMAT file generated using MCQComposites and afterward edited using a text editor (as discussed in Chapter 6: ACCOUNTING FOR TEMPERATURE EFFECTS). No further modification of the UMAT was necessary, though it is important to note that it must be in a “.umat” file format in order for the generator to recognize the file.

The third (optional) file input is the external mesh. One may elect to employ the internal meshing feature by simply leaving the external mesh field blank, whereby a mesh is generated from the G-code. Alternately, one may prescribe an external mesh which defines the contours of the simulated part. If an external mesh is to be employed, the PathCoverage module must be loaded and run, and the necessary steps to modify the input files differ slightly. A depiction of the external mesh used is shown below, as Figure 58.

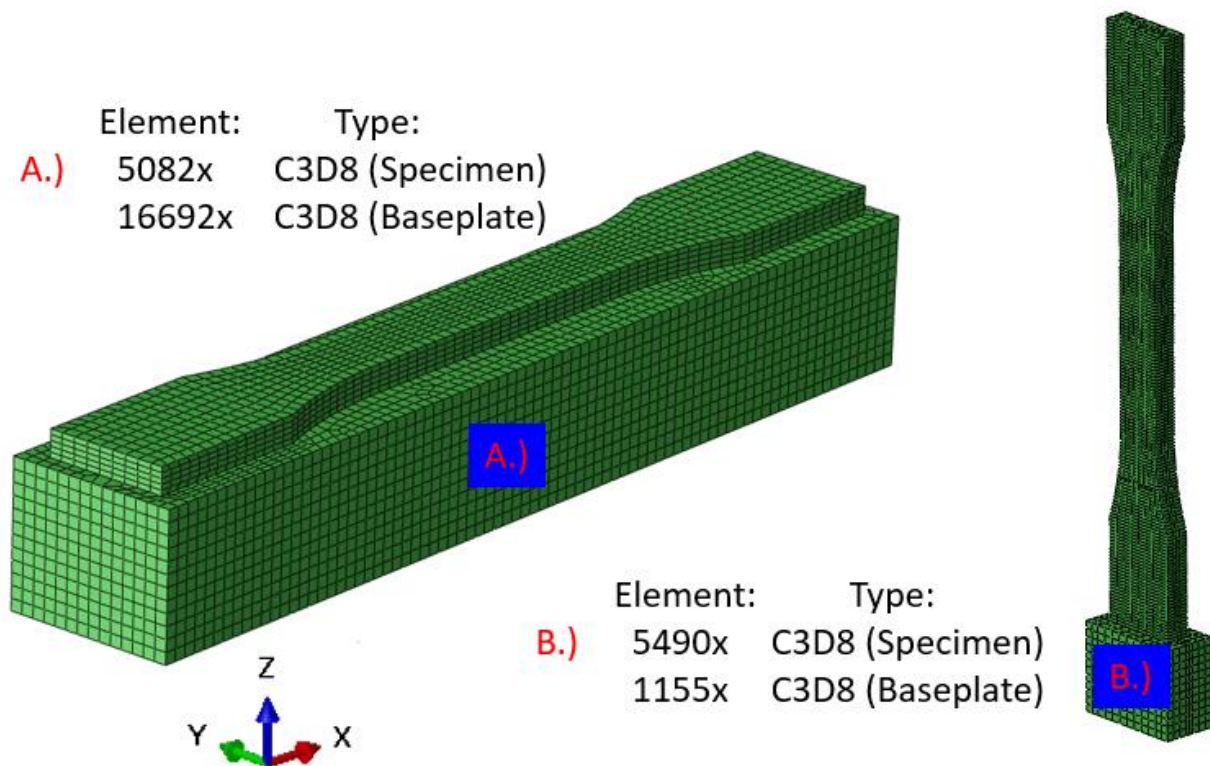


Figure 58: A visualization of the external mesh for A.) 11 & 22 specimen, and B.) 33 specimen

The definition of the external mesh (when required per analysis technique) was performed in ABAQUS, and the general technique employed began with the geometry exported from the CAD model, and continued to make partitions between individual layers, and as necessary across the other dimensions in order to define the most uniform mesh possible. The external mesh for the 11 and 22 specimens were

identical, but very slight modifications were made to the 33 geometry to achieve contour points along the gauge reduction which would not introduce oddities in the mesh.

7.1.2: DESCRIPTION AND SPECIFICATION OF THE TEXT-FIELD BASED INPUTS

In addition to the file-based inputs, there are several text-field-based inputs which are necessary to generate the ABAQUS input files to simulate the printing process. Some text fields change in value over the course of pursuing several differing simulations, while others remain constant. The general strategy for specifying the values in these fields are presented on a field-by-field basis, for each subsection of the Mesh/Model Generator (Geometry, Model, and Bottom Plate). In the instances where the values remain constant during various simulations, the values themselves are cited. The Mesh/Model generator is set to an additive method “FDM”, and an FEM solver of “ABAQUS_OPTION_1”, greying out the category “Laser”.

In Figure 55, there are seven fields under the Geometry category. The bead width is that defined in the slicer (0.35 mm). All the offset fields are left as zero. The Conversion Length Ratio is set to 0.001 (as the length unit in G-code is in millimeters, but in the material file is in meters). The Number of X and Y Divisions differ from case to case, with the objective generally being to number divisions across one dimension in a manner which would capture each full raster width with one finite element, and to number the other dimension in a manner which would create the most uniform element possible.

In Figure 55, there are ten fields under the Model category. The Output File Prefix designates the name for the input file, which differs from case to case. The Lumped Elements (which represents the number

of mesh elements calculated before writing a result to the output file) is taken to be 10000; the value specified for Lumped Elements is purposefully set to a value larger than the number of elements in each layer. As the software allows a minimum of one output file write action per calculated layer, specifying Lumped Elements in this manner results in one output database write action per layer. The Conversion Time Ratio is set to 1. The Initial Temperature is set to 240 °C to be consistent with the nozzle temperature, the Reference Temperature is set equal to the glass transition temperature of PLA, 60 °C, and the Ambient Temperature is set to 35 °C. The Convection Coefficient is taken to be 50 (W/m²°C). The Emissivity Coefficient is taken to be 0.45 (W/m²). The values of Ambient Temperature, Convection Coefficient, and Emissivity Coefficient were all tuned by a trial and error approach for the simulated temperature gradient to match the gradient observed by a thermal imaging camera. This is discussed further in the following paragraphs. The value of Heating Ratio, which is defined as the ratio of heating time (i.e., time to print one element) to cooling time (i.e., time to print one layer), varies from simulation to simulation. The Heating Ratio value is typically set to unity (1) over the number of elements in one layer. This assumption holds true as long as one raster width is equal in dimension to the length of one finite element. More generically, the Heating Ratio value may be given by the ratio of one raster width to the distance travelled by the nozzle in one printed layer. The value for dwell time, i.e., the amount of time the nozzle remains parked due to layer completion prior to the slicer setting “minimum layer time”, is set to zero.

In Figure 55, there are 5 fields in the Bottom Plate category, all of which need to first be activated by selecting both the “Bottom Plate Support”, and the “Use Bottom Plate BC” checkboxes. The Bottom Surface Temperature was taken to be 60 °C. The “dimensions” field may be specified in one of two manners. The first manner is to specify one numeric value, in millimeters, to represent the z-dimension of the plate, with the other two dimensions being automatically selected on the basis of defining a

rectangular perimeter extending slightly outward beyond the footprint of the first layer. The second manner is to specify three values all separated by the lowercase character “x”, to represent the desired dimension of the plate in the x-dimension, the y-dimension, and the z-dimension, respectively. In the analysis performed in this work, the singular dimension of 4 was prescribed for all generated simulations. The “Number of Divisions” field was specified to be 4 for all investigated simulations. The value of Convection Coefficient and Emissivity Coefficient were taken to be 12.5 and 0.45, respectively, remaining unchanged from the tutorial from which they were obtained (AM3DP-FDM-ABS). [41]

7.2: PROCESS OF GENERATING ALL SIMULATION FILES

The Mesh/Model Generator only makes the files necessary to simulate the printing process itself: a thermal simulation, and a coupled thermal-displacement simulation. The simulation of a service loading, covered further in Subsection 7.3.3, is a third file which is most conveniently created by modifying a copy of the coupled thermal-displacement simulation. The process for generating these files, provided the requisite file-based and text-field-based inputs, may require one or several steps, depending on the analysis technique (internal or external mesh). If an internal mesh is used, files are generated by selecting the “Export Model” button in the lower left corner of the Mesh/Model Generator. If an external mesh is used, files are also generated in the same manner, but further generation and post processing steps are necessary for successful execution of said files. Given the latter approach, following the selection of the “Export Model” button, the PathCoverage module must be loaded and run (the adjacent button to “Export Model”, seen as a greyed option in Figure 55). This will bring up another window depicting the footprint of the first printed layer, as shown in Figure 59.

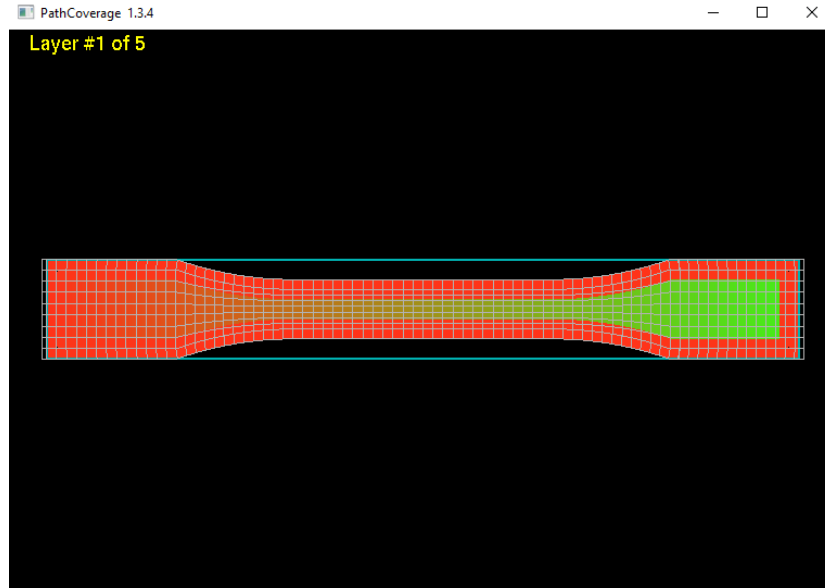


Figure 59: Visualization of the scan strategy for layer 1 of 22 specimen in PathCoverage

To utilize this interface in many ways, key functions are bound to characters on the keyboard. To toggle the display of key bindings, the character "h" may be keyed. This brings up the key binding legend shown below, in Figure 60.

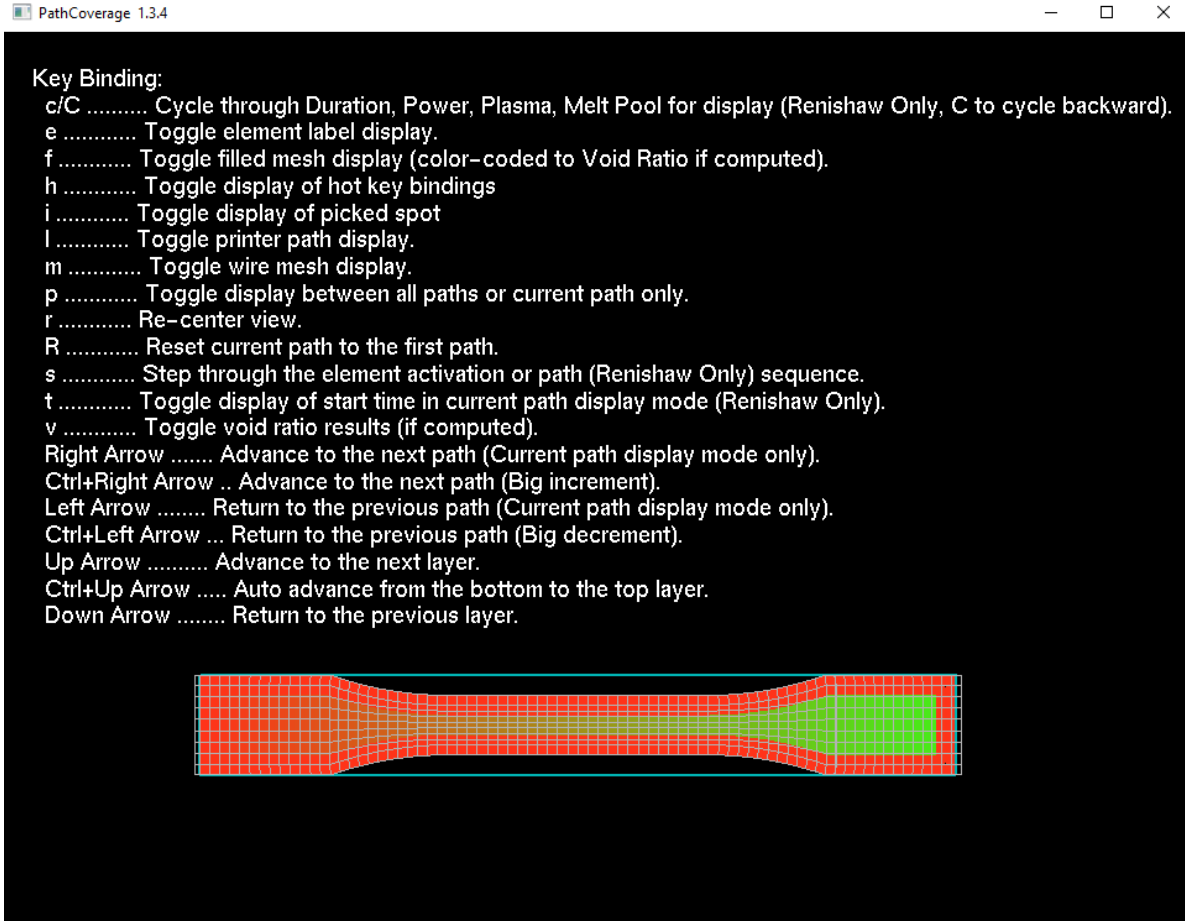


Figure 60: Display of key bindings in PathCoverage

The only function in PathCoverage necessary for simulation is the calculation of void ratios on an element-by-element basis from the bead width and the scan strategy, represented by the fraction of each mesh element which is empty (not fully filled with the printed material). By clicking with the scroll wheel on the mouse, and selecting “enter void ratio computation mode”, one may enter void computation mode. This will replace the window visualizing the layer footprint with another smaller window visualizing a single element and its neighboring elements. By clicking the scroll wheel on the mouse again, one may select “Calculate Void Ratios for ALL layers”, initializing void ratio calculation. As the void ratios are being calculated, the visualization will cycle through the depiction of each element. Once complete, the interface will return to depicting the footprint of each layer, but rather than

showing the scan strategy, the interface will show a color-scaled map of the calculated void ratios, with a dark blue representing 0% void, and red representing 100% void. An example of this map is shown in Figure 61.

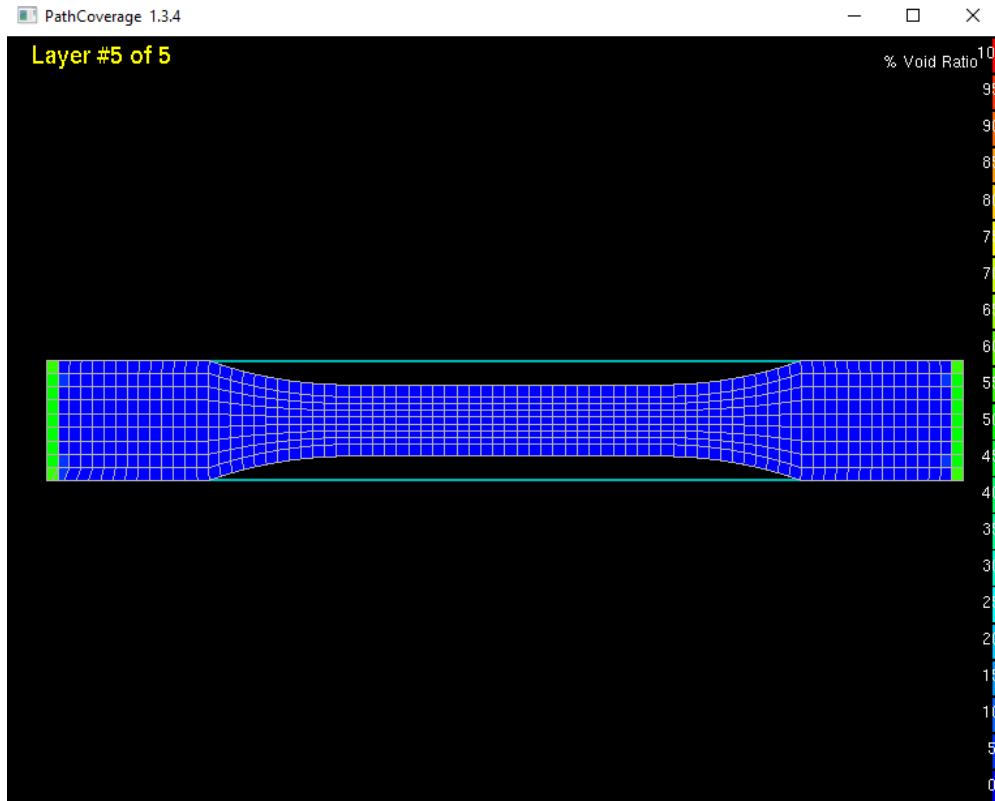


Figure 61: A depiction of the calculated void ratio map in PathCoverage

Nothing further must be done inside this interface regarding simulation, but the execution of this process also writes several text files regarding void ratio calculations to the same directory containing the thermal and thermal-displacement input files. The first text file (ElementVoidRatio_ABAQUS_Implicit_Run1.txt) must be loaded with a text editor such as Notepad++, and saved with a filename to match the name of the thermal-displacement simulation with a filename extension of ".asc". The second text file (ElementVoidRatio_ABAQUS_Explicit_Run1.txt) must be loaded

with a text editor such as Notepad++, and saved with a filename extension of “.inp”. Both these files must be moved to the ABAQUS working directory with both the input files for the thermal and thermal-displacement simulation files to allow the necessary post-generation edits to the input files to reference the void ratio calculations. In the case of using an internal mesh, no additional file generation is necessary, only the two input files for thermal and thermal-displacement simulation must be relocated to the ABAQUS working directory.

7.3 MODIFICATION OF INPUT FILES

Once the necessary files have been moved to the ABAQUS working directory, a series of post-processing edits must be made to the thermal simulation, including a calibration process to refine estimates for the heat transmission coefficients specified in the Mesh/Model Generator. Depending upon the meshing technique, differing edits also need be made to the thermal-displacement simulation. Additionally, the input file for the service loading simulation must also be created (as discussed later in Subsection 7.3.3).

7.3.1: MODIFICATION OF THE THERMAL SIMULATION

By loading the input file in a text editor (such as Notepad++), a find-and-replace function is generally the most efficient means of making the necessary post-generation edits. The first edits are located by finding the text “solid” to locate the specification of the solid section. Two definitions of solid section are made in the input file, which are given place-holder material definitions by the mesh-model generator of “bottom_material”, and “material”, to represent the material for the base plate, and the 3D-printed material, respectively. These place-holder material definitions must be replaced with “mat_bottom_plate”, and “TNPLY0001”, respectively.

The second edit is located by finding the text “initial”. Two instances of the text “initial” should be present in the input file for the thermal simulation, the second instance, which specifies the initialization temperature of the elements, needs to be changed from a value of 240°C to 60°C. The reasoning behind why this change should be made is discussed as follows: the purpose of the sequential simulation process is to predict the pattern of residual stress development, with the fundamental mechanism introducing the stress being the restraint of thermal expansion/contraction. In an FFF process, this restraint cannot occur significantly above the glass transition temperature in either the bonding between the base plate and the first layer, or the bonding between sequential layers, as the material cannot support a significant shear load in this state. The Mesh/Model generator likely sets this value to default to the printing temperature because, for example, in a laser powder bed fusion process (LPBF), solid material is fused at the printing temperature which is capable of supporting a mechanical load in shear.

The third edit is executed with the same find-and-replace technique, however, it requires an iterative process of running the simulation to determine the appropriate values for transmission coefficients and ambient temperature. In order to understand the edits which need be made to the input file, one must first understand the structure of the input file. Toward the end of the input file for the thermal simulation, the steps which simulate the printing process are defined. The initial step in the simulation removes all printed elements, leaving behind only the base plate, initializing the printing process. The structure of the steps which follow begin with a first sub-step to add elements and to heat the added elements to the printing temperature, followed by a second sub-step which allows an appropriate interval of cooling time for the heated elements to equilibrate with the surroundings. During the second sub-step, heat transmission losses are calculated due to both radiative and convective heat transfer,

referring directly to the definitions made for these coefficients (and for the ambient temperature) in the Mesh/Model Generator. The self-contained goal of the thermal simulation is to simulate a temperature gradient across the geometry of the printed specimen, throughout the printing process. By using a thermal imaging camera to capture an in-situ image of a printing process of the same geometry, one can determine, roughly, an empirical evaluation of the same gradient. The depiction of the photo capture of the thermal imaging camera and the as-simulated gradient are shown in Figure 62 and in Figure 63, respectively.

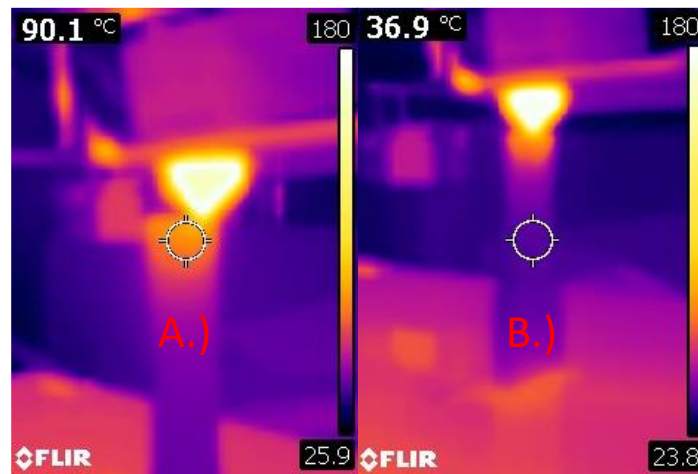


Figure 62: A depiction of the empirically evaluated temperature gradient during 3D-printing
A capture is shown of a tensile specimen, showing averaged values at A.) near proximity to the printing surface, and B.) the steady state layers

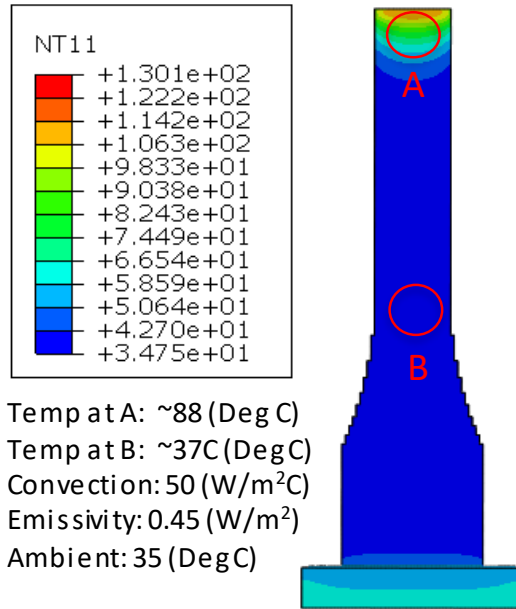


Figure 63: The post-calibration temperature gradient for a 3D-printed tensile specimen
(The transmission coefficients resulting from the calibration process are also shown)

During the calibration process, the most efficient approach is to repeatedly run a single (fully post-processed) thermal simulation by adjusting only the values of convection coefficient, emissivity coefficient, and ambient temperature. Alternately, one may return with each trial to the Mesh/Model Generator, revise values there, regenerate the files with the revised estimates, and post-process the files as necessary, though this is usually a more time-consuming approach. Once the values of the ambient temperature and heat transmission coefficients are determined through the calibration process, post-processing edits of the thermal simulation may be significantly reduced by keying the calibrated values into the Mesh/Model Generator, and generating the input files.

It is assumed in the scope of this work that the values of convection and emissivity coefficients, as well as ambient temperature remain constant throughout the simulation process, though with an arbitrary geometry, this may not be the case, particularly with the value of convection coefficient. It should also be noted that the tuning of the emissivity reading of a thermal imaging camera such as the one

employed here should be a requisite step for the calibration process illustrated above. Moreover, another potentially important source of error which may be easily eliminated would be to seek a “front-on” camera angle in attempting to capture an empirical gradient, eliminating any skew effects from the parallax effect.

7.3.2: THE MODIFICATION OF THE RESIDUAL STRESS SIMULATION

The modification strategy for the thermal displacement simulation depends on the meshing technique. If an internal mesh is employed, the same place-holder material definitions of “bottom_material”, and “material” sought and replaced in the thermal simulation must be found and replaced in the thermal-displacement simulation with “mat_bottom_plate”, and “TNPLY0001”, respectively. Given the use of an external mesh, these same place-holder definitions must be replaced with “mat_bottom_plate”, and “TNPLY0001-VOID”, respectively. Additionally, the material definition in the beginning of the file must also be renamed to have the suffix “-VOID” (as by default it will not), this gives the UMAT knowledge of the execution of PathCoverage, prompting the interface to search the working directory for void ratio calculations. Regardless of meshing technique/strategy, two step definitions must be made at the end of the file: a cool down step, and a base plate removal step. The addition of these two steps amount to 28 lines of added text, but the content of the added text should not change in any regard besides the desired step labels from the post-processing of one thermal-displacement file to the next. The cooldown step and the plate removal step for a five-step thermal-displacement simulation are shown in Figure 64, with the strategy of the desired step labels being to retain the ability to reference the numeric order of execution. Retaining the ability to reference the number of a specific step may be useful when troubleshooting a simulation which may be struggling to complete a certain step.

```

*STEP, NAME=STEP-6-COOLDOWN, NLGEOM=YES
*STATIC
100.0, 500.0, 1.0E-10, 100.0
*TEMPERATURE
NSET, ALL_NODES, 25.0
*OUTPUT, FIELD
*NODE OUTPUT
NT, RF, U
*ELEMENT OUTPUT
LE, PE, SDV, S, TEMP
*OUTPUT, HISTORY, VARIABLE=PRESELECT, FREQUENCY=10
*END STEP
**
*STEP, NAME=STEP-7-PLATE-REMOVE, NLGEOM=YES
*STATIC
1E-8, 1E-8, 1E-8, 1E-8,
*MODEL CHANGE, REMOVE
BOTTOM_PLATE
*CONTROLS, RESET
*CONTROLS, PARAMETERS=FIELD, FIELD=DISPLACEMENT
, 1., , , , ,
*OUTPUT, FIELD, FREQUENCY=10
*NODE OUTPUT
NT, RF, U
*ELEMENT OUTPUT
LE, PE, SDV, S, TEMP
*OUTPUT, HISTORY, VARIABLE=PRESELECT, FREQUENCY=10
*END STEP

```

Figure 64: The cooldown step and the plate removal step for the residual stress simulation

7.3.3: THE GENERATION OF THE SERVICE LOADING SIMULATION

The generation of the service loading simulation is generally the most time-consuming part of the post-processing. In a generic sense, this part of the simulation stands apart from process simulation and involves the definition of loading cases that the part is anticipated to withstand during service life. In the scope of this work involving tensile specimens, the only load case which is investigated is the behavior involved with a strain-to-fracture test. The structure of the input file is in many ways similar to both the thermal and the thermal-displacement simulations, making the thermal-displacement file a sensible choice for a template.

Beginning by modifying a copy of the thermal-displacement file, the first difference is the material definition, which, as the material is all cooled to ambient temperature prior to loading, reduces to a temperature independent definition. The material definition itself is derived by exporting the

temperature-independent definition given by MCQ-Chopped. This temperature-independent definition was first stated in Figure 41, but is re-stated below, as Figure 65.

```

*MATERIAL, NAME = SPLYOrthotropic
*USER MATERIAL,CONSTANTS= 45
**      E11,      E22,      E33,      G12,      G13,      G23,      NU12,      NU13,
3.376820E+09, 3.183950E+09, 3.183950E+09, 1200070000, 1200070000, 1177620000, 3.600140E-01, 3.600140E-01,
**      NU23,      S11T,      S11C,      S22T,      S22C,      S33T,      S33C,      S12S,
3.518570E-01, 59830200, 106150000, 52570900, 93270900, 52570900, 93270900, 29965400,
**      S13S,      S23S,      RHO,      DFACTT,      DFACTC,      DFACTS,      FFACT,      DAMAGE,
29965400, 29770500, 1.196650E+03, 1.000000E-02, 2.000000E-01, 1.000000E-01, 1.000000E-02, 67109377,
** FRACTURE,      EPS11T,      EPS11C,      EPS22T,      EPS22C,      EPS33T,      EPS33C,      EPS12S,
67109377, 1, 1, 1, 1, 1, 1, 1,
**      EPS23S,      EPS13S,      STRAIN_1,      STRESS_1,      STRAIN_2,      STRESS_2,      STRAIN_3,      STRESS_3,
1, 1, 0, 0, 4.591180E-03, 1.561074E+07, 1.160373E-02, 3.761987E+07,
** STRAIN_4,      STRESS_4,      STRAIN_5,      STRESS_5,      MUP,
1.456068E-02, 4.534584E+07, 1.857702E-02, 5.302805E+07, 0,

```

Figure 65: The temperature-independent material definition provided to service loading

An “*INCLUDE” statement must be added to the UMAT shown in Figure 65, to prompt it to browse the working directory for void ratio calculations. The material is named “SPLY0001-VOID”, rather than “TNPLY00001-VOID” (assuming the use of an external mesh), designating a temperature independent material definition, and (if the suffix “-VOID” is present), again prompting the UMAT to search the working directory for void ratio calculations. By deleting the temperature related fields, the material definition collapses from 341 user material constants down to 45. The solution dependent variable definitions (DEPVAR) are ten in number, with element deletion mapped to variable number four. The density given under “*DENSITY” is a factor of 1000 times more than the actual density (listed as “RHO in Figure 63), indicating a fairly high factor of mass scaling. As the stable time step increment in an explicit simulation is governed by a dilatational wave speed over the smallest element, this is done to provide a considerable computational advantage, and holds valid as long as the simulation is representing a quasi-static loading.

The next difference in the modification process is the removal of all the elements which define the base plate. The nodes which constitute the corners of each element definition need not be deleted, but the definition of the elements themselves are removed.

Next, the element definitions are all changed from “C3D8” to “C3D8R”, again, for a computational advantage. This represents and calculates all stresses on an element basis, rather than a nodal basis, reducing the number of necessary calculations. This step is optional, and the simulation will complete with either technique with a negligible difference in result. It should be noted that this will likely present a difference in maximum and minimum stress between the end of the residual stress simulation (thermal-displacement), and the beginning of the loading simulation, as the residual stress simulation is an implicit process which is performed on a nodal basis. The peak stresses observed on a nodal basis will be essentially averaged on an element-by-element basis to define element-based stress initial conditions.

The next modification is the definition of the solid section, which must match the material definition “SPLY0001-VOID”, also, the solid section defining the material for the base plate must be deleted, as the element definitions representing the base plate have also been deleted.

The following modification requires the specification of the loading cases, and will vary from simulation to simulation. In the scope of this work, two node sets representing the grip regions of each tensile specimen were defined, allowing a displacement boundary condition to be imposed on the node set representing one grip region, while holding the other grip region fixed. To define these node sets, a copy of the thermal simulation must be created and truncated after all node and element definitions, after which it is loaded in ABAQUS CAE as an imported model. Two node sets are then defined:

Fixed_node, and Load_node. Following the definition of the node sets in CAE, a job is created, and an input file is written for that job. That job is then loaded in a text editor (Notepad++), and the text representing the two node set definitions is located, copied, and pasted into the end of *NSET section of the service loading file. When pasting the node set definitions in, the syntax changes slightly, omitting any references to part instances. The truncation point of the copied thermal simulation, the creation of the node set “Fixed_node” in CAE, and the omitted syntax concerning part instances are shown in Figure 66, Figure 67, and Figure 68, respectively.

```

544, 3273, 3274, 3287, 3286, 3651, 3652, 3665, 3664
543, 3272, 3273, 3286, 3285, 3650, 3651, 3664, 3663
542, 3271, 3272, 3285, 3284, 3649, 3650, 3663, 3662
*NSET, NSET=NSET_NODE_LAYER_1, ELSET=ELSET_PART_LAYER_1
*NSET, NSET=NSET_NODE_LAYER_2, ELSET=ELSET_PART_LAYER_2
*NSET, NSET=NSET_NODE_LAYER_3, ELSET=ELSET_PART_LAYER_3
*NSET, NSET=NSET_NODE_LAYER_4, ELSET=ELSET_PART_LAYER_4
*NSET, NSET=NSET_NODE_LAYER_5, ELSET=ELSET_PART_LAYER_5
*ELSET, ELSET=ELSET_WHOLE_PART
ELSET_PART_LAYER_1,
ELSET_PART_LAYER_2,
ELSET_PART_LAYER_3,
ELSET_PART_LAYER_4,
ELSET_PART_LAYER_5,
**create external surfaces of the whole part
*SURFACE, NAME=ALL_EXTERNAL_SURFACES, TYPE=ELEMENT
ELSET_WHOLE_PART
*elset, elset=elset_angle_0, GENERATE
4, 7, 1
87, 98, 1
102, 112, 1

```

← EVERYTHING FROM THIS POINT DOWNWARDS
MUST BE DELETED BEFORE LOADING THE FILE
IN ABAQUS CAE:

Figure 66: The truncation point in the thermal simulation copy

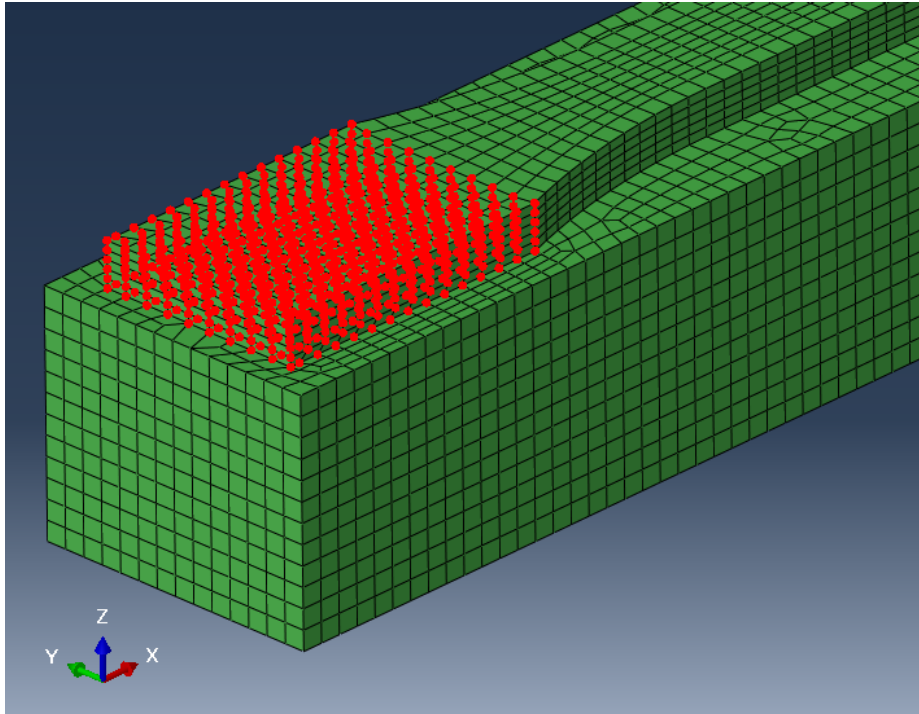


Figure 67: Selection of the set "Fixed_node" in ABAQUS CAE

```
*Nset, nset=Fixed_node, instance=PART-1-1 OMIT THESE 19 CHARACTERS
  9, 10, 11, 12, 13, 14, 15, 16, 17, 18, 19, 20, 41, 44, 47, 48
 53, 54, 55, 56, 57, 58, 59, 72, 75, 76, 79, 80, 89, 91, 92, 93
 94, 95, 106, 107, 117, 118, 121, 122, 123, 124, 127, 128, 142, 144, 145, 146
147, 148, 149, 150, 151, 152, 153, 154, 261, 262, 263, 264, 265, 266, 267, 268
269, 270, 271, 272, 273, 274, 275, 276, 277, 278, 279, 280, 281, 282, 283, 284
285, 286, 287, 288, 289, 290, 291, 292, 293, 294, 295, 296, 297, 298, 299, 300
301, 302, 303, 304, 305, 306, 307, 308, 309, 310, 311, 312, 313, 314, 315, 316
317, 318, 319, 320, 321, 322, 323, 324, 325, 326, 327, 328, 329, 330, 331, 332
```

... 900 node numbers, 56 Lines ...

```
4453, 4454, 4455, 4456, 4457, 4458, 4735, 4736, 4737, 4738, 4739, 4740, 4741, 4742, 4743, 4744
4745, 4746, 4747, 4748, 4749, 4750, 4751, 4752, 4753, 4754, 4755, 4756, 4757, 4758, 4759, 4760
4761, 4762, 4763, 4764, 4765, 4766, 4767, 4768, 4769, 4770, 4771, 4772, 4773, 4774, 4775, 4776
4777, 4778, 4779, 4780, 4781, 4782, 4783, 4784, 4785, 4786, 4787, 4788, 4789, 4790, 4791, 4792
4793, 4794, 4795, 4796, 4797, 4798, 4799, 4800, 4801, 4802, 4803, 4804, 4805, 4806, 4807, 4808
4809, 4810, 4811, 4812
```

Figure 68: The omitted part instance references in the copied node set definitions

As with any ABAQUS explicit simulation, a definition of amplitude of loading and a definition of bulk viscosity must be defined. In addition, one must specify: the boundary condition to be enforced at “Load_node”, and to be held at “Fixed_node”, the definition of the dynamic step itself, the specification of the file which specifies the initially stressed state given by the thermal-displacement simulation, and the output history and output fields desired to be written to the output database. These definitions are shown in Figure 69.

```

*Amplitude, name=Amp-1, definition=EQUALLY SPACED, fixed interval=1.0
    0., 1.
*Boundary
Fixed_node, 1, 1
Fixed_node, 4, 6
Load_node, 4, 6
**
*STEP, NAME=Tension
*DYNAMIC, EXPLICIT
,1.0
*Bulk Viscosity
0.06, 1.2
*INITIAL CONDITIONS, TYPE=STRESS, FILE=TGL22PL_disp, STEP=8, INC=1
*Boundary, amplitude=Amp-1
Load_node, 1, 1, 0.00045
*OUTPUT, FIELD, TIME INTERVAL=.01
*NODE OUTPUT
RF, U
*ELEMENT OUTPUT
LE, PE, SDV, S, TEMP, STATUS
*OUTPUT, HISTORY, VARIABLE=PRESELECT, TIME INTERVAL=.01
*END STEP

```

Figure 69: Specifications of at the end of a service loading input file

7.4: RUNNING THE FILES AND PROCESSING THE OUTPUTS

Once appropriately post-processed, the input files are executed through a command window, much as they would be for a standard submission of a traditional ABAQUS job. The syntax of the submission

differs slightly, as a user subroutine is used. The syntax for the submission of a thermal simulation, a thermal-displacement simulation, and a service loading simulation are shown in Figure 70.

```
C:\temp\5-17-19-1>abqumat2017 job=LGL11PL_heat inter cpus=4  
C:\temp\5-17-19-1>abqumat2017 job=LGL11PL_disp inter cpus=4  
C:\temp\5-17-19-1>abqumat2017 job=LGL11PL_load inter cpus=4
```

Figure 70: Command window syntax for the submission of simulations

In analyzing the geometric configuration described, each stage of the job took between 10 and 20 minutes on a PC with an Intel i7-7700 4-core processor at 3.6 Gigahertz. If and when the running of PathCoverage was necessary, this also took between 10 and 20 minutes.

Upon running the simulation, if the output interval is too seldom, one of the recognizable symptoms will be the production of a response that appears to significantly under-predict the maximum stress and strain of the specimen (by as much as 5%). One possible issue in this case is that the tensile testing process is a continuous elongation at a specified rate, whereas the readable output of a simulated tensile testing process is a series of still-frame captures given by specified intervals throughout the process. Fracture will almost always occur between one output interval and the next, so the quality of the simulated continuous representation largely depends on minimizing the interval size. As the number of still-frame captures is increased, the overall simulated representation of the stress-strain response will grow to depict the continuous nature of reality, though this discontinuity is unavoidably a characteristic of the explicit process.

The magnitude of the displacement for the boundary condition in the loading simulation was adjusted until a fracture response was observed toward the end of the specified number of output intervals (100 was deemed sufficient in this case). In the output file, engineering stress was manually derived by summing the contributions of nodal reaction forces, and dividing by the cross-sectional measurement. Engineering strain was derived by querying the difference between two points at opposing ends of the gauge length for displacement along the axis of the specimen (providing elongation), and dividing this value by the original distance between those two points.

Chapter 8: RESULTS AND DISCUSSION FOR VALIDATION OF THE DEFAULT APPROACH

Three simulation strategies for three orientations of tensile specimen were investigated with the process-modeling technique presented throughout Chapter 7. Defining the simulation strategy consists of two parts, the first defining the specifics of scan strategy absent specifications of raster orientation, and the second defining the mesh strategy. The depiction of the differences in simulation strategy were presented first in Figure 57, this depiction is re-presented below, as Figure 71.

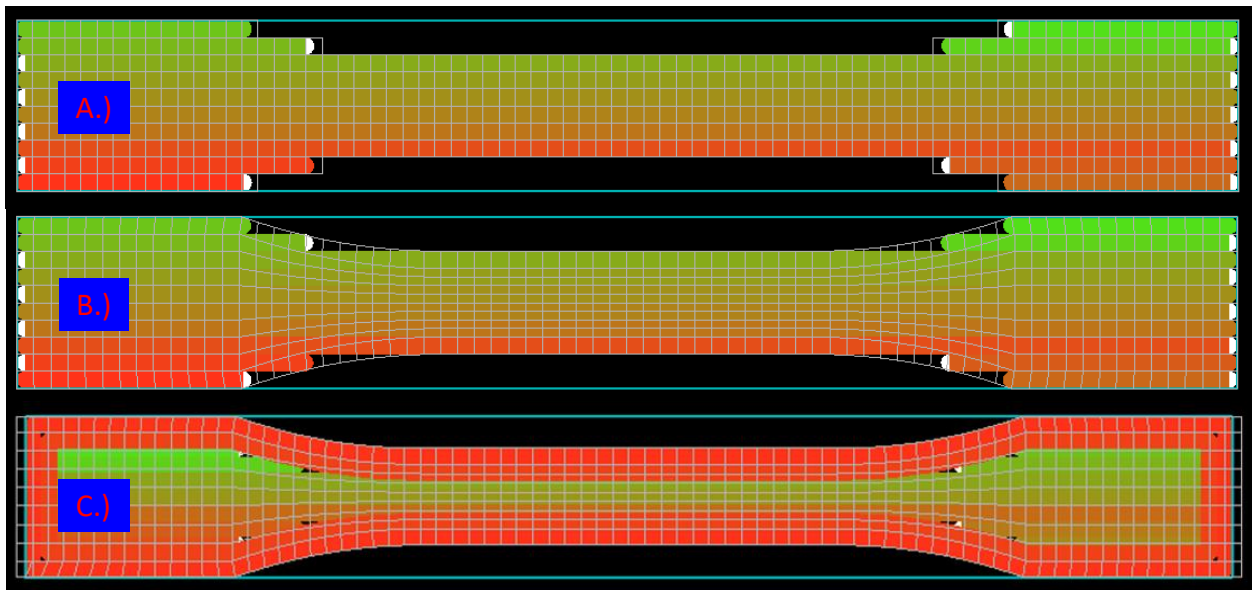


Figure 71: Graphical depictions shown when loading the PathCoverage module

The PathCoverage module is loaded for A.) No perimeter rasters and an internal mesh, B.) No perimeter rasters and an external mesh, and C.) 2 perimeter rasters and an external mesh

Figure 71A represents a simulation strategy given by a mesh generated internal of the mesh/model generator (internal mesh), and a scan strategy absent perimeter rasters. The results of the case presented by Figure 71A are shown in Figure 74. Figure 71B represents a simulation strategy given by a mesh generated external of the mesh/model generator (external mesh), and a scan strategy absent

perimeter rasters. The results of the case presented by Figure 71B are shown in Figure 77. Figure 71C represents a simulation strategy given by a mesh generated external of the mesh/model generator (external mesh), and a scan strategy with two perimeter rasters. The results of the case presented by Figure 71B are shown in Figure 84.

In addition to varying specifics of simulation strategies, Figure 74, Figure 77, and Figure 84 present results varying in orientation. The details of these orientations were first presented in Figure 10, and are re-presented below, as Figure 72.

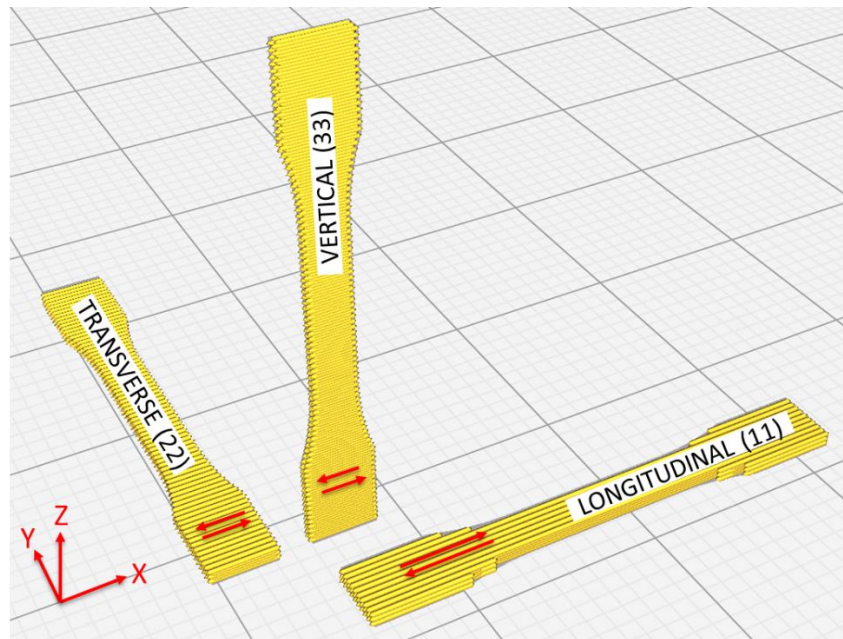


Figure 72: Depiction of raster orientations for 11, 22, and 33 tensile specimen

(Note: 1:8 scale specimens are depicted for the purpose of better rendering of raster strategy)

Part of the process in MCQ-Chopped involved tuning a predicted Baseline Material definition to a near-perfect match with an empirical tensile response. Therefore, comparing Baseline Material tensile response in various orientations to a manually-extracted simulated tensile response in various orientations was thought to be a reasonable metric for evaluating the quality of the model.

Traditionally, one might expect to see an empirical tensile result compared to a simulated tensile result, however, this distinction is made to illustrate that either of the two above mentioned comparisons would present largely the same graph, with the same level of discrepancy. Though these Baseline Material responses are generated by a software interface, they are essentially an exact match to empirical data, though dissimilar enough for the distinction to be noted. To illustrate how closely the presented Baseline Material definition was tuned to match empirical data, a graph of a Baseline Material tensile 11-response compared against an empirical 11-response is presented below, as Figure 73.

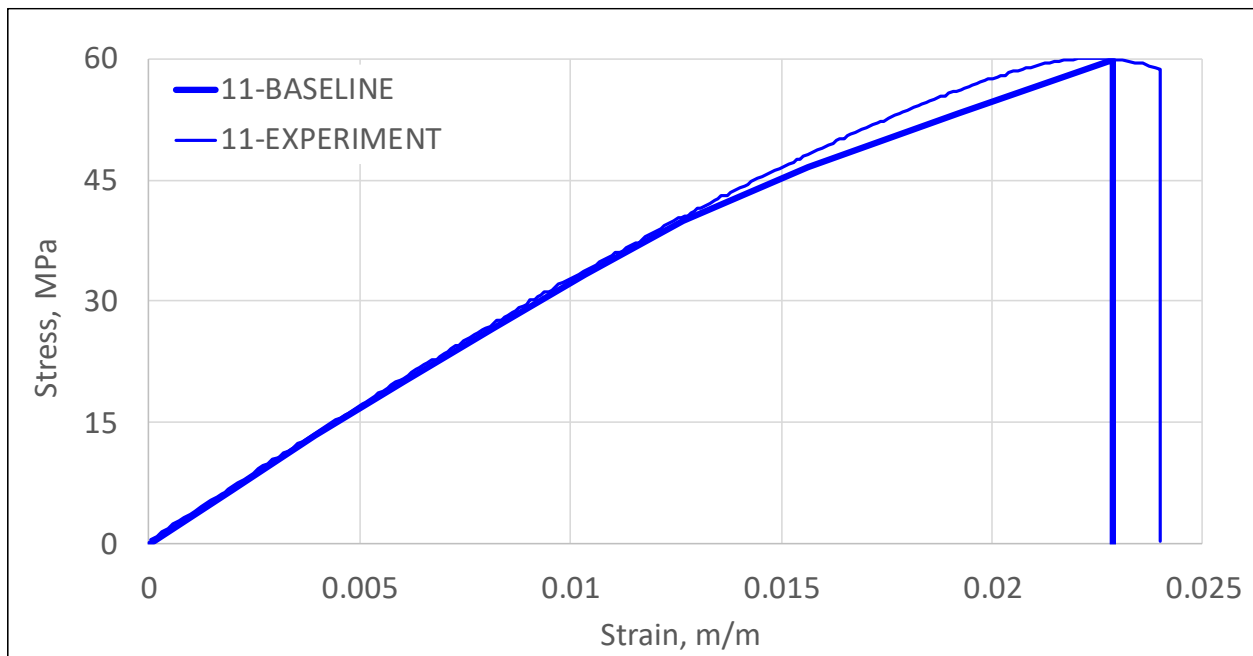


Figure 73: Baseline 11-tensile response compared to an experimental 11- tensile response

In addition to the above distinction regarding presentation of Baseline response, given the nature of the transverse isotropic assumption, “22” Baseline tensile responses (solid red) and “33” Baseline tensile responses (solid green) correspond to the same line. The simulated results of manually derived engineering stress vs engineering strain, obtained using ABAQUS to execute a strain-to-fracture response are shown as a dotted line of the corresponding color.

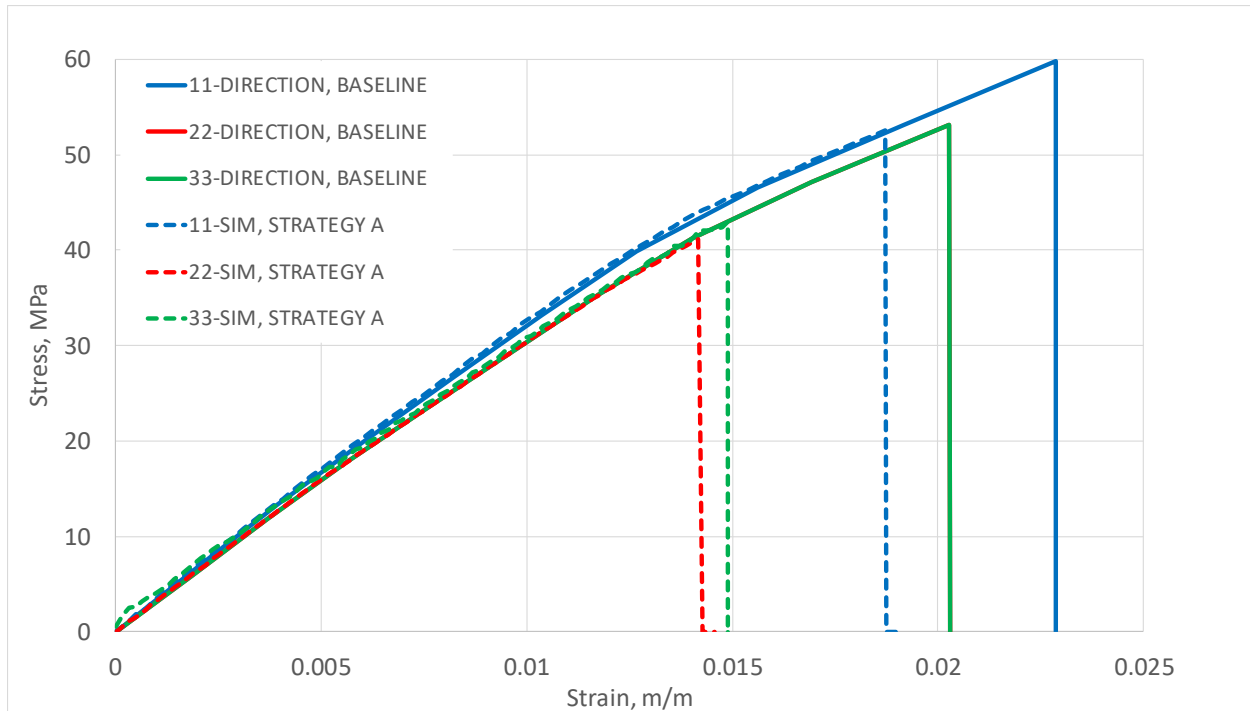


Figure 74: Simulated vs Baseline tensile response, strategy of Figure 71A

(22-Baseline & 33-Baseline correspond to the same line)

In Figure 74, there is roughly a uniform 15-20% discrepancy between all orientations of the Baseline Material tensile response and the respective orientation of simulated tensile response derived manually from the simulation in ABAQUS. Modulus is seen to track very well, but fracture occurs earlier than expected. One reasoning for this discrepancy is that the sharp-cornered nature of the mesh presents a fundamental non-convergent condition. In pursuing further mesh refinement, this condition is seen to only worsen, producing a peak stress that grows higher and higher with mesh refinement, giving rise to an earlier and earlier failure. For various degrees of mesh refinement of a simulated 11-specimen in a tensile strain-to-fracture simulation conducted in ABAQUS, this worsening condition is shown below, in Figure 75.

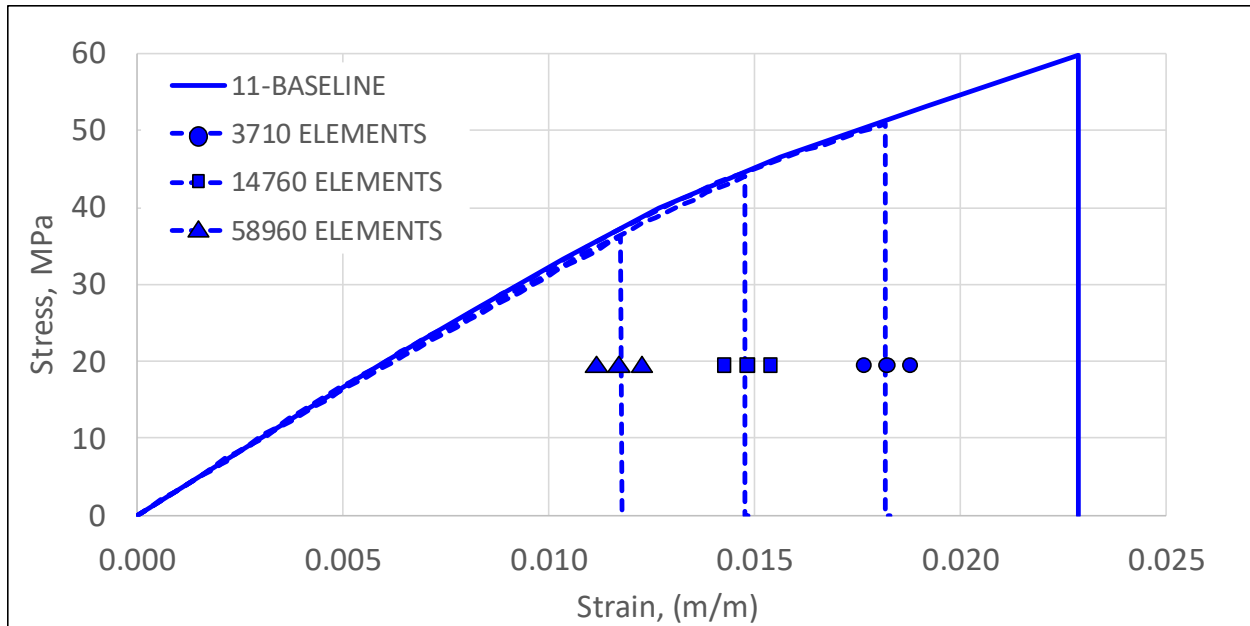


Figure 75: The worsening non-convergent condition provided by a sharp-cornered mesh

In both Figure 74 and Figure 75, it is worth note that PathCoverage is not recommended to be run when employing use of the internal mesh feature in GENOA, and that recommendation was heeded in this study. That recommendation is most likely due to the means used to construct the internal mesh feature in the software. The internal mesh feature looks directly at the G-code, and uses an estimate of bead width to define the boundaries of the domain. If that G-code defines a rectangular part absent contours, or internal features, and the G-code utilizes a well-executed perimeter raster, running PathCoverage will overlay the G-code with a mesh domain defined by the G-code, and resultantly predict few if any voids present to account for. However, given the case of a domain defined with sharp corners by design, or a G-code absent a perimeter raster in the scan strategy, the strategy the internal mesh feature uses to define the domain is limited to producing a sharp-cornered geometry. In the case of a tensile specimen in 11-loading, whether PathCoverage is run or not is of little difference, as the contributions that PathCoverage is seen to make produce essentially the same end result. This case is shown in Figure 76.

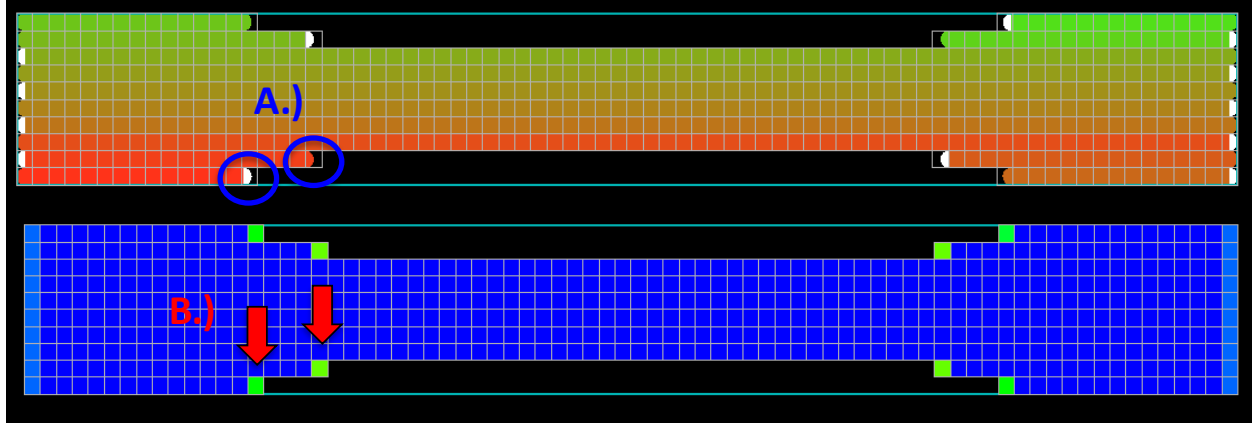


Figure 76: Running PathCoverage on a domain generated by the internal mesh feature

In Figure 76A, one may see that PathCoverage is approximating the ends of each raster as semi-circular, then overlaying a user-defined grid of elements to define the domain of the part. Elements are either kept or discarded on the basis of intersection (full or partial) between raster boundaries defined by the g-code and the user-defined grid of elements. In Figure 76B, PathCoverage then analyzes each remaining element to produce an estimate of the end-of-raster void effect to in each element. When using the internal mesh strategy, the only elements that end up with end-of-raster effects present at the ends of each raster. These elements are next prescribed an end-of-raster void ratio to account for the presence of void. However, in the case of Figure 76, the effect of accounting for end-of-raster voids is negligible, as weakening these elements gives rise to an element deletion early in the loading response, but the resultant response is largely the same response as one would have obtained from neglecting to run PathCoverage altogether. Given use of the internal mesh feature, whether one runs PathCoverage or not, the end result is the same, a non-convergent mesh for most levels of geometric complexity. This supports the assessment that a successful simulation strategy, regardless of the details of scan strategy, must be built on the basis of a convergent mesh. This is next discussed, referencing Figure 77, and Figure 71b.

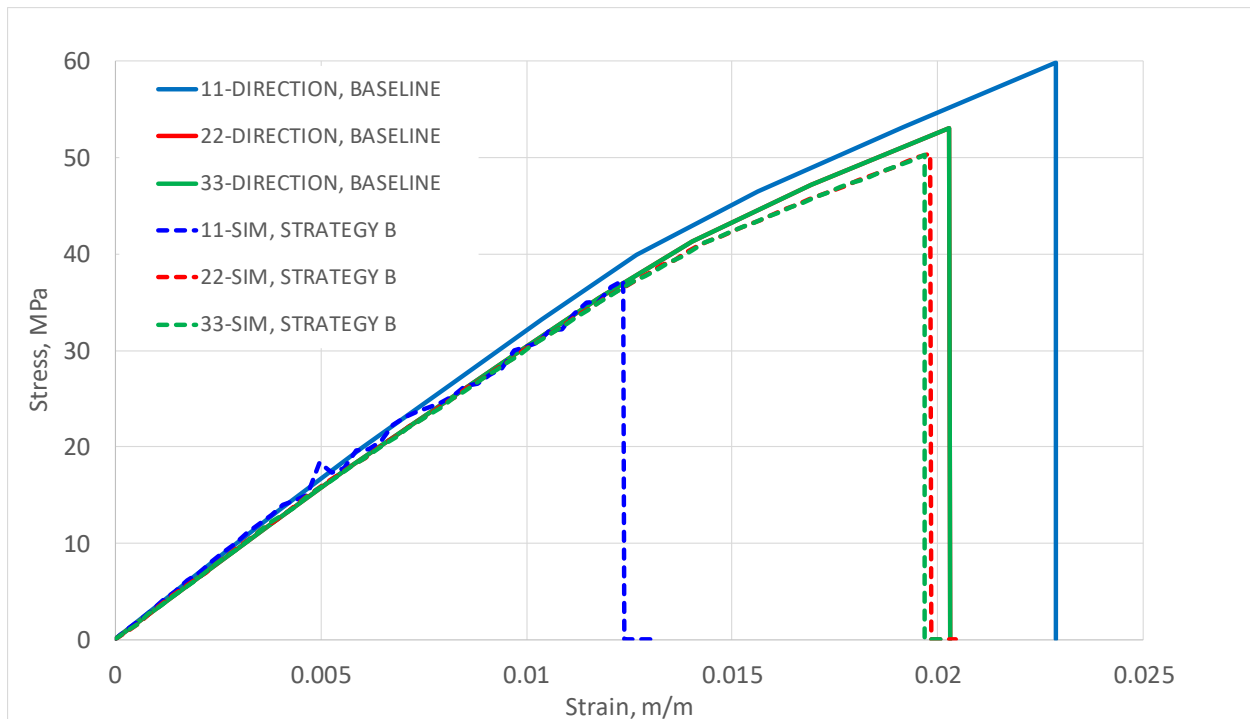


Figure 77: Simulated vs Baseline tensile response, strategy of Figure 71b

In Figure 77, a smooth-contoured mesh is used to represent the gauge reduction. This is shown in Figure 71b. However, as this mesh strategy cannot define mesh boundaries that coincide with raster boundaries without disregarding the need for smooth outer contours to create a convergent mesh, the question arises: How does one properly locate mesh boundaries to arrive at an accurate simulation? There are three potential solutions to this query: a.) allow the mesh boundaries to fall fully outside raster boundaries, b.) allow mesh boundaries to fall fully inside raster boundaries, c.) pass consistent 3D data to both a slicer and a mesh software. In investigating potential solutions a.) and b.), reference Figure 78a and Figure 78b, and for potential solution c.), reference Figure 79.

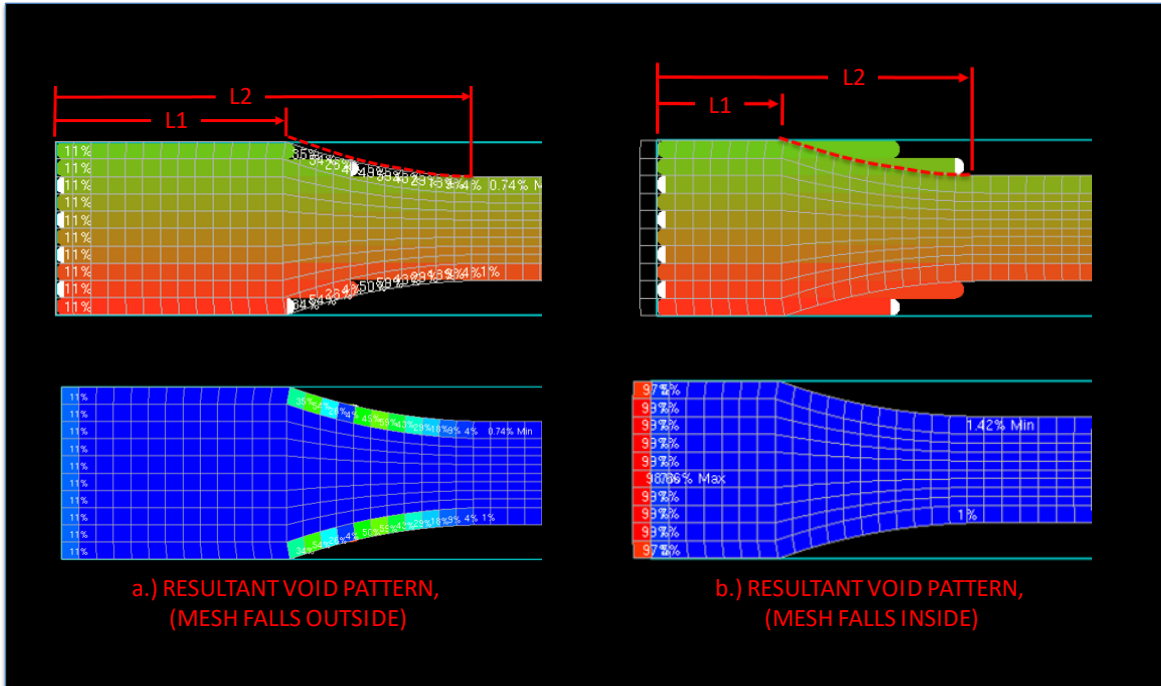


Figure 78: The void patterns generated by PathCoverage given differing mesh boundaries

a.) mesh boundaries fall outside rasters, and b.) mesh boundaries fall inside rasters

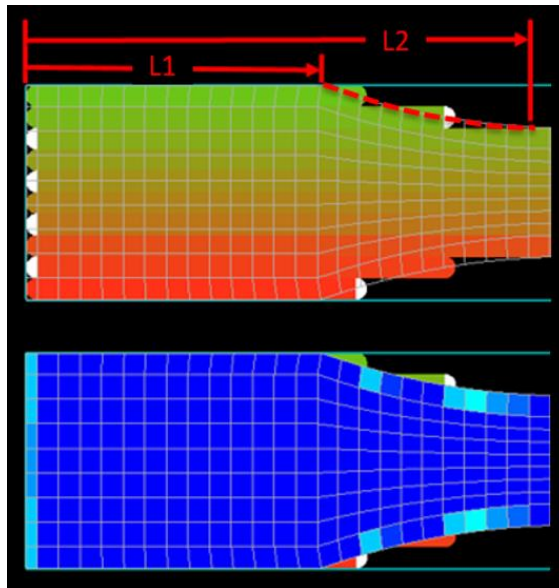


Figure 79: The void patterns generated by PathCoverage given consistent 3D data

Given the solution presented by Figure 78a, one may observe that, by defining mesh boundaries beyond the domain of where the g-code specifies rasters be located, one is allowing regions of space that exist physically outside the domain of the printed part to contribute to void calculations for elements inside the domain of the printed part. The solution presented by Figure 78a gave rise to the result shown in Figure 77. In Figure 77, the effect of introducing end-of-raster void results based on solution presented by Figure 78a is seen to govern the simulated tensile response in ABAQUS to a much higher degree given a 11-scan strategy than the same effect introduced to a 22 or a 33 scan strategy. This is attributed to the difference in approach angle between the differing infill orientations and a tangent line drawn on the outer boundary of where zero-width infill would terminate. This is shown in Figure 80.

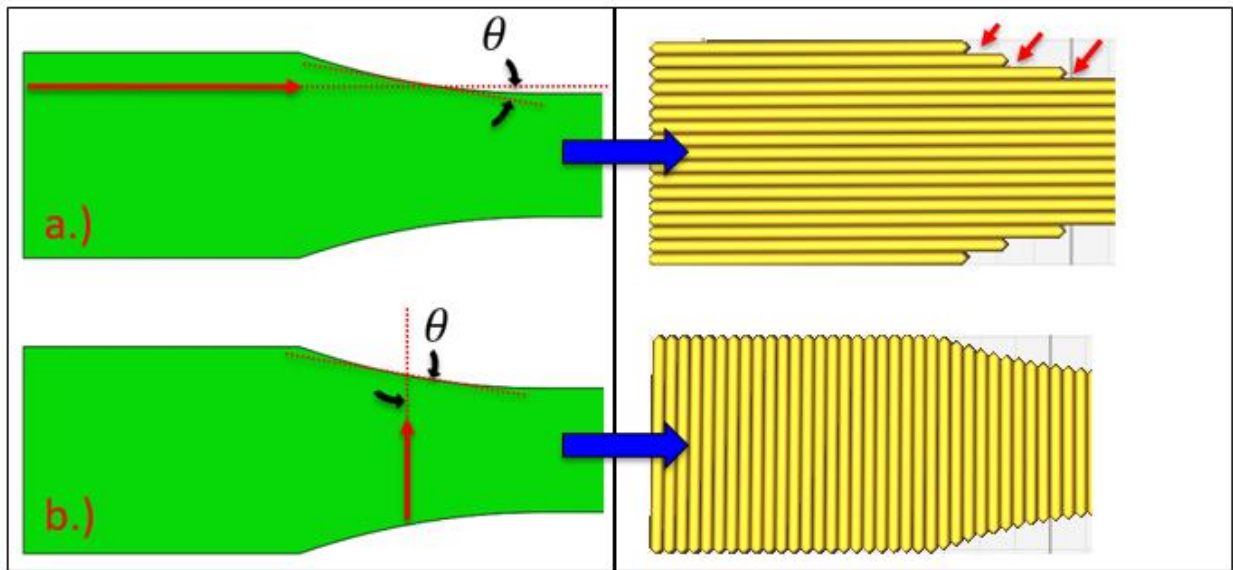


Figure 80: The approach angle comparison for 11 specimens (a) versus 22 & 33 specimens (b)

In Figure 80, the particularly narrow approach angle that must be employed by 11-direction specimens leaves significant shortages in material along the gauge reduction. The mesh, based upon the original design intent, is largely unrestricted to conform to this contour while the g-code is restricted to

unidirectional infill rasters of a finite width. The wider the infill rasters and the narrower the angle, the more severe the condition.

Given the solution presented by Figure 78b, there are two effects of note. First, by allowing mesh boundaries to fall fully within the boundaries of where the G-code specifies rasters be located, the end-of-raster void ratio results are eliminated along the gauge reduction contour. This is because the stratagem of mesh creation seeks to avoid the investigation of any area that is seen to be less than 100% filled, giving rise to no end-of-raster void results, no detrimental effect, and a near-perfect match to Baseline Material response. Second, note a pattern of void ratio results presenting along the end of the grip region. This pattern is from a necessary extension of the mesh representing the end of the specimen. This extension must be performed because otherwise, the boundary of the mesh truncates the boundary defined by the g-code. It is clear that this boundary must be extended, though unclear what dimension of extension makes for the right amount. Consider the flow diagram presented below, as Figure 81.

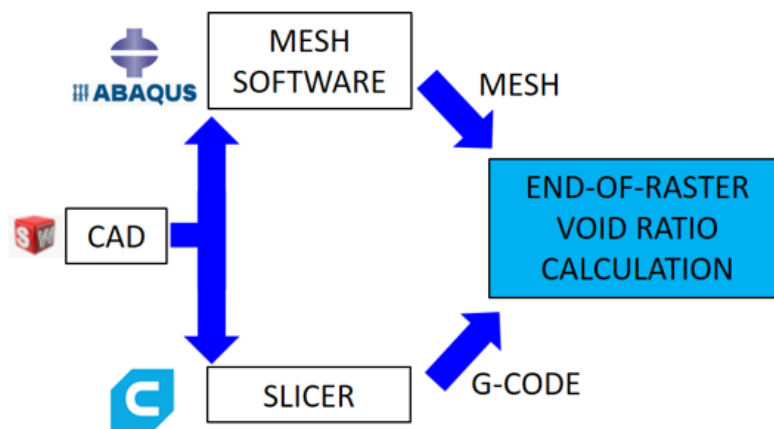


Figure 81: The flow of 3D data from the CAD model to PathCoverage

Many would likely pose that to pursue either the simulation strategy offered by Figure 78a or the simulation strategy offered by Figure 78b assumes a design freedom of technique that should not be afforded. Given the solution presented by Figure 79, one would follow the logic presented by Figure 81, proceeding to offer the same 3D data to both the mesh software and the slicer. The slicer would produce a G-code, and the mesh software would produce a mesh, and by feeding both files to PathCoverage, the effect of end-of-raster voids would be determined. Though this may seem like consistent logic, the approach outlined by Figure 81 simply defers the decisions regarding how to make a mesh to the mesh software, and defers the decisions regarding how to discretize the domain to the slicer. Various mesh interfaces were not explored, but a notable difference in discretization strategy was observed between slicer interfaces. Consider the void pattern generated by PathCoverage in Figure 82, and the void pattern created by PathCoverage in Figure 83. In Figure 82, the same 3D data was passed to both Cura and ABAQUS CAE, giving rise to the end-of-raster void pattern shown in the bottom-left of Figure 82. In Figure 83, the same 3D data was passed to both Slic3R and ABAQUS CAE, giving rise to the end-of-raster void pattern shown in the bottom-left of Figure 83.

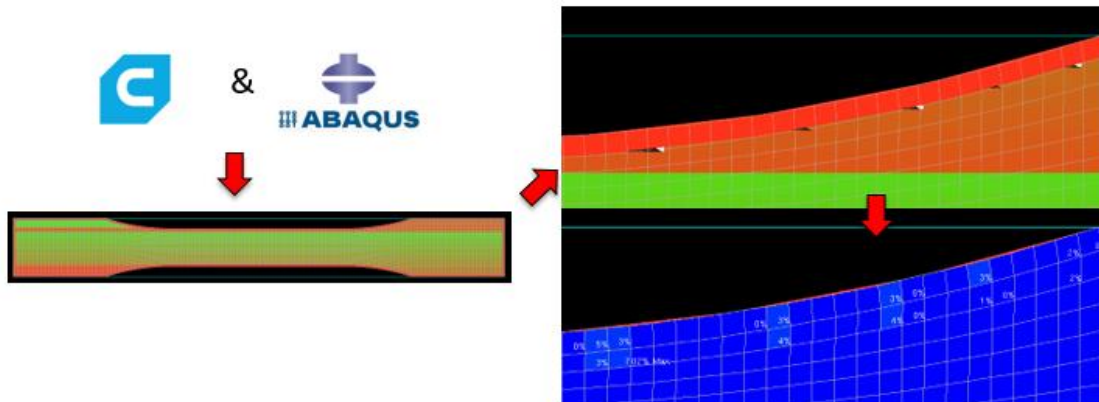


Figure 82: Void pattern generated by passing the same 3D data to Cura and ABAQUS

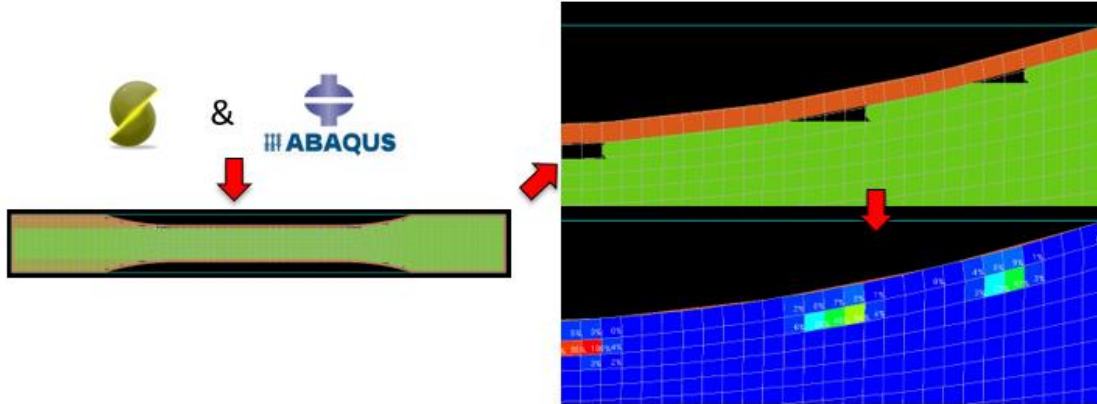


Figure 83: Void pattern generated by passing the same 3D data to Slic3R and ABAQUS

In both the case presented for Figure 82, as well as the case presented for Figure 83, every effort was made to specify consistent slicer settings, however, there were several places where it was unclear how a specific setting was being established. In addition, there were several fundamental places where Cura was seen to offer freedoms to adjust G-code parameters where Slic3r did not. In particular, Cura offers the ability to adjust “Infill Overlap”, “Infill Wipe Distance”, and the ability to print infill prior to perimeter rasters by activating “Infill Before Walls”. In Slic3r, the comparable parameter specifies infill overlap as a percentage of raster width, but how exactly this was defined was not clear. Cura also has the ability to specify a unidirectional infill, a parameter which is important for the completion of this study. In Slic3r, raster orientation may be specified, but this only specifies the first layer, (even numbered layers following the first are orthogonal) To use Slic3r given this inability would require a large degree of post-processing, at minimum, complete a study such as this. Given the case of Figure 79, mesh contours are seen to bisect, giving rise to another series of under-predicted Baseline Property responses, but to a lesser extent than is shown in Figure 77. A 3D printer does not require the creation of a mesh to specify a part. It is posed that the most convenient implementation would aim to combine the best parts of the internal meshing strategy and the external meshing strategy, gaining the convergent behavior of the external mesh strategy, and requiring the time commitment of the internal mesh strategy.

Figure 71C represents a simulation strategy that is given by a mesh generated external of the mesh/model generator (in ABAQUS CAE), and a scan strategy with two perimeter rasters. The results of the simulation strategy given by this case is shown in Figure 84.

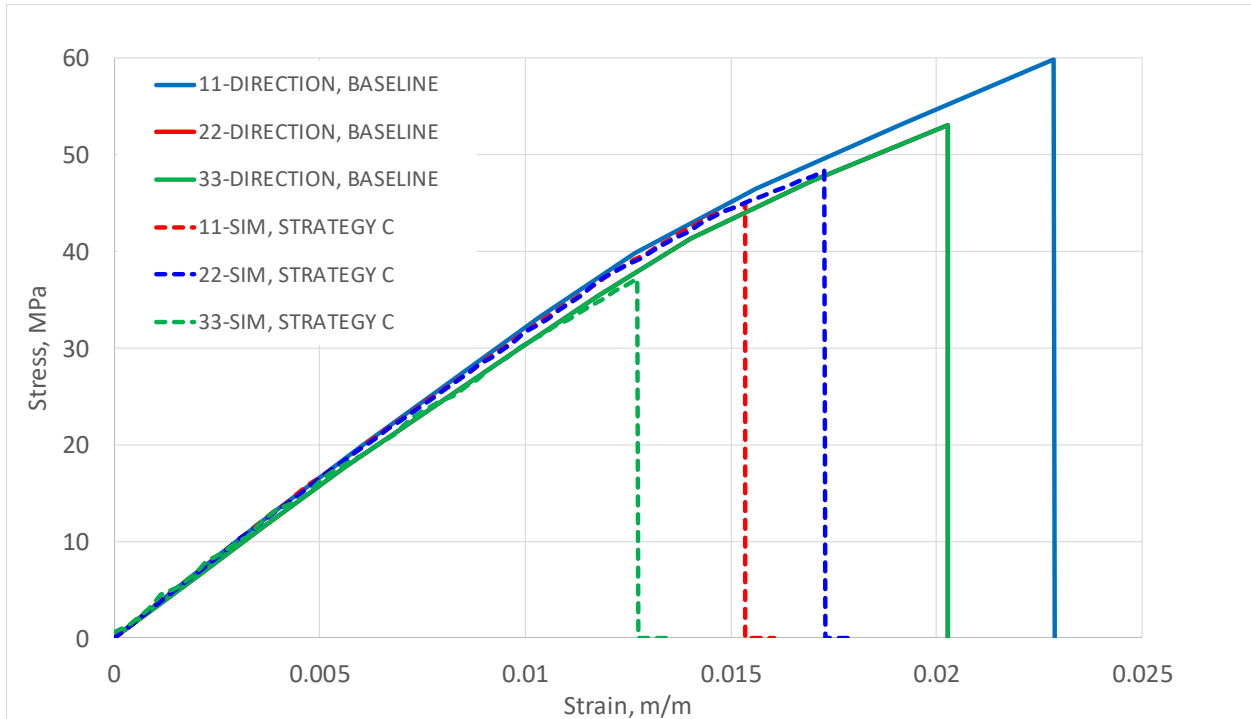


Figure 84: Simulated vs Baseline tensile response, strategy of Figure 71c

Comparing the quality of match achieved in Figure 77 to the quality of match achieved in Figure 84, a much more efficient filling of the domain may be accomplished with a 11-oriented specimen, given the freedom to employ perimeter rasters, but these perimeter rasters introduce end-of-raster void effects to the other two orientations of specimens, giving a more favorable prediction of 11-Baseline tensile response at the expense of a less favorable prediction of 22-Baseline and 33-Baseline tensile response.

8.1: DISCUSSION OF SIMULATION RESULTS FOR THE DEFAULT APPROACH

Though multiple other sources are cited, one of the main sources of discrepancy undermining the results shown in Figure 74, Figure 77, and Figure 84 is that tensile behavior was matched at the stage of this procedure when the only present source of detrimental effect was homogenized voids. The empirical source of tensile data that was matched at this stage contained both the effects of residual stress and the effects of end-of-raster voids. The formulation then continued to calculate, formulate, and introduce both the effect of residual stress, and the effect of end-of-raster voids.

Given the variety of techniques, and the goodness of match across the differing orientations, the internal meshing technique most likely provides the most desirable match, though an under-prediction of 15-20% on the basis of strength is not the most desirable, this level of dissimilarity between semi-empirical result and simulated result is at least observed to be somewhat uniform across all orientations with this technique. Given the external meshing technique with no perimeter rasters, a much improved match may be realized in 22 and 33 specimens, but the result in the 11-direction load case suffers resultantly, differing by about 40% on the basis of strength. Introducing perimeter rasters with the external meshing technique appears to improve the goodness of match in the 22-direction, but the match in the 11-direction and the match in the 33-direction both significantly under-predict strength, differing by 25% and 30%, respectively. It should be noted that a high-quality match may be realized on the basis of predicted modulus, even beyond the yield point. This is most true of the internal meshing technique.

It is believed that if several more iterations were performed with the Default Approach, returning with each iteration to reform the estimate of neat material properties, that a convergent material definition

could be obtained. However, one source of questionability with this model is that it is founded in a material state that no test can verify, and no analytical determination can prove. The entire aim of the Default approach aims to close the gap between the fictitiously perfect state of material and a realistic response by introducing three main sources of detrimental effects: a.) homogenized voids, b.) residual stress, and c.) end-of-raster voids. However, it is not a complete validation of this model to present a match for a single load case that assumes the summation of three separately formulated detrimental effects, none of which may be independently verified. One of the best means to offer support to the validity of the formulation would aim to introduce a test which could validate a match to an earlier stage of this framework. In doing so, one may determine a means of dividing the contributions of the individual detrimental effects offered by homogenized voids, residual stress, and end-of-raster voids. That is, in essence, the aim of the User-Informed-Calibration Approach.

Chapter 9: THE USER-INFORMED CALIBRATION APPROACH

In 5.4, the User-Informed-Calibration Approach was qualified by four main recommendations. In this chapter, the User-Informed-Calibration Approach is presented, followed by a presentation of the resultant material definition. The detailed presentation of the approach is discussed in section 9.1. The resultant material definition, and involved discussion is presented in section 9.2.

9.1: THE PRESENTATION OF THE USER-INFORMED CALIBRATION APPROACH

The implementation of the User-Informed Calibration approach is preceded by modifying the Baseline material definition generated in MCQ-Chopped, earlier shown in Figure 41. At the beginning of the modification process, the material definition is modified to the definition shown below, as Figure 85.

```
*MATERIAL, NAME = SPLYOrthotropic
*USER MATERIAL, CONSTANTS= 45
**      E11,      E22,      E33,      G12,      G13,      G23,      NU12,      NU13,
3.376820E+09, 3.183950E+09, 3.183950E+09, 1200070000, 1200070000, 1177620000, 3.600140E-01, 3.600140E-01,
**      NU23,      S11T,      S11C,      S22T,      S22C,      S33T,      S33C,      S12S,
3.518570E-01, 59830200, 106150000, 52570900, 93270900, 52570900, 93270900, 29965400,
**      S13S,      S23S,      RHO,      DFACTT,      DFACTC,      DFACTS,      FFACT,      DAMAGE,
29965400, 29770500, 1.196650E+03, 1.000000E-02, 2.000000E-01, 1.000000E-01, 1.000000E-02, 67109377,
** FRACTURE,      EPS11T,      EPS11C,      EPS22T,      EPS22C,      EPS33T,      EPS33C,      EPS12S,
67109377, 1, 1, 1, 1, 1, 1, 1,
** EPS23S,      EPS13S,      STRAIN_1,      STRESS_1,      STRAIN_2,      STRESS_2,      STRAIN_3,      STRESS_3,
1, 1, 0, 0, 4.591180E-03, 1.561074E+07, 1.160373E-02, 3.761987E+07,
** STRAIN_4,      STRESS_4,      STRAIN_5,      STRESS_5,      MUP,
1.456068E-02, 4.534584E+07, 1.857702E-02, 5.302805E+07, 0,
```

Figure 85: Reformed definition at the initiation of the User-Informed Calibration approach

A series of changes are made to transform the Baseline material definition shown in Figure 85, all occurring prior to beginning the User-Informed Calibration approach. First, all values depicted by scientific notation are truncated to the nearest third significant figure. Next, the Young's moduli E11, E22, and E33 are changed to 3.27E+09, 3.27E+09, and 3.44E+09, respectively. To be consistent with the

tensile elastic modulus measurement of three test specimens generated to verify consistent properties at the beginning of a fresh filament reel procurement. The moduli measurements for the 11, 22, and 33-orientation tensile specimens are shown below, as Figure 86, Figure 87, and Figure 88, respectively.

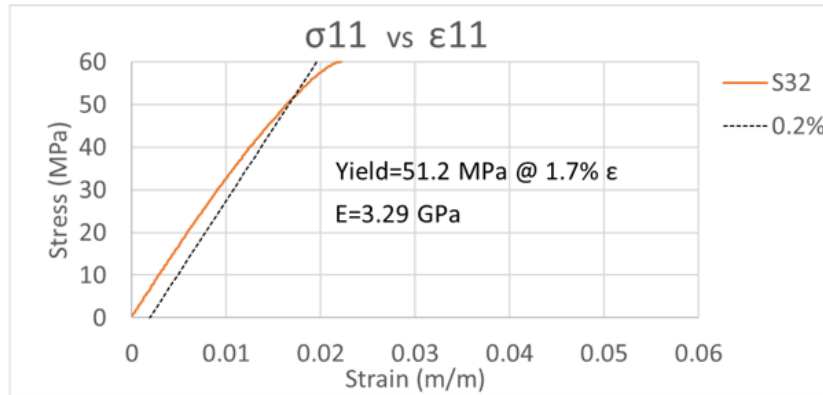


Figure 86: The verification tensile test for the 11-direction, given a new filament reel

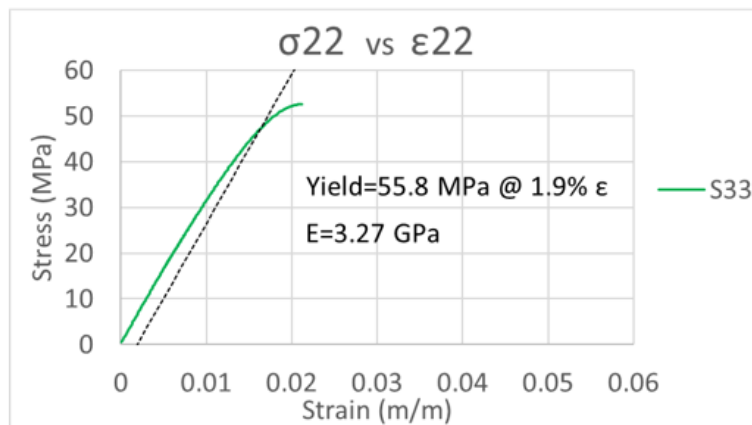


Figure 87: The verification tensile test for the 22-direction, given a new filament reel

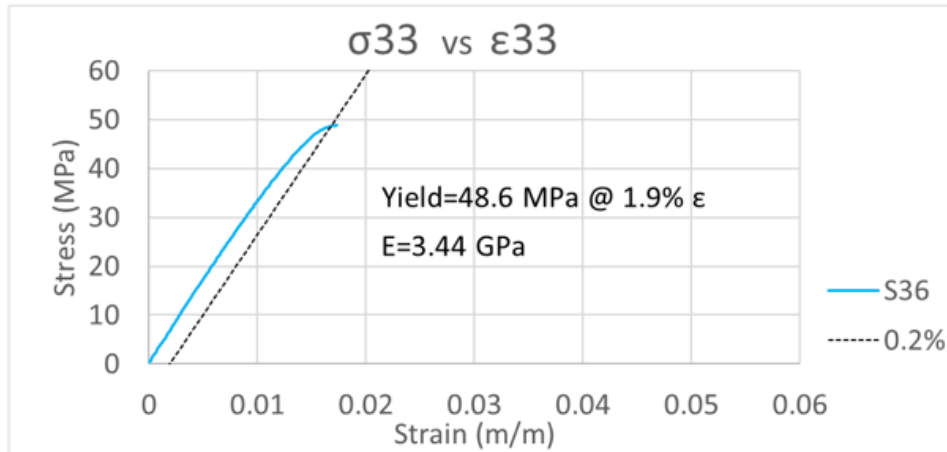


Figure 88: The verification tensile test for the 33-direction, given a new filament reel

The final change before beginning the approach is to set the damage degradation factors for tensile, compressive, and shear to “1.0E+00” to nullify any effect they might introduce. These factors govern behavior associated with the time-dependent progression of damage following ultimate loading, requiring an explicit simulation to introduce their effects, however, the procedure presented in this chapter is implicit, and only aims to match behavior leading up to ultimate loading. The first phase of the approach begins via a process of modifying the material definition, as informed by the results of iterative service loading simulations to match 11, 22, and 33 empirical bending data. This phase of the approach is discussed in 9.1.1. The second phase applies the material definition obtained by the first phase to 11, 22, and 33 tensile specimens, and then aims to achieve a match to respective 11, 22, and 33 tensile data by introducing a small defective portion of material to each specimen. The pattern of defective material is informed by details of the scan strategy specific to each orientation of specimen, and the magnitude of the reduction in properties is given by iterative trials of the service loading simulation. The second phase of the approach is discussed further in 9.1.2.

9.1.1: THE FIRST PHASE OF THE USER-INFORMED CALIBRATION APPROACH

The User-Informed-Calibration Approach begins by defining a service loading simulation with the Baseline Material definition specified in Figure 85, the geometric definition of a 11-bending specimen shown in Figure 89, and the scan strategy shown in Table 2.1 and Table A.1. It should be noted that in order to generate the service loading simulation, the process of using the mesh-model generator must be followed, as detailed in 7.1.1 through 7.3.3. The steps for generating the two simulations “-heat” and “-disp” are followed, though the steps to post-process these two simulations may be skipped, as the “-heat” and “-disp” simulations are not executed. For rapid iterative trials, a coarse mesh is preferred for the mesh/model generator, with an element size that spans three raster-widths across the x-and-y-dimensions and 14 elements to cross the domain in the z-dimension. This mesh is shown in Figure 90.

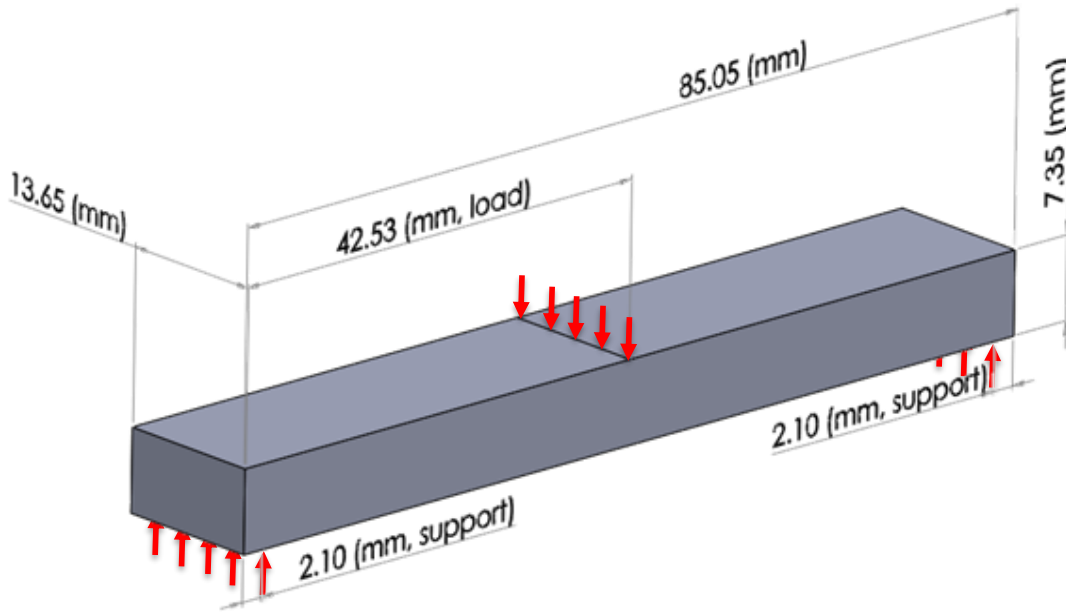


Figure 89: The geometry of the 3D-printed bending specimen
(depicting loads and overall dimensions; the same geometry applies to 11, 22, and 33 bending specimens)

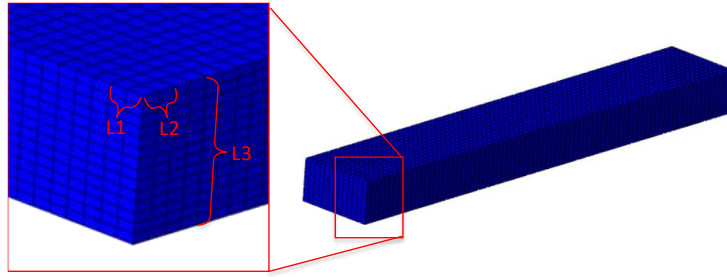


Figure 90: A depiction of the mesh for the 11-bending and 22-bending specimens

(L1=L2=2.1mm, L3=14 elements=7.35mm)

The service loading simulation is seen to produce an under-prediction of the 11-load-vs-deflection response, both in characteristic of elastic stiffness, and in characteristic of load-supporting capability. This gives rise to a dual material definition, with the first representing the compressive material on the top of the beam, and the second representing the tensile material on the bottom of the beam. The dual definition is done mainly to support the ability to prescribe different moduli in compression and tension. Further iterative trials of the service loading simulation reveal a stiffness of 3.5 GPa is necessarily specified to the compressive definition of E11, E22, and E33 in order for the dual definition to achieve a match to the load vs deflection response. The dual material definition is shown below, as Figure 91.

```

*MATERIAL, NAME = SPLY0001-VOID ** FOR COMPRESSIVE MATERIAL
*USER MATERIAL,CONSTANTS= 45
**      E11,      E22,      E33,      G12,      G13,      G23,      NU12,      NU13,
3.50E+09, 3.50E+09, 3.50E+09, 1.20E+09, 1.20E+09, 1.20E+09, 3.60E-01, 3.60E-01,
**      NU23,      S11T,      S11C,      S22T,      S22C,      S33T,      S33C,      S12S,
3.51E-01, 5.98E+07, 1.06E+08, 5.25E+07, 9.32E+07, 5.25E+07, 9.32E+07, 2.99E+07,
**      S13S,      S23S,      RHO,      DFACTT,      DFACTC,      DFACTS,      FFACT,      DAMAGE,
2.99E+07, 2.97E+01, 1.19E+03, 1.00E+00, 1.00E+00, 1.00E+00, 1.00E-01, 67109377,
**      FRACTURE,      EPS11T,      EPS11C,      EPS22T,      EPS22C,      EPS33T,      EPS33C,      EPS12S,
67109377, 1, 1, 1, 1, 1, 1, 1,
**      EPS23S,      EPS13S,      STRAIN_1,      STRESS_1,      STRAIN_2,      STRESS_2,      STRAIN_3,      STRESS_3,
1, 1, 0, 0, 4.591180E-03, 1.561074E+07, 1.160373E-02, 3.761987E+07,
**      STRAIN_4,      STRESS_4,      STRAIN_5,      STRESS_5,      MUP,
1.456068E-02, 4.534584E+07, 1.857702E-02, 5.302805E+07, 0,
*DEPVAR
6
*DENSITY
1.250000E+07
*MATERIAL, NAME = SPLY0002-VOID ** FOR TENSILE MATERIAL
*USER MATERIAL,CONSTANTS= 45
**      E11,      E22,      E33,      G12,      G13,      G23,      NU12,      NU13,
3.27E+09, 3.29E+09, 3.44E+09, 1.20E+09, 1.20E+09, 1.20E+09, 3.60E-01, 3.60E-01,
**      NU23,      S11T,      S11C,      S22T,      S22C,      S33T,      S33C,      S12S,
3.51E-01, 5.98E+07, 1.06E+08, 5.25E+07, 9.32E+07, 5.25E+07, 9.32E+07, 2.99E+07,
**      S13S,      S23S,      RHO,      DFACTT,      DFACTC,      DFACTS,      FFACT,      DAMAGE,
2.99E+07, 2.97E+01, 1.19E+03, 1.00E+00, 1.00E+00, 1.00E+00, 1.00E-01, 67109377,
**      FRACTURE,      EPS11T,      EPS11C,      EPS22T,      EPS22C,      EPS33T,      EPS33C,      EPS12S,
67109377, 1, 1, 1, 1, 1, 1, 1,
**      EPS23S,      EPS13S,      STRAIN_1,      STRESS_1,      STRAIN_2,      STRESS_2,      STRAIN_3,      STRESS_3,
1, 1, 0, 0, 4.591180E-03, 1.561074E+07, 1.160373E-02, 3.761987E+07,
**      STRAIN_4,      STRESS_4,      STRAIN_5,      STRESS_5,      MUP,
1.456068E-02, 4.534584E+07, 1.857702E-02, 5.302805E+07, 0,
*DEPVAR
6
*DENSITY
1.250000E+07

```

Figure 91: A dual definition, separating the compressive definition from the tensile definition

(Tensile material is used on the bottom of the beam, and compressive material is used on the top)

An iterative process of modifying the stress-strain response and re-running the service loading simulation is performed next. This iterative process is performed toward the target of matching the simulated load vs deflection to the empirically-derived load-vs-deflection. This iterative process is suggested to be most efficiently conducted by first elevating the tensile and compressive strength to levels that will not allow failure to occur until an unrealistically high peak load, for example, $S11T=1.0E+08$, $S11C=1.50E+08$. Next, each point on the stress-strain curve is iteratively modified, targeting a match to lower portions of the curve with earlier iterations, and building toward matching upper portions of the curve with later iterations. In the final stages of the iterative process, the values of $S11T$ and $S11C$ are iteratively lowered such that a peak load is predicted both in the correct

magnitude and the correct characteristic. In the case of this specimen, the response is tensile-dominated, so the value of S11T must be specified such that tensile failure is seen to occur at a peak load of 645 N, and S11C must be specified such that compressive failure does not occur prior to that load state. Several examples of these iterative trials are shown below, in Figure 92, where the line labeled: “11-EXP” shows the response of the empirical bending result. The line labeled: “11-SIM, FIRST TRIAL” shows the under-prediction using the material definition shown in Figure 85. The line “11-SIM, DUAL DEFINITION 1” matches the 3rd point of 5 in the stress-strain curve definition. The line “11-SIM, DUAL DEFINITION 2” matches the 4th point of 5 in the stress-strain curve definition. The line “11-SIM, DUAL DEFINITION 3” matches the 5th point of 5 in the stress-strain curve definition. The line “11-SIM, FINAL TRIAL” matches the ultimate tensile strength, S11T, to a value of 75 MPa, and bounds the value of ultimate strength in compression above 110 MPa, below which compressive-dominated failure is seen to occur on the top of the specimen.

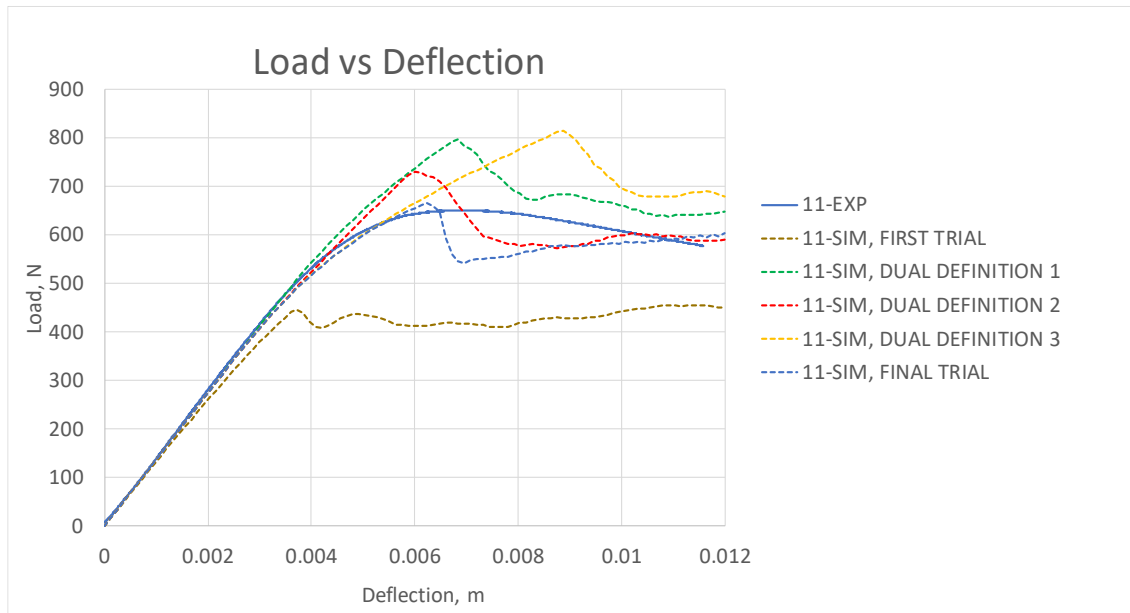


Figure 92: Iterative trials given by adjusting the stress-strain response of the bending simulation

The process then follows to define a 3-point bending simulation for a 22-specimen, as given by the raster strategy shown below in, and the mesh strategy shown in Figure 90 .

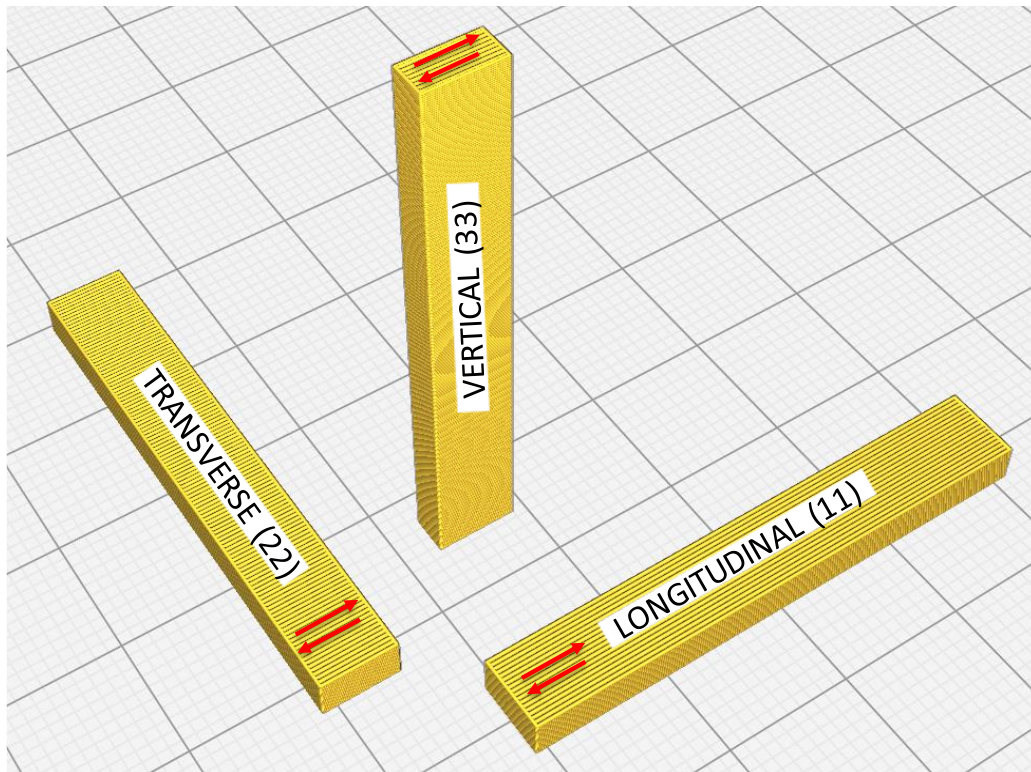


Figure 93: Depiction of raster strategies for 11, 22, and 33 bending specimens

This process begins with the material definition that gave rise to the line “11-SIM, FINAL TRIAL” in Figure 92, and aims to achieve a matching 22 response by running iterative service loading simulation trials, adjusting only the values of S22T and S22C. The process then continues to define a 3-point bending simulation for a 33-specimen, as given by the raster strategy shown in Figure 78, and the mesh strategy shown below, as Figure 94.

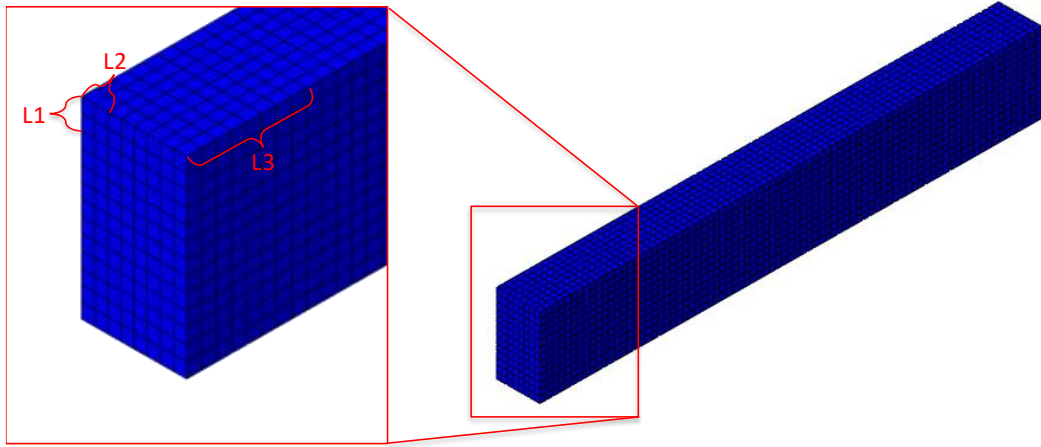


Figure 94: A depiction of the mesh for the 33-bending specimen
($L1=L2=2.1\text{mm}$, $L3=8\text{ elements}=8.4\text{mm}$)

Similar to the approach executed for the matching of the 22-bending specimen, the process of matching the 33-bending specimen begins with the material definition concluded following the definition of S22T and S22C, and aims to achieve a matching 33 response by adjusting only the values of S33T and S33C. Matching the 22 bending response and the 33 bending response gives rise to the final Baseline Material definition, and the load-vs-deflection response shown below, as Figure 95.

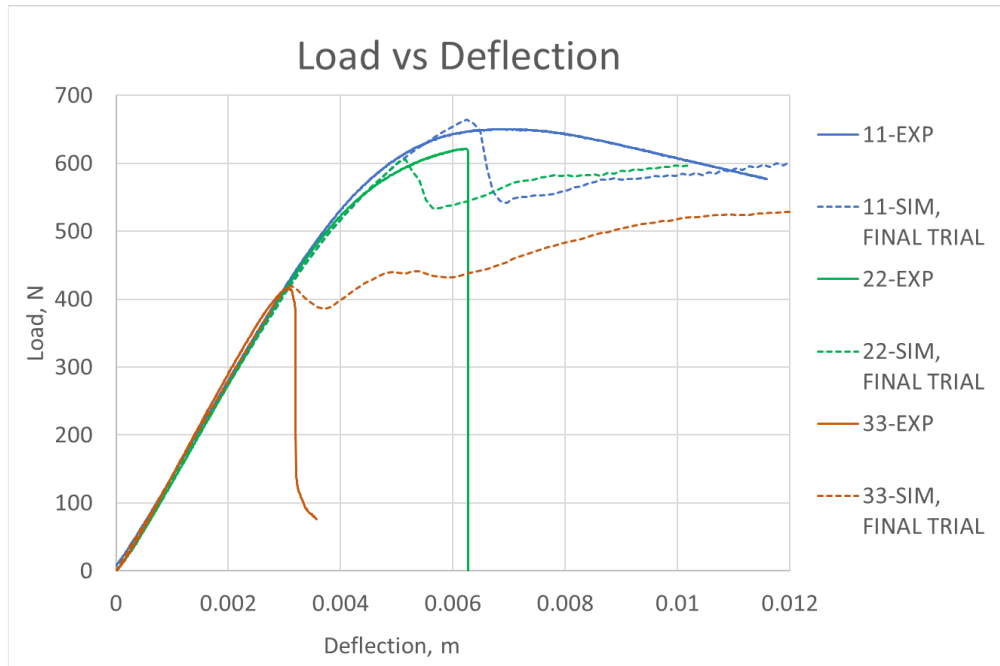


Figure 95: The Load vs Deflection response given by calibration to 11, 22, and 33 bending data

9.1.2: THE SECOND PHASE OF THE USER-INFORMED CALIBRATION APPROACH

The second phase of the User-Informed Calibration approach aims to match tensile responses in the 3 studied printing orientations given by Figure 10. The procedure of matching a tensile response begins by applying the tensile portion of the final Baseline Material definition to tensile specimen geometries for 11, 22, and 33 orientations. Next, a pattern of defective material with degraded properties is introduced to each tensile specimen, with the defective material pattern being specific to the scan strategy employed to print each orientation of tensile specimen. Next, the iterative service loading simulation is run toward the goal of determining the level of property degrade that must be necessarily introduced to achieve a match to empirical tensile data for each orientation of specimen.

Prior to beginning the second phase of the approach, a service loading simulation must be defined, requiring a complete definition of a geometry, a mesh, a scan strategy, a material definition, and a defective region. The geometry is defined as shown below, in Figure 96.

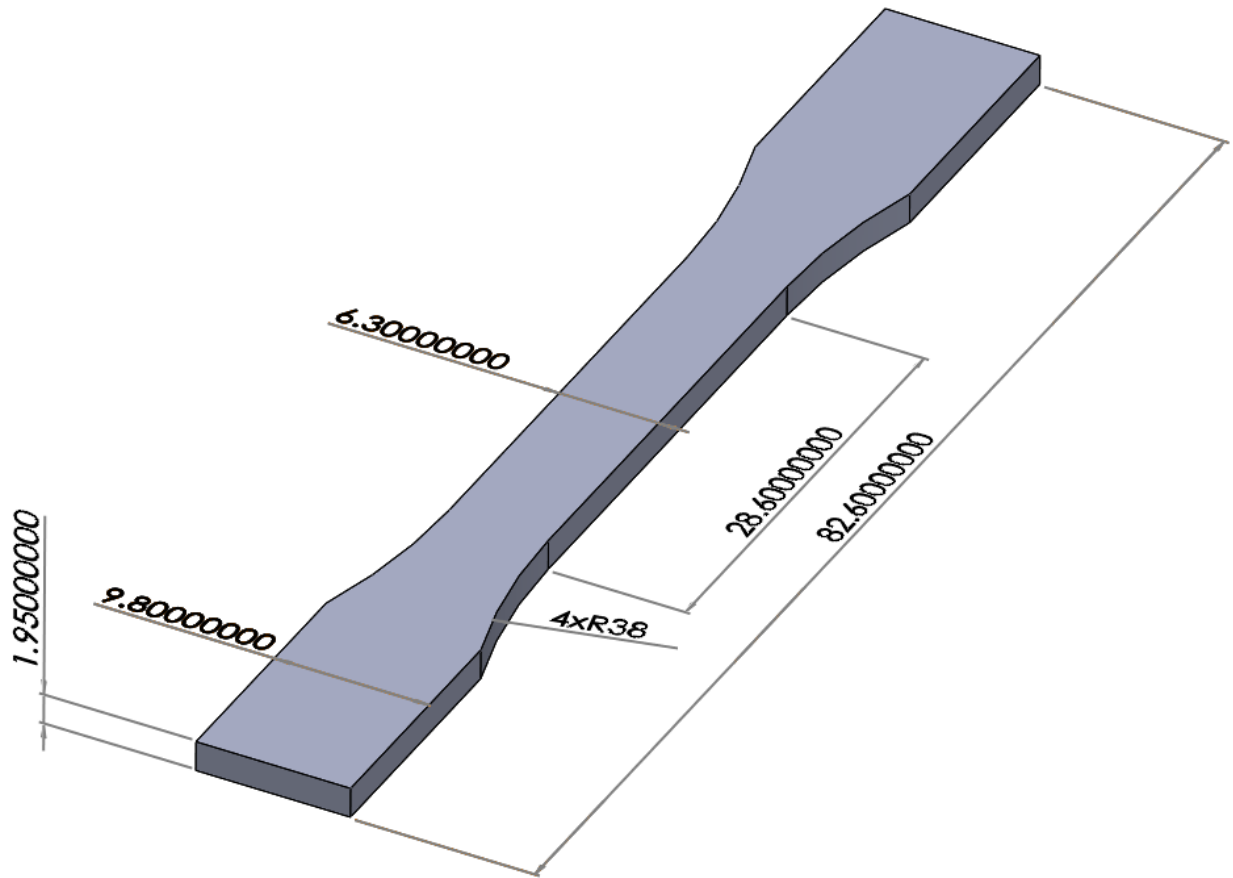


Figure 96: The geometry used to match the 11, 22, and 33 tensile response
(Given the User-Informed Calibration approach)

As with the bending simulations in 9.1.1, the same mesh for tensile specimen geometries is seen to be compatible with 11 and 22 tensile specimen simulations, and the mesh differs in orientation for the 33 tensile specimen simulation. The mesh used for the 11 and 22 tensile specimen was generated with the

partitioning and meshing strategy shown in APPENDIX A, save for that a global seed size of 1.05 mm was preferred. The scan strategy follows the settings shown in Table 2.1 and Table A.1.

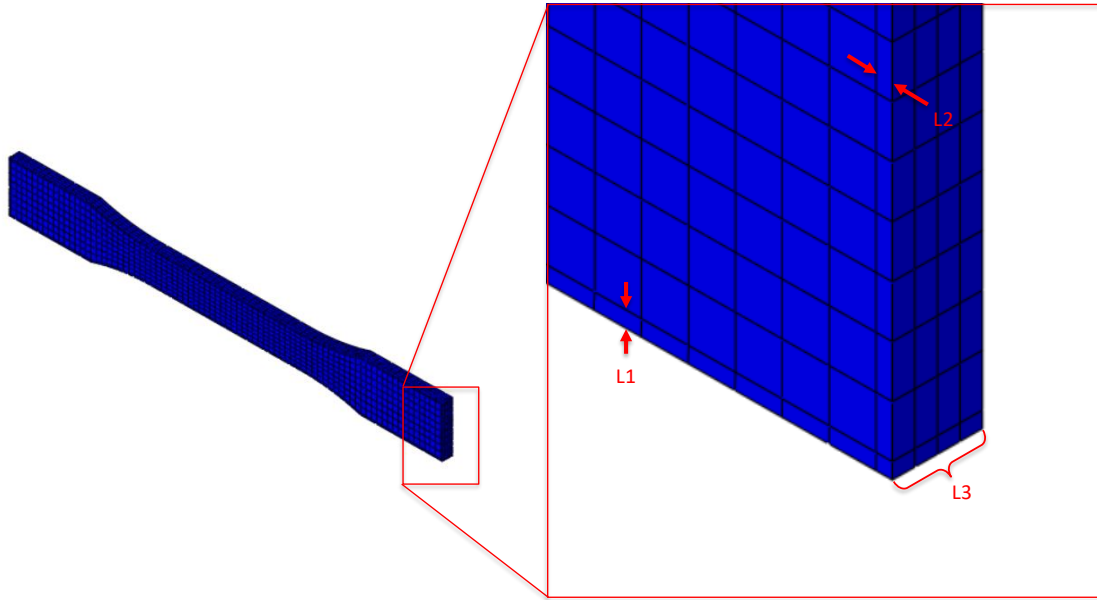


Figure 97: A depiction of the mesh strategy for 11 and 22 tensile specimen

(Given the User-Informed Calibration approach, global seed size=1.05mm, L1=L2=0.35 mm, L3=1.95 mm)

To define the material properties in the tensile simulation, a dual material definition is provided to the service loading simulation. The dual definition used for the tensile simulations is similar in format to the dual definition employed for the bending simulation. However, the purpose of 1st part of the dual definition in the tensile simulation is to represent the properties of the majority of the specimen save for the defective region. The purpose of the 2nd part of the dual definition in the tensile simulation is to represent the properties of the defective region. The dual definition used for the first trial of the 11-tensile specimen simulation is shown below, as Figure 98.

```

*MATERIAL, NAME = SPLY0001-VOID
*USER MATERIAL,CONSTANTS= 45
**      E11,      E22,      E33,      G12,      G13,      G23,      NU12,      NU13,
3.27E+09,  3.29E+09,  3.44E+09,  1.20E+09,  1.20E+09,  1.20E+09,  3.54E-01,  3.54E-01,
**      NU23,      S11T,      S11C,      S22T,      S22C,      S33T,      S33C,      S12S,
3.54E-01,  7.50E+07,  1.38E+08,  7.30E+07,  1.38E+08,  5.70E+07,  1.38E+08,  4.28E+07,
**      S13S,      S23S,      RHO,      DFACTT,      DFACTC,      DFACTS,      FFACT,      DAMAGE,
4.28E+07,  4.28E+07,  1.25E+03,  1.00E+00,  1.00E+00,  1.00E+00,  1.00E-01,  67109377,
**      FRACTURE,  EPS11T,      EPS11C,      EPS22T,      EPS22C,      EPS33T,      EPS33C,      EPS12S,
67109377,  1,      1,      1,      1,      1,      1,      1,
**      EPS23S,      EPS13S,      STRAIN_1,      STRESS_1,      STRAIN_2,      STRESS_2,      STRAIN_3,      STRESS_3,
1,      1,      0.00E+00,  0.00E+00,  1.53E-02,  4.58E+07,  2.25E-02,  6.06E+07,
**      STRAIN_4,      STRESS_4,      STRAIN_5,      STRESS_5,      MUP,
3.72E-02,  7.20E+07,  8.01E-02,  7.80E+07,  0.00E+00,
*DEPVAR
6
*DENSITY
1.250000E+07
*MATERIAL, NAME = SPLY0002-VOID
*USER MATERIAL,CONSTANTS= 45
**      E11,      E22,      E33,      G12,      G13,      G23,      NU12,      NU13,
3.27E+09,  3.29E+09,  3.44E+09,  1.20E+09,  1.20E+09,  1.20E+09,  3.54E-01,  3.54E-01,
**      NU23,      S11T,      S11C,      S22T,      S22C,      S33T,      S33C,      S12S,
3.54E-01,  7.50E+07,  1.38E+08,  7.30E+07,  1.38E+08,  5.70E+07,  1.38E+08,  4.28E+07,
**      S13S,      S23S,      RHO,      DFACTT,      DFACTC,      DFACTS,      FFACT,      DAMAGE,
4.28E+07,  4.28E+07,  1.25E+03,  1.00E+00,  1.00E+00,  1.00E+00,  1.00E-01,  67109377,
**      FRACTURE,  EPS11T,      EPS11C,      EPS22T,      EPS22C,      EPS33T,      EPS33C,      EPS12S,
67109377,  1,      1,      1,      1,      1,      1,      1,
**      EPS23S,      EPS13S,      STRAIN_1,      STRESS_1,      STRAIN_2,      STRESS_2,      STRAIN_3,      STRESS_3,
1,      1,      0.00E+00,  0.00E+00,  1.53E-02,  4.58E+07,  2.25E-02,  6.06E+07,
**      STRAIN_4,      STRESS_4,      STRAIN_5,      STRESS_5,      MUP,
3.72E-02,  7.20E+07,  8.01E-02,  7.80E+07,  0.00E+00,
*DEPVAR
6
*DENSITY
1.250000E+07

```

Figure 98: The material definition used for the first trial of matching a 11-tension

(SPLY0001 represents the properties of all material save the defective region, SPLY0002 represents the properties of the defective region)

To define the defective region, the scan strategy for each orientation is assessed for where infill raster patterns are seen to overlap with perimeter raster patterns. This is seen to differ depending upon the orientation, as, of course, does the scan strategy. The assumed defective region for each orientation of specimen is shown below, as Figure 99, noting that the defective region is expected to extend through the thickness of each specimen, in the direction normal to the page in Figure 99.

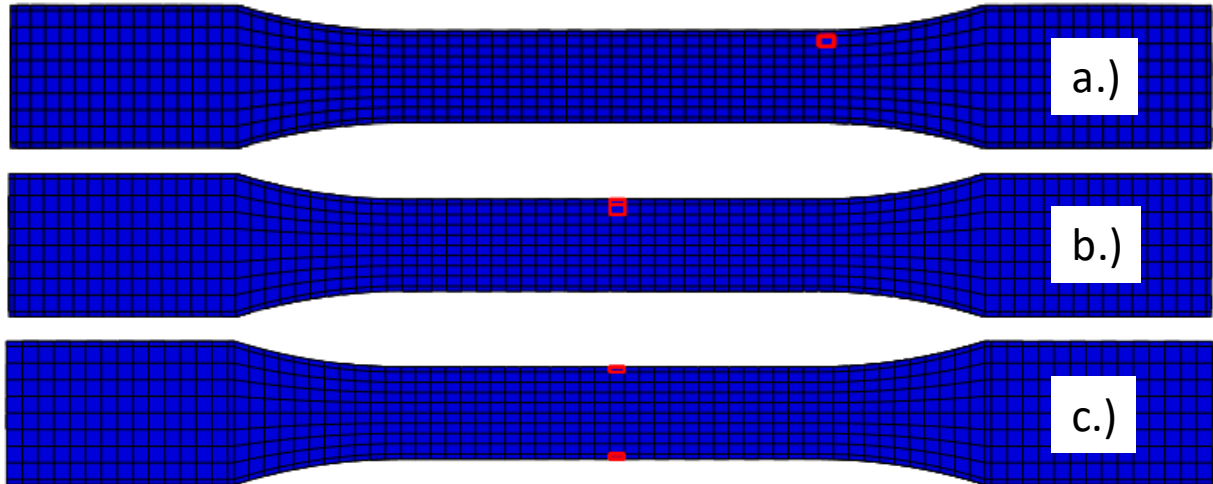


Figure 99: the defective region assumed to exist given the details of the scan strategy
(Shown for: a.) a 11-tensile specimen, b.) a 22-tensile specimen, and c.) a 33-tensile specimen)

The second phase of the User-Informed Calibration approach is performed next, by executing trials of the service loading simulation for each orientation. The 11-simulated tensile response is matched by iteratively lowering the value of S_{11T} in the defective material properties, the same process is conducted on the basis of lowering S_{22T} to achieve a match to a 22-simulated tensile response, and similarly again the value of S_{33T} may be lowered to match a 33-simulated tensile response. Matching these three tests gives rise to the stress-strain responses for the various orientations shown below, as Figure 100, Figure 101, and Figure 102. Matching these three tests gave rise to defective material definitions with S_{11T} , S_{22T} , and S_{33T} values of 60 MPa, 30 MPa, and 47 MPa, respectively. The results are discussed further in 9.2.

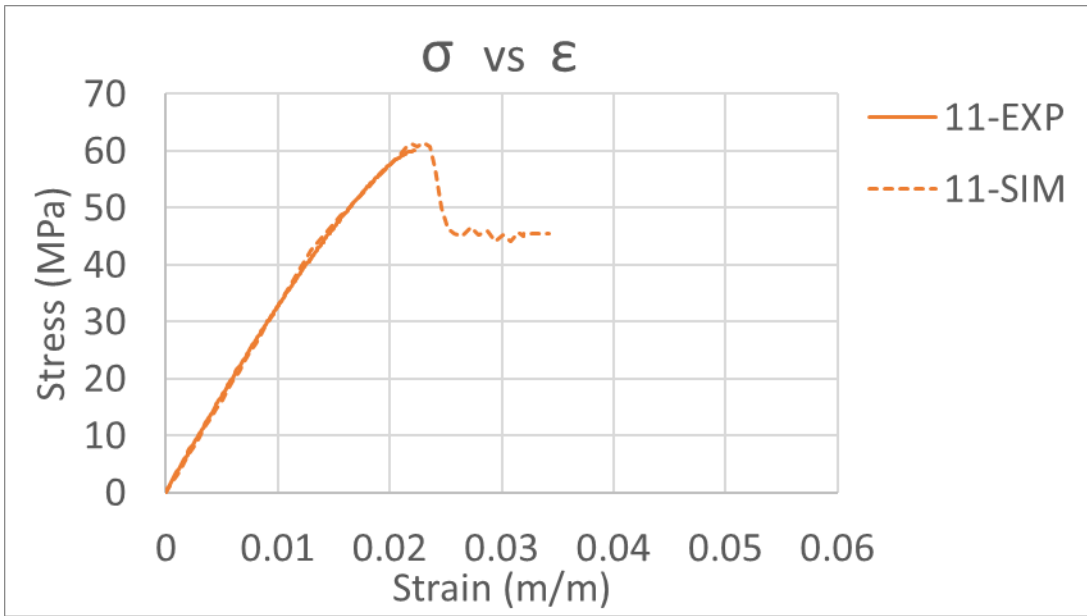


Figure 100: The simulated 11-tensile response given the User-Informed Calibration Approach

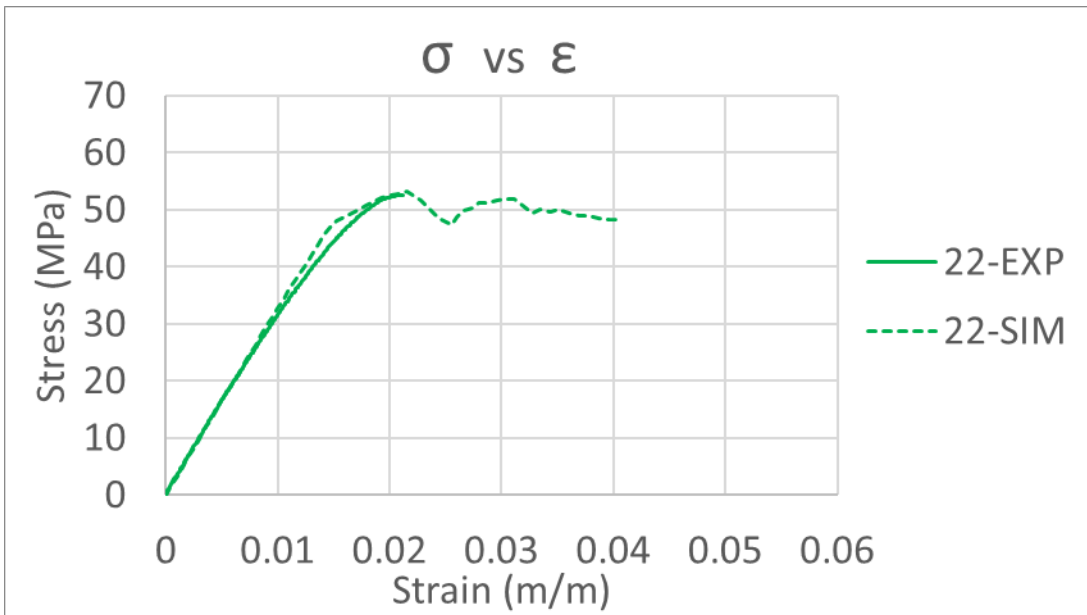


Figure 101: The simulated 22-tensile response given the User-Informed Calibration Approach

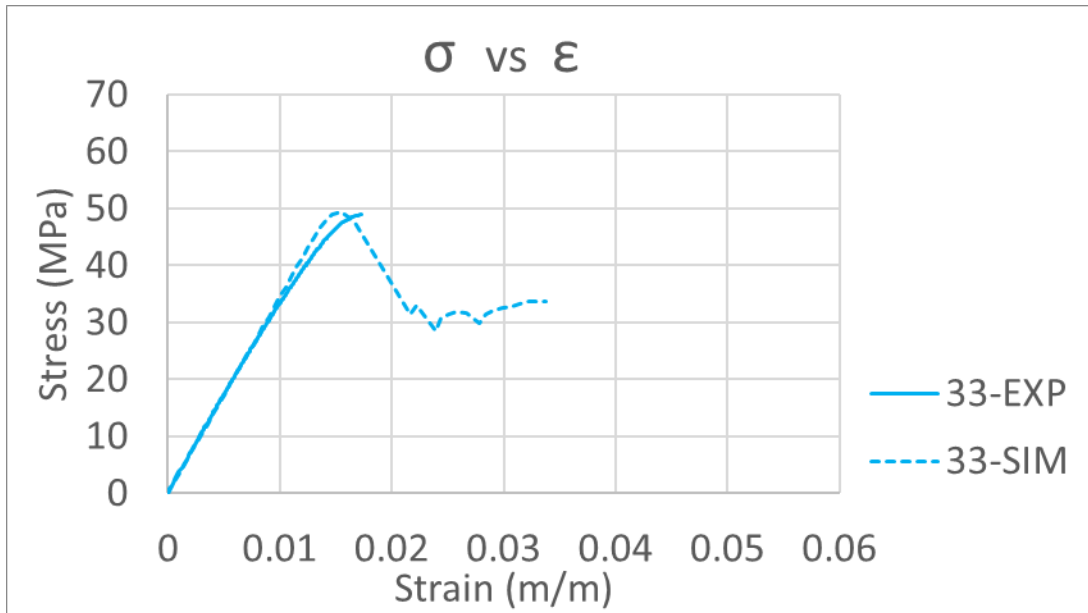


Figure 102: The simulated 33-tensile response given the User-Informed Calibration Approach

9.2: RESULTS AND DISCUSSION OF THE USER-INFORMED CALIBRATION APPROACH

The User-Informed Calibration Approach aimed to match 6 tests in this work, 3 bending tests, and 3 tensile tests. The load vs deflection test result for both empirical and simulated bending tests is shown in Figure 103 (Same as Figure 95). Following the load vs deflection test result, a comparison of empirical tensile data to simulated tensile results is presented for 11, 22, and 33 raster orientations, as Figure 104. Given the nature of the User-Informed Calibration approach, the material definition itself may be reasoned to be the result that arises from this strategy. As such, the final material definition for both a simulation configured for bending prediction and a simulation configured for tensile prediction are presented following, as Figure 105 and Figure 106. Following the logic of the fourth recommendation cited toward the end of section 5.4, an equivalent strategy to match a tensile response should have been to provide PathCoverage with the modified Baseline Material definition after calibrating to a bending test, proceed to run PathCoverage, thereby introducing an end-of-raster void result, and the

reserve mechanical response obtained in a tensile service loading simulation should match an empirical tensile result. This equivalent strategy was not performed due to the assessment that PathCoverage treats voids equally regardless of raster orientation, and therefore fundamentally lacks the ability to match all three orientations of tensile response. This assessment is further supported in 9.2.1. Following the discussion of PathCoverage, a discussion of overall results of the User-Informed-Calibration Approach is presented in 9.2.2.

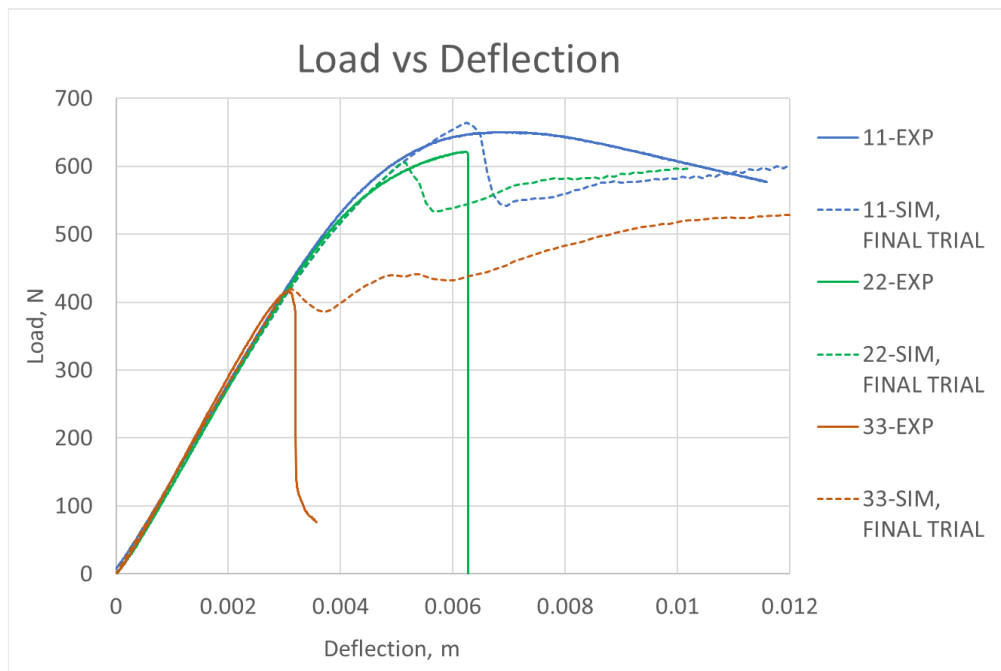


Figure 103: The Load vs Deflection response for both simulated and empirical bending specimens (11, 22, and 33, bending specimens shown, raster strategy shown in Figure 93)

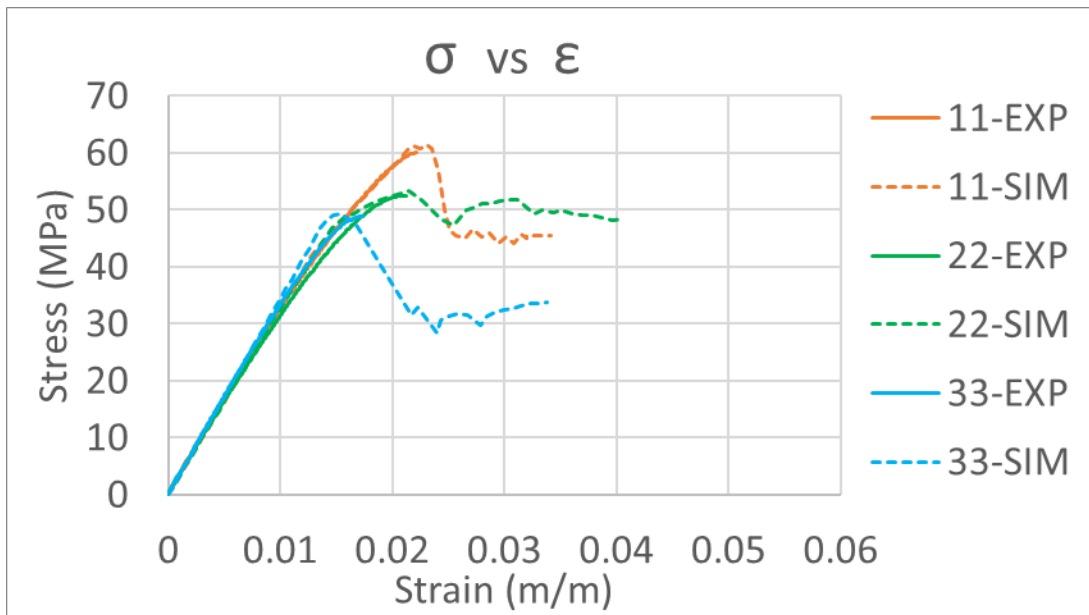


Figure 104: The Stress vs Strain response for both simulated and empirical tensile specimens (Given 11-, 22-, and 33-oriented infill raster patterns and a scan strategy with one perimeter raster, infill raster strategy shown in Figure 10)

```

***** CONFIGURED FOR BENDING SIMULATION
** ABAQUS GENOA UMAT PROPPERTIES (created by GENOA-MCQ) ** SPLY0001-VOID is for compression,
***** SPLY0002-VOID is for tension
***INCLUDE, INPUT=ElementVoidRatio_ABAQUS_Explicit_Run1.inp
*MATERIAL, NAME=SPLY0001-VOID
*USER MATERIAL,CONSTANTS= 45
**
**      E11,      E22,      E33,      G12,      G13,      G23,      NU12,      NU13,
**      3.50E+09,  3.50E+09,  3.50E+09,  1.20E+09,  1.20E+09,  1.20E+09,  3.54E-01,  3.54E-01,
**      NU23,      S11T,      S11C,      S22T,      S22C,      S33T,      S33C,      S12S,
**      3.54E-01,  7.50E+07,  1.38E+08,  7.30E+07,  1.38E+08,  5.70E+07,  1.38E+08,  4.28E+07,
**      S13S,      S23S,      RHO,      DFACTT,      DFACTC,      DFACTS,      FFACT,      DAMAGE,
**      4.28E+07,  4.28E+07,  1.25E+03,  1.00E+00,  1.00E+00,  1.00E+00,  1.30E-01,  67109377,
**      FRACTURE,  EPS11T,      EPS11C,      EPS22T,      EPS22C,      EPS33T,      EPS33C,      EPS12S,
**      67109377,  1,      1,      1,      1,      1,      1,      1,
**      EPS23S,      EPS13S,      STRAIN_1,      STRESS_1,      STRAIN_2,      STRESS_2,      STRAIN_3,      STRESS_3,
**      1,      1,      0.00E+00,  0.00E+00,  1.53E-02,  4.58E+07,  2.25E-02,  6.06E+07,
**      STRAIN_4,      STRESS_4,      STRAIN_5,      STRESS_5,      MUP,
**      3.72E-02,  7.20E+07,  8.01E-02,  7.80E+07,  0.00E+00,
*DEPVAR
6
*DENSITY
1.250000E+07
*MATERIAL, NAME = SPLY0002-VOID
*USER MATERIAL,CONSTANTS= 45
**
**      E11,      E22,      E33,      G12,      G13,      G23,      NU12,      NU13,
**      3.27E+09,  3.29E+09,  3.44E+09,  1.20E+09,  1.20E+09,  1.20E+09,  3.54E-01,  3.54E-01,
**      NU23,      S11T,      S11C,      S22T,      S22C,      S33T,      S33C,      S12S,
**      3.54E-01,  7.50E+07,  1.38E+08,  7.30E+07,  1.38E+08,  5.70E+07,  1.38E+08,  4.28E+07,
**      S13S,      S23S,      RHO,      DFACTT,      DFACTC,      DFACTS,      FFACT,      DAMAGE,
**      4.28E+07,  4.28E+07,  1.25E+03,  1.00E+00,  1.00E+00,  1.00E+00,  1.30E-01,  67109377,
**      FRACTURE,  EPS11T,      EPS11C,      EPS22T,      EPS22C,      EPS33T,      EPS33C,      EPS12S,
**      67109377,  1,      1,      1,      1,      1,      1,      1,
**      EPS23S,      EPS13S,      STRAIN_1,      STRESS_1,      STRAIN_2,      STRESS_2,      STRAIN_3,      STRESS_3,
**      1,      1,      0.00E+00,  0.00E+00,  1.53E-02,  4.58E+07,  2.25E-02,  6.06E+07,
**      STRAIN_4,      STRESS_4,      STRAIN_5,      STRESS_5,      MUP,
**      3.72E-02,  7.20E+07,  8.01E-02,  7.80E+07,  0.00E+00,
*DEPVAR
6
*DENSITY
1.250000E+07

```

Figure 105: The final material definition configured for prediction of a bending response

```

***** CONFIGURED FOR TENSILE SIMULATION
** ABAQUS GENOA UMAT PROPPERTIES (created by GENOA-MCQ) ** SPLY0001-VOID for regular,
***** SPLY0002-VOID for defective region
***INCLUDE, INPUT=ElementVoidRatio_ABAQUS_Explicit_Run1.inp
*MATERIAL, NAME = SPLY0001-VOID
*USER MATERIAL,CONSTANTS= 45
**      E11,      E22,      E33,      G12,      G13,      G23,      NU12,      NU13,
**      3.27E+09,  3.29E+09,  3.44E+09,  1.20E+09,  1.20E+09,  1.20E+09,  3.54E-01,  3.54E-01,
**      NU23,      S11T,      S11C,      S22T,      S22C,      S33T,      S33C,      S12S,
**      3.54E-01,  7.50E+07,  1.38E+08,  7.30E+07,  1.38E+08,  5.70E+07,  1.38E+08,  4.28E+07,
**      S13S,      S23S,      RHO,      DFACT,      DFACTC,      DFACTS,      FFACT,      DAMAGE,
**      4.28E+07,  4.28E+07,  1.25E+03,  1.00E+00,  1.00E+00,  1.00E+00,  1.00E-01,  67109377,
**      FRACTURE,  EPS11T,  EPS11C,  EPS22T,  EPS22C,  EPS33T,  EPS33C,  EPS12S,
**      67109377,  1,      1,      1,      1,      1,      1,      1,
**      EPS23S,  EPS13S,  STRAIN_1,  STRESS_1,  STRAIN_2,  STRESS_2,  STRAIN_3,  STRESS_3,
**      1,      1,      0.00E+00,  0.00E+00,  1.53E-02,  4.58E+07,  2.25E-02,  6.06E+07,
**      STRAIN_4,  STRESS_4,  STRAIN_5,  STRESS_5,      MUP,
**      3.72E-02,  7.20E+07,  8.01E-02,  7.80E+07,  0.00E+00,
*DEPVAR
6
*DENSITY
1.250000E+07
*MATERIAL, NAME = SPLY0002-VOID
*USER MATERIAL,CONSTANTS= 45
**      E11,      E22,      E33,      G12,      G13,      G23,      NU12,      NU13,
**      3.27E+09,  3.29E+09,  3.44E+09,  1.20E+09,  1.20E+09,  1.20E+09,  3.54E-01,  3.54E-01,
**      NU23,      S11T,      S11C,      S22T,      S22C,      S33T,      S33C,      S12S,
**      3.54E-01,  6.00E+07,  1.38E+08,  3.00E+07,  1.38E+08,  4.70E+07,  1.38E+08,  4.28E+07,
**      S13S,      S23S,      RHO,      DFACT,      DFACTC,      DFACTS,      FFACT,      DAMAGE,
**      4.28E+07,  4.28E+07,  1.25E+03,  1.00E+00,  1.00E+00,  1.00E+00,  1.00E-01,  67109377,
**      FRACTURE,  EPS11T,  EPS11C,  EPS22T,  EPS22C,  EPS33T,  EPS33C,  EPS12S,
**      67109377,  1,      1,      1,      1,      1,      1,      1,
**      EPS23S,  EPS13S,  STRAIN_1,  STRESS_1,  STRAIN_2,  STRESS_2,  STRAIN_3,  STRESS_3,
**      1,      1,      0.00E+00,  0.00E+00,  1.53E-02,  4.58E+07,  2.25E-02,  6.06E+07,
**      STRAIN_4,  STRESS_4,  STRAIN_5,  STRESS_5,      MUP,
**      3.72E-02,  7.20E+07,  8.01E-02,  7.80E+07,  0.00E+00,
*DEPVAR
6
*DENSITY
1.250000E+07

```

Figure 106: The final material definition configured for prediction of a tensile response

9.2.1: DISCUSSION REGARDING PATHCOVERAGE

After calibrating the Baseline material definition to the bending load cases, but unlike the Default approach that uses PathCoverage to introduce the end-of-raster void effects, an iterative approach was conducted to match the various orientations of tensile response. A brief series of trials were conducted on the basis of testing a theory that PathCoverage was treating all voids as contributing an equivalent detrimental effect. These trials consisted of logic presented in a graphical interface being very consistent with the void ratio results which were seen to be reported by the interface. Shown below is a screenshot of the PathCoverage interface, as Figure 107.

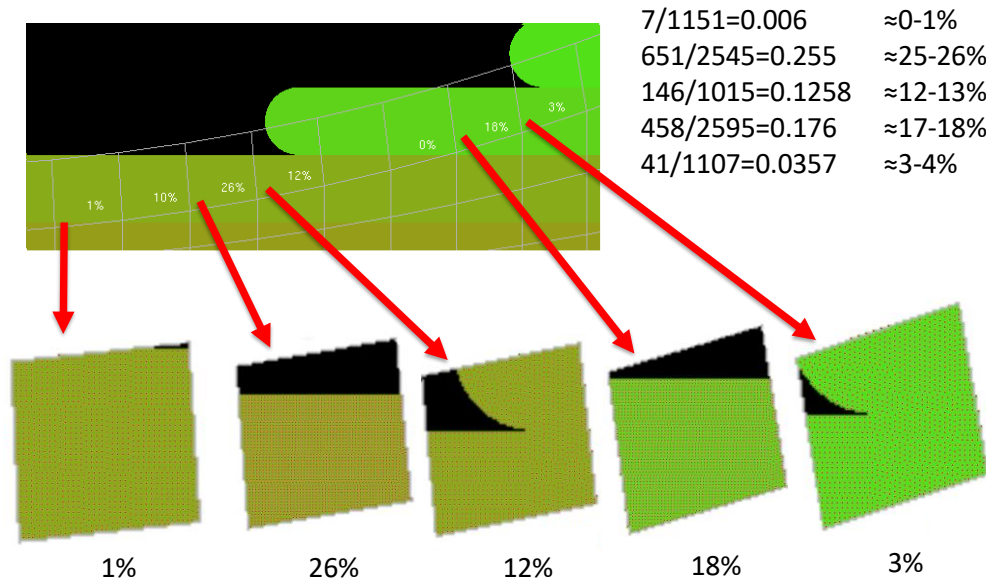


Figure 107: Screenshot of PathCoverage interface, isolating results of 5 elements

(The fractions in the upper left indicate the ratio of points seen to fill the black region of each element to the number of points seen to fill the entire element)

In Figure 107, the five elements shown were isolated from the interface, trimmed to a clean boundary with a paint tool, and analyzed with a plot digitizer. From the readout with the plot digitizer, on the basis of filled-to-void ratio, it was determined that the graphical readout was consistent to a reasonable level of certainty with the reported void result. Next, the void result was traced to the file generated by PathCoverage, giving rise to the screenshot shown below, as Figure 108.

```

ELEMENT 1012
a.) → 0.00000E+00 0.0947247 ← c.)
b.) → 1.00000E+05 0.0947247 ← d.)
ELEMENT 1013
0.00000E+00 0.0853014
1.00000E+05 0.0853014

```

Figure 108: Structure of the PathCoverage readout

In Figure 108, it was determined that both a.) and b.) were repetitions of the same static value for each line, and that c.) and d.) were simply repetitions of the void ratio result being reported specific to each element. From this evaluation of file structure, it was determined that PathCoverage is essentially passing a 1-dimensional array of scalar values to evaluate end-of-raster void effect.

To confirm this theory, a readout of void ratio was mimicked, and was prescribed to series of uniaxial service loading tension simulations, conducted on a small scale rectangular bar geometry. The series of simulations were first conducted on the basis of 11-direction raster orientation, as shown in Figure 109a, then, the series of simulations were repeated on the basis of 22-direction raster orientation, as shown in Figure 109b. A schematic of the test performed is shown following, as Figure 110. The results of the performed tests were then normalized to each orientations respective failure load at 0% void, and plotted on a chart depicting normalized failure load vs. void percentage. This is shown in Figure 111.

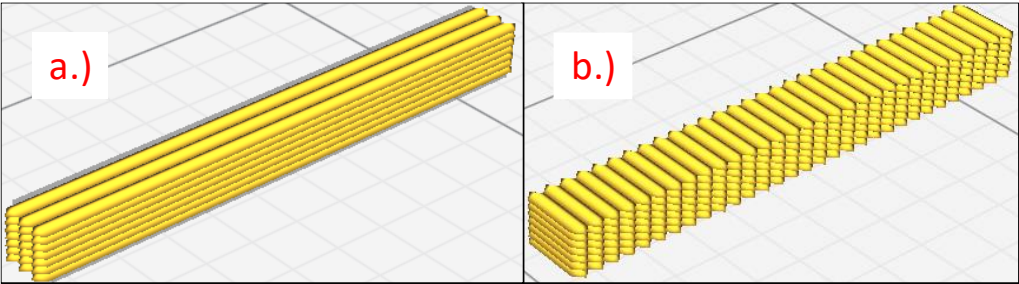


Figure 109: Raster orientations for uniaxial service loading trials

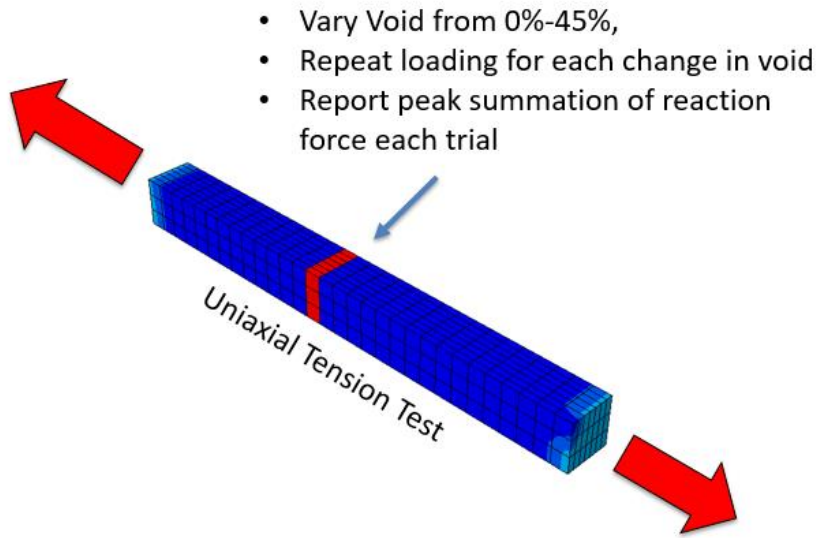


Figure 110: A schematic of the uniaxial service loading simulation to test void result

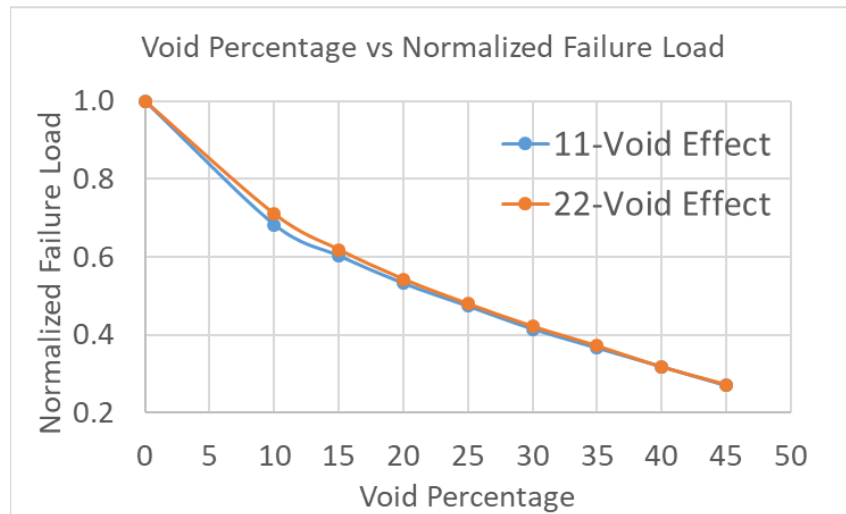


Figure 111: The result of varying void on normalized strength across a rectangular section

From the result shown Figure 111, it was concluded that PathCoverage is essentially treating all voids as inducing an equivalent end-of-raster-void effect. Comparing this to the result of the second phase of the User-Informed-Calibration Approach, it may be seen that a much more prevalent defect in the 22-direction is necessary to match tension after first calibrating the baseline definition to bending. This assessment is illustrated by defining a ratio of the magnitude of the tensile defect necessary to match

tension to the magnitude of the tensile baseline material definition. This ratio is defined for each orientation, and is shown below, as Figure 112.

		Orientation		
		11	22	33
Tensile-Defect	=	0.80	0.41	0.82
<hr style="width: 100%; border: 0.5px solid black; margin-bottom: 2px;"/> Tensile-Baseline				

Figure 112: Tensile defect magnitude over tensile baseline magnitude for various orientations

The conclusion made from standing the result of Figure 111 against the result shown in Figure 112 was that voids are being treated as “equal”, where they apparently need to be given a much more prevalent effect when occurring across parting boundaries of 22-tensile loading.

9.2.2: DISCUSSION REGARDING THE USER-INFORMED CALIBRATION APPROACH

A key value of numerical simulation is in the ability to make blind predictions. Whether one chooses to reference the Default Approach, or the User-Informed Calibration approach, it is clear that a blind prediction is not what has been done here.

The other concept to consider is that the finite element method is an imperfect method itself. As such, any approach which aims to build a formulation upon the finite element method, and in doing so, aims to arrive at a matching test result, that approach will ultimately have to absorb the discrepancies of both the formulation and the finite method itself in order to arrive at matching results. Any such approach

would fundamentally need to have a means of resolving, estimating or mitigating the discrepancies from the finite element method, or such a matching result might be impossible to achieve.

For example, throughout section 8.1, much of the discussion revolves around how to best select a mesh technique for a tensile specimen absent a perimeter raster. Several techniques are overviewed for their worthiness; the internal mesh feature produces a mesh demonstrating non-convergent behavior in Figure 75. The external mesh feature relies on the user to specify a mesh, but depending upon the definition of the mesh boundaries defined by the user, the pattern and magnitude of the voids predicted by PathCoverage are seen to entirely govern the result in Figure 77 and Figure 84. The limitations associated with the internal and external mesh techniques in conjunction lead to only one reasonable conclusion: one cannot expect to capture the behavior of a sharp-cornered domain. The only path that might prove a fruitful way to advert this limitation is the investigation of a means to build a mesh that is strategically built in an arbitrary fashion to arrive at a reasonable answer. However, such a path would need to begin with the most basic pieces and parts, the mesh and the G-code. Dependence on a particular slicer (i.e., Slic3r, Cura), followed by a compensation overlay (PathCoverage) with insufficient level of fidelity in capturing the end of raster effects offer an opportunity for future developments in support of process-structure-property modeling in additive manufacturing in general and FFF in particular.

Chapter 10: CONCLUSION

In the scope of this work, AM FFF tensile specimens were printed using a strategy that generally sought to pursue the improvement of ultimate strength in tensile loading. Nearly 300 tensile specimens were printed in an effort to explore the effects of process-structure-property-performance relationships. Exploring these relations involved a range of strategies, from modifying one-factor-at-a-time, to conducting a DOE on a combination of process parameters. In addition to the development of understanding of the material, there was also significant development of the printing process itself, as well as the testing strategy. Refinement of the printing strategy sought to create a consistent, repeatable specimen that would minimize defects, and refinement of the testing strategy sought to create a test procedure that would minimize sources of inconsistency in data capture. Once the printing process was defined to a reasonable level of refinement, a strategy for simulating the printing process was explored, which generally sought to inform a material definition in an ABAQUS UMAT with 3D-printed tensile specimen test data, as well as several other test data sources from literature. The process of simulating the printing process aimed to capture the process-structure-property-performance relationships in the net contribution of three main detrimental effects: homogenized voids, residual stress, and end-of-raster voids. These three detrimental effects were imposed on a neat material definition which was found to need be iteratively defined by nature of the neat material definition. In pursuing a validation path, this research continued toward the pursuit of aiming to match a simulated tensile response to the test data that originally informed the material definition. In failing to achieve said match, citing undesirable test characteristics, undesirable framework definition, and the necessity of lengthy iterative cycles, this research pursued an alternate approach, termed the “User-Informed-Calibration Approach”. Though the approach succeeded in matching three orientations of infill rasters in both a flexure test as well as a tensile test, the procedure was User-Informed, so it does not extend to

being a strategy of an arbitrary predictive nature. The success of the User-Informed-Calibration Approach does support, however, that further fidelity needs be built into the predictive strategy offered to simulate the printing process. Success of the User-Informed-Calibration Approach also supports that the framework of the approach suggested by the developers, termed “The Default Approach”, may be improved by introducing the means to separate the contributions of each of the three considered detrimental effects. This will likely be accomplished by matching the definition of the model at various stages throughout the development process to empirical data, though determining the best means to make this match is an avenue of continued work.

Additive manufacturing offers plenty of potential, but the technology currently stands in a state that can only support complex parts with an ad-hoc strategy to correct printing flaws on an as-incurred basis. By comparing the strength of some of the first printed specimens with that of the final printed specimens, one may observe a large variation in material property on the basis of process variables. While variability in the latter samples was reduced, it remains to be seen what other modifications to the printing process might yet bring significant gains to the structures or properties that may be achieved. One of the largest gains realized in the context of experimentation was in conducting a design of experiments on the basis of varying nozzle temperature, fan speed and extruder flow. Although the result of this experiment pointed to a prominent optimum point, the physics of what makes this optimum so prominent is not fully understood. The DOE conducted successfully casts strength as a function of process parameters toward the goal of optimizing strength, but the process-structure relations may only be known given the results of further experimentation and investigation. It is clear that defects play a disproportionately large role in the performance that may be expected from AM parts; however, it is unclear whether the most tractable path to employing AM may be realized through attempting to mitigate the mechanisms that introduce these defects directly, or whether simulation of

defects offers a path that might eventually extend to a predictive nature, allowing these defects to be avoided. In the context of this work, it may be easy to conclude that simulation of an additive process is somewhat impractical from either the standpoint of framework definition, computational cost, or time investment of the end user, but there was a day that such arguments were made concerning the finite element method as a whole, and the practicality of programs like ABAQUS, and now these methods are so successful on the basis of incremental development that they have many engineering students convinced of the obsolescence of math.

In terms of next steps, there are multiple directions that should be investigated. PLA is an excellent material in terms of providing a large volume of literary data, and high strength polymer parts, but the processing temperatures which it starts to degrade limits its practical applications for production-scale parts. Investigation of another material is probably worth consideration. Apart from another material to investigate, the issue of printing speed should be addressed, as it seems the current approach only manages to match bed translation rate to extrusion rate successfully enough to optimize strength at very low speeds. It is also unclear whether a design of experiments for 11 and 33 direction specimens might yield differing process parameters. Concerning the simulation of defect modeling, it should be established whether there is, or is not an “accepted approach”. Were we simply trying to construct too large a model with not enough data, or does this framework fail to achieve a full definition? Furthering the understanding of the way this framework works, and should work, is an important step toward improving the design of a FFF part.

REFERENCES

- [1] Ultimaker, "Cura Users Manual," 2019. [Online]. Available: https://ultimaker.com/download/170/Cura_User-Manual_v1.0.pdf.
- [2] H. Bensoussan, "The History of 3D Printing_ From the 80s to Today." 2016.
- [3] J. Scott and P. Leader, "Additive Manufacturing : Status and Opportunities Additive Manufacturing : Status and Opportunities," *IDA Sci. Technol. Policy Inst.*, no. January 2012, 2017.
- [4] A. International, "Additive Manufacturing Technologies 1,2." pp. 2–4, 2013.
- [5] WordPress, "Latest News of 3D Printing," *Morgen*, 2019. [Online]. Available: <https://www.morgen-filament.de/category/sponsored/>.
- [6] L. L. N. Laboratory, "Powder bed AM." .
- [7] T. DebRoy *et al.*, "Additive manufacturing of metallic components – Process, structure and properties," *Prog. Mater. Sci.*, vol. 92, pp. 112–224, 2018.
- [8] A. Levy, A. Miriyev, A. Elliott, S. Suresh, and N. Frage, "Additive manufacturing of complex-shaped graded TiC / steel composites," *Mater. Des.*, vol. 118, pp. 198–203, 2017.
- [9] J. Benedyk, "Additive Manufacturing of Aluminum Alloys," *Light Metal Age*, 2018. [Online]. Available: <https://www.lightmetalage.com/news/industry-news/3d-printing/article-additive-manufacturing-of-aluminum-alloys/>.
- [10] S. Inc, "Electron Beam Additive Manufacturing (EBAM) – Advantages of Wire AM vs," *AMazing*, 2015. .
- [11] S. Inc, "Make Metal Parts Faster & Cheaper with EBAM® Metal 3D Printing Technology," 2019. [Online]. Available: <https://www.sciaky.com/additive-manufacturing/electron-beam-additive-manufacturing-technology>.
- [12] A. Nikhil, "3D Printing Processes - Binder Jetting." p. 4/8, 2016.
- [13] I. Durgun and R. Ertan, "Experimental investigation of FDM process for improvement of mechanical properties and," *Rapid Prototyp. J.*, pp. 228–235, 2015.
- [14] B. E. Carroll, A. Palmer, and A. M. Beese, "Anisotropic tensile behavior of Ti – 6Al – 4V components fabricated with directed energy deposition additive manufacturing," *Acta Mater.*, vol. 87, pp. 309–320, 2015.
- [15] J. A. Gonzalez, J. Mireles, Y. Lin, and R. B. Wicker, "Characterization of ceramic components fabricated using binder jetting additive manufacturing technology," *Ceram. Int.*, vol. 42, no. 9, pp. 10559–10564, 2016.

- [16] P. Nandwana, A. M. Elliott, D. Siddel, A. Merriman, W. H. Peter, and S. S. Babu, "Powder bed binder jet 3D printing of Inconel 718 : Densification , microstructural evolution and challenges," *Curr. Opin. Solid State Mater. Sci.*, vol. 21, no. 4, pp. 207–218, 2017.
- [17] Y. Song, Y. Li, W. Song, K. Yee, K. Lee, and V. L. Tagarielli, "Measurements of the mechanical response of unidirectional 3D-printed PLA," *Mater. Des.*, vol. 123, pp. 154–164, 2017.
- [18] S. A. Tronvoll, T. Welo, and C. W. Elverum, "The effects of voids on structural properties of fused deposition modelled parts : a probabilistic approach," *Int J Adv. Manuf. Technol.*, pp. 3607–3618, 2018.
- [19] J. S. Keist and T. A. Palmer, "Role of geometry on properties of additively manufactured Ti-6Al-4V structures fabricated using laser based directed energy deposition," *Mater. Des.*, vol. 106, pp. 482–494, 2016.
- [20] Z. Wang, T. A. Palmer, and A. M. Beese, "Effect of processing parameters on microstructure and tensile properties of austenitic stainless steel 304L made by directed energy deposition additive manufacturing," *Acta Mater.*, vol. 110, pp. 226–235, 2016.
- [21] W. Sarah, L. Taekyung, E. Faierson, K. Ehmann, and J. Cao, "Anisotropic Properties of Directed Energy Deposition (DED)-Processed Ti-6Al-4V," *J. Manuf. Process.*, 2016.
- [22] T. Letcher and M. Waytashek, "Material Property Testing of 3D-Printed Specimen in PLA on an Entry-Level 3D Printer," in *International Mechanical Engineering Congress & Exposition*, 2015, no. February.
- [23] A. Lanzotti, M. Grasso, G. Staiano, and M. Martorelli, "The impact of process parameters on mechanical properties of parts fabricated in PLA with an open-source 3-D printer," *Rapid Prototyp. J.*, 2015.
- [24] J. Torres, M. Cole, A. Owji, Z. Demastry, and A. P. Gordon, "An approach for mechanical property optimization of fused deposition modeling with polylactic acid via design of experiments," *Rapid Prototyp. J.*, vol. 2, no. February 2015, pp. 387–404, 2016.
- [25] J. M. Chacón, M. A. Caminero, E. García-plaza, and P. J. Núñez, "Additive manufacturing of PLA structures using fused deposition modelling : Effect of process parameters on mechanical properties and their optimal selection," *Mater. Des.*, vol. 124, pp. 143–157, 2017.
- [26] B. M. Tymrak, M. Kreiger, and J. M. Pearce, "Mechanical properties of components fabricated with open-source 3-D printers under realistic environmental conditions," *Mater. Des.*, vol. 58, pp. 242–246, 2014.
- [27] B. E. Enno, E. Fachhochschule, F. Maschinenbau, S. Fachhochschule, and F. Maschinenbau, "Fabrication of FDM 3D objects with ABS and PLA and determination of their mechanical properties," *Forum of Rapid Technnology*, pp. 0–7.
- [28] B. Wittbrodt and J. M. Pearce, "The effects of PLA color on material properties of 3-D printed components," *Addit. Manuf.*, vol. 8, pp. 110–116, 2015.

- [29] H. Li, T. Wang, J. Sun, and Z. Yu, "The effect of process parameters in fused deposition modelling on bonding degree and mechanical properties," *Rapid Prototyp. J.*, vol. 1, no. February 2017, pp. 80–92, 2018.
- [30] X. Liu, M. Zhang, S. Li, L. Si, J. Peng, and Y. Hu, "Mechanical property parametric appraisal of fused deposition modeling parts based on the gray Taguchi method," *Int J Adv. Manuf. Technol.*, pp. 2387–2397, 2017.
- [31] T. Kalil and C. Wadia, "Materials Genome Initiative for Global Competitiveness," no. June. 2011.
- [32] I. Gibson and D. Rosen, *Additive Manufacturing Technologies*. 2014.
- [33] ASTM D 638 -02a, "Standard test method for tensile properties of plastics," *ASTM D 638 -02a*, vol. 08, pp. 46–58, 2003.
- [34] Ultimaker, "Ultimaker 2 Users Manual," 2019. [Online]. Available: <https://ultimaker.com/download/7385/UserManual-UM2-v2.1.pdf>.
- [35] M. A. Cuiffo, J. Snyder, A. M. Elliott, N. Romero, S. Kannan, and G. P. Halada, "Impact of the Fused Deposition (FDM) Printing Process on Polylactic Acid (PLA) Chemistry and Structure," *Appl. Sci.*, pp. 1–14, 2017.
- [36] Mathworks, "Matlab User Documentation." [Online]. Available: <https://www.mathworks.com/help/matlab/>.
- [37] D. Chakravorty, "G-Code 3D Printing Commands 2019 - Programming Tutorial." [Online]. Available: <https://all3dp.com/g-code-tutorial-3d-printer-gcode-commands/>.
- [38] MTS, "MTS Criterion® Series 40 Electromechanical Universal Test Systems," 2018. [Online]. Available: https://www.mts.com/cs/groups/public/documents/library/mts_006225.pdf.
- [39] L. Wang, D. Beeson, G. Wiggs, and M. Rayasam, "A Comparison Meta-Modeling Methods Using Practical Industry Requirements," *47th AIAA/ASME/ASCE/AHS/ASC Struct. Struct. Dyn. Mater. Conf. 14th AIAA/ASME/AHS Adapt. Struct. Conf. 7th*, no. May, pp. 1–25, 2006.
- [40] W. Mathworld, "Method of Steepest Descent." [Online]. Available: <http://mathworld.wolfram.com/MethodofSteepestDescent.html>.
- [41] AlphaSTAR, "GENOA 2017 Build 7.8.18 User Manual," 2017.
- [42] N. LLC, "Ingeo™ Biopolymer 2003D." pp. 1–3.
- [43] A. Grant, B. D. Ellis, and M. Rais-rohani, "Exploring the relationship between process and properties of 3D-printed PLA : Towards process-informed simulation," in *Nanotech 2019*, 2019, pp. 1–2.
- [44] C. Zhou *et al.*, "Temperature dependence of poly(lactic acid) mechanical properties," *RSC Adv.*, vol. 6, no. 114, pp. 113762–113772, 2016.

- [45] J. Vogel, "Activation Energy for Diffusion and Welding of PLA films," *Polym. Eng. Sci.*, 2012.
- [46] Moldflow Plastics Labs, "Moldflow Material Testing Report MAT2238 NatureWorks PLA," 2007.
- [47] E. José, P. Júnior, R. D. P. Soares, N. Sérgio, and M. Cardozo, "Analysis of equations of state for polymers," *Sci. Tech.*, vol. 25, no. 3, pp. 277–288, 2015.
- [48] DURAN inc, "Properties of Borosilicate Glass." pp. 16–17.
- [49] ASTM D5379, "Standard Test Method for Shear Properties of Composite Materials by the V-Notched," *Annu. B. ASTM Stand.*, no. March, pp. 1–13, 2012.

APPENDIX A: A TUTORIAL TRACING THE GENERATION OF A SIMULATED TENSILE RESPONSE

This tutorial specifies the creation of a 1:2 scale model of a ASTM D638 Type 1 tensile specimen. The involved steps and software are presented in the order in which they are used. The first step is to draft the geometry which is done in Solidworks (filename: D638HS). One should be certain that the unit system is set to "MKS", which is accessed by clicking the lower right toolbar. The dimensions for the model are obtained in a 2-step process. First, 1:2 scale working dimensions are obtained by dividing the ASTM D638 dimensions for the Type 1 specimen by 2. These dimensions are shown in Figure 113.

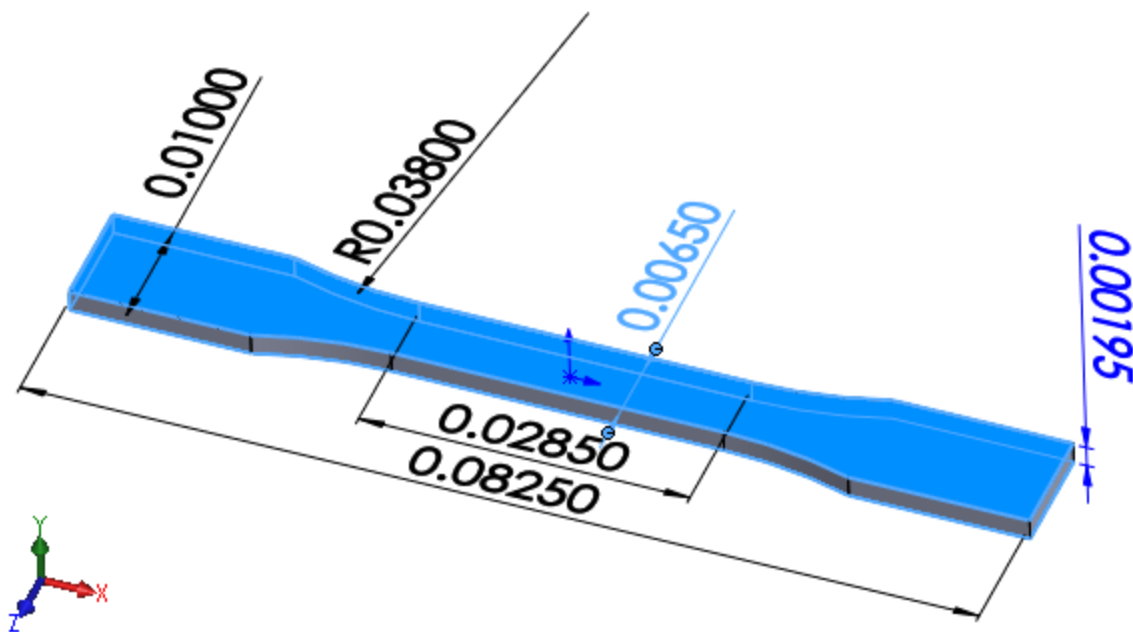


Figure 113: The 1:2 scale working dimensions

Second, three 1:2 scale working dimensions are rounded to the nearest multiple of raster width: the width of the gauge length ($18 \times 0.35\text{mm}$), the width of the grip section ($28 \times 0.35\text{mm}$), and the length of the specimen ($236 \times 0.35\text{mm}$). The thickness of the specimen needs also be verified to be rounded to the

nearest multiple of layer height ($13 \times 0.15\text{mm}$). These operations may be executed with a single "Extruded Cut", and two "Mirror" commands. A depiction of the cut rounding these dimensions is shown in Figure 114, noting that the dimensions shown in Figure 114 correspond to half the dimensions of the appropriately mirrored specimen.

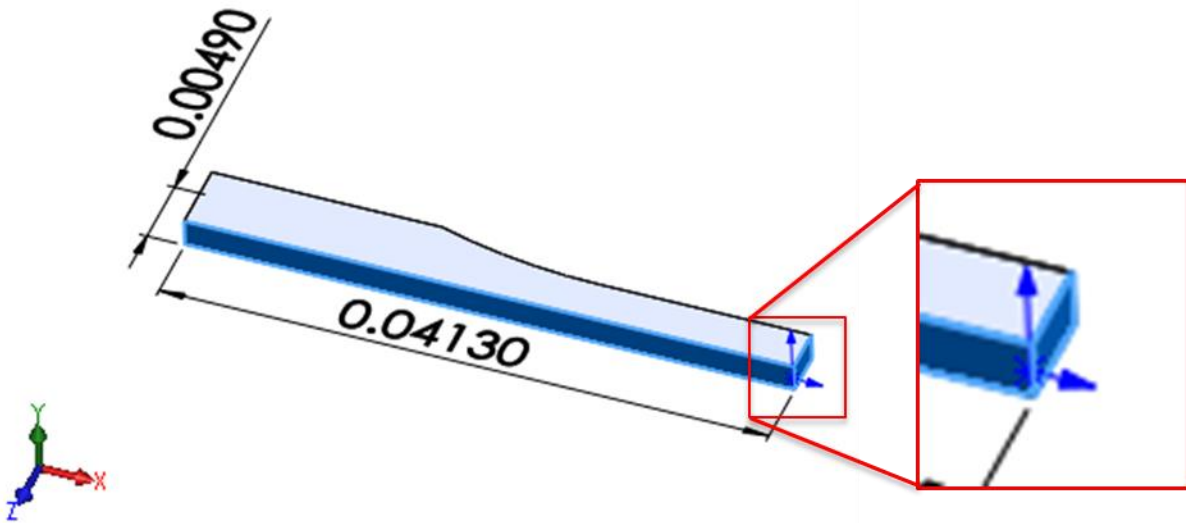


Figure 114: The cut rounding the 1:2 scale working dimensions

The next step involves matching the orientation and locale of the part's coordinate system in Solidworks to the orientation and locale of coordinate system in 3D printing convention. The coordinate system origin in the part is depicted in Solidworks with a short blue arrow indicating the positive X direction, and a slightly longer blue arrow indicating the positive Y direction. This symbol is shown in the expanded view in Figure 114. The orientation of 3D printing coordinate system convention is, as observed by a user standing in front of a 3D printer, positive X right, positive Y forward, and positive Z upward. The locale of the 3D printing coordinate system convention is on the back left-hand corner of the top surface of the print bed. This locale and orientation is shown in Figure 115.

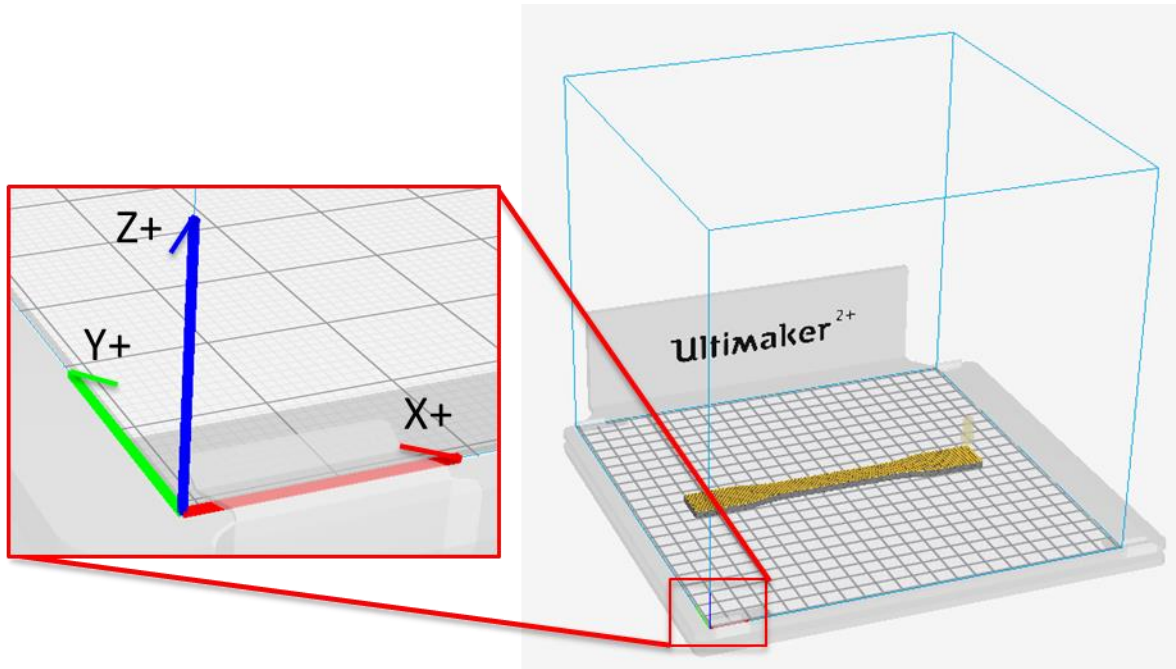


Figure 115: The orientation and locale of 3D-printing coordinate system convention

To match the orientation and locale of the two coordinate systems, a two-step process is employed.

The first step aims to reorient the part's coordinate system to match 3D printing convention, and relocate the origin to the back left lower corner of part. The second step involves shifting the part in the XY-plane to match the part's location in Solidworks to the part's location on the print bed.

It is worthy of note that, given the appropriate level of forethought, many simple parts may be drawn on the front plane with the lower left corner placed at the origin, and extruded in the +Z direction, rendering the first step of this process unnecessary. However, many factors may preclude the practicality of planning to avoid this step.

Relocating and reorienting an existing coordinate system in Solidworks is not accomplished by performing operations on the coordinate system itself, but rather by moving the part with respect to the part's native coordinate system. The component magnitudes of the required translation in the x, y, and z-directions may be given directly by querying the distance between the current locale of the origin, and the locale of the desired origin. It is often helpful to screenshot the output of this query using the "Measure Tool". To make the necessary translation, the "Move Face" command is used, the geometry is box-selected, and the component magnitudes are keyed into their respective fields, noting some of these components may be negative. This operation is shown in Figure 116.

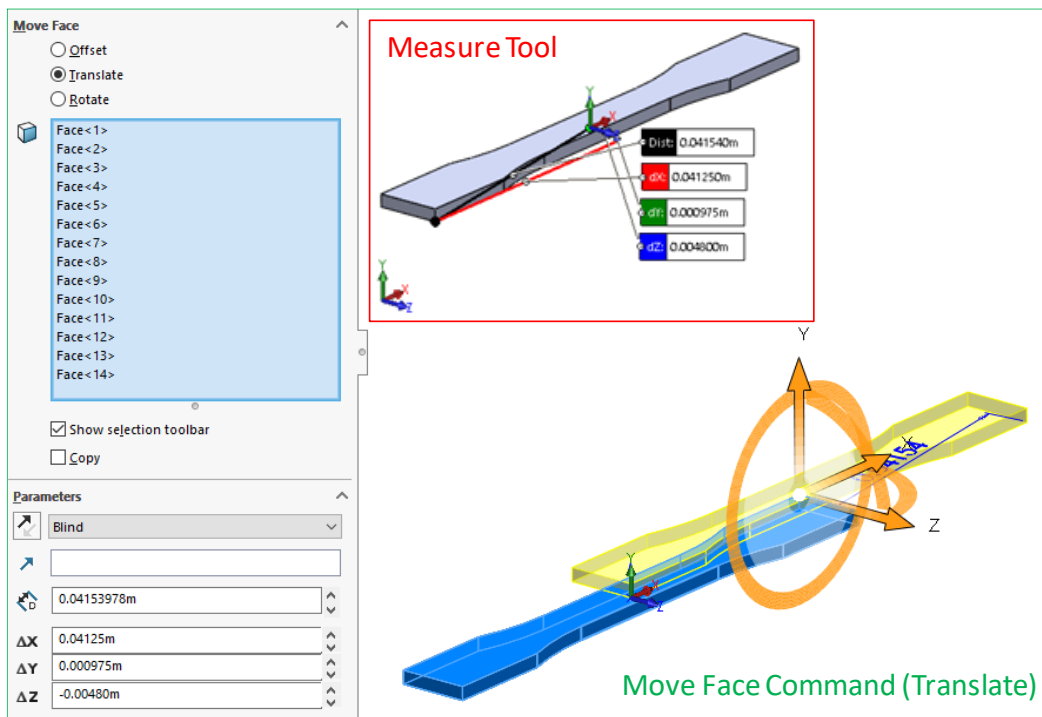


Figure 116: Magnitudes from the "measure "tool" and application of the "Move Face" command

By again applying the "Move Face" command, box-selecting the geometry, and instead specifying a 90-degree rotation about an edge coinciding with the x-axis, the part is reoriented in the intended fashion.

This operation is shown in Figure 117.

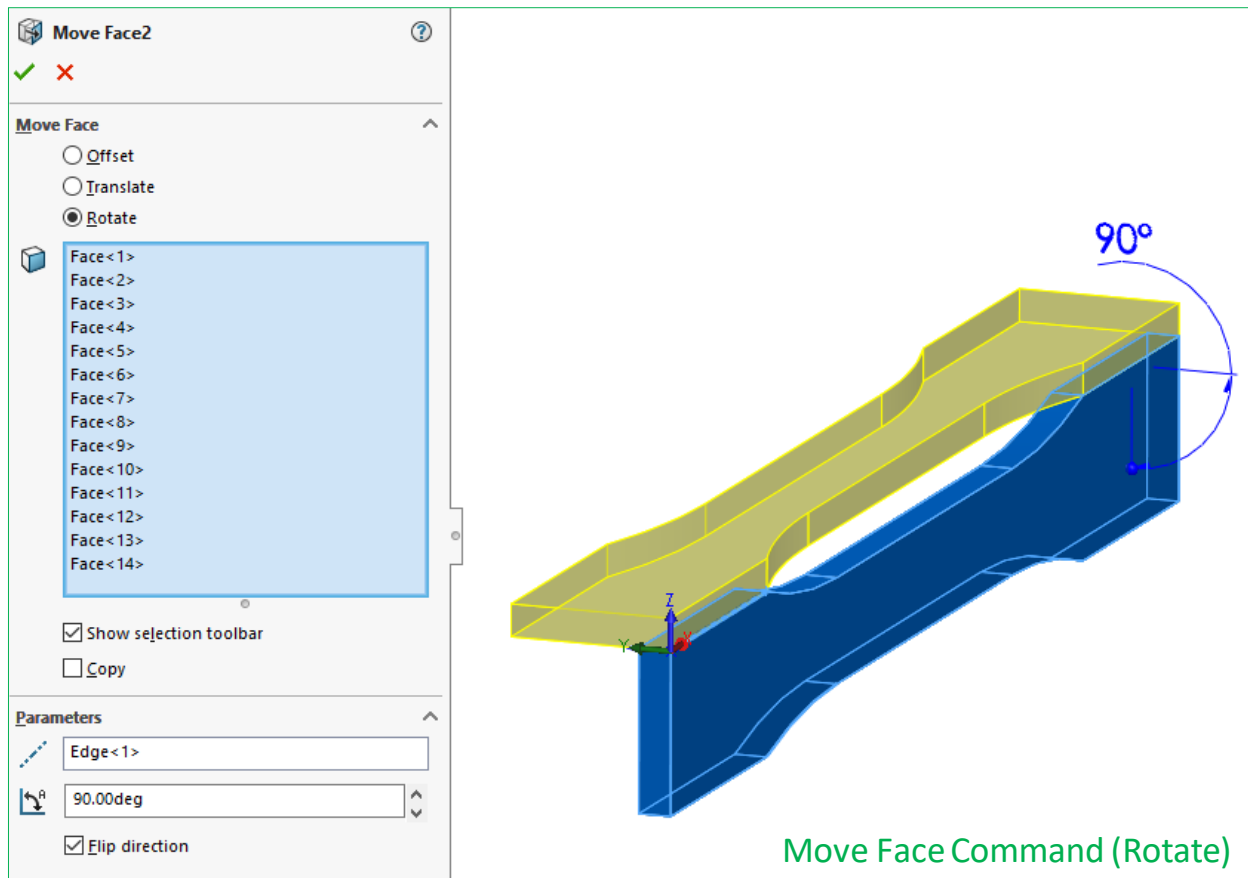


Figure 117: The application of a rotational “Move Face” to align coordinate system convention

The geometry used by ABAQUS to generate a mesh must be consistent in the measure of offset from the origin by the same measures as to match the offsets given by the g-code. Ensuring this consistency will require generating the g-code in Cura, extracting these offsets, and returning to Solidworks to apply the offsets before generating the IGES file. Save the current Solidworks file as a STL format (filename: D638HS, file path: C:\Users\User\Downloads\3D Print Test Parts), and open Cura v3.6.0 [1].

To import the part in Cura, press Ctrl+O. Navigate to and open the previously exported STL file (filename: D638HS, filepath: C:\Users\User\Downloads\3D Print Test Parts). To specify the slicer settings, either open the following “3mf” file: (filename: TUTORIAL_D638HS filepath: C:\Users\User\Downloads\3D Print Test Parts) or refer to the settings defined in Table 2.1. If manually defining the settings per Table 2.1, refer to the additional specifications below in Table A.1 to fully define the settings which were defined to vary from dataset to dataset:

Table A.1 : Case specific Cura v3.6.0 [1] slicing parameters for D638HS simulation

Quality settings:	(Fully specified by Table 2.1)
Shell settings:	
Wall Line Count:	1 (This setting is specific to this instance)
Alternate Extra Wall:	Disabled
Z Seam X, Z Seam Y:	(0 mm, 0 mm)
Infill Settings:	
Infill Line Directions:	[90] (This setting is specific to this instance)
Material Settings:	
Retraction Minimum Travel:	3.0 mm (This setting is specific to this instance)
Speed Settings:	
Print Speed:	15 mm/s (This setting is specific to this instance)
Travel Settings:	
Combing Mode:	Off
Layer Start X:	0 mm (This setting is specific to this instance)
Layer Start Y:	0 mm (This setting is specific to this instance)
Cooling Settings:	(Fully specified by Table 2.1)
Support Settings:	(Activated)
Build Plate Adhesion Settings:	
Build Plate Adhesion Type:	None (Fully specified by Table 2.1)

Dual Extrusion Settings: (No modified settings)

Mesh Fixes: (No modified settings) (Fully specified by Table 2.1)

Special Modes: (No modified settings) (Fully specified by Table 2.1)

Experimental Settings: (Fully specified by Table 2.1)

Click "Prepare" in the lower right corner of the graphics area to slice the part. One may view the scan strategy by changing the dropdown near the top from "Solid view" to "Layer view". If desired, one may animate this strategy by pressing the "play" icon. At the bottom right, click the blue button "Save to file" to export the g-code. This button may automatically default to "Save to removable drive" if a thumb drive or SD-card reader is currently in the computer. If so, the button may be modified as a typical dropdown menu. Save the file as a g-code format (filename: D638HS_GCODE11_LH15mm.gcode, filepath: C:\Users\User\Downloads\3D Print Test Parts)

Open the g-code in Notepad++. Both "G0" and "G1" commands represent linear move commands in 3D printing g-code. Many slicers, such as Cura v3.6.0 [1], distinguish travel moves with a "G0", whereas extrusion moves begin with "G1". GENOA is only compatible with slicers which only use "G1" commands, therefore, use a "find and replace" function to replace all occurrences of "G0" with "G1". Save the file in the same location as it was obtained. Before closing the file, locate the first G1 command: (G1 F1800 X70.375 Y106.775 Z0.15). This command specifies to start the part at X=70.375 mm, Y=106.775 mm and Z=0.15 mm, with a federate of 1800 mm/min. The X-and-Y-coordinates of this command provide the earlier specified necessary offsets to be applied in Solidworks, however, as each element is 0.35 mm square, half this measure (0.175 mm) must be deducted from both X and Y

coordinates before returning to Solidworks and applying the offsets with the “Move Face” command. The application of these offsets is shown in Figure 118.

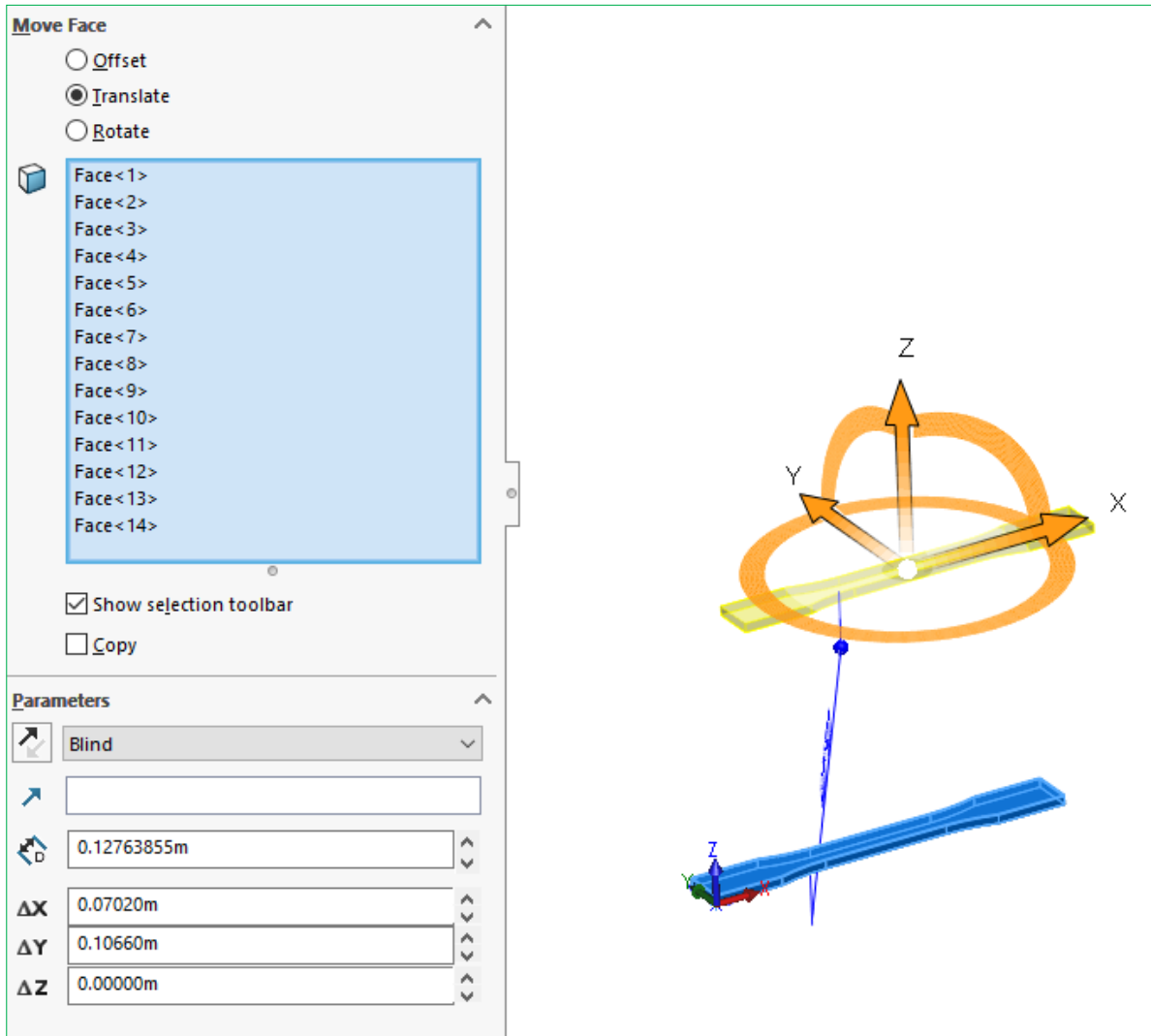


Figure 118: Using “Move Face” to apply the g-code offsets from the first travel command

Next, a 4mm thick baseplate is added by extruding a rectangle centered on the part footprint in the -Z direction. The rectangle extends 5 mm past the boundaries of the part in both the X and Y-dimensions as shown in Figure 119.

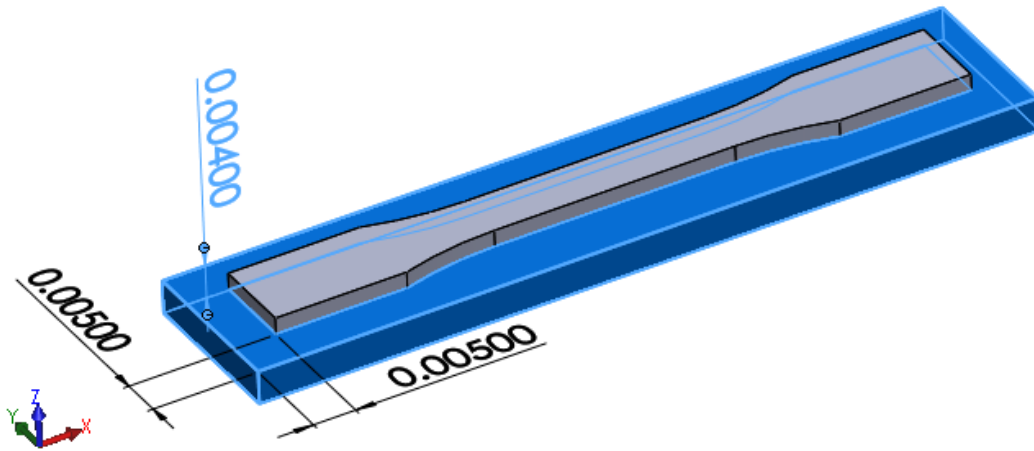


Figure 119: Adding the baseplate geometry in Solidworks

Quarter this geometry, leaving the quarter in the upper-left quadrant. This is most easily done by checking the “Flip side to cut” box on the “Extruded Cut” command in Solidworks. This operation is shown in Figure 120.

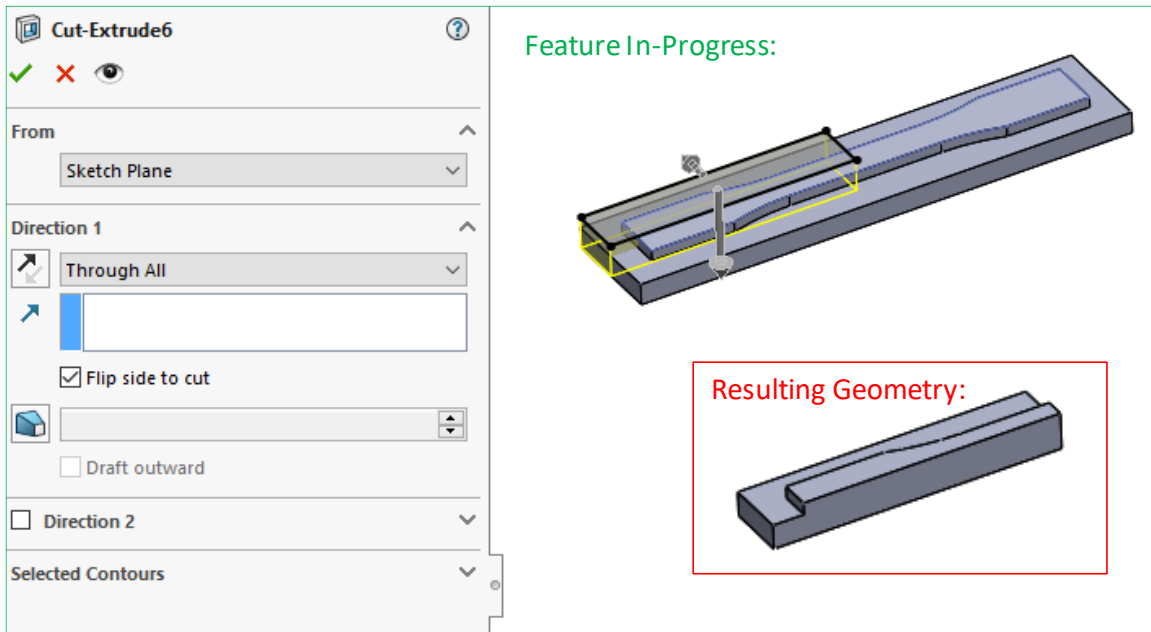


Figure 120: Quartering the tensile specimen and baseplate

Save the file in an IGES format (filename: D638HS.igs, filepath: C:\Users\User\Downloads\3D Print Test Parts). Next, close Solidworks and open the exported file in ABAQUS CAE by using File>Import>Part. Click "OK" to the "Create Part from IGES File" dialog box, the part will then appear in the graphics area, as shown in Figure 121.

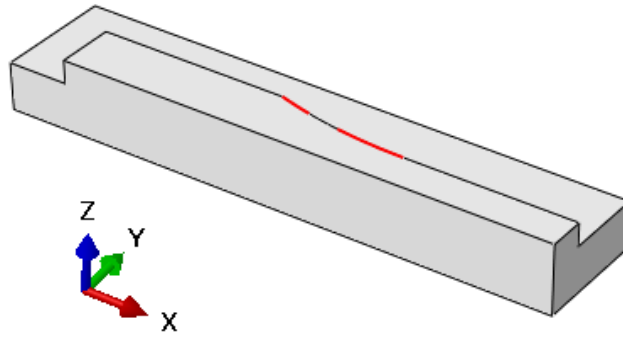


Figure 121: D638HS.IGES import in ABAQUS, highlighting the 1st and 3rd gauge length contours

By hovering the mouse over the gauge length reduction contour edges, one may see that the default IGES import settings leave this curved edge split into three approximated curve segments. The endpoints of these curve segments will force a node to be located at these locations, raising a potential geometric oddity in the surrounding element definitions. This is a condition that could be corrected by re-performing the import, returning to the “Create Part from IGES File” dialog box, navigating to the “IGES Options” tab, and selecting “Always use 3D data”. Alternately, the geometric condition may be automatically corrected by mirroring the part and cutting away the original geometry (instructions provided for the latter approach).

On the icon toolbar, select the “Create Mirror” icon, then select the cut face in the XZ plane. Next, select “Create Cut: Extrude”. This will prompt the user to select a plane to define a cut profile on, followed by a prompt to orient and scale the visualization of this plane. Draw and dimension a rectangle on the top surface of the specimen, and click the mouse wheel (MB3) to complete the sketch. Extrude a cut in the -Z direction, through the entirety of the original IGES import. These steps are shown in Figure 122.

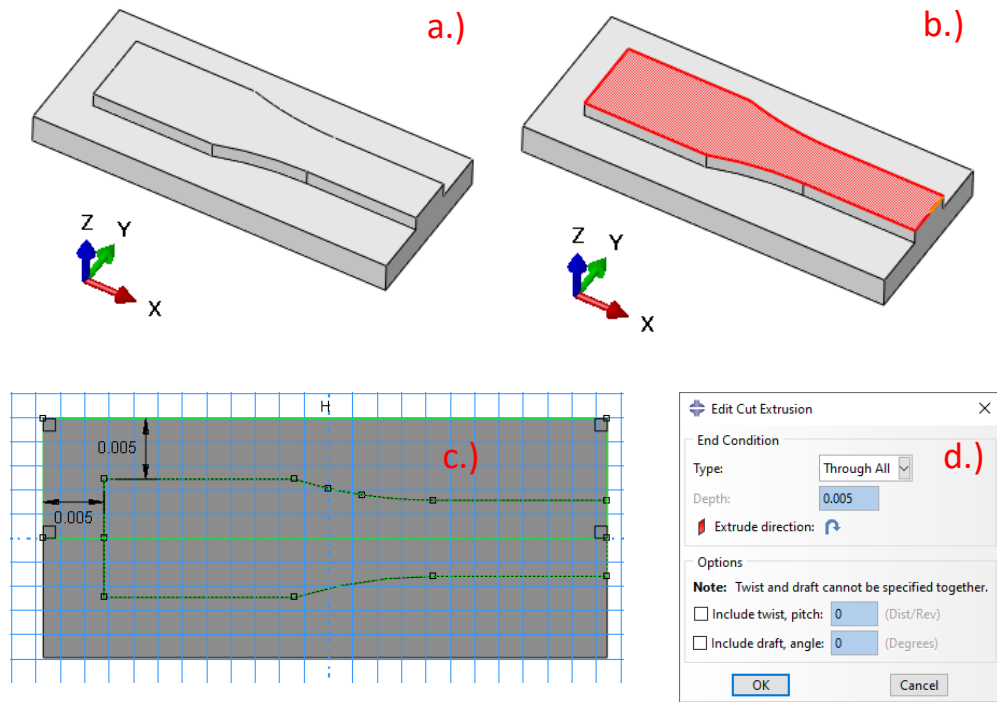


Figure 122: Display of ABAQUS mirror and cut operations

a.) mirror across XZ cut face, b.) selection of cut plane and vertical right hand edge, c.) definition of two line-to-point dimensions to define cut profile, and d.) specification of extruded cut settings

Once the steps in Figure 122 are complete, it may be seen that this cut eliminates the issue by hovering the mouse over the mirrored arc silhouette. Next, select "Property" from the module dropdown, and select the "Partition Face" command. Select the top face of the tensile specimen & click the middle mouse wheel (indicating "complete with command"). Next, select the intersection of the YZ cut plane with this top face, bring up the same sketch plane as was used for the extruded cut in Figure 122.

Use the "Project Edges" tool and select the 5 segments outlining the boundary of the part. Set the segments along symmetric boundaries to construction geometry by using "Set as Construction". Then, use 4 instances of the "Offset curves" tool to outline the inner boundary of the perimeter raster, offsetting each segment by 0.00035(m). Next, trim 4 line segments, and add 2 coincident and one

tangent constraint. Next, add 3 dimensions, fully-defining the sketch. These steps are shown in Figure 123. When complete, exit the partition sketch by clicking the mouse wheel.

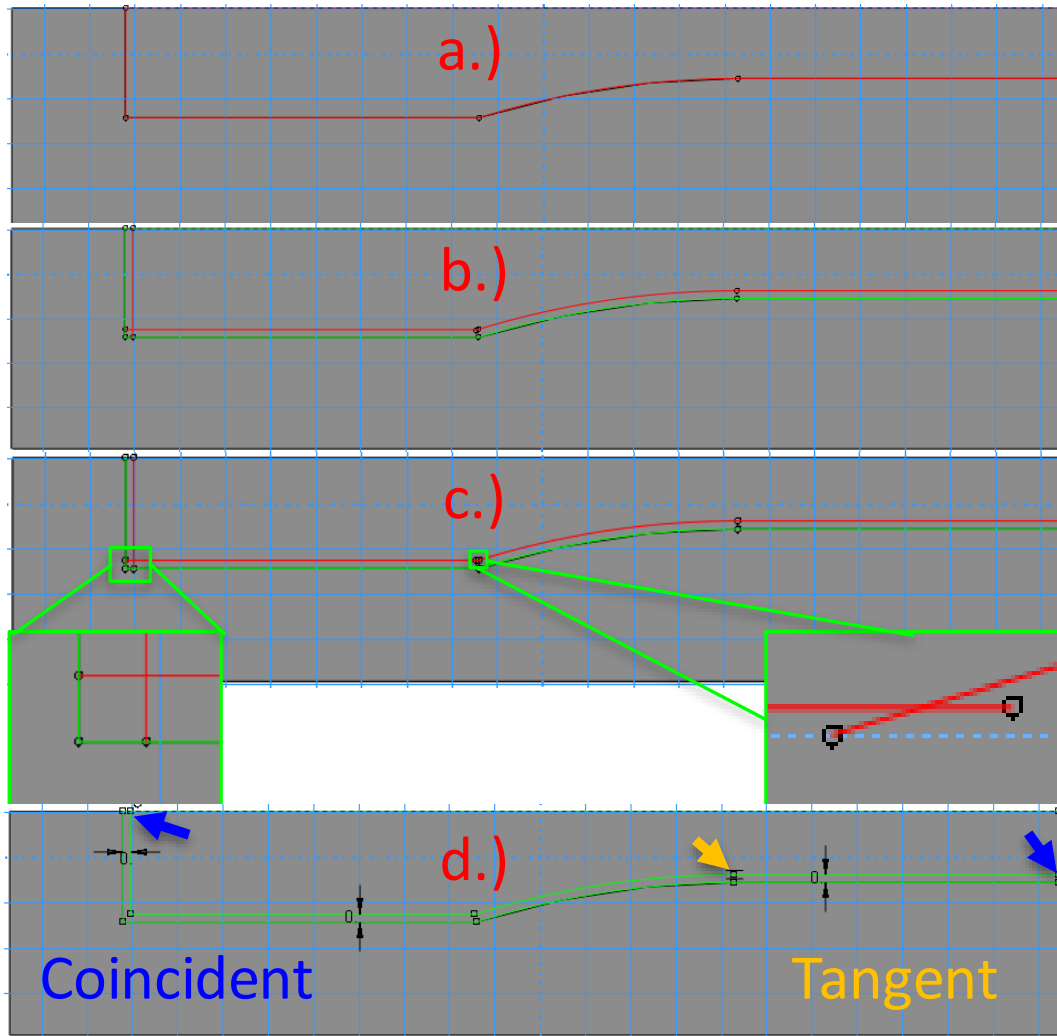


Figure 123: Various partitioning sketch steps to isolate the outer raster boundary (showing: a.) projection of 5x edges, b.) offsetting curve segments, c.) trim curve locations, and d.) added dimensions and constraints)

Employing a similar technique, apply a series of “Partition Face” commands, executed on the same plane, to complete the partitioning of the top face as shown in Figure 124.

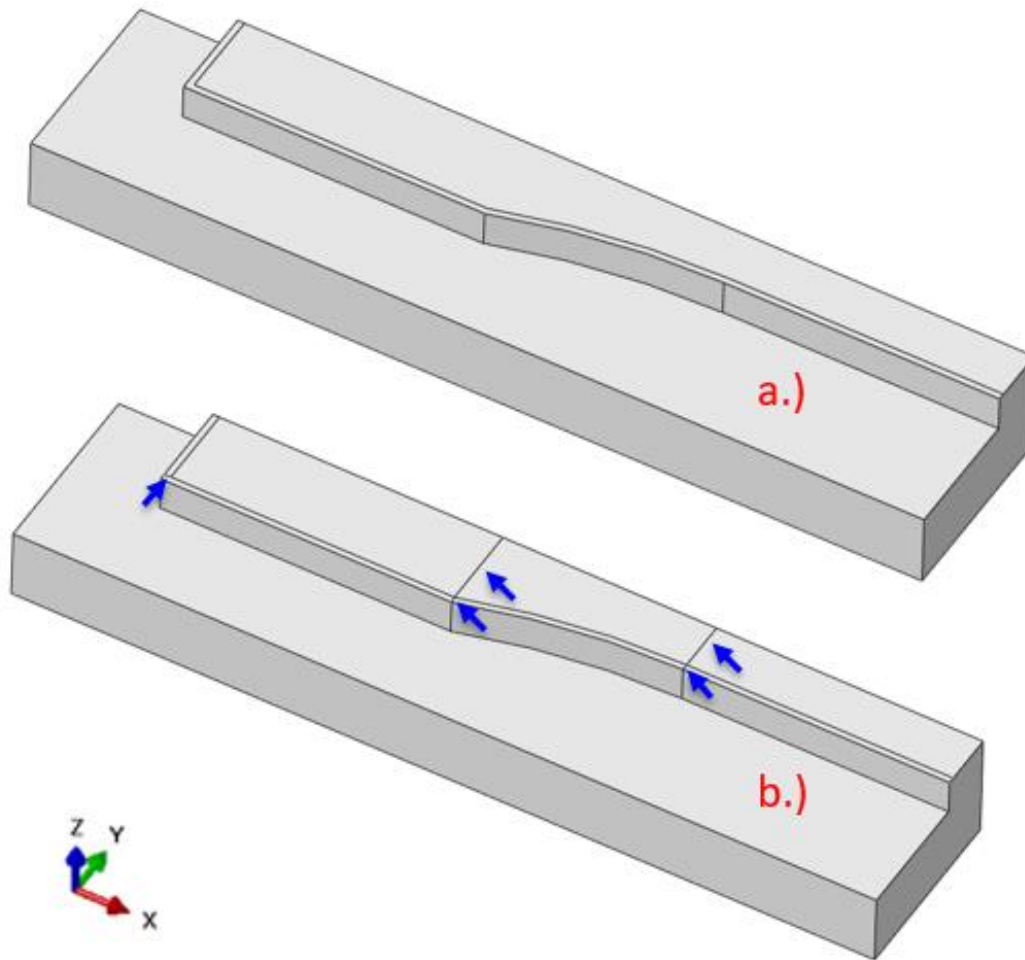


Figure 124: A depiction of the tensile specimen before and after completion of partitioning (Showing a.) after the partition depicted in Figure 123 is complete, b.) after completing all top surface partitions)

The next stage involves the creation of datum planes used to partition the thickness dimension of the part. For many of the following steps, it is desirable to have perspective turned off. Deactivate perspective view by clicking the straight railroad icon on the top toolbar.

By clicking and holding the bottom icon on the vertical toolbar, “Create Datum Plane: Offset from Principle Plane”, one may expose a fly-out menu allowing the selection of several differing strategies for datum plane creation. Select “Create Datum Plane: 3 Points”, and select the three points shown in Figure 125.

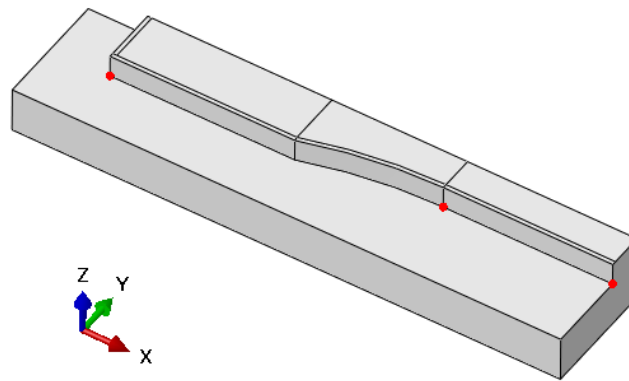


Figure 125: A depiction of three points used to create a datum plane

Activate “Left view” by clicking the icon on the top toolbar corresponding to +Y upward, +Z left. Next, expand the datum plane fly-out menu again, this time selecting “Create Datum Plane: Offset from Plane”. Select the plane created between the baseplate and the first layer, select “Enter Value”, specify an offset in the +Z-direction, and define an offset of 0.00015(m). Copy this operation a total of 12 times, creating planes which divide the thickness of the specimen into 13 equal layers. Once the assumed normal of the offset plane has been flipped on two consecutive plane creation commands, the assumed normal reverses in direction. After executing this second flipped plane creation, the necessary operation may be repeated quickly by copying the plane offset distance to the clipboard, selecting the plane to offset from, double-clicking MB3, Pasting the value, and clicking MB3 again. Next, repeat the same command 3 times to create 3 planes offset from the original in the opposite direction, with a

spacing of 0.001(m). When complete, the graphical display should match the depiction shown in Figure 126.

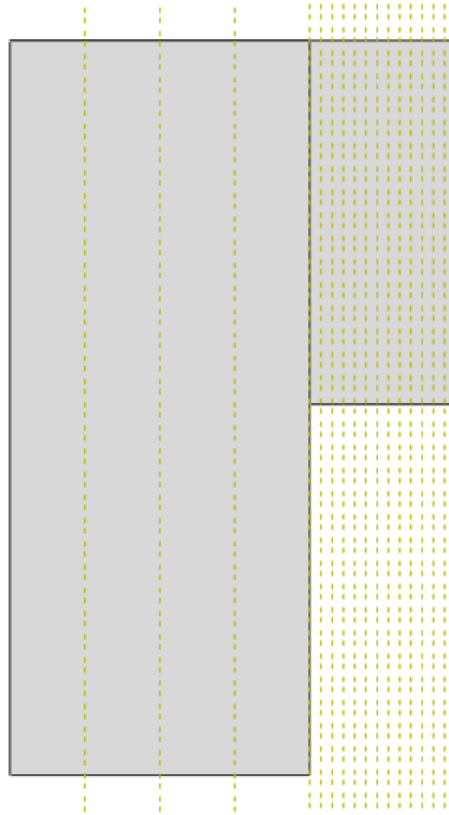


Figure 126: A depiction of the spacing of datum planes

Showing 1 mm spacing across the baseplate thickness, and 0.15mm spacing across the part thickness

By clicking and holding “Partition cell, Define Cutting Plane”, one may expose a fly-out menu allow many variants of cell partitioning strategies. Select the “Partition Cell, Use Datum Plane” command, partition the geometry using the plane all the way to the left. This command will need be executed for all 16 datum planes, dividing the baseplate into 4 layers of elements, and the part into 13 layers of elements. Cell partitions following the first require an additional specification of which cells to partition. This

command may be quickly repeated by selecting the cell(s), clicking MB3, select plane, and clicking MB3 again. Box selections in this command are easiest made in “Left View”.

By clicking and holding the icon for previous command, expose the cell partition fly-out menu again, this time to select the command: “Partition Cell, Extrude/Sweep Edges”. This command is used to sweep an edge or contour through the thickness of a part, defining cell boundaries in the process. In this case, the command will be used to extend the face partitions defined on the top face of the part all the way to the bottom of the baseplate. This command is repeated seven times, once to sweep each of the seven closed contours shown in Figure 127.

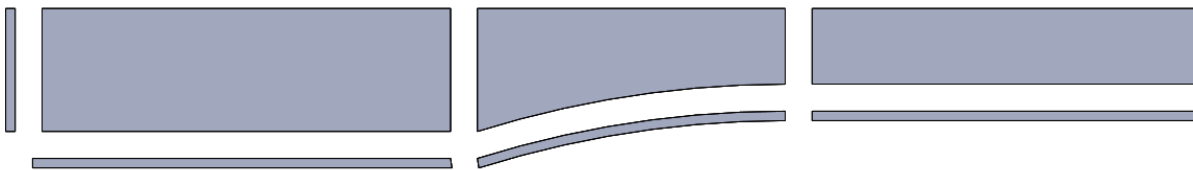


Figure 127: An exploded view of the seven closed contours defined by face partitions

When first prompted to select cells to partition, the first prompt is selection of cells. One may box select the desired cells, or hold Ctrl+A to select all cells. In this prompt, there is no fault introduced by selecting excess cells not swept by the desired edge or contour. If the excess cells are not swept through by the edge or contour, there are simply no new cell boundaries defined in those cells. The next prompt is the selection of edge or contour. Select edges on the top face that form the complete perimeter of one of the seven shapes shown in Figure 127. As this command only works for one closed contour at a time, the command will need be repeated seven times. The next prompt is to select between “Extrude Along Direction” or “Sweep Along Edge”. The specification of “Sweep Along Edge”

begins and terminates the sweep at the starting point and endpoint of the selected line, respectively. As the aim is to extend the cell boundary creation through the entire geometry, select “Extrude Along Direction”, and specify any edge parallel to the Z-axis. Verify the sweep direction is pointing in the -Z direction, and complete the command by clicking MB3. After repeating the command for each of the seven closed contours in Figure 127, the best way to verify correct completion of all the necessary cell partitions is to hold both Ctrl and Alt, and left click and drag in the graphics area. This will bring up a virtual circular boundary in the graphics area, as shown in Figure 128. Dragging the mouse inside the virtual boundary will rotate the model about the 3D origin of the virtual boundary, dragging the mouse outside the virtual boundary will roll the model about the axis normal to the screen. Rotate and roll the model as necessary to visualize the bottom of the baseplate, the previous swept partition commands, if correctly executed, should produce geometry consistent with Figure 128.

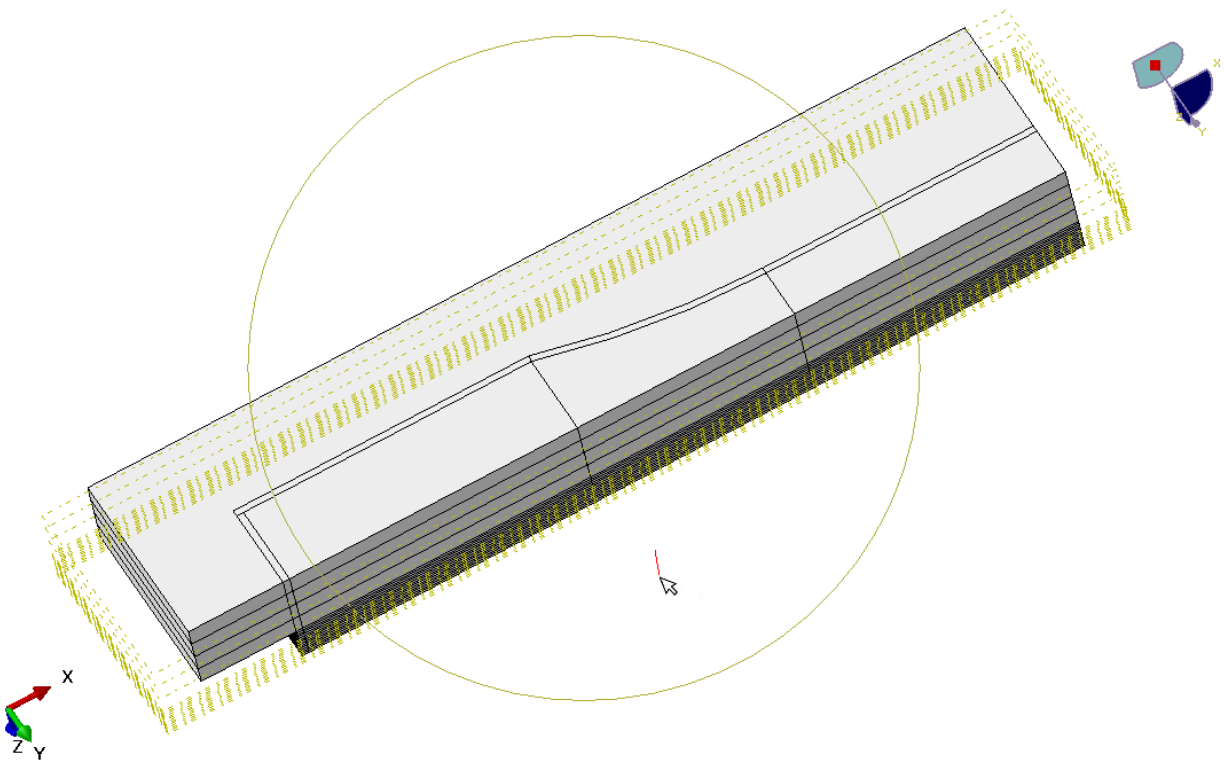


Figure 128: Using Ctrl and Alt click and drag to reposition the graphics in ABAQUS CAE

The next series of commands involve partitioning the baseplate such that the mesh for the baseplate will generate evenly. Create four datum planes using the command “Create Datum Plane: 3 Points”, the series of points to use are annotated in four sets of three points in Figure 129.

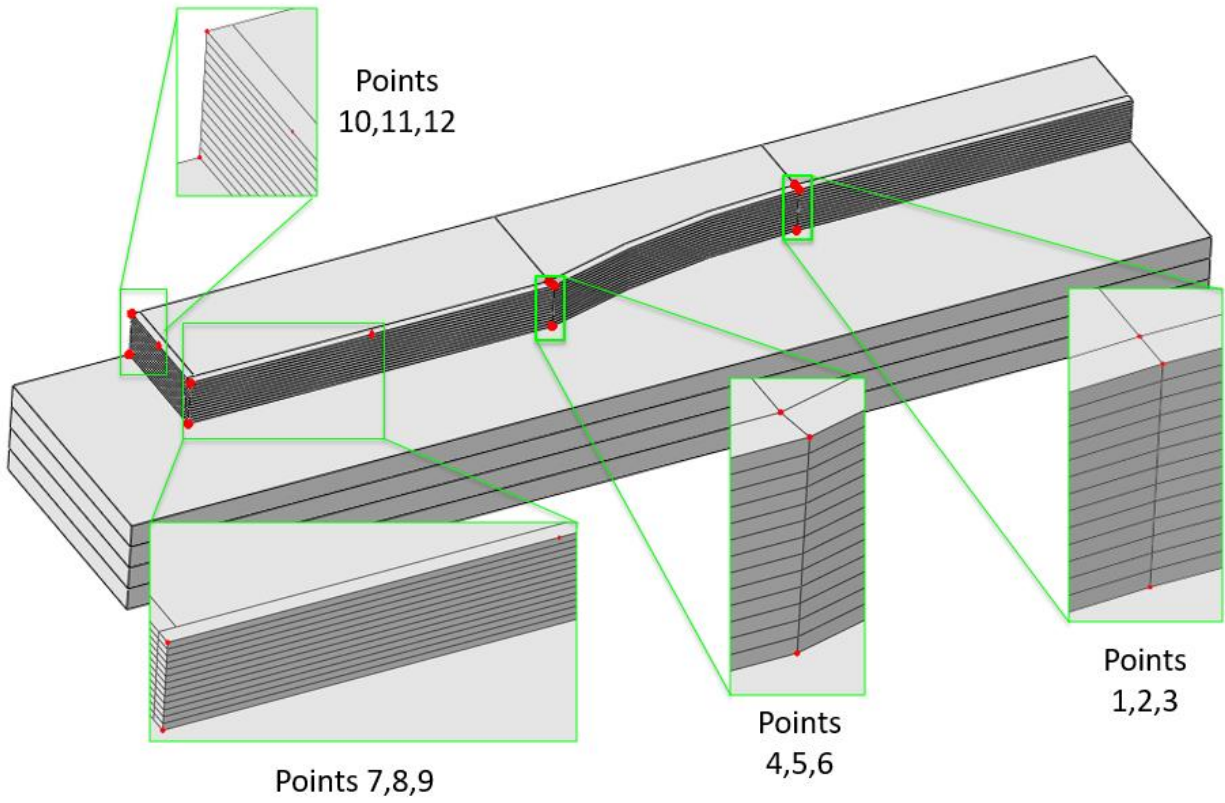


Figure 129: The four sets of points used to create 3-point planes for baseplate partitioning

Next, jump to a “Top view”, and employ four instances of the command “Create Partition, Use Datum Plane” to make the cell partitions shown in Figure 130. When making the cell selections for the first prompt of each command, be certain to only select baseplate geometry, and only the baseplate geometry necessary for making the current partition. Extend the partition lines through the entirety of the baseplate. When complete, the geometry should be consistent with Figure 131.

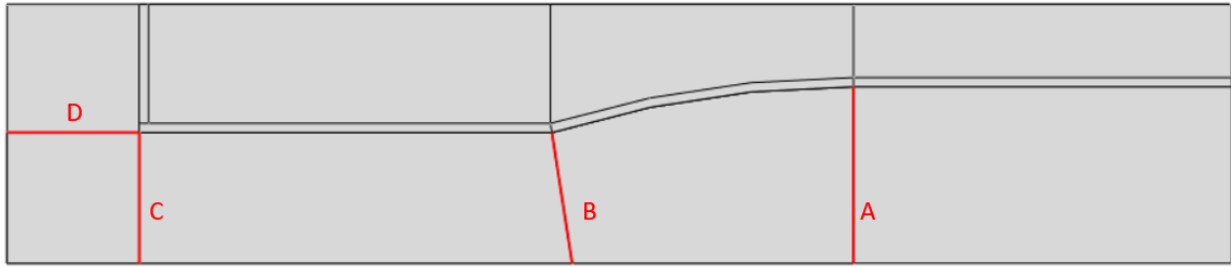


Figure 130: The four baseplate cell partitions made using “Partition Cell: Use Datum Plane”

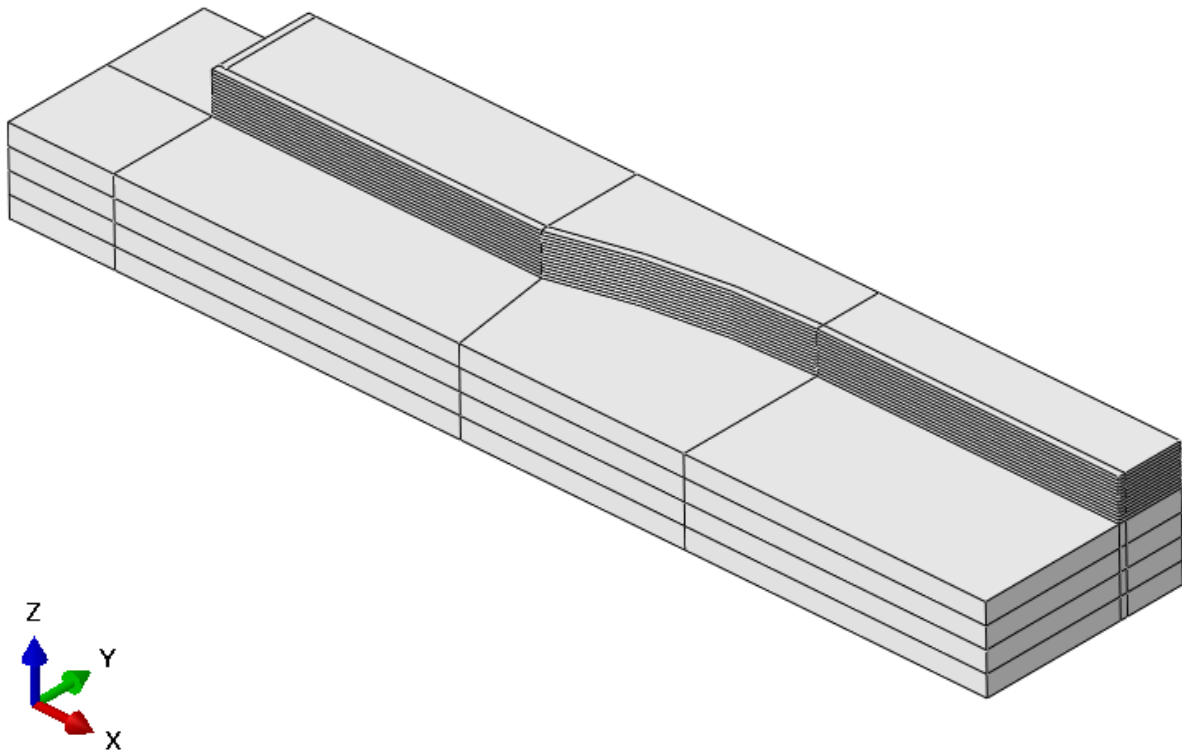


Figure 131: The geometry after all quarter-model partitioning is complete

After confirming geometry consistent with Figure 131, the toolbar module selection is changed from “Property” to “Part”, and two “Create Mirror” commands are executed. When executing both of these

“Create Mirror” commands, be certain to select the checkbox: “Keep internal boundaries”. When complete with this step, the part should be consistent with the model shown in Figure 132.

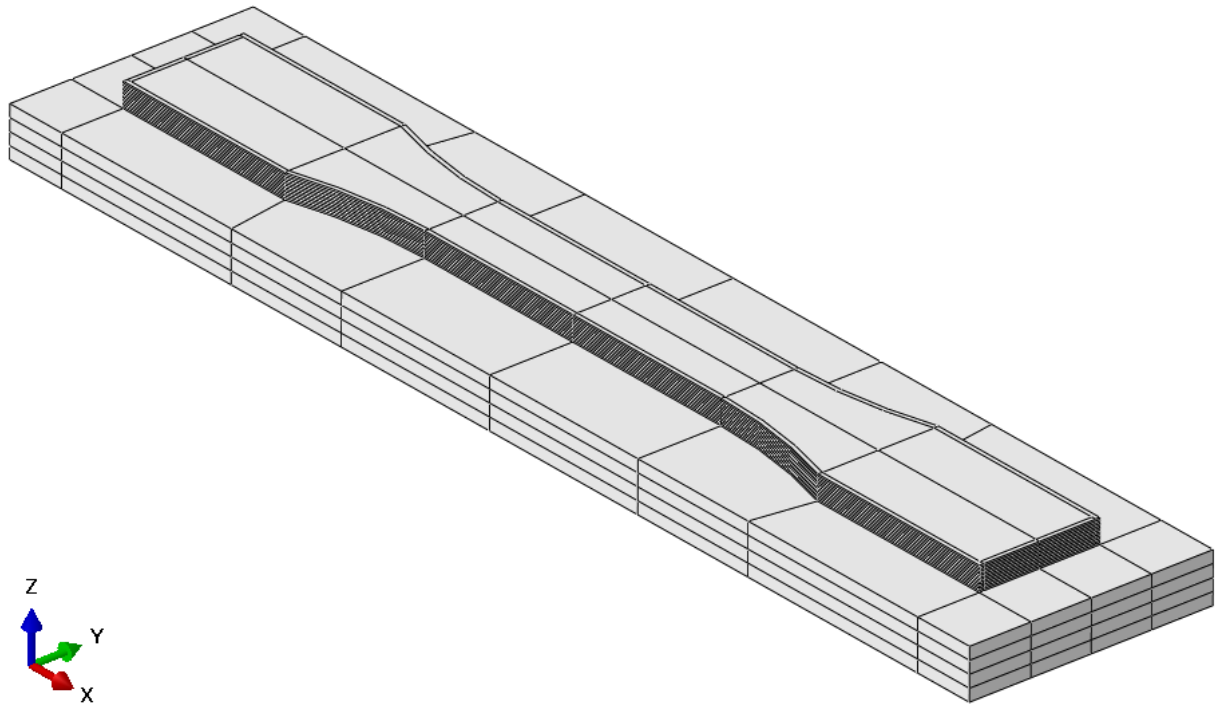


Figure 132: The model after both “Create Mirror” commands have been executed

Next, switch the module dropdown menu from “Part” to “Assembly”, and select the command “Create Instance”. Select “OK” to the dialog box that comes up. Next, switch the module to “Mesh”. On the same horizontal toolbar as the module selection, switch the object from “Assembly” to “Part”. The entire part should turn green, indicating the availability to specify a structured-type mesh. Next, select the command: “Seed Part”. In the dialog box that appears, specify the “Approximate global size” to be 0.00035(m). Next, local seeds are applied to the edges parallel to the Z-axis in the baseplate. These

edges are easiest to isolate by activating the “Left View”, holding the shift key, and making four tall, narrow box selections between the thickness partitions of the baseplate, as shown in Figure 133.

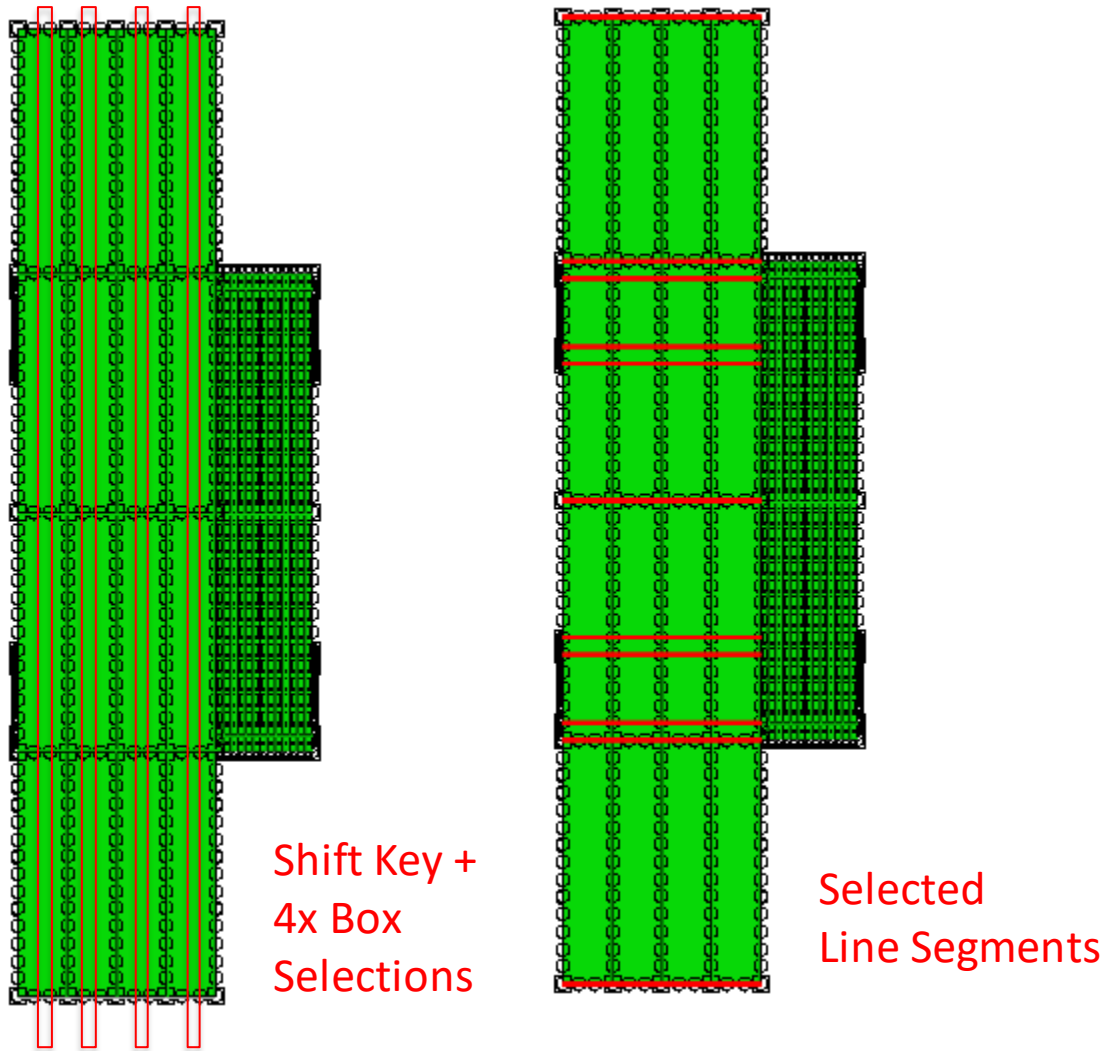


Figure 133: Four box selections to isolate vertical edges in the baseplate while in “Left View”

When complete with the selection of line segments, press MB3. In the dialog box that appears, specify the edge seeds “By number”, and under “Sizing controls”, select “1”. This will allow one element per selected edge to generate, limiting the number of elements which, by default, are generated through

the thickness of the baseplate. This is done because the additional devotion of computational cost to calculating the baseplate does not further the goal currently being pursued. Next, on the icon toolbar, click “Mesh Part”. A total of 128544 elements should generate on the part. This may be verified by an automatically generated readout in the “Message Area”.

Next, in the tree, under “Models (1)”, right click on “Model 1”, and click “Edit Attributes”. In the dialog box that appears, select the box: “Do not use parts and assemblies in input files”, as shown in Figure 134. When complete, select “Ok”. If this step is not performed with each mesh generation, the PathCoverage executable (if used) will initially boot, only to immediately close.

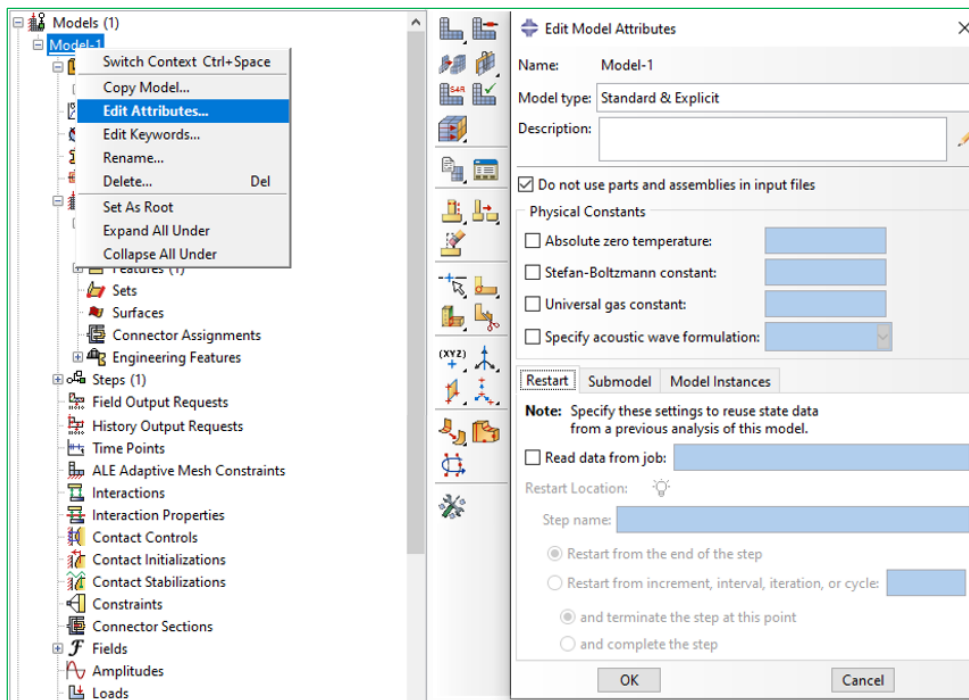


Figure 134: The deactivation of instance keywords in part and assembly files

Next, on the left side of the screen, scroll to the bottom of the tree, and, under the “Analysis” branch, right-click “Job”, followed by selecting the bold option “Create...”. In the “Create Job” dialog box that

appears, specify a name of “D638HS_MESH”, then click “Continue”, followed by “Ok” to the next dialog that appears. Next, right-click on the job name in the tree, and select “Write Input”. Select “Ok” to the overwrite existing file, and “Yes” no assigned section warning. These steps are shown in Figure 135.

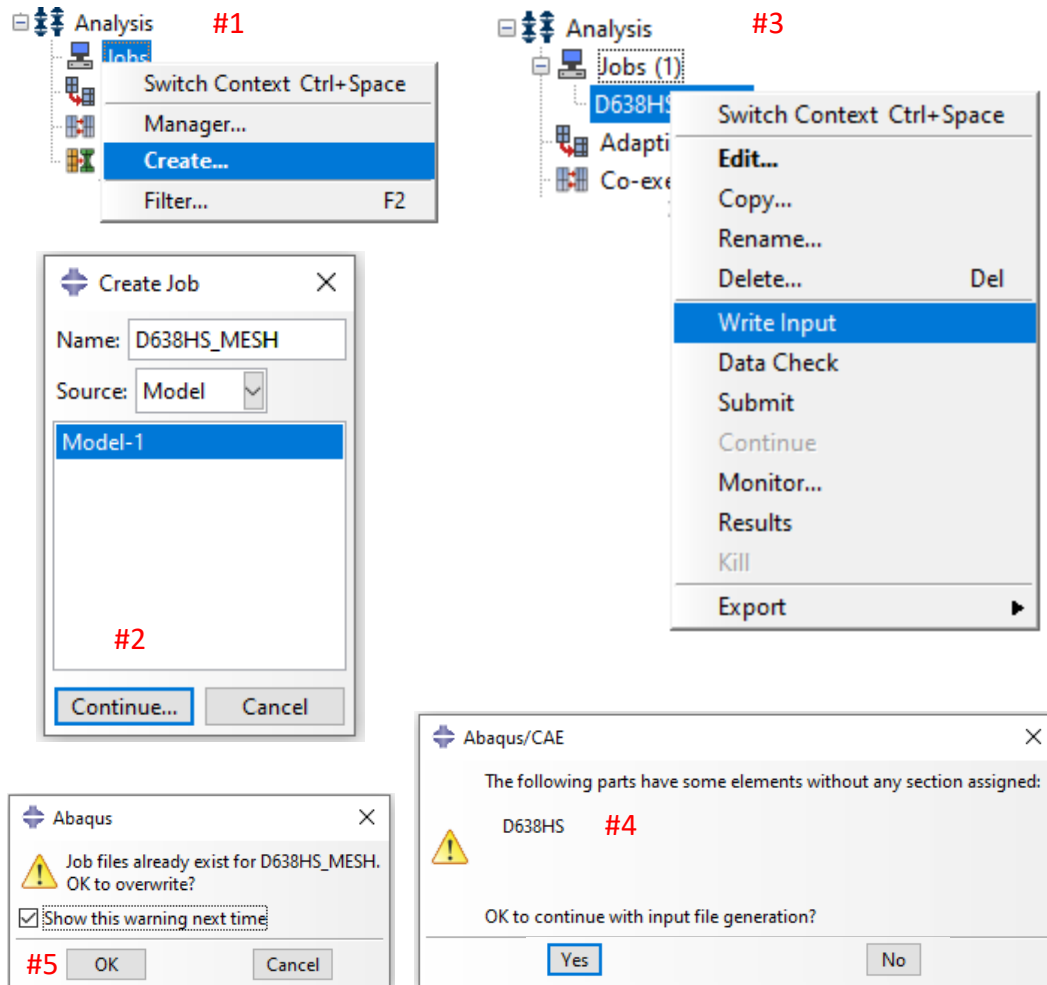


Figure 135: The five steps involved in job creation and writing a mesh input file

The steps leading to Figure 135 should generate a file in the directory: C:\temp. (filename: D638HS_MESH, filepath: C:\temp). At this stage, one would typically create a new working directory for

GENOA write and read files to and from, respectively. The location for previous folders of this type were located at C:\Users\User\Desktop\GL1122_Inputs, and the convention previously used for naming the folders was to name the folder today's date, followed by "input-output. For example: "9-17-19 input-output". If more than one such folder existed on a given day, as it may be recommended practice to generate one per generated job or per simulation attempt, a "-folder number" is added to the date of the additional folder. For example: "9-17-19-2 input-output". For the purposes of this tutorial, an example directory has already been made (filepath: C:\Users\User\Desktop\GL1122_Inputs\MM-DD-YY input-output).

There are three files which need be added to this directory to provide GENOA the requisite files it needs to generate outputs: The g-code, the external mesh, and the material definition. Optionally, a fourth file may be included to specify previously used settings. In the interest of verifying consistency, copies of the g-code, the mesh, and the material definition are provided in the necessary corresponding directory, with the extension "_COPY" added to the specified filename. The default file paths and naming conventions are discussed for the g-code, the mesh, and for the material definition in the following paragraph.

Navigate to the Cura working directory (filepath: C:\Users\User\Downloads\3D Print Test Parts), and copy the g-code to the GENOA working directory (Filename: D638HS_GCODE11_LH15mm, filepath: C:\Users\User\Desktop\GL1122_Inputs\MM-DD-YY input-output). Navigate to the ABAQUS working directory (C:\temp), and copy the mesh input file to the GENOA working directory (Filename: D638HS_MESH, filepath: C:\Users\User\Desktop\GL1122_Inputs\MM-DD-YY input-output). The latest version of the material definition should exist in the GENOA working directory (Filename: PLA-UMAT-IMPLICIT, filepath: C:\Users\User\Desktop\GL1122_Inputs\MM-DD-YY input-output). Next, ensure the

file “TDP_input.txt” exists in the current genoa working directory from a previous genoa working directory. (Filename: TDP_input.txt filepath: C:\Users\User\Desktop\GL1122_Inputs\MM-DD-YY input-output)

Open GENOA via the start menu or a desktop icon. Start a new project from either the top icon toolbar or the file menu. In the tree structure to the left, right-click on analysis, select “Add”, and select “3D Printing”. In the branch options that appear, right-click “Mesh-Model Generator”, and select “Model/PathCoverage/3DViz”. In the “Mesh/Model Generator” dialogue window that appears, under “Geometry”, select “Browse G-Code File”, and select “Yes” to the prompt to restore previous settings. These steps are shown in Figure 136.

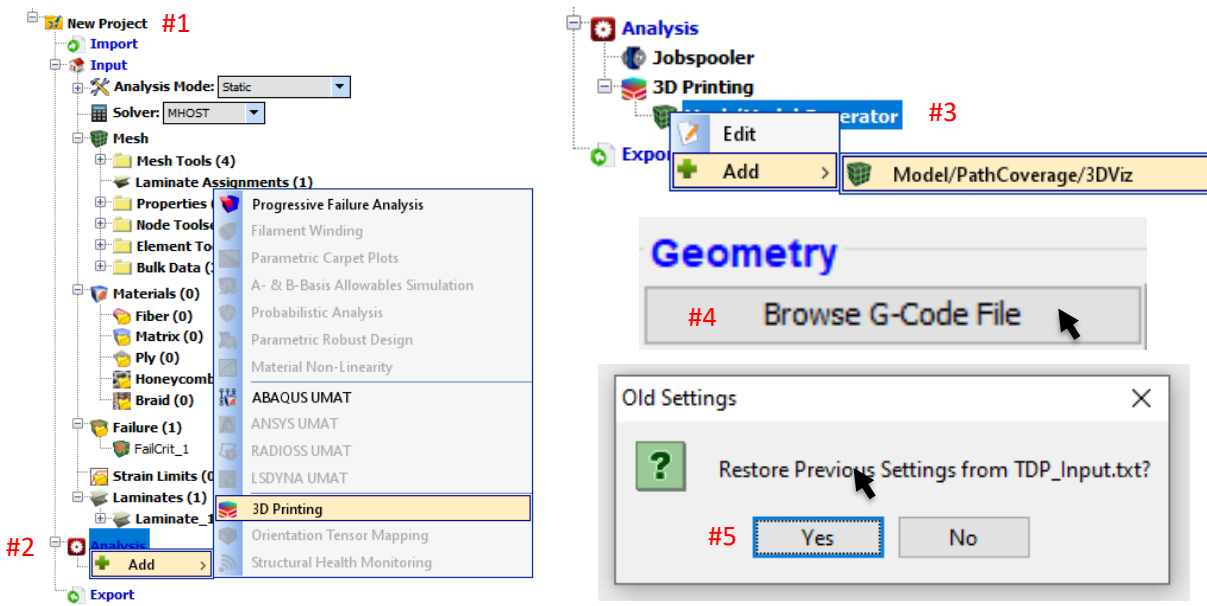


Figure 136: The 5-step process to restoring previous settings from a blank GENOA project

The presence of the file “TDP_input.txt” in the genoa working directory allows the majority of text-field-based settings keyed into the “Mesh/Model Generator” dialog window to be saved upon successful input file generation. In the event of the absence of this file, the necessary settings should match the screen capture of the mesh/model generator shown in Figure 137.

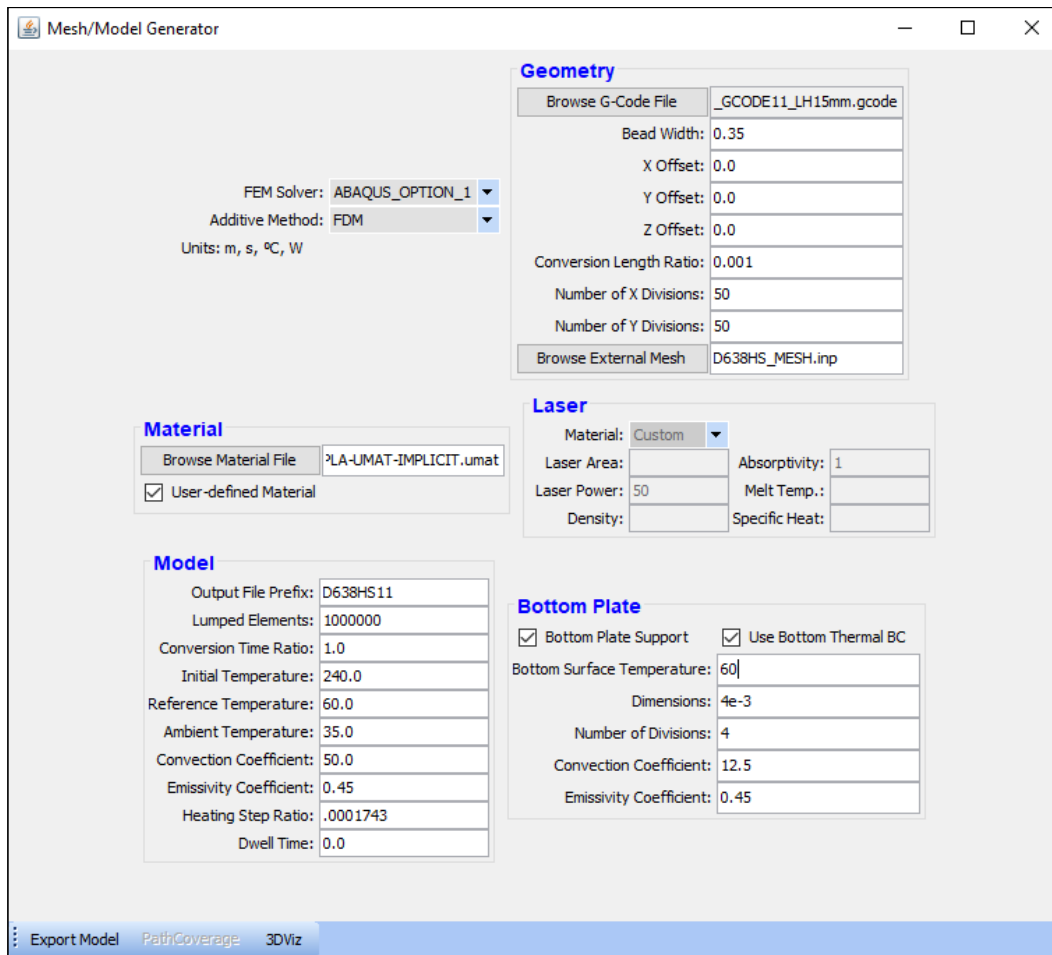


Figure 137: The required text-field-based and file-based settings to generate input files (associated with the D638 half-scale geometry)

The logic defining the values of the field-based settings for the Mesh/Model Generator in Figure 137 is presented in the following four paragraphs, one for each of the settings in the categories: “Geometry”, “Material”, “Model”, and “Bottom Plate”.

Under “Geometry”, the value of “Bead Width” is specified to be consistent with the value of “Line Width” in Cura. The next three settings, X, Y, and Z offset provide an alternate mechanism for achieving consistency between the offset between the g-code and the mesh. As this alternate mechanism is not used, they are given null values. The “Conversion Length Ratio” is a ratio of a unit length in the unit system for the g-code to a unit length in the unit system for the material definition. As the g-code provides length units in millimeters, and the material definition provides length units in meters, this ratio is 0.001. An alternate feature of the Mesh/Model generator is the “internal meshing” capability, in which, absent a specification of an external mesh filepath, the generator will generate a mesh from a.) the g-code coordinates, b.) the specification of “Number of X Divisions” and c.) the specification of “Number of Y Divisions”. Though this is a potentially useful feature in concept, the mesh generated from this approach was found to offer fundamental convergence issues due to the sharp-cornered nature of the mesh.

Under The box “User Defined Material” was specified by Alphastar to always be checked. No further logic was presented at the time, nor made available subsequent to the inquiry.

Under “Model”, the “Output File Prefix” designates the name of the input file one generates upon clicking the “Export Model” button in the lower left corner of the “Mesh/Model Generator”. For the purpose of this tutorial, the geometry is a D638 tensile specimen, half scale, with rasters aligned in the 11-direction, thus the prefix is “D638HS11”. The “Lumped Elements” setting specifies how many

elements of the mesh are to be calculated before making a write operation to update the output database (ODB) file. Though “Lumped Elements” may be specified to be any positive integer, a specification of any number exceeding the number of elements in each layer will specify to calculate one full layer per ODB write operation. The value of “Lumped Elements”, 1000000 in this case, is specified to be any large enough integer to always be governed by this limit. The “Conversion Time Ratio” is an artifact of a former level of capability in the “Mesh/Model Generator” where the input files generated would need be augmented by an estimation of the ratio of “simulation time” to “printing time”. Subsequent to the original version, an update to the software brought the ability to automatically extract an approximation of the actual print time by summing contributions from each extrude or travel move command given in the g-code. This update rendered the default value of “Conversion Time Ratio” to be 1, as is the specified instruction for this tutorial, though it is noted that further refinement of the actual print time approximation may be made by further refinement of the “Conversion Time Ratio”. The values of is the nozzle temperature in Celsius, for the test data the model was calibrated to. Assign “240.0” to the “Initial Temperature” field. The “Reference Temperature” is the glass transition for the printed material, in Celsius. Assign “60” for the “Reference Temperature”. The values for “Ambient Temperature”, “Convection Coefficient”, and “Emissivity Coefficient” are given by an iterative calibration process to match the gradient predicted by the thermal simulation to the gradient observed empirically. This process is further detailed in Chapter 8. Assign the values “35.0”, “50.0” and “0.45” to the settings “Ambient Temperature”, “Convection Coefficient”, and “Emissivity Coefficient”, respectively. By hovering the mouse over the input field for “Heating Step Ratio”, the definition is given as “the ratio of the first simulation sub-step (heating) to the second sub-step (cooling)”. The first simulation refers to a thermal simulation, in which a series of two sub-step operations are made. The first sub-step creates a number of finite elements in the quantity specified by “lumped elements”, up to but not exceeding a full layer of finite elements. The created elements are initialized at the printing

temperature, and are then allowed to undergo cooling due to heat transfer with the surroundings during the second sub-step. As the measure of time allotted for the first sub-step is in terms of simulation time, even if a layer time is approximated from the g-code, there exists the need for another relation to establish a relationship for element creation in terms of real time. Thus, the heating ratio is expressed as the ratio of time to complete the creation of one element to the time to complete the creation of one layer. This relation is shown in Equation 13. The parameter “Dwell Time” is set to zero. “Dwell Time” will generally be set to zero, save for cases in which exceedingly small cross-sections are repeatedly printed atop the last with print settings as to be governed by the slicer setting “Minimum Layer Time”. In such a case, the value of “Dwell Time” would correspond to the time interval, in seconds, that the print gantry remains parked awaiting the completion of the “Minimum Layer Time”. For example, if a cross-section takes seven seconds to print, with a “Minimum Layer Time” of ten seconds, “Dwell Time” would be specified to be “3”.

$$HR = \frac{\textit{Element Creation Time}}{\textit{Layer Creation Time}} = \frac{\frac{\textit{Raster Width}}{\textit{Print Velocity}}}{\frac{\textit{Cura Print Time Estimate}}{\textit{Number of Layers}}} = .0001743 \quad \text{Equation 13}$$

Under the category “Bottom Plate”, check both the box “Bottom Plate Support” and the box “Use Bottom Thermal BC”, indicating the use of a heated baseplate. Specify the setting “Bottom Surface Temperature” to “60”. The thickness of the glass build plate on the Ultimaker 2+ is 4mm, and the thickness is divided into 4 thickness divisions in the external mesh. Specify “4e-3” under “Dimensions”, and “4” under “Number of Divisions”. The specified values for “Convection Coefficient” and “Emissivity Coefficient” were taken as default values for a steel baseplate from the GENOA tutorial “AM3DP-FDM-

ABS". Specify the values "12.5" and "0.45" for "Convection Coefficient" and "Emissivity Coefficient", respectively.

In the lower left corner of the "Mesh/Model Generator" dialog window, click the button "Export Model". In the GENOA working directory, this will generate two input files: "D638HS11_heat.inp", and "D638HS11_disp.inp". The successful generation of the files will allow PathCoverage to be run. Though the approach this tutorial details does not make use of the PathCoverage module or the PathCoverage outputs, all the requisite inputs to run PathCoverage are currently present, so a brief instructional tangent is provided, that it may be used in the future for a possible alternate approach. Click PathCoverage on the Mesh/Model generator. This will bring up the window shown in Figure 138.

When the PathCoverage interface comes up, it will show a color-coded chronology of the raster pattern, overlaid by the mesh. This color-coded chronology is shown in Figure 138. If the window attempts to come up, but crashes, it likely means there is no overlap between the coordinates defined by mesh and the coordinates defined by the g-code. This can often be caused by one of two errors in the process: 1.) forgetting to generate the part in Solidworks in the correct unit system (MKS), or 2.) failing to check the "Do not use parts and assemblies in input files" checkbox before exporting the mesh. Provided that the interface does come up without incident, left-click a single time inside the window, then use the up and down arrow keys to scroll through the layers. Particularly, note that on layer number 13, the color-coded path lines from the g-code show up, but the mesh overlay disappears. This flaw is shown in Figure 139.

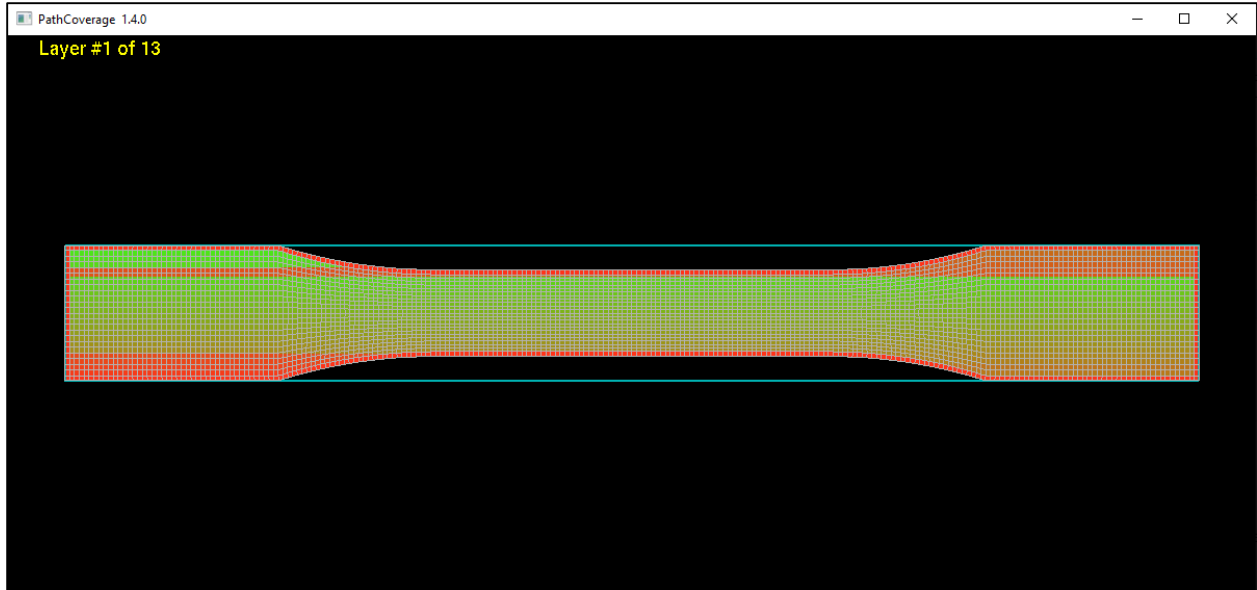


Figure 138: The color-coded chronology shown by PathCoverage

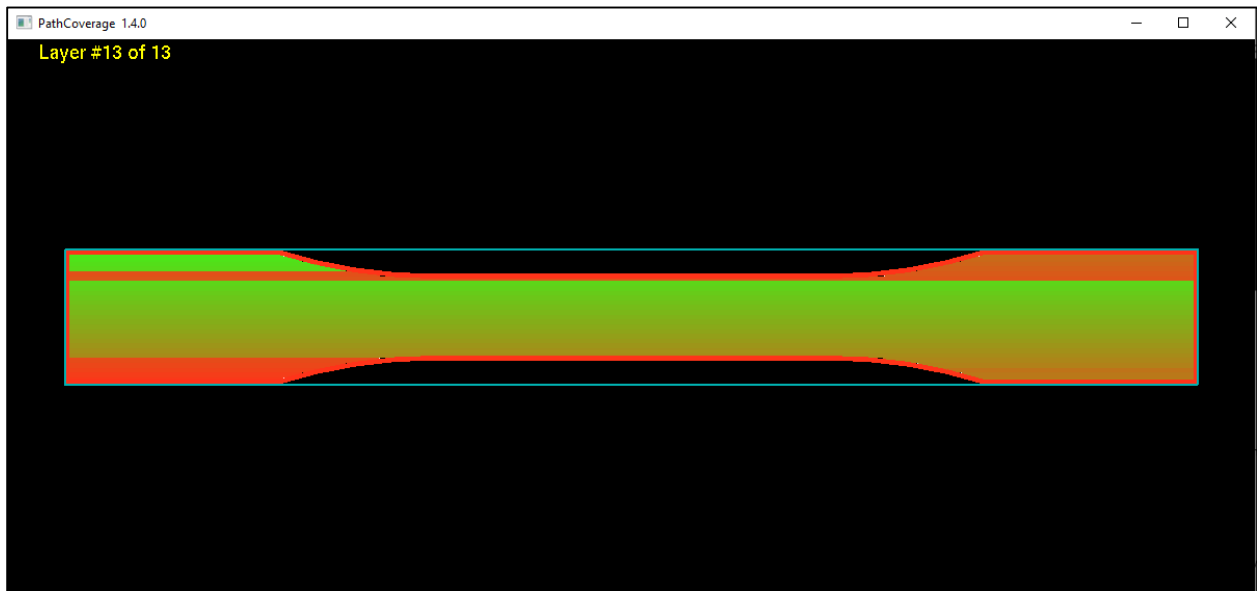


Figure 139: A depiction of the missing mesh overlay on layer 13 in PathCoverage

Due to this flaw in PathCoverage, a downward adjustment must be made to the layer height in the g-code which will allow the PathCoverage interface to recognize the last layer. Return to Cura, adjust the layer height downward from 0.15mm to 0.148mm, and re-generate the g-code. Generally, the magnitude of this downward adjustment, if necessary, should be such that the number of layers remains the same. Save the file with the following name and location: (filename:

D638HS_GCODE11_LH148mm.gcode, filepath: C:\Users\User\Downloads\3D Print Test Parts)

Open the modified file in Notepad++ (filename: D638HS_GCODE11_LH148mm.gcode, filepath: C:\Users\User\Downloads\3D Print Test Parts). Execute a “find and replace” function to replace all occurrences of "G0" with "G1". Save a copy of the file in the current GENOA working directory (filename: D638HS_GCODE11_LH148mm.gcode, filepath: C:\Users\User\Desktop\GL1122_Inputs\MM-DD-YY input-output).

Bring back up the “Mesh/Model Generator” window again, and browse for the revised g-code. This time, when the “restore previous settings” window comes up, select “No”, as confirming this selection will force one to need to browse for the mesh and material file again. Next, click the “Export Model” button again, generating another set of input files. Once the prompt completes, Click the “PathCoverage” button.

Once PathCoverage opens, confirm the interface recognizes all the layers by using the up and down arrow keys, then, click the mouse wheel (MB3), and select “Enter Void Ratio Computation Mode”. This should reduce the PathCoverage window to a fraction of its former size and display a message: “*Please do not resize window”. (You have to resize the window to read the entire message, don’t do that.) This window is shown in Figure 140.

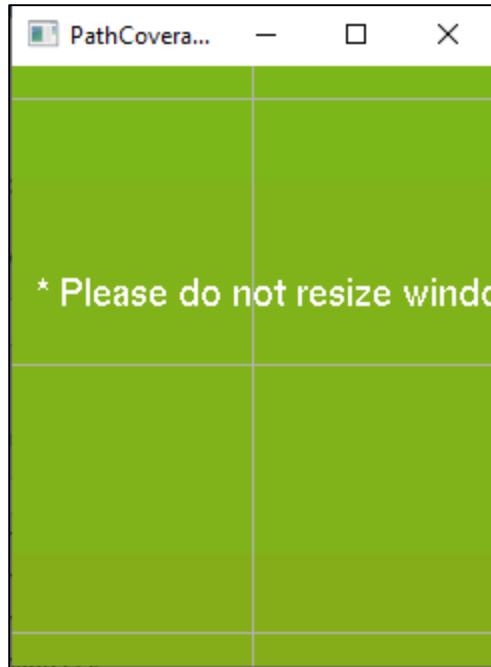


Figure 140: The PathCoverage void computation mode window

Use the top toolbar handle to move the window to a convenient part of the screen, such as the lower right corner. If and when the computation crashes, Often the crash will freeze the graphical display, forcing the user to tolerate an irremovable flashing from the desktop space the window occupies, so it is best to relocate this to a lesser-seen portion of the monitor before attempting to execute the computation. Once relocated, click the middle mouse wheel again and select “Compute Void Ratio for all Layers”.

One may view the progress of the simulation in real-time by viewing the command window corresponding to the GENOA graphic interface. As the simulation completes each layer’s void ratio computations, a summary will be written to this command window. Additionally, a more comprehensive version of this output is written to a text file generated in the working directory (filename: PathCoverage.txt, filepath: C:\Users\User\Desktop\GL1122_Inputs\MM-DD-YY input-output).

After the void computation completes, the window will return to its original dimensions, depicting a color-coded contour map of the calculated voids. One may need to left-click inside this window, and press the up-and-down arrow keys to get the graphical display to refresh. To display a legend of key-bindings which execute differing commands, press “h”. In terms of file generation, nothing further needs be done with this interface, this visualization stage is displayed for the purposes of graphically depicting void ratios only.

At this stage, one would typically use a file browser to create a folder in the ABAQUS working directory to contain generated GENOA files. Previously kept file folders followed the convention: “MM-DD-YY-simulation number”, For example, a folder called: “9-17-19-1” would correspond to the first simulation on 9-17-19. For the purposes of this tutorial, an example directory has already been defined and populated with the necessary files: (filepath: C:\temp\MM-DD-YY-1). Populating this example directory involved copying four files from the GENOA working directory into the newly created directory: “D638HS11_heat.inp”, “D638HS11_disp.inp”, “ElementVoidRatio_ABAQUS_Implicit_Run1.txt”, and “ElementVoidRatio_ABAQUS_Explicit_Run1.txt”. Next, open two of the pasted files in Notepad++: “ElementVoidRatio_ABAQUS_Explicit_Run1.txt”, and “ElementVoidRatio_ABAQUS_Implicit_Run1.txt”. Save the explicit void ratio text file as: “ElementVoidRatio_ABAQUS_Explicit_Run1.inp”, and the implicit void ratio text file as: “D638HS11_disp.asc”. In a Windows explorer window browsed to the ABAQUS working directory, the text based versions of the format-modified files may now be deleted. Next, select the file “D638HS11_heat”, copy the file to the clipboard, and paste a duplicate into the same directory, automatically naming the copy “D638HS11_heat - Copy”. Similarly, clipboard duplicate the file: “D638HS11_disp” and rename the copy “D638HS11_load”. The steps illustrated in this paragraph

are shown in Figure 141, however, all steps illustrated in this paragraph have been executed in the creation of the example working directory.

Name	Type
 D638HS11_disp	INP File
 D638HS11_heat	INP File
 ElementVoidRatio_ABAQUS_Explicit_Run1	Text Document
 ElementVoidRatio_ABAQUS_Implicit_Run1	Text Document

a.)

Name	Type
 D638HS11_heat	INP File
 D638HS11_disp	INP File
 ElementVoidRatio_ABAQUS_Explicit_Run1	INP File
 D638HS11_disp.asc	ASC File

b.)

Name	Type
 D638HS11_heat	INP File
 D638HS11_disp	INP File
 ElementVoidRatio_ABAQUS_Explicit_Run1	INP File
 D638HS11_disp.asc	ASC File
 D638HS11_heat - Copy	INP File
 D638HS11_load	INP File

c.)

Figure 141: The ABAQUS working directory at various stages throughout the procedure (located at the filepath: C:\temp\MM-DD-YY-1. Showing contents: a.) after pasting the 4 files from the GENOA working directory, b.) after modifying the format and name of the void ratio files, c.) after creating copies of the “heat” and “disp” input files)

There are three input files which are sequentially executed to model the process and apply a service loading. The thermal simulation, designated by the suffix “_heat”, predicts a time-and-position-

dependent thermal field. The thermo-structural simulation, designated by the suffix “_disp”, couples the results of the thermal simulation with: a.) a temperature-dependent modulus (TDM), and b.) a temperature-dependent coefficient of thermal expansion (TDCTE) to predict residual stresses on an element-by-element basis. The dissimilarity in temperature-driven properties (TDM, TDCTE) both a.) between consecutive layers, and b.) between the 1st layer and the baseplate are the mechanisms for the development of thermally-induced residual stresses. The exact formulation of these thermally-induced residual stresses have yet to be provided. The service loading simulation, designated by “_load”, accepts stress-based initial conditions from the thermo-structural simulation, and applies a temperature-independent material definition to the modeled geometry. Service loads are applied, and a response is predicted. In the case of the tensile specimen geometry, applying the service loads entails forcing a displacement at opposing ends of the specimen sufficient to peak the stress-strain curve. Loads and displacements are then extracted following the loading simulation in ABAQUS CAE. Prior to the execution of the three sequentially executed input files, designated: “_heat”, “_disp”, and “_load”, a series of post-processing edits must be made.

Open the thermal simulation in Notepad++: (filename: “D638HS11_heat”, filepath: C:\temp\MM-DD-YY-1), and execute a find function (Ctrl+F), searching for the word “solid”. The first occurrence should show in the section assignment, as shown in Figure 142. The second reference should present on the following line. Two replacements are made, the first replacing the text “bottom_material” with “mat_bottom_plate”, the second replaces the text “material” with the text “TNPLY00001”. The syntax for these replacements are shown in Figure 142.

```

*solid section, elset=bottom_plate, orientation=orien_bottom_plate, material=bottom_material
**
*solid section, elset=elset_whole_part, orientation=dist_orientation, material=material      a.)

*solid section, elset=bottom_plate, orientation=orien_bottom_plate, material=mat_bottom_plate
**
*solid section, elset=elset_whole_part, orientation=dist_orientation, material=material      b.)

*solid section, elset=bottom_plate, orientation=orien_bottom_plate, material=mat_bottom_plate
**
*solid section, elset=elset_whole_part, orientation=dist_orientation, material=INPLY00001    c.)

```

Figure 142: A depiction of the section assignments made in the thermal simulation input file (Showing: a.) as exported by GENOA, b.) specifying the material for the bottom plate, c.) specifying the material for the bottom plate and for the printed material)

Next, another find function is executed, searching for the word “initial”. This brings the user to the specification of initial conditions. The specification of nodal temperatures for the printed material is changed from “240.0” to “60.0”, as is shown in Figure 143.

```

*initial conditions, type=temperature
NSET_ALL_NODES, 240.0
NSET_BOTTOM_PLATE_NODES, 60.0      a.)

*initial conditions, type=temperature
NSET_ALL_NODES, 60.0
NSET_BOTTOM_PLATE_NODES, 60.0      b.)

```

Figure 143: the specification of initial conditions for the printed material (Showing: a.) as exported by GENOA, b.) following amendment of the initialization temperature to the glass transition temperature)

The thermal simulation is executed via the command prompt, by first navigating the directory to the file path of the current ABAQUS working directory, then, by using the syntax shown in Figure 144.

```

C:\> Command Prompt
Microsoft Windows [Version 10.0.18362.356]
(c) 2019 Microsoft Corporation. All rights reserved.

C:\Users\User>cd\temp\MM-DD-YY-1 a.)
C:\temp\MM-DD-YY-1>abqumat2017 job=D638HS11_heat int cpus=4_ b.)

```

Figure 144: A depiction of the syntax for executing the thermal simulation

(Showing: a.) changing the directory to the ABAQUS working directory, b.) specifying the job name, activating interactive mode, and specifying four processor cores)

When viewing the command window during the execution of the thermal simulation, there is little output available to be viewed. To monitor intervals of progress in the simulation, one must open the status file generated upon the initiation of the thermal simulation (filename: "D638HS11_heat.sta",

filepath: C:\temp\MM-DD-YY-1). A depiction of a status file is shown in

Figure 145. As the calculation of each layer consists of two sub-steps, the steps to completion in the status file will correspond to twice the layer count plus one initialization step.

Abaqus/Standard 3DEXPERIENCE R2017x										DATE 17-Sep-2019 TIME 12:31:57	
SUMMARY OF JOB INFORMATION:											
STEP	INC	ATT	SEVERE	EQUIL	TOTAL	TOTAL	STEP	INC OF	DOF	IF	
			DISCON	ITERS	ITERS	TIME/	TIME/LPF	TIME/LPF	MONITOR	RIKS	
			ITERS			FREQ					
1	1	1	0	1	1	1.00e-008	1.00e-008	1.000e-008			
2	1	1	0	1	1	0.00234	0.00234	0.002341			
2	2	1	0	1	1	0.00468	0.00468	0.002341			
2	3	1	0	1	1	0.00702	0.00702	0.002341			
2	4	1	0	1	1	0.0117	0.0117	0.004693			
2	5	1	0	1	1	0.0211	0.0211	0.009366			
2	6	1	0	1	1	0.0234	0.0234	0.002341			
3	1	1	0	3	3	13.5	13.4	13.43			
3	2	1	0	3	3	26.9	26.9	13.43			
3	3	1	0	3	3	40.3	40.3	13.43			
3	4	1	0	2	2	53.7	53.7	13.43			
3	5	1	0	2	2	73.9	73.9	20.14			
3	6	1	0	2	2	104.	104.	30.22			
3	7	1	0	2	2	134.	134.	30.22			
4	1	1	0	2	2	134.	0.00234	0.002341			
4	2	1	0	1	1	134.	0.00468	0.002341			
4	3	1	0	1	1	134.	0.00702	0.002341			
4	4	1	0	1	1	134.	0.0117	0.004693			
4	5	1	0	1	1	134.	0.0211	0.009366			

Figure 145: The viewing of a status file in Notepad++

After submitting the thermal simulation, open the residual stress simulation in Notepad++: (filename: “D638HS11_disp”, filepath: C:\temp\MM-DD-YY-1), and add the suffix “-VOID” to the end of the material name under both the shell section and the material name assignments, as is shown in Figure 146.

```

*****
**      ABAQUS GENOA UMAT PROPPERTIES (created by GENOA-MCQ)      **
*****
*SHELL SECTION, ELSET=ELSET_UMAT_SHELL, COMPOSITE
  0.1397E-03, 1, TNPLY00001-VOID, 0.0000E+00      a.)
*TRANSVERSE SHEAR STIFFNESS
  1.370224E+05, 1.397000E+05
*INITIAL CONDITIONS, TYPE=SOLUTION,USER      b.)
*MATERIAL, NAME=TNPLY00001-VOID

```

Figure 146: Two instances of adding the “-VOID” suffix to the material name (Showing the suffix: a.) in the shell section, and b.) in the definition of the material name)

Next, similar to the replacement performed in the editing of the thermal simulation, execute a find function (Ctrl+F), searching for the word “solid”. Make the replacements shown in Figure 147, noting that this differs slightly from the replacement made in the thermal simulation.

```

*solid section, elset=bottom_plate, orientation=orien_bottom_plate, material=bottom_material
**
*solid section, elset=elset_whole_part, orientation=dist_orientation, material=material      a.)

*solid section, elset=bottom_plate, orientation=orien_bottom_plate, material=mat_bottom_plate
**
*solid section, elset=elset_whole_part, orientation=dist_orientation, material=material      b.)

*solid section, elset=bottom_plate, orientation=orien_bottom_plate, material=mat_bottom_plate
**
*solid section, elset=elset_whole_part, orientation=dist_orientation, material=TNPLY00001-VOID      c.)

```

Figure 147: A depiction of the section assignments made in the residual stress input file (Showing: a.) as exported by GENOA, b.) specifying the material for the bottom plate, c.) specifying the material for the bottom plate and for the printed material, including the suffix “-VOID”)

The final edit made to the residual stress file is the addition of two step definitions at the end of the input file. The first added step cools the part to room temperature, the second added step establishes equilibrium following the removal of the base plate geometry. The syntax for these steps are shown in Figure 148. Rather than transcribing Figure 148 manually, a file has been provided which may be readily copied and pasted (filename: "DISP_ADDED_STEPS", filepath: C:\temp\Tutorial Files)

```
*STEP, NAME=COOLDOWN, NLGEOM=YES
*STATIC
100.0, 500.0, 1.0E-10, 100.0
*TEMPERATURE
NSET_ALL_NODES, 25.0
*OUTPUT, FIELD
*NODE OUTPUT
NT, RF, U
*ELEMENT OUTPUT
LE, PE, SDV, S, TEMP
*OUTPUT, HISTORY, VARIABLE=PRESELECT, FREQUENCY=10
*END STEP
*STEP, NAME=PLATE_REMOVE, NLGEOM=YES
*STATIC
1E-8, 1E-8, 1E-8, 1E-8,
*MODEL CHANGE, REMOVE
BOTTOM_PLATE
*CONTROLS, RESET
*CONTROLS, PARAMETERS=FIELD, FIELD=DISPLACEMENT
, 1., , , , ,
*OUTPUT, FIELD, FREQUENCY=10
*NODE OUTPUT
NT, RF, U
*ELEMENT OUTPUT
LE, PE, SDV, S, TEMP
*OUTPUT, HISTORY, VARIABLE=PRESELECT, FREQUENCY=10
*END STEP
```

Figure 148: The syntax for two added steps at the end of the residual stress input file

Executing the residual stress input file is done much in the same fashion as was shown in Figure 144, save to the specification of the file name suffix of “_disp”, rather than “_heat”. During the execution of

the residual stress simulation, contrary to the thermal simulation, a summary of progress intervals will display in the command window.

Open the service loading simulation in Notepad++: (filename: "D638HS11_load", filepath: C:\temp\MM-DD-YY-1). The loading simulation at the present stage is an as-exported copy of the residual stress simulation. As loading takes place at room temperature, the length of the material definition specified for the loading simulation is significantly shorter. The first step in the processing of the loading simulation is replacing this material definition with the appropriate temperature independent definition. Replace the first 168 lines of the loading simulation with the provided temperature independent definition: (filename: "PLA-SPLY0001-ORIGINAL", filepath: C:\temp\Tutorial Files). A depiction of this definition is shown in Figure 149.

```

*heading
Combine all layers together
*Preprint, echo=NO, model=NO, history=NO, contact=NO
*****
**      ABAQUS GENOA UMAT PROPERTIES (created by GENOA-MCQ)      ** Original, Configured for Explicit
*****
***INCLUDE, INPUT=ElementVoidRatio_ABAQUS_Explicit_Run1.inp
**MATERIAL, NAME = SPLY0001-VOID
*USER MATERIAL, CONSTANTS= 59
**      E11,          E22,          E33,          G12,          G13,          G23,          NU12,          NU13,
3.376000E+09, 3.183000E+09, 3.183000E+09, 1.177000E+09, 1.177000E+09, 1.200000E+09, 3.548900E-01, 3.548900E-01,
**      NU23,          S11T,          S11C,          S22T,          S22C,          S33T,          S33C,          S12S,
3.548900E-01, 6.000000E+07, 1.102170E+08, 5.270000E+07, 1.102170E+08, 5.270000E+07, 1.562170E+08, 3.432805E+07,
**      S13S,          S23S,          RHO,          DFACIT,          DFAC1C,          DFAC1S,          FFACT,          DAMAGE,
3.432805E+07, 3.432805E+07, 1.250000E+03, 1.000000E+00, 1.000000E+00, 1.000000E+00, 1.000000E-01, 16212,
**      FRACTURE,     EPS11T,          EPS11C,          EPS22T,          EPS22C,          EPS33T,          EPS33C,          EPS12S,
16212,
1, 1, 1, 1, 1, 1, 1, 1,
**      EPS23S,          EPS13S,          STRAIN_1,          STRESS_1,          STRAIN_2,          STRESS_2,          STRAIN_3,          STRESS_3,
1, 1, 0.000000E+00, 0.000000E+00, 1.611104E-03, 5.439087E+06, 3.222205E-03, 1.087817E+07,
**      STRAIN_4,          STRESS_4,          STRAIN_5,          STRESS_5,          STRAIN_6,          STRESS_6,          STRAIN_7,          STRESS_7,
4.858686E-03, 1.631726E+07, 6.624450E-03, 2.175635E+07, 8.401236E-03, 2.719544E+07, 1.017801E-02, 3.263452E+07,
**      STRAIN_8,          STRESS_8,          STRAIN_9,          STRESS_9,          STRAIN_10,          STRESS_10,          STRAIN_11,          STRESS_11,
1.200080E-02, 3.807361E+07, 1.412164E-02, 4.351270E+07, 1.689852E-02, 4.895179E+07, 1.989775E-02, 5.439087E+07,
**      STRAIN_12,          STRESS_12,          MUP,
2.291548E-02, 6.000000E+07, 0.000000E+00,
*DEPVAR, DELETE = 4
10,
***DEPVAR
** 6
*DENSITY
1.250000E+07

```

Figure 149: The material definition for the loading simulation, “D638HS11_load”

Next, execute a find function, searching for the text “*ELEMENT”. Find the first occurrence of this text, and make note of the line number. Then, press the enter key, navigating the find function to the second occurrence of “*ELEMENT”. The lines between the first and second occurrences of the text “*ELEMENT” correspond to the element definitions for the bottom plate. These definitions need be deleted as the bottom plate was removed at the end of the residual stress simulation. Place the cursor at the end of the line immediately prior to the second instance of “*ELEMENT”. Next, using either the scroll wheel or the scroll bar to navigate back to the first instance (without moving the cursor). Select all the element definitions for the bottom plate by holding “shift”, and clicking the beginning of the line containing the first instance of “*ELEMENT”. Delete this selection. These steps are shown in Figure 150:

147416	147247,	1.128951240E-01,	1.140454560E-01,	1.799999970E-03						
147417	147248,	1.125463400E-01,	1.140454560E-01,	1.799999970E-03						
147418	147249,	1.121975630E-01,	1.140454560E-01,	1.799999970E-03						
147419	147250,	1.118487790E-01,	1.140454560E-01,	1.799999970E-03						
147420	*ELEMENT, TYPE=C3D8, ELSET=BOTMOM_PLATE									a.)
147421	1,	29031,	936,	1,	859,	29200,	911,	4,	884	
147422	2,	29032,	29031,	859,	860,	29201,	29200,	884,	883	
147423	3,	29033,	29032,	860,	861,	29202,	29201,	883,	882	
147424	4,	29034,	29033,	861,	862,	29203,	29202,	882,	881	

202330	122679,	141649,	141648,	27873,	27872,	142049,	142048,	27913,	27912	
202331	122680,	141650,	141649,	27872,	27871,	142050,	142049,	27912,	27911	
202332	122681,	15040,	141650,	27871,	451,	15050,	142050,	27911,	452	
202333	*ELEMENT, TYPE=C3D8, ELSET=ELSET_PART_LAYER_1									b.)
202334	8252,	4,	1783,	72,	23,	128,	2944,	76,	77	
202335	8253,	1783,	1782,	3070,	72,	2944,	2945,	3028,	76	
202336	8254,	1782,	1781,	3069,	3070,	2945,	2946,	3027,	3028	

147417	147248,	1.125463400E-01,	1.140454560E-01,	1.799999970E-03						
147418	147249,	1.121975630E-01,	1.140454560E-01,	1.799999970E-03						
147419	147250,	1.118487790E-01,	1.140454560E-01,	1.799999970E-03						
147420	*ELEMENT, TYPE=C3D8, ELSET=ELSET_PART_LAYER_1									c.)
147421	8252,	4,	1783,	72,	23,	128,	2944,	76,	77	
147422	8253,	1783,	1782,	3070,	72,	2944,	2945,	3028,	76	
147423	8254,	1782,	1781,	3069,	3070,	2945,	2946,	3027,	3028	

Figure 150: The process of removing the base plate element definitions

(Showing a.) Finding the 1st occurrence of the text “*ELEMENT”, b.) Finding the 2nd occurrence, c.) The input file after removing the element definitions)

Next, execute a find function, searching for the text “solid”, leading the cursor to the specification of the solid section assignment. The line corresponding to the section assignment for the base plate is deleted, and the section assignment corresponding to the printed material is modified from “material=material” to “material=SPLY0001-VOID”. These modifications are shown completed in Figure 151.

```

*orientation, name=orien_bottom_plate
 1., 0., 0., 0., 1., 0.
 3, 0
**
*solid section, elset=elset_whole_part, orientation=dist_orientation, material=SPLY0001-VOID
*orientation, name=dist_orientation
 1.,0.,0.,0.,1.,0.
 3, distribution_angle

```

Figure 151: The solid section assignment in the loading simulation

Next, execute a find function, searching for the text “*INITIAL”, bringing the cursor to the specification of initial conditions. Delete all lines between the beginning of this line and the end of the file. This step is shown completed in Figure 152.

```

221952 105188, 105231, 1
221953 112503, 112975, 1
221954 113977, 114372, 1
221955 120755, 120795, 1
221956 127643, 128093, 1
221957 *NSET, NSET=HAZ_NOD_00013, ELSET=HAZ_ELM_00013
221958
221959

```

Figure 152: The loading simulation following the removal of all residual stress step definitions

The next step involves the creation of node sets to specify boundary conditions. In the case of a uniaxial tension test, this involves fixing one end of the tensile specimen geometry at the grip section, and forcing a displacement upon the grip section of the opposing end sufficient to strain the gauge length to fracture. In order to create the node sets, a copy of the thermal simulation must be truncated and read into ABAQUS CAE as an imported model. The node sets are then defined on this imported model, and a disposable job is created and written. The disposable job is opened in Notepad++, and the node set definitions are found, edited, and copied into the loading simulation.

Open the copy of the thermal simulation in Notepad++: (filename: "D638HS11_heat - Copy", filepath: C:\temp\MM-DD-YY-1). Execute a find function, searching for the text "*ELSET". Delete all lines following the first instance of "*ELSET" and the end of the file. This step is shown completed in Figure 153.

```
275988 *NSET, NSET=NSET_NODE_LAYER_10, ELSET=ELSET_PART_LAYER_10
275989 *NSET, NSET=NSET_NODE_LAYER_11, ELSET=ELSET_PART_LAYER_11
275990 *NSET, NSET=NSET_NODE_LAYER_12, ELSET=ELSET_PART_LAYER_12
275991 *NSET, NSET=NSET_NODE_LAYER_13, ELSET=ELSET_PART_LAYER_13
275992 *ELSET, ELSET=ELSET_WHOLE_PART
275993
275994
```

Figure 153: The truncation of the copy of the thermal simulation in Notepad++.

Save the file in Notepad++, and open ABAQUS CAE. On the character-based toolbar, under "File", select File>>Import>>Model.... A dialog window will appear. Under the "File Filter" dropdown, select the "*.inp, *.pes" file extensions, and browse for the modified copy of the thermal simulation: (filename: "D638HS11_heat - Copy", filepath: C:\temp\MM-DD-YY-1). The copy of the thermal simulation is truncated as to allow the import process to complete in a reasonable time interval. The processing of step definitions imported in this manner are particularly time consuming. Upon the completion of the import process, an orphan mesh will appear in the graphics area, dark green in color. This is shown in Figure 154.

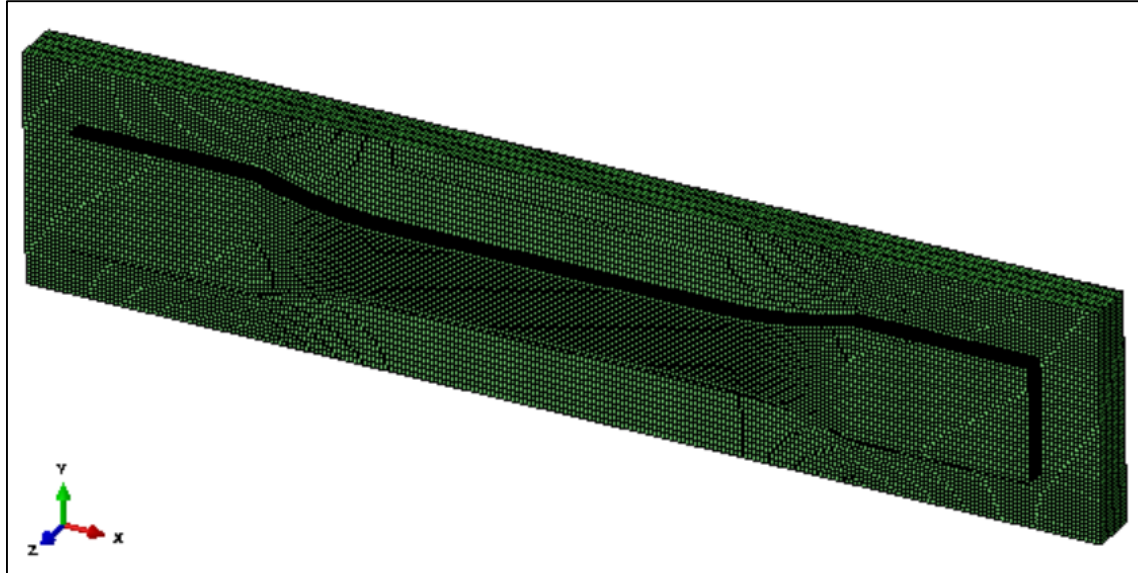


Figure 154: The orphan mesh from the imported copy of the thermal simulation

Navigate to a front view by using the icon toolbar. Using the scroll wheel, zoom the selection to the left end of the tensile specimen, producing the graphical depiction shown in Figure 155

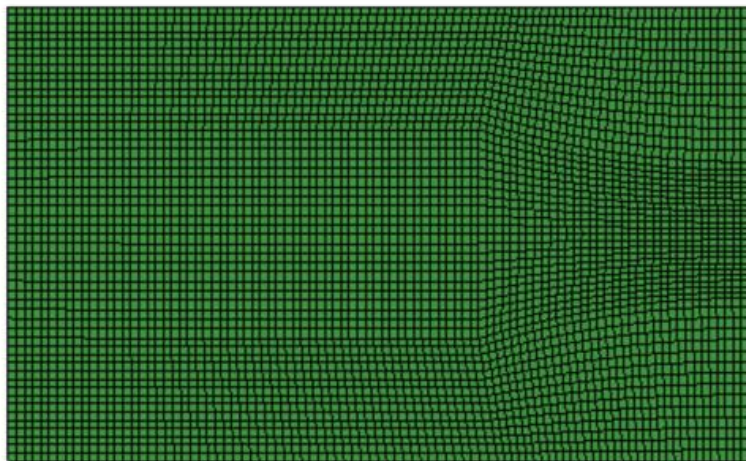


Figure 155: A front view of the orphan mesh of the tensile specimen and baseplate
(Shown zoomed to the region surrounding the grip specified as fixed)

On the character-based toolbar, under “Tools”, select Tools>>Set>>Create.... In the dialog window that appears, specify “Node” set, specify a name of “Fixed_node”, and select “OK”. Box-select the nodes corresponding to the grip-region. In doing so, it is best advised to overestimate the boundary of this box selection rather than underestimate it. By reorienting the view with either the view toolbar, or (Ctrl+Alt+MB1), one may hold the Ctrl key and make a box selection to remove a selection of nodes not intended to be a part of the specified set. It is worth noting that even a perfectly outlined selection of the grip region from a front view will still require a view reorientation to deselect nodes belonging strictly to the base plate. It is also worth noting that nodes belonging both to the grip region and to the base plate must be included in the node set definition. Complete the set definition by pressing MB3. In the “Message Area”, verify that the number of nodes in “Fixed_node” is 15750. If the definition is incorrect in name or number, another attempt may be made to reform the set definition by navigating to the set definition in the tree structure to the left-hand side of the screen. Given the case of incorrect definition, the set may be reformed by: a.) expanding the branch “D638HS11_heat - Copy”, b.) expanding the branch “Assembly”, c.) expanding the branch “Set”, and d.) selecting the set name with MB2 to bring up a pop-up menu, offering either the option to “Rename...” to amend a faulty name assignment, or “Edit...” to reform the node selection. This path is outlined graphically in Figure 156.

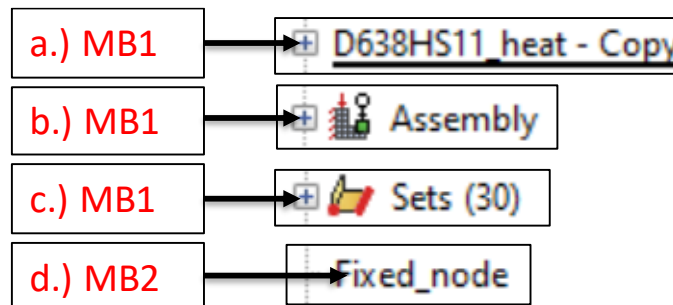


Figure 156: Navigating to a set definition to reform either the name or node assignments

Provided that the definition of the set “Fixed_node” is completed as intended, repeat the process outlining the node set definition to define a node set named “Load_node” corresponding to the grip region on the opposing end of the tensile specimen. A depiction of the complete selection of both “Fixed_node” and “Load_node” are shown in Figure 157.

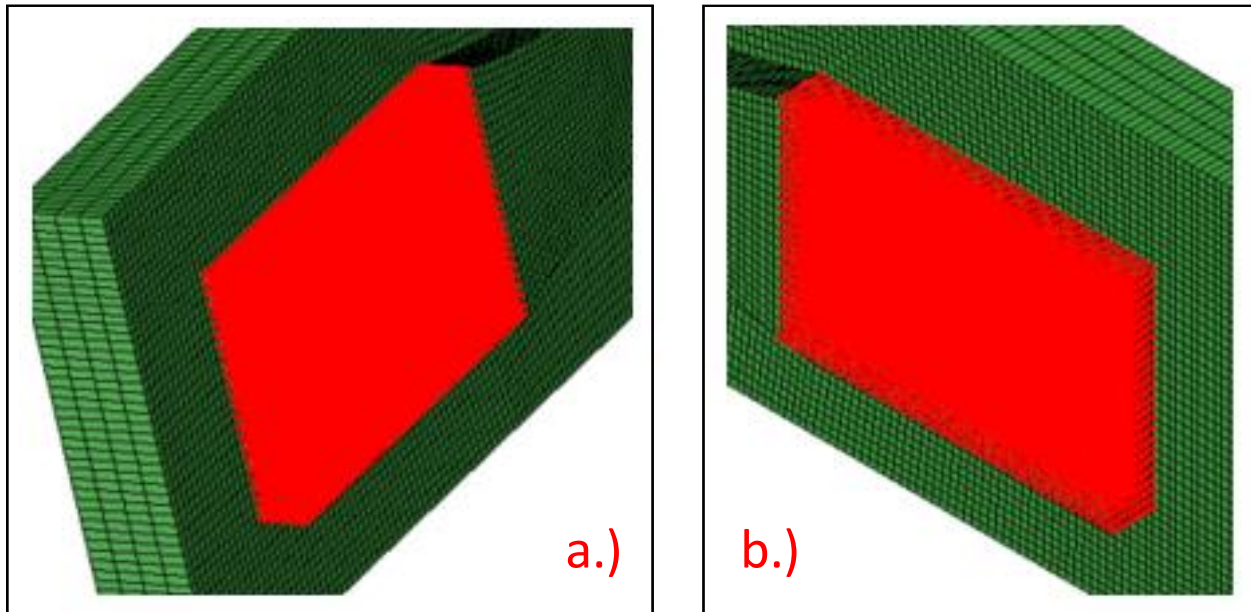


Figure 157: A depiction of the selection of “Fixed_node” and “Load_node”

After completing the definition of the node sets “Fixed_node” and “Load_node”, in the tree structure to the left-hand side of the screen, select “Jobs” with MB2, and select “Create” in the pop-up window that appears. Create a job named “Discard”, select “Continue” in the dialog window that appears, and select “OK” in the following dialog window. Once the job is created, a plus symbol will appear to the left of the “Jobs” category. Click this plus symbol to expand this branch, select the job “Discard” with MB2, and select “Write Input”. Select “Yes” to the missing section assignment prompt to complete the file write.

Next, open Notepad++, and open the job with the node set definitions: (filename: "Discard", filepath: C:\temp). Execute a find function, searching for the text "Fixed", leading the cursor to the beginning of the "Fixed_node" definition. Delete the instance definition at the end of the line, beginning with the comma following "*Nset, nset=Fixed_node". Similarly, execute a find function searching for "Load", leading the cursor to the beginning of the "Load_node" definition. Delete the instance definition at the end of the line, beginning with the comma following "*Nset, nset=Load_node". The exact boundaries of the removed text for both node sets are shown in Figure 158.

```

283863 *Nset, nset=Fixed_node, instance=PART-1-1
283864     4,    23,    26,    43,    72,    73,
283865     86,    87,    88,    89,    90,    91,
283866    102,   103,   104,   105,   106,   107,

284849 *Nset, nset=Load_node, instance=PART-1-1
284850     487,   501,   502,   524,   543,
284851     555,   556,   557,   558,   559,
284852     571,   572,   573,   574,   575,

```

Figure 158: Instance keyword removal for discarded input files to extract node set definitions

Next, copy and paste the entirety of both the "Fixed_node" and the "Load_node" set definitions into the service loading simulation, locating the pasted selection at the end of the file. With an input file size of this length, simply locating the boundaries of the node set definitions may prove cumbersome, however, as each line corresponds to sixteen node definitions, one may elect to use the line tags in Notepad++ to approximate the boundaries of the copied selections. For example, the node set "Fixed_node" was verified to contain 15,750 nodes upon writing the input file "Discard". If a find function is used to

determine that the definition “Fixed_node” starts on line 283864, dividing 15,750 by sixteen and adding the quotient to the starting line number would conclude the set “Fixed_node” ends at approximately line 284848. In the event that the beginning of the node set “Load_node” may be seen to immediately follow the end of “Fixed_node”, as is shown in Figure 158, this calculated quotient may be doubled and added to the starting line of “Fixed_node” to calculate the approximate boundary of the entire copied selection extracted from the file “Discard”.

After extracting the node sets from the file “Discard”, and pasting them into the service loading simulation, one must next define the tensile loading step. Navigate to the tutorial files directory, and open the file containing the tensile loading step definition: (filename: “TENSILE-LOAD-DEF.inp”, filepath: C:\temp\Tutorial Files). Copy the content of the tensile load file into the service loading simulation, at the bottom of the file.

In configuring the solver of the service loading simulation, there are two options, explicit and implicit. To specify an explicit solver, the content of the material definition and tensile load step need not be modified. To specify an implicit solver, minor revisions are required to the content of the material definition: “PLA-SPLY0001-ORIGINAL.inp”, and the tensile loading step: “TENSILE-LOAD-DEF.inp”. the user need only uncomment the lines in the material definition and the tensile loading definition that apply to implicit simulations and comment the lines (in both places) that apply to explicit simulations. These two modifications are shown below, as Figure 159, and Figure 160. Additionally, in order to bring in the void ratio results to an implicit simulation, the void ratio results earlier created for the “_disp” simulation must be duplicated, and specified a suffix “_load”.

```

*heading
Combine all layers together
*Preprint, echo=NO, model=NO, history=NO, contact=NO
*****
**      ABAQUS GENOA UMAT PROPERTIES (created by GENOA-MCQ)      ** Original, Configured for Explicit
*****
***INCLUDE, INPUT=ElementVoidRatio_ABAQUS_Explicit_Run1.inp
*MATERIAL, NAME = SPLY0001-VOID
*USER MATERIAL,CONSTANTS= 59
**      E11,      E22,      E33,      G12,      G13,      G23,      NU12,      NU13,
3.376000E+09, 3.183000E+09, 3.183000E+09, 1.177000E+09, 1.177000E+09, 1.200000E+09, 3.548900E-01, 3.548900E-01,
**      NU23,      S11T,      S11C,      S22T,      S22C,      S33T,      S33C,      S12S,
3.548900E-01, 6.000000E+07, 1.102170E+08, 5.270000E+07, 1.102170E+08, 5.270000E+07, 1.562170E+08, 3.432805E+07,
**      S13S,      S23S,      RHO,      DFACTT,      DFACTC,      DFACTS,      FFACT,      DAMAGE,
3.432805E+07, 3.432805E+07, 1.250000E+03, 1.000000E+00, 1.000000E+00, 1.000000E+00, 1.000000E-01, 16212,
**      FRACTURE,      EPS11T,      EPS11C,      EPS22T,      EPS22C,      EPS33T,      EPS33C,      EPS12S,
16212, 1, 1, 1, 1, 1, 1, 1,
**      EPS23S,      EPS13S,      STRAIN_1,      STRESS_1,      STRAIN_2,      STRESS_2,      STRAIN_3,      STRESS_3,
1, 1, 0.000000E+00, 0.000000E+00, 1.611104E-03, 5.439087E+06, 3.222205E-03, 1.087817E+07,
**      STRAIN_4,      STRESS_4,      STRAIN_5,      STRESS_5,      STRAIN_6,      STRESS_6,      STRAIN_7,      STRESS_7,
4.858686E-03, 1.631726E+07, 6.624450E-03, 2.175635E+07, 8.401236E-03, 2.719544E+07, 1.017801E-02, 3.263452E+07,
**      STRAIN_8,      STRESS_8,      STRAIN_9,      STRESS_9,      STRAIN_10,      STRESS_10,      STRAIN_11,      STRESS_11,
1.200080E-02, 3.807361E+07, 1.412164E-02, 4.351270E+07, 1.689852E-02, 4.895175E+07, 1.989775E-02, 5.439087E+07,
**      STRAIN_12,      STRESS_12,      MUP,
2.291548E-02, 6.000000E+07, 0.000000E+00,
*DEPVAR, DELETE = 4
10,
***DEPVAR
** 6
*DENSITY
1.250000E+07

```

Figure 159: The lines to change the material definition to an implicit simulation

```

*Amplitude, name=Amp-1, definition=EQUALLY SPACED, fixed interval=1.0
0., 1.
*Boundary
Fixed_node, 1, 1
Fixed_node, 4, 6
Load_node, 2, 6
**
*STEP, NAME=Tension
*DYNAMIC, EXPLICIT
,1.0
*Bulk Viscosity
0.06, 1.2
***STATIC
**0.01, 1, 1E-8, 0.01,
*INITIAL CONDITIONS, TYPE=STRESS, FILE=D638QHS11_disp, STEP=15, INC=1
*Boundary, amplitude=Amp-1
Load_node, 1, 1, 0.0013
*OUTPUT, FIELD, TIME INTERVAL=.005
*NODE OUTPUT
RF, U
*ELEMENT OUTPUT
LE, PE, SDV, S, TEMP, STATUS
***Output, history
**OUTPUT, HISTORY, VARIABLE=PRESELECT, TIME INTERVAL=.01
*END STEP

```

Figure 160: The lines to change the loading step to an implicit simulation

Executing the service loading simulation is done much in the same fashion as was shown in Figure 144, save for the specification of the file name suffix of “_load”, rather than “_heat”. As the procedure for

post-processing the simulation files will need likely be conducted many times for multiple simulations, the bulk of the instructional tutorial is shown in a truncated form below, as Figure 161.

Changes to Filename_heat:

- Make edit to temperature initial condition, change from 240 to 60
- Make edit to solid section, change elset bottom_plate from "bottom_material" to "mat_bottom_plate"
- Make edit to solid section, change elset elset_whole_part from "material" to "TNPLY00001"

Changes to Filename_disp:

- Add "-VOID" extension to material definition in *shell section
- Add "-VOID" extension to material definition in *material
- Make edit to solid section, change elset bottom_plate from "bottom_material" to "mat_bottom_plate"
- Make edit to solid section, change elset elset_whole_part from "material" to "TNPLY00001-VOID"
- Add 2x *STEP definitions, one for cooldown, one for plate removal

Changes to Filename_load:

- Add command *INCLUDE, INPUT=ElementVoidRatio_ABAQUS_Explicit_Run1.inp to bring in void result
- Copy "_disp" file to use as a template
- Delete material definition, and replace with definition from MCQ-Chopped
- Change *DEPVAR, DELETE = 3 to *DEPVAR, DELETE = 4
- Change line following *DEPVAR from 9 to 10
- Delete all element definitions corresponding to ELSET=BOTTOM_PLATE
- Change all element types from C3D8 to C3D8R
- Delete solid sections corresponding to "elset=bottom_plate"
- Modify solid section from "TNPLY00001-VOID" to "SPLY0001-VOID"
- Delete all text following initial conditions corresponding to temperature
- Copy "_heat" file to "_heatCOPY", open and delete all text after first found "**ELSET"
- Open "_heatCOPY" in CAE, define node sets for loading, create a job and write input
- Copy node set definitions out of written job and into Filename_load
- Clear "instance" types out of the copied node sets
- Paste definition of tensile definition, or other simulated service loading step
- Verify the direction of the loading versus the test being performed in both fixed and loaded boundary

Figure 161: Post-process steps for thermal, residual stress, and service loading simulations

To query the service loading response, the output database (.odb) file must be opened in ABAQUS CAE, and several quantities must be queried in order to define engineering stress and engineering strain. The

first quantity, engineering stress, is calculated as the summation of reaction forces over the cross-sectional area. The processes of querying reaction forces, summing reaction forces, measuring cross-section, and calculating engineering stress, are shown in Figure 162, Figure 163, Figure 164, and Figure 165, respectively.

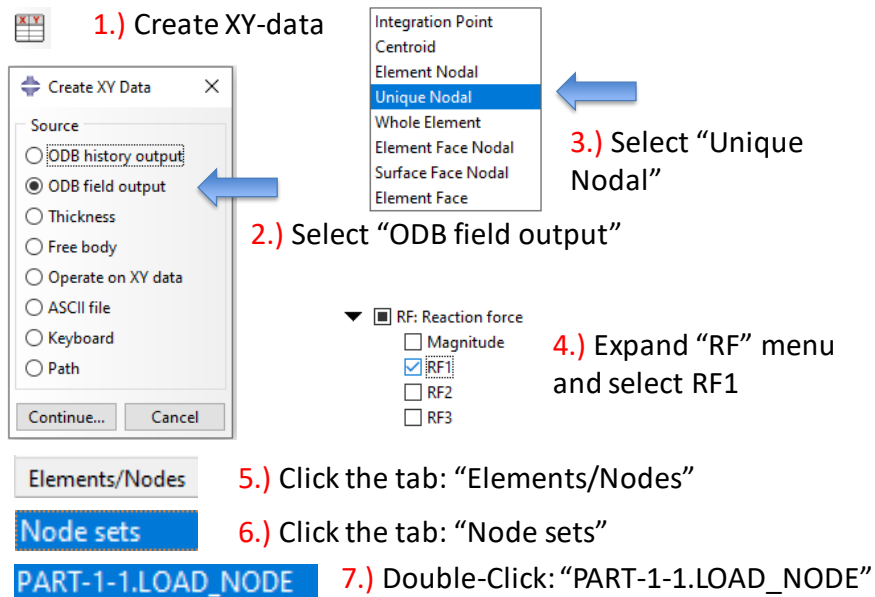


Figure 162: The 7-step process to query reaction forces

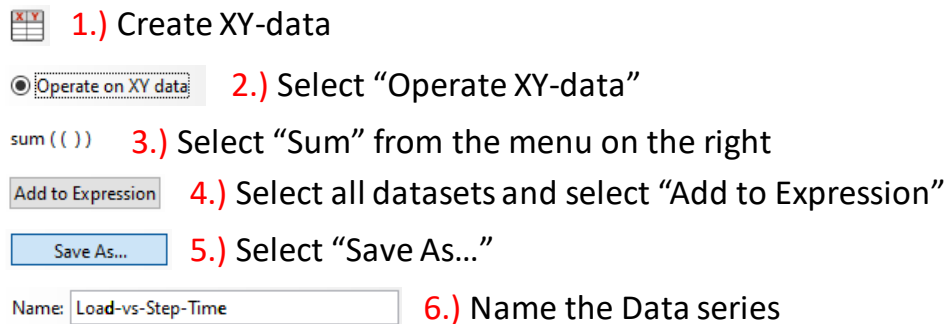


Figure 163: The 6-step process to sum reaction forces

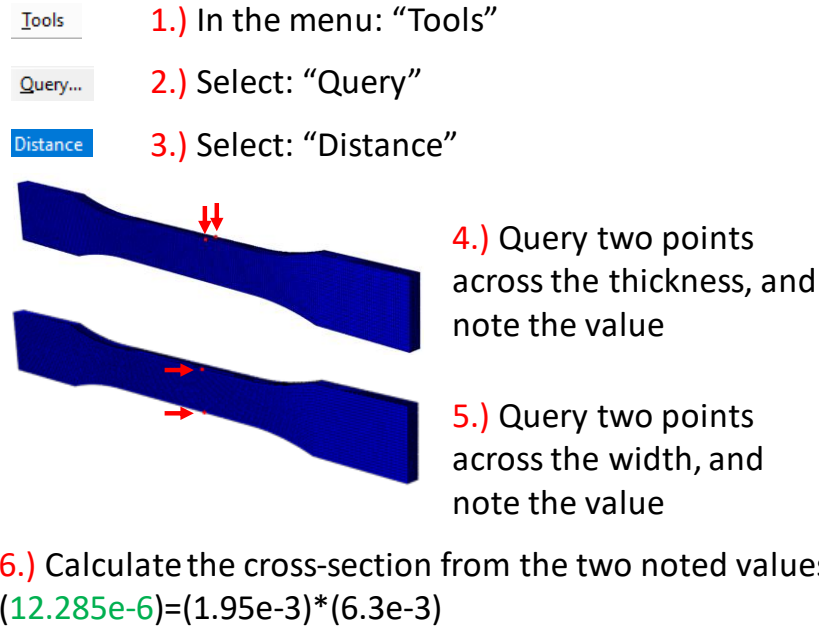


Figure 164: The 6-step process to measure the cross-sectional area

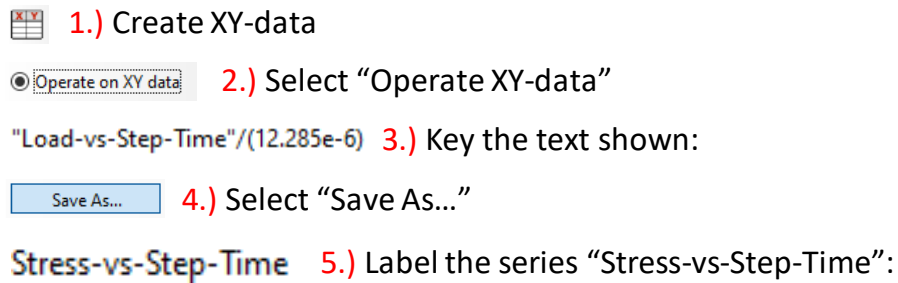


Figure 165: The 5-step process of calculating engineering stress

The second quantity, engineering strain, is calculated as the nodal displacement of a point on one end of the gauge length relative to a point on the opposing end of the gauge length. The processes of querying nodal displacement, determining engineering strain, and determining engineering-stress-vs-engineering-strain are shown in Figure 166, Figure 167, and Figure 168, respectively. A comparison of simulated result to material definition is shown following, as Figure 169.

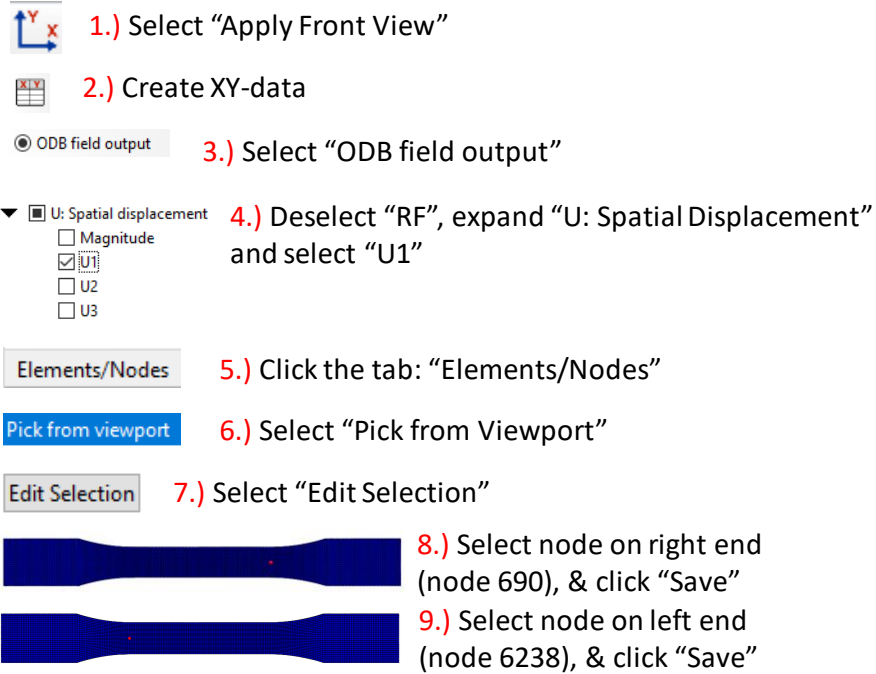


Figure 166: The 9-step process of querying nodal displacement

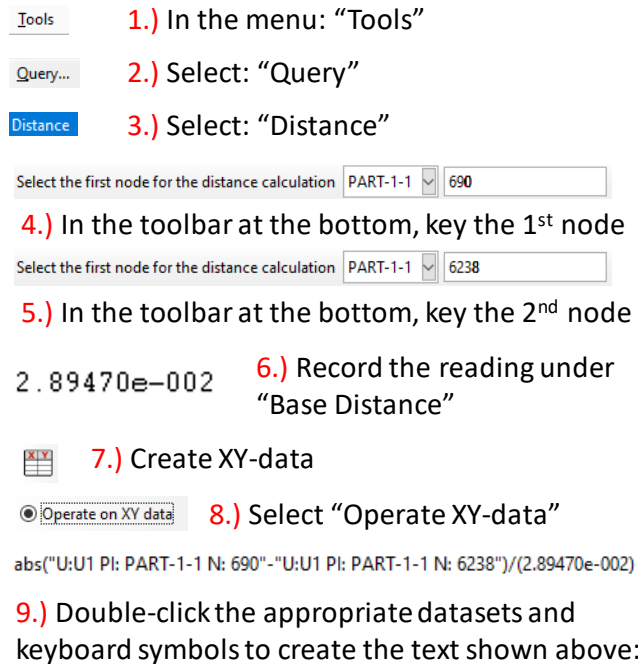


Figure 167: The 9-step process of determining strain

- 1.) Create XY-data
- 2.) Select "Operate XY-data"
combine ("Strain-vs-Step-Time", "Stress-vs-Step-Time")
- 3.) Click the datasets and use the keyboard to create the text shown above:

Save As...

- 5.) Once created, expand the XY-datasets to the left, right-click the series "Stress-vs-Strain", and select "Edit..."
- 6.) The first 81 cell pairs in this window represent simulated tensile stress-strain response, they may be copied to an interface such as Excel

Figure 168: The process of determining engineering stress vs engineering strain

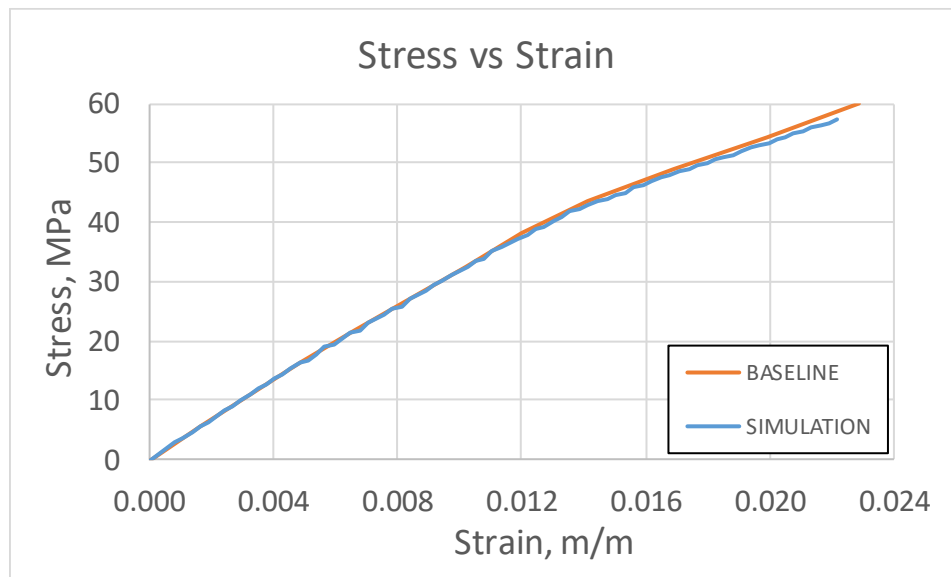


Figure 169: Simulated tensile response compared to Baseline definition tensile response

APPENDIX B: PRESENTATION OF SHEAR DATA FROM DIC TESTING

In the process of qualifying the behavior of printed material, a series of shear tests were conducted, generally following the test practice put forth by ASTM D5379 [49]. Three articles of three raster orientations were tested, similar to the strategy of investigation for tensile specimens introduced in Figure 10, and the strategy of bending specimens introduced in Figure 93. The orientations of the shear specimens are shown below, as Figure 170.

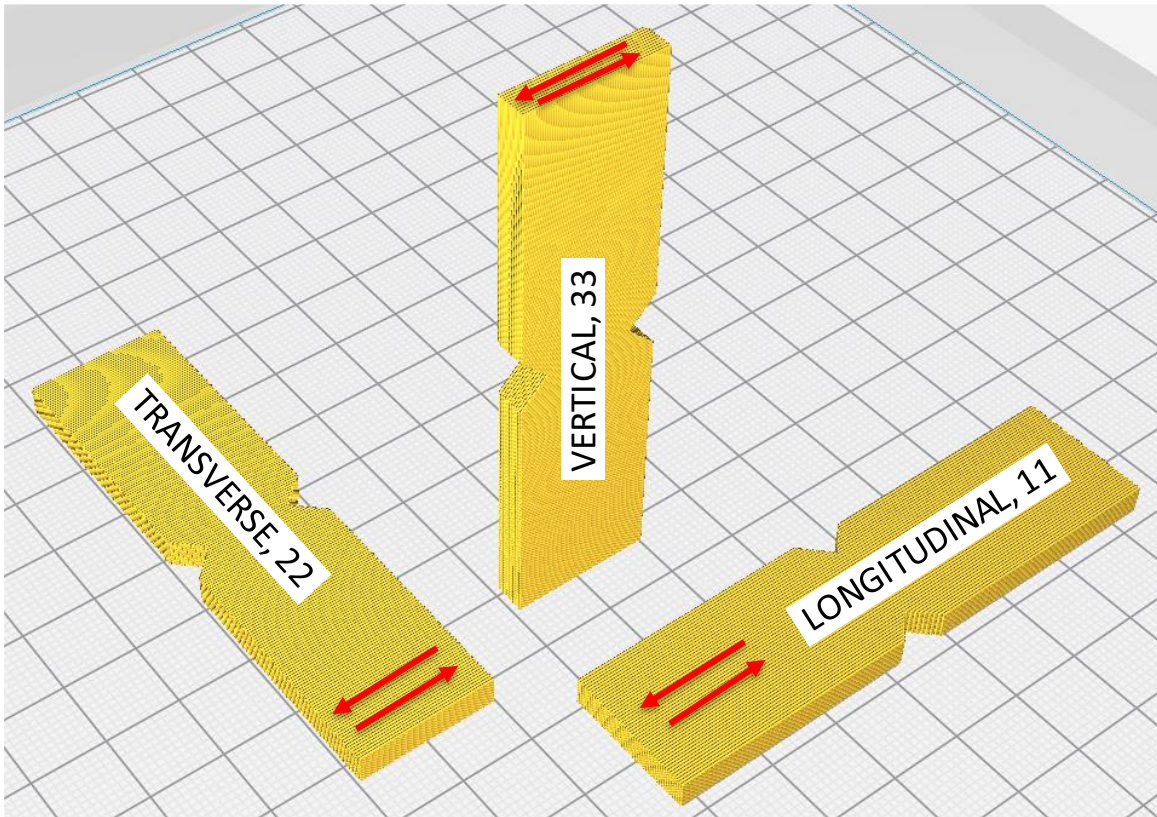


Figure 170: The orientations investigated for shear testing per ASTM 5379

The dimensions of each specimen were consistent with the geometry put forth by ASTM D5379, these dimensions are shown below, as Figure 171.

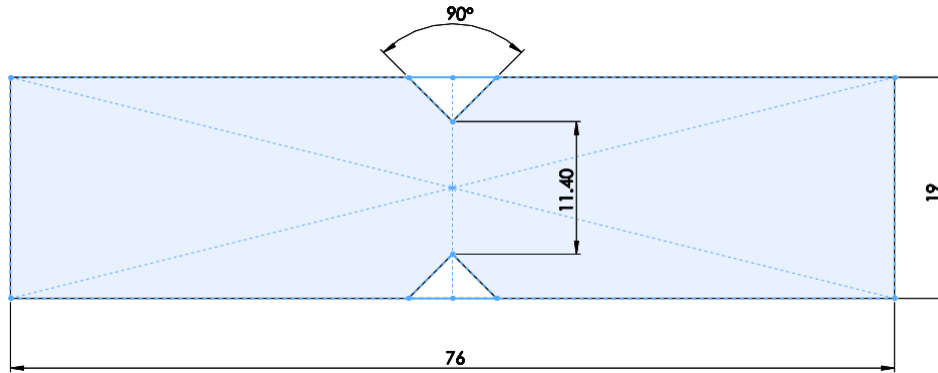


Figure 171: The dimensions of the printed shear specimen (millimeters)

Each specimen was printed with the scan strategy details largely defined in Table 2.1 and in Table A.1. The only difference in scan strategy concerns the omission of perimeter rasters, and omission of retractions in vertical specimen. The shear specimens in this study were printed absent perimeter rasters. Additionally, concerning vertical specimen only, odd-numbered layers had the path of the nozzle reversed, such that the end of one layer would simply be a vertical nozzle shift from the beginning of the next. The path of odd-numbered layers is shown below, as Figure 172a, the path of even-numbered layers is shown below, as Figure 172b.

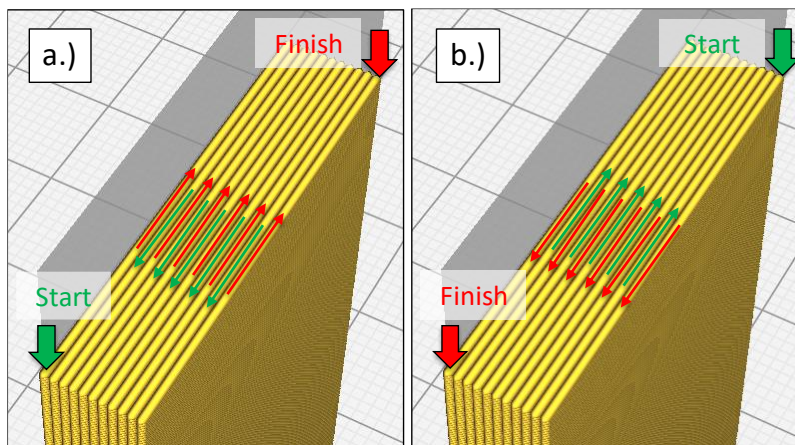


Figure 172: Depiction of the scan strategy for vertical specimens

A reversal of the scan strategy for odd-numbered layers was made because, upon printing specimen absent this change, a notable flaw was observed at both the site of the filament retraction (stop point of each layer), and the site of the filament forward (start point of each layer). These points, layer after layer, formed a ridge of material which was thought to promote difficulties in fixturing, so a strategy to print specimens in a vertical orientation which did not beget the introduction of retractions was sought. This ridge is easier to visualize and depict in an exaggerated nominal sense than with a realistic photo. As such, a CAD representation of the ridge is shown below, as Figure 173. In Figure 173a, a depiction of the actual geometry is shown absent the ridge. In Figure 173b, a depiction of the actual geometry with the ridge is shown.

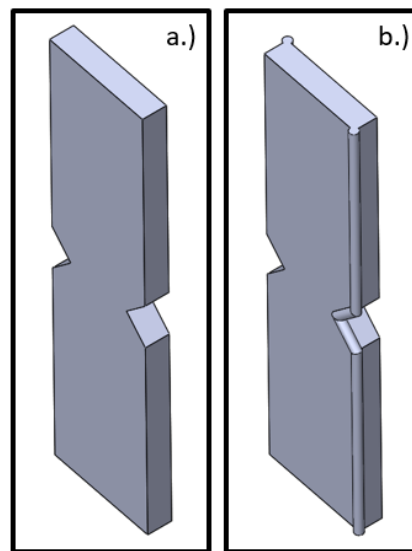


Figure 173: A depiction of the geometry of the vertical shear specimens

A total of thirteen specimens were printed, data capture was omitted for the three specimens presenting the ridge depicted in Figure 173b. Additionally, a data-capture flaw prevented the capture of the 7th shear specimen tested. The net result was the successful data capture for nine shear specimens, three in each investigated orientation. The nine successfully tested specimens are shown below, as Figure 174.

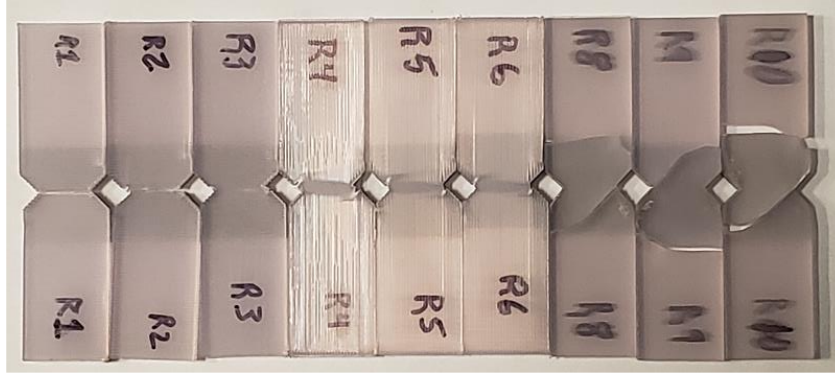


Figure 174: The shear specimens tested, after undergoing testing

In Figure 174, specimens R1-R3 are transverse strategy, specimens R4-R6 are longitudinal specimens, and specimens R8-R10 are vertical specimens. A black-and-white speckled pattern was laid across the bowtie section of each specimen (on the side opposing the label), and each specimen was sheared in an losipesque-shear apparatus, while under observation of a digital-image-correlation (DIC) apparatus. The raw imaging data was read into a post-processing interface to generate shear load versus shear-strain data. The data for each of the nine shear tests is shown below, as Figure 175 through Figure 183.

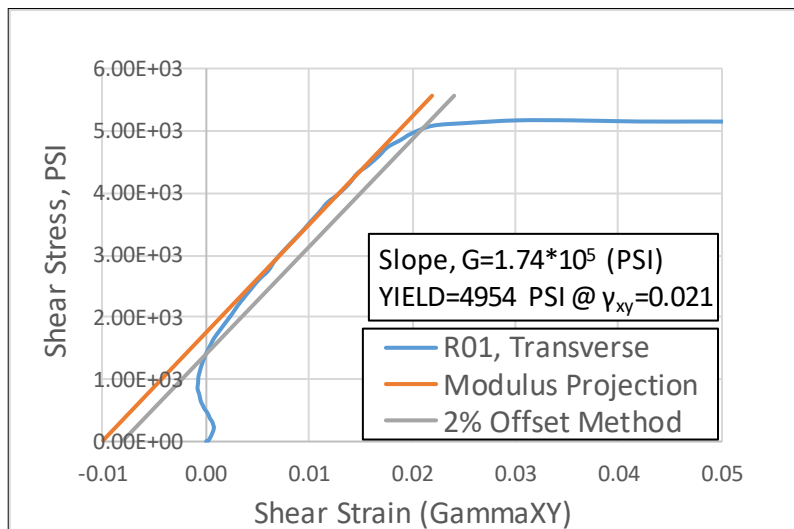


Figure 175: Shear Stress vs Shear Strain, Specimen "R01"

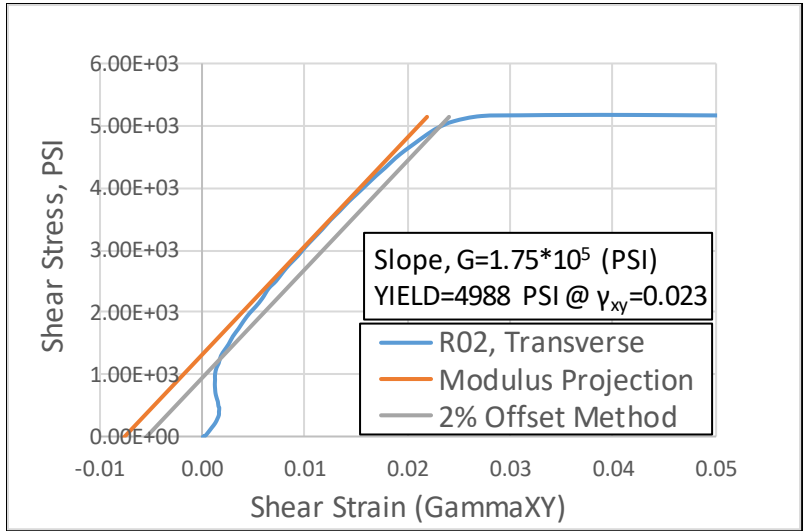


Figure 176: Shear Stress vs Shear Strain, Specimen "R02"

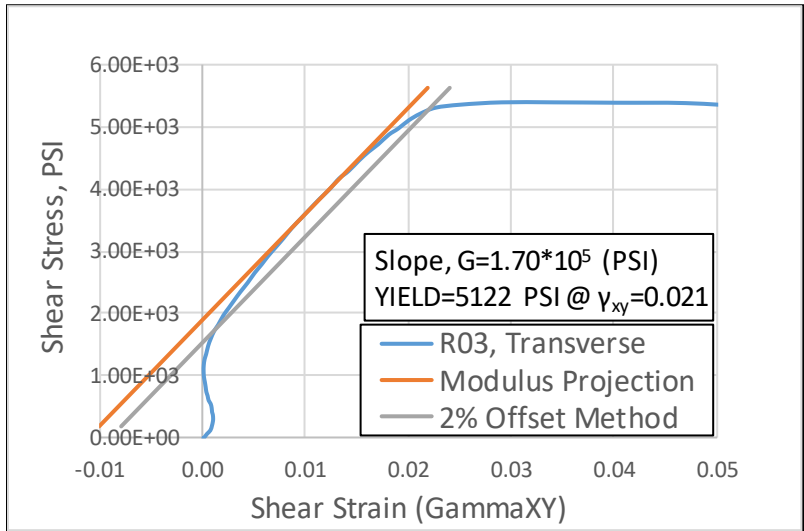


Figure 177: Shear Stress vs Shear Strain, Specimen "R03"

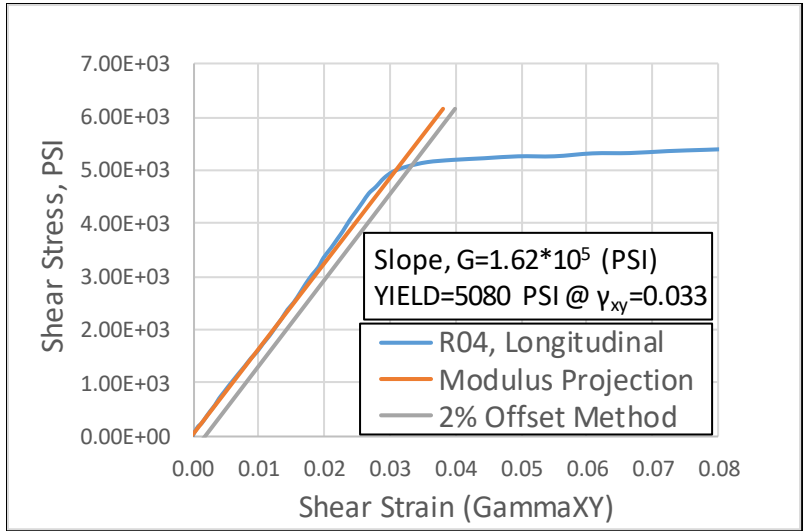


Figure 178: Shear Stress vs Shear Strain, Specimen "R04"

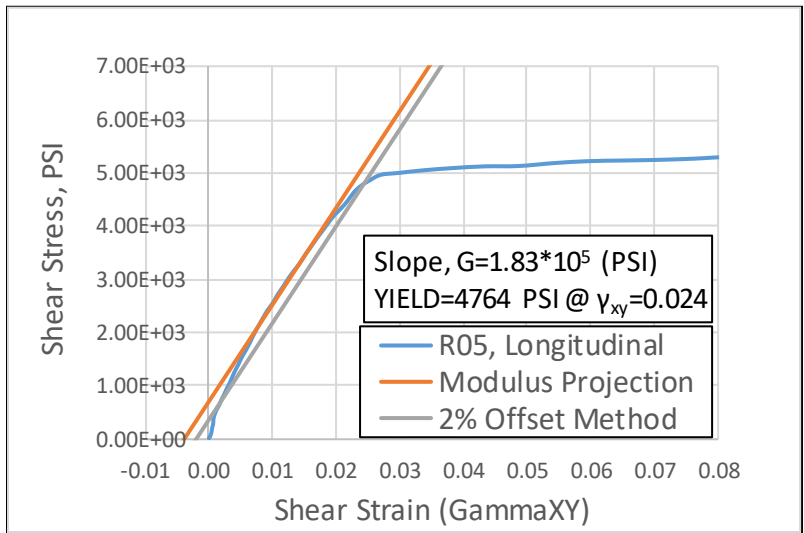


Figure 179: Shear Stress vs Shear Strain, Specimen "R05"

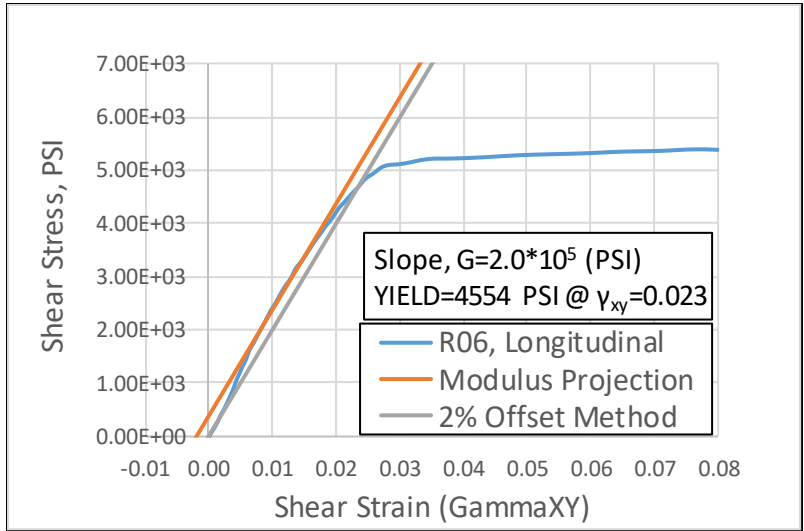


Figure 180: Shear Stress vs Shear Strain, Specimen "R06"

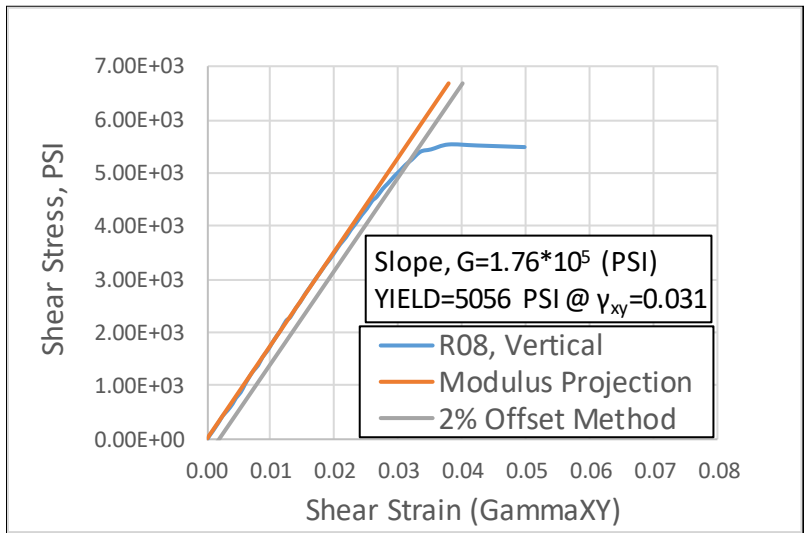


Figure 181: Shear Stress vs Shear Strain, Specimen "R08"

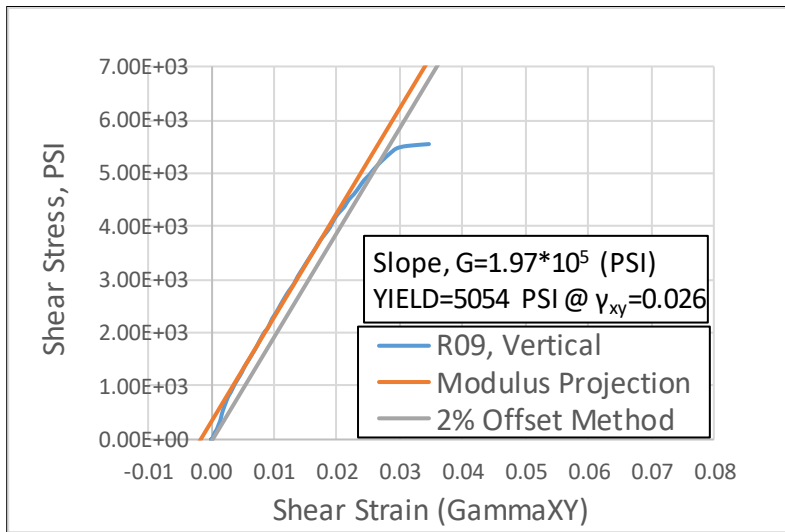


Figure 182: Shear Stress vs Shear Strain, Specimen "R09"

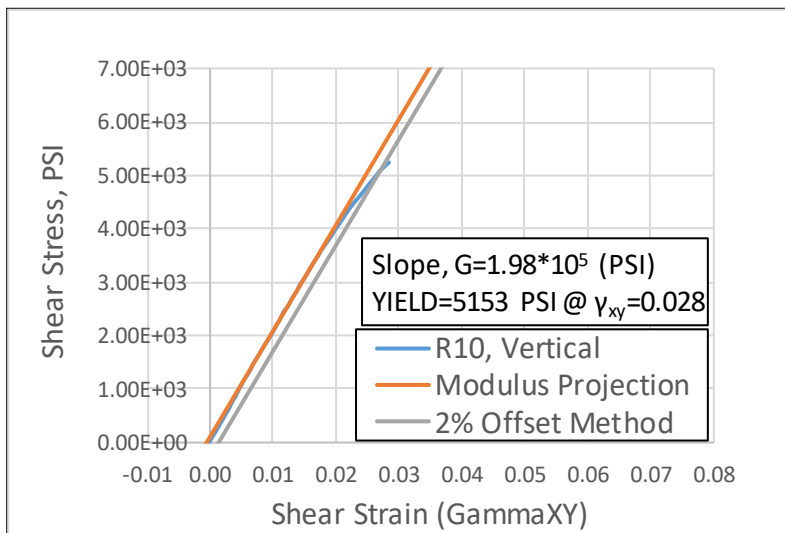


Figure 183: Shear Stress vs Shear Strain, Specimen "R10"

The characteristic of fracture observed during testing for the transverse specimens was a slow, ductile straining to fracture, and the fracture occurred along raster boundaries. The characteristic of fracture that was observed for the longitudinal specimens was also slow and ductile, but straining did not lead to a fracture event, instead exhibiting a large degree of plastic shear behavior. The characteristic of

fracture observed for the vertical specimens was a brittle fracture, at times throwing pieces of the specimen out of the fixture.

BIOGRAPHY OF THE AUTHOR

Aaron Grant was born in Middlebury, Vermont on July 7, 1986. He was raised in Ellsworth, Maine and graduated from Ellsworth High School in 2004. He attended the University of Maine and graduated in 2013 with a Bachelor's degree in Mechanical Engineering. He returned to Maine and entered the Mechanical Engineering graduate program at The University of Maine in the spring of 2018. After receiving his degree, Aaron will be joining Navatek. Aaron Grant is a candidate for the Master of Science degree in Mechanical Engineering from the University of Maine in December 2019.